frontiers | Research Topics

Advanced technologies of UAV application in crop pest, disease and weed control

Edited by
Ruirui Zhang, J. Connor Ferguson, Huizhu Yuan and Andrew Hewitt

Published in
Frontiers in Plant Science

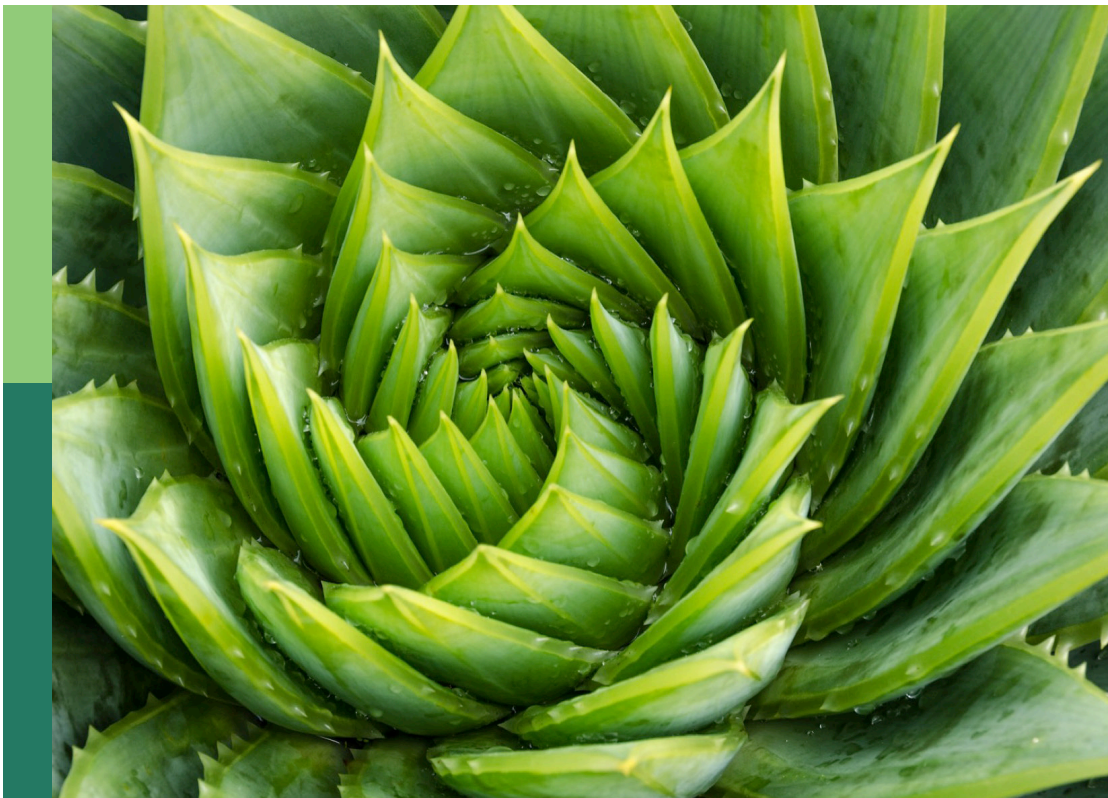

ISSN 1664-8714
ISBN 978-2-8325-1179-4
DOI 10.3389/978-2-8325-1179-4

About Frontiers

Frontiers is more than just an open access publisher of scholarly articles: it is a pioneering approach to the world of academia, radically improving the way scholarly research is managed. The grand vision of Frontiers is a world where all people have an equal opportunity to seek, share and generate knowledge. Frontiers provides immediate and permanent online open access to all its publications, but this alone is not enough to realize our grand goals.

Frontiers journal series

The Frontiers journal series is a multi-tier and interdisciplinary set of open-access, online journals, promising a paradigm shift from the current review, selection and dissemination processes in academic publishing. All Frontiers journals are driven by researchers for researchers; therefore, they constitute a service to the scholarly community. At the same time, the *Frontiers journal series* operates on a revolutionary invention, the tiered publishing system, initially addressing specific communities of scholars, and gradually climbing up to broader public understanding, thus serving the interests of the lay society, too.

Dedication to quality

Each Frontiers article is a landmark of the highest quality, thanks to genuinely collaborative interactions between authors and review editors, who include some of the world's best academicians. Research must be certified by peers before entering a stream of knowledge that may eventually reach the public - and shape society; therefore, Frontiers only applies the most rigorous and unbiased reviews. Frontiers revolutionizes research publishing by freely delivering the most outstanding research, evaluated with no bias from both the academic and social point of view. By applying the most advanced information technologies, Frontiers is catapulting scholarly publishing into a new generation.

What are Frontiers Research Topics?

Frontiers Research Topics are very popular trademarks of the *Frontiers journals series*: they are collections of at least ten articles, all centered on a particular subject. With their unique mix of varied contributions from Original Research to Review Articles, Frontiers Research Topics unify the most influential researchers, the latest key findings and historical advances in a hot research area.

Find out more on how to host your own Frontiers Research Topic or contribute to one as an author by contacting the Frontiers editorial office: frontiersin.org/about/contact

Advanced technologies of UAV application in crop pest, disease and weed control

Topic editors

Ruirui Zhang — Beijing Academy of Agricultural and Forestry Sciences, China

J. Connor Ferguson — Sesaco Corporation, United States

Huizhu Yuan — State Key Laboratory for Biology of Plant Diseases and Insect Pests, Institute of Plant Protection (CAAS), China

Andrew Hewitt — The University of Queensland, Australia

Citation

Zhang, R., Ferguson, J. C., Yuan, H., Hewitt, A., eds. (2023). *Advanced technologies of UAV application in crop pest, disease and weed control*.

Lausanne: Frontiers Media SA. doi: 10.3389/978-2-8325-1179-4

Table of contents

frontiers | Frontiers in Plant Science

TYPE Editorial
PUBLISHED 16 August 2023
DOI 10.3389/fpls.2023.1253841

OPEN ACCESS

EDITED AND REVIEWED BY
Roger Deal,
Emory University, United States

*CORRESPONDENCE
Ruirui Zhang
rui7986@126.com

RECEIVED 06 July 2023
ACCEPTED 03 August 2023
PUBLISHED 16 August 2023

CITATION
Zhang R, Hewitt A, Li L, Yuan H, Ferguson JC and Chen L (2023) Editorial: Advanced technologies of UAV application in crop pest, disease and weed control. *Front. Plant Sci.* 14:1253841. doi: 10.3389/fpls.2023.1253841

Editorial: Advanced technologies of UAV application in crop pest, disease and weed control

Ruirui Zhang[1,2]*, Andrew Hewitt[3], Longlong Li[1,2], Huizhu Yuan[4], J. Connor Ferguson[5] and Liping Chen[1,2]

[1]National Research Center of Intelligent Equipment for Agriculture, Beijing Academy of Agricultural and Forestry Sciences, Beijing, China, [2]National Center for International Research on Agricultural Aerial Application Technology, Beijing, China, [3]Centre for Pesticide Application and Safety, The University of Queensland, Brisbane, QLD, Australia, [4]State Key Laboratory for Biology of Plant Diseases and Insect Pests, Institute of Plant Protection, Chinese Academy of Agricultural Sciences (CAAS), Beijing, China, [5]Sesaco Corporation, Austin, TX, United States

KEYWORDS

UAV (unmanned aerial vehicle), plant protection, aerial spray application, remote sensing, chemical application

Editorial on the Research Topic
Advanced technologies of UAV application in crop pest, disease and weed control

In recent years, the use of unmanned aerial vehicles (UAVs) as auto-spraying machines for plant protection has been increasing (Hu et al., 2022). Recent research has been conducted on the spray deposition/drift patterns of plant protection UAVs (Tang et al., 2020; Li et al., 2022), but further exploration is required to ensure their efficient and accurate application. This Research Topic aims to conduct in-depth studies on new technologies for the application of plant protection UAVs in crop pest, disease, and weed control. The published articles cover four topics including pest, disease, weed detection, and identification; canopy remote sensing and identification; strategies for improving the spray quality of UAV applications; and spray drift assessment. This research aims to serve as a reference for new theories and advanced technologies and to optimize the use of UAVs in crop pest, disease, and weed control, helping to expand the application potential of plant-protection UAVs.

Pest, disease, and weed detection and identification

Accurate target detection is crucial for establishing prescriptions for chemical applications and enabling variable spraying with UAVs. This has become even more important in the application of high-speed plant-protection UAVs, where there is increased demand for precise target identification.

Xia et al. presented a method for identifying resistant weed biotypes using multispectral and RGB images based on a deep convolutional neural network (DCNN). They developed a weed spectral resistance index (WSRI) that compared susceptible and resistant weed biotypes. By fusing multispectral and RGB images, they enhanced the accuracy of

resistance identification. The DCNN achieved impressive field accuracies of 81.1% and 92.4% for barnyard grass and velvet leaves, respectively.

In another study, Yu et al. developed a weed vegetation index ($WDVI_{NIR}$) by utilizing the reflectance of three bands—red, green, and near-infrared— captured by multispectral images. Compared with the traditional vegetation indices of NDVI, LCI, NDRE, and OSAVI, $WDVI_{NIR}$ showed the most effective ability to identify weeds from rice, water cotton, and soil, with a weed identification accuracy of 93.47% and a kappa coefficient of 0.859.

In addition to weed identification, Lu et al. proposed a method for estimating leaf chlorophyll content in jujube leaves infested by leaf mites using soil plant analysis development (SPAD). Their approach aimed to estimate the severity of mite infestation by correlating it with the SPAD values of jujube leaves. A particle swarm optimization-extreme learning machine (PSO-ELM) for SPAD and vegetation indices were established and exhibited superior accuracy ($R^2 = 0.856$, $RMSE = 0.796$) when compared with the ELM model alone ($R^2 = 0.748$, $RMSE = 1.689$). This indirect measurement approach is a novel method for detecting and identifying pests and diseases.

Canopy remote sensing and identification

A high-precision canopy segmentation methodology called MPAPR R-CNN, specifically designed for high-density cultivation orchards, was proposed utilizing low-altitude visible light images (Zhang et al.). This method accurately identifies and segments the canopy edge, which can be affected by tree branch extensions and shadow obstructions. The researchers employed a Mask R-CNN as the base segmentation algorithm, incorporating a path augmentation feature pyramid network (PAFPN) and the PointRend algorithm to achieve precise boundary delineation of apple tree canopies. Training with the PAFPN and Point-Rend backbone head resulted in significant improvements, with average precision scores increasing by 8.96%.

Li et al. introduced a deep-learning-based method for counting maize plants using image datasets. A real-time detection model for maize plants was trained based on YOLOv5, and a tracking and counting approach was developed using Hungarian matching and Kalman filtering algorithms. The maize plant counts using this method exhibited a high correlation with the manual count results ($R^2 = 0.92$). In a separate study, Zhang et al. proposed an improved lightweight network, improved YOLOv5s, for dragon fruit detection in an all-weather environment. The results demonstrated that the model achieved a mean average precision (mAP) of 97.4%, precision (P) of 96.4%, and recall rate (R) of 95.2%. Compared with the original YOLOv5s network, the improved model exhibited a reduction in model size, params, and floating-point operations (FLOPs) by 20.6%, 18.75%, and 27.8%, respectively.

Strategies for improving spray quality of UAV application

Liu et al. conducted a study that investigated the impact of adjuvants on the physicochemical properties of defoliant solutions and droplet deposition in defoliation spraying using plant-protection UAVs. They aimed to determine the type of adjuvant that enhances the effect of defoliation on pepper plants. Previous research has demonstrated that the appropriate addition of additives to a spray solution can reduce spray drift and improve droplet adhesion to leaves. By employing this method, droplet deposition increases, and the defoliation effect is achieved. Among the adjuvants used in their study, Puliwang was the most efficient for the aerial application of defoliants.

Downwash airflow is a prominent characteristic of plant-protection UAV operations. Chang et al. employed the Lattice Boltzmann Method (LBM) to investigate the rotor flow field of a quadrotor plant-protection UAV at different speeds. As the rotor speed increased, the maximum velocity and vorticity of the wind field under the rotor increased gradually, whereas the ultimate values of the velocity and vorticity decreased owing to the emergence of turbulence. This is expected to reveal and comprehend the changes in the rotor flow field of plant-protection UAVs as the pesticide loading dynamically evolves.

Considering the limited deposition in the lower canopy when using plant-protection UAVs, particularly in high-density fruit trees, Jiang et al. developed a stereoscopic plant-protection system (SPS) consisting of a small swing-arm ground sprayer and a UAV sprayer. This approach demonstrated that the density of vertical droplet deposition in the canopies ranged from 90 to 107 deposits/cm^2, and the uniformity was 38.3% higher than that of conventional methods.

Spray drift assessment

The primary current challenge to the widespread adoption of plant-protection UAVs is the potential risk associated with spray drift exposure in pesticide applications. Accurate measurement of spray drift is crucial because it serves as the basis for scientifically developing spray technology and selecting appropriate operating environments. Li et al. presented a method for evaluating spray drift based on 3D point cloud data from a light detection and range technique (LiDAR). LiDAR measurements provide valuable spatial information, including the height and width of drifting droplets (Liu et al., 2022). However, it is important to note that LiDAR detection is sensitive to droplet density or drift mass in space, and drift clouds with lower densities and smaller droplet sizes may not be effectively detected by LiDAR. This method has the potential to serve as an alternative tool for evaluating the drifts of different spray configurations, although it may not provide direct measurements of the actual spray drift mass.

Conclusion

Plant-protection UAVs are a promising tool, having shown significant success in East Asia, particularly in China, which is the focus of the articles in this Research Topic. All of these published manuscripts were funded by the Chinese government. Australian scholars have also contributed to the study of spray drift evaluation using 3D LiDAR. The greatest challenges faced by plant-protection UAVs in global applications are safety concerns and incidents of environmental pollution caused by the off-target drift of high-concentration pesticides induced by downwash flow at a higher operating altitude. In addition, some users have a limited understanding of plant-protection UAVs, particularly regarding the feasibility of using a minimal application volume rate for pest and disease control. Nevertheless, the situation may eventually change with new technological developments, given the exceptional operational capabilities of plant-protection UAVs in China.

We hope that the readers will find this Research Topic a valuable reference for understanding state-of-the-art advanced technologies in UAV chemical applications and their practical implications for precise spraying.

Author contributions

RZ: Conceptualization, Funding acquisition, Investigation, Project administration, Writing – original draft, Writing – review & editing. AH: Validation, Writing – review & editing. LL: Data curation, Writing – original draft, Writing – review & editing. HY: Validation, Writing – review & editing. JF: Validation, Writing – review & editing. LC: Validation, Writing – review & editing.

Funding

We acknowledge support from the National Natural Science Foundation of China (Grant no. 32071907).

Acknowledgments

The editors would like to thank the authors, reviewers, and Frontiers in Plant Science team, whose efforts contributed to the creation of this Research Topic.

Conflict of interest

JF was employed by the Sesaco Corporation.

The authors declare that the research was conducted in the absence of commercial or financial relationships that could be construed as potential conflicts of interest.

Publisher's note

References

Hu, P., Zhang, R., Yang, J., and Chen, L. (2022). Development status and key technologies of plant protection UAVs in China: A review. *Drones* 6, 354. doi: 10.3390/drones6110354

Li, L., Hu, Z., Liu, Q., Yi, T., Han, P., Zhang, R., et al. (2022). Effect of flight velocity on droplet deposition and drift of combined pesticides sprayed using an unmanned aerial vehicle sprayer in a peach orchard. *Front. Plant Sci.* 13, 981494. doi: 10.3389/fpls.2022.981494

Liu, B., Li, L., Zhang, R., Tang, Q., Ding, C., Xu, G., et al. (2022). Analysis of the spatial and temporal distribution of a spray cloud using commercial LiDAR. *Biosyst. Eng.* 223, 78. doi: 10.1016/j.biosystemseng.2022.08.017

Tang, Q., Zhang, R., Chen, L., Deng, W., Xu, M., Xu, G., et al. (2020). Numerical simulation of the downwash flow field and droplet movement from an unmanned helicopter for crop spraying. *Comput. Electron. Agric.* 174, 105468. doi: 10.1016/j.compag.2020.105468

frontiers | Frontiers in Plant Science

ORIGINAL RESEARCH
published: 05 July 2022
doi: 10.3389/fpls.2022.938604

Identification and Comprehensive Evaluation of Resistant Weeds Using Unmanned Aerial Vehicle-Based Multispectral Imagery

Fulin Xia[2], Longzhe Quan[1,2], Zhaoxia Lou[2], Deng Sun[2], Hailong Li[1] and Xiaolan Lv[3]*

[1] College of Engineering, Anhui Agricultural University, Anhui, China, [2] College of Engineering, Northeast Agricultural University, Harbin, China, [3] Institute of Agricultural Facilities and Equipment, Jiangsu Academy of Agricultural Sciences (JAAS), Jiangsu, China

Atrazine is one of the most widely used herbicides in weed management. However, the widespread use of atrazine has concurrently accelerated the evolution of weed resistance mechanisms. Resistant weeds were identified early to contribute to crop protection in precision agriculture before visible symptoms of atrazine application to weeds in actual field environments. New developments in unmanned aerial vehicle (UAV) platforms and sensor technologies promote cost-effective data collection by collecting multi-modal data at very high spatial and spectral resolution. In this study, we obtained multispectral and RGB images using UAVs, increased available information with the help of image fusion technology, and developed a weed spectral resistance index, WSRI = (RE-R)/(RE-B), based on the difference between susceptible and resistant weed biotypes. A deep convolutional neural network (DCNN) was applied to evaluate the potential for identifying resistant weeds in the field. Comparing the WSRI introduced in this study with previously published vegetation indices (VIs) shows that the WSRI is better at classifying susceptible and resistant weed biotypes. Fusing multispectral and RGB images improved the resistance identification accuracy, and the DCNN achieved high field accuracies of 81.1% for barnyardgrass and 92.4% for velvetleaf. Time series and weed density influenced the study of weed resistance, with 4 days after application (4DAA) identified as a watershed timeframe in the study of weed resistance, while different weed densities resulted in changes in classification accuracy. Multispectral and deep learning proved to be effective phenotypic techniques that can thoroughly analyze weed resistance dynamic response and provide valuable methods for high-throughput phenotyping and accurate field management of resistant weeds.

Keywords: atrazine-resistant weed, multispectral reflectance, vegetation indices (VIs), unmanned aerial vehicle (UAV), deep convolutional neural networks (DCNNs)

Abbreviations: UAV, unmanned aerial vehicle; DCNN, deep convolutional neural network; VIs, vegetation index; WSRI, weed spectral resistance index; B, blue band; G, green band; R, red band; NIR, near-infrared band; RE, red edge band; RTK, real-time kinematic; GCPs, round control points; GS, Gram–Schmidt; DOM, digital orthophoto maps; BAD, before application day; AD, application day; DAA, days after application; RES, resistant weeds; SUP, susceptible weeds.

OPEN ACCESS

Edited by:
Ruirui Zhang,
Beijing Academy of Agricultural and Forestry Sciences, China

Reviewed by:
Pei Wang,
Southwest University, China
Lang Xia,
Institute of Agricultural Resources and Regional Planning (CAAS), China
Jianli Song,
China Agricultural University, China

****Correspondence:***
Longzhe Quan
quanlongzhe@163.com

Specialty section:
This article was submitted to Technical Advances in Plant Science, a section of the journal Frontiers in Plant Science

Received: *07 May 2022*
Accepted: *10 June 2022*
Published: *05 July 2022*

Citation:
Xia F, Quan L, Lou Z, Sun D, Li H and Lv X (2022) Identification and Comprehensive Evaluation of Resistant Weeds Using Unmanned Aerial Vehicle-Based Multispectral Imagery. Front. Plant Sci. 13:938604. doi: 10.3389/fpls.2022.938604

INTRODUCTION

Weeds are one of the major factors affecting crop growth and are the most significant contributors to yield loss globally (Quan et al., 2021). Overreliance on commonly used chemical herbicides has resulted in the appearance of several herbicide-resistant weed biotypes (Colbach et al., 2017). Developing a method that can indicate herbicide resistance within an acceptable timeframe after an application can potentially help growers manage their fields more effectively (Krähmer et al., 2020).

Atrazine (chemical name: 2-chloro-4-ethylamino-6-isopropylamino-1,3,5-triazine) belongs to the S-triazine class of herbicides and blocks the electron flow between photosystems (Foyer and Mullineaux, 1994). Atrazine herbicide can significantly reduce photosynthesis by reducing photosystem II (Sher et al., 2021) and is a widely used herbicide in maize fields to control broadleaf and grassy weeds (Williams et al., 2011). Its widespread use has also accelerated the evolution of weed resistance mechanisms (Kelly et al., 1999; Williams et al., 2011; Perotti et al., 2020).

However, high-throughput herbicide resistance phenotyping remains a technical bottleneck, limiting the ability to effectively manage weeds in the field. Before herbicide application, there is no significant difference in the visual appearance of susceptible and resistant weeds of the same species (Eide et al., 2021a). Laboratory determination of various enzymes present within plant leaves can identify atrazine resistance but is impractical to use in large-scale applications (Liu et al., 2018). Hyperspectral systems to detect differences between resistant and susceptible biotypes have shown potential in controlled environments (Shirzadifar et al., 2020b), but their effectiveness is drastically reduced once introduced into field conditions (Shirzadifar et al., 2020a). The unstable performance of thermal imagery further suggested that canopy temperature data were likewise not a reliable predictor of weed resistance (Eide et al., 2021b). Outdoor resistance identification methods include whole-plant dose–response assay tests (Huan et al., 2011), but their investigation area is fixed and limited, resulting in high deployment expense and poor timeliness. Thus, current phenotypic analysis methods can hardly satisfy the high-throughput survey requirements for resistant weeds in the field.

Field-based fast, accurate, and robust phenotyping methods are essential for atrazine-resistant weed investigation. Atrazine applications reduce the efficiency of the photosynthetic mechanism and affect chlorophyll and other pigments, which change the spectral reflectance of plants in the visible/near-infrared range (Sher et al., 2021). Therefore, it is assumed that the spectral characteristics of susceptible weeds should show different pathways compared to resistant weeds after herbicide application. These physiological changes induced by herbicide stress have laid the foundation for monitoring resistance using vegetation indices (VIs) (Duddu et al., 2019). Multispectral bands and the normalized difference vegetation index (NDVI) provide improved glyphosate resistance classification (Eide et al., 2021a). Therefore, Vis-based high-throughput phenotyping methods can be reliably applied to atrazine-resistant weed investigation in the field.

Unmanned aerial vehicles (UAVs) are a popular remote sensing platform successfully used to obtain high-resolution aerial images for weed detection and mapping (Su et al., 2022) because they can be equipped with various imaging sensors to collect high-spatial, -spectral, and -temporal resolution images (Yang et al., 2017, 2020). For example, UAVs have been used for physiological and geometric plant characterization (Zhang et al., 2020; Meiyan et al., 2022), as well as for pest and disease classification (Dai et al., 2020; Xia et al., 2021) and resistant weed identification (Eide et al., 2021a). In addition, remote sensing imagery is linked to specific farm problems through deep learning for the identification of biological and non-biological stresses in crops (Francesconi et al., 2021; Ishengoma et al., 2021; Jiang et al., 2021; Zhou et al., 2021), segmentation, and classification (He et al., 2021; Osco et al., 2021; Vong et al., 2021). These studies show that the combination of UAV remote sensing and deep learning provides the scope for large-scale resistant weed evaluation (Krähmer et al., 2020; Wang et al., 2022).

This study explores the potential for using multispectral images collected by UAVs in crop fields for identifying resistant weeds and proposes an effective method to identify resistant weeds in real field environments. We propose a weed spectral resistance index called WSRI = (RE-R)/(RE-B) to investigate resistant weeds by analyzing the canopy spectral response of barnyardgrass and velvetleaf. The fusion of multispectral and RGB images combining canopy spectral and texture feature information and applying a deep convolutional neural network (DCNN) are carried out to evaluate the potential for identifying resistant weeds in the field based on their dynamic response.

MATERIALS AND METHODS

Test Site and Experimental Setup

The weed resistance experiment was conducted at the Xiangyang Farm, Northeast Agricultural University, Harbin, Heilongjiang, China (45°61′ N, 126°97′ E), as shown **Figure 1**. The region has a cold-temperate continental climate, with average annual precipitation of 400–600 mm and an average annual effective temperature of 2,800°C. The experimental soil type is black soil, with a soil tillage layer, a nitrogen content of 0.07–0.11%, a fast-acting phosphorous content of 20.5–55.8 mg/kg, and a fast-acting potassium content of 116.6–128.1 mg/kg.

Two different weed species were selected for this study. Common broadleaf and grassy weeds in the Heilongjiang region include barnyardgrass (Echinochloa crusgalli (L.) Beauv) and velvetleaf (Abutilon theophrasti Medicus). Weed seeds were collected from 20 different fields in Heilongjiang and confirmed to be atrazine-susceptible and -resistant biotypes (Liu et al., 2018). The seeds were air-dried and stored at 4°C. The field was treated with glufosinate at 0.45 kg active ingredient (AI) ha^{-1} plus pendimethalin at 1.12 kg AI ha^{-1} before planting to kill existing vegetation and provide residual weed control 1 week before crop planting.

In this trial, maize seeds were first sown in black soil on May 13. The weed seeds were mixed with sand, dropped on

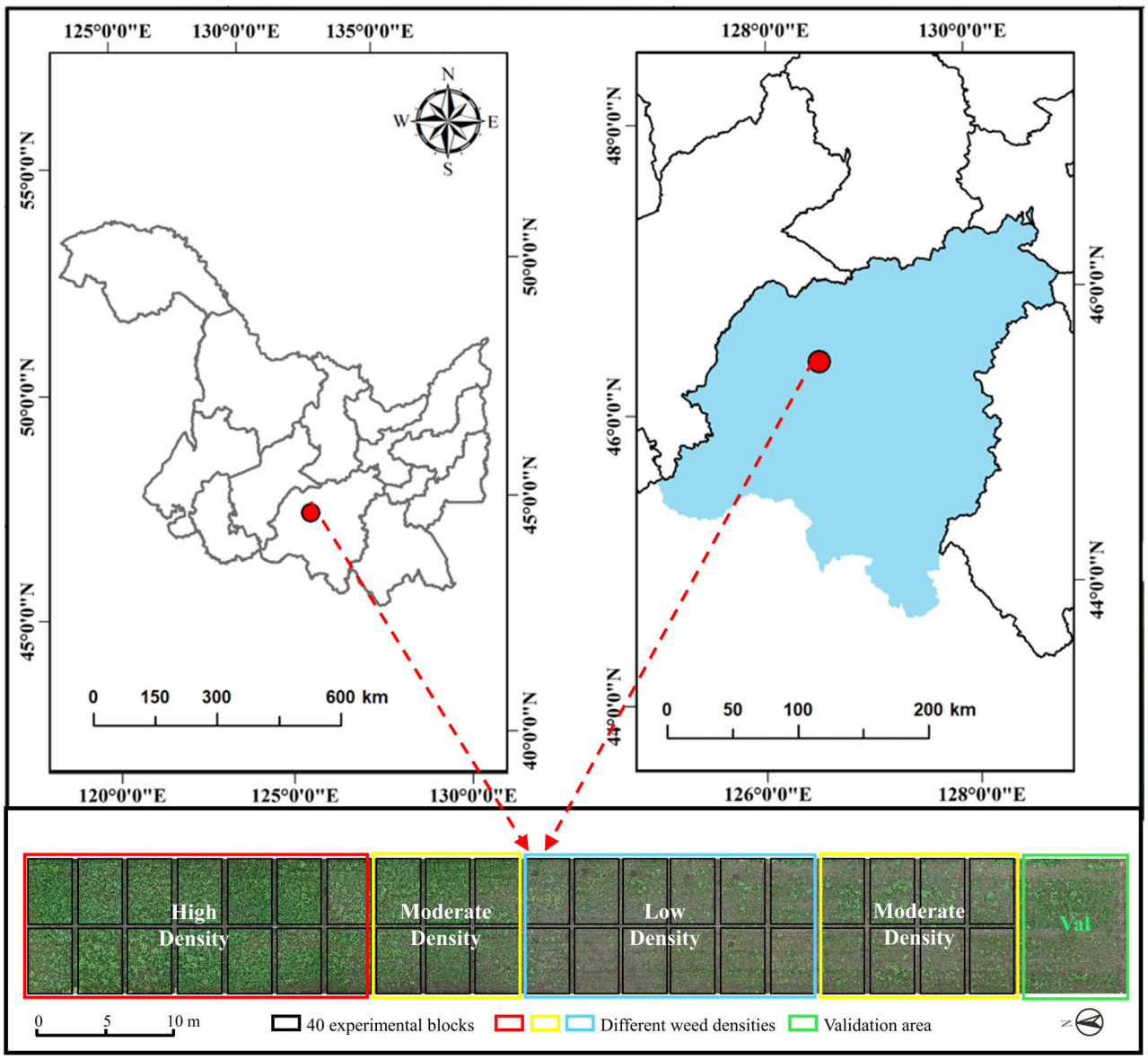

FIGURE 1 | Distribution of test sites and test fields.

the soil surface, and then harrowed immediately after maize sowing. Weed seed dropping is divided into three densities (low, 40 seeds m^{-2}; moderate, 160 seeds m^{-2}; high, 320 seeds m^{-2}). After maize germination, slight spray irrigation was applied to the whole field to accelerate weed germination. The herbicide atrazine (Ji Feng Pesticide Co., Jilin, China) was then sprayed at a uniform rate on 1st June when the maize reached the three-leaf stage.

In the experimental field, 40 plots were divided into three weed density treatments (**Figure 2B**). Each treatment consisted of 12 or 14 plots measuring 3 m × 5 m in six rows with a 0.6-m row spacing. A 1-meter-wide protection plot surrounded the entire field to reduce edge effects. This study investigated the ground truthing data before the atrazine application day. The manual measurements for ground truthing consisted of the survival status of the two weed types and geographical coordinates after application.

Data Acquisition

Unmanned Aerial Vehicle Image Collection

Multispectral and RGB images were collected with DJI Phantom 4 Multispectral and DJI Phantom 4 RTK UAVs (SZ DJI Technology Co., Ltd., Shenzhen, China), as shown in **Figure 2A**. The UAVs are equipped with centimeter-level navigation and positioning systems. The DJI Phantom 4 Multispectral camera simultaneously acquires images in blue (B), green (G), red (R), red edge (RE), and near-infrared (NIR) bands (**Table 1**) at a 1600 × 1300 pixel resolutions. The DJI Phantom 4 RTK has a

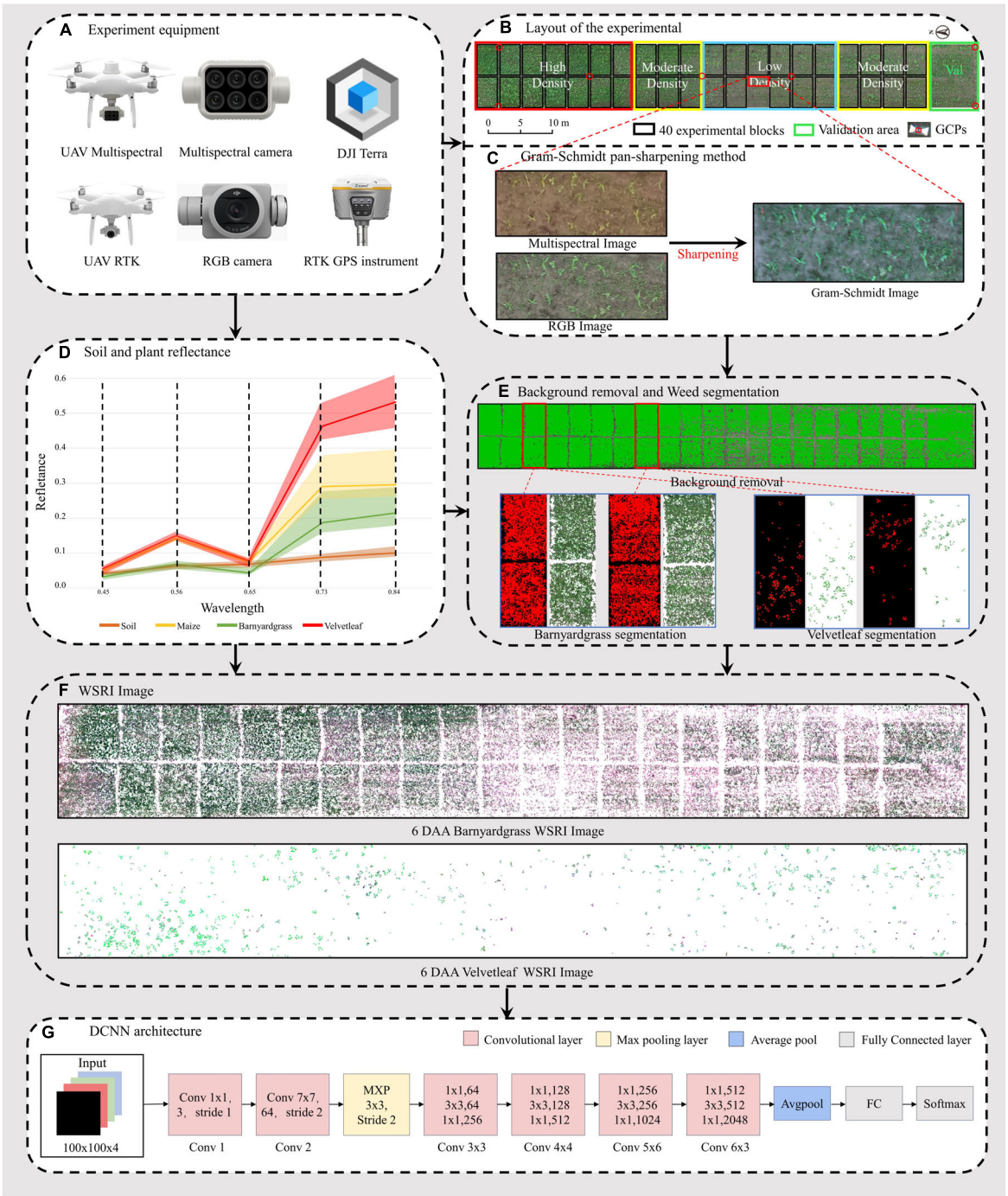

FIGURE 2 | Workflow of the unmanned aerial vehicle (UAV) high-throughput field weed resistance approach. **(A)** DJI Phantom 4 Multispectral, DJI Phantom 4 RTK, DJI Terra, and RTK GPS instrument for collecting field images. **(B)** Digital orthophoto maps (DOM) of three maize field densities (low, moderate, high) for weed resistance research. **(C)** Gram–Schmidt sharpening for improving spectral image information. **(D)** Reflectance values of four objects in the orthophoto (soil, maize, barnyardgrass, and velvetleaf). **(E)** Soil and maize removal and two types of weed segmentation, including barnyardgrass and velvetleaf. **(F)** Two weed image datasets from 6 days after atrazine application (6 DAA) used in the classification models. **(G)** Deep convolutional neural network (DCNN) architecture.

camera with an FC6310R lens (f = 8.8 mm) and a 4864 × 3648 pixel resolution. Based on a UAV flight test with manually controlled height varying from 10 to 30 m above ground, the UAV altitude was finally set to 15 m with no disturbance to the leaves. The ground sampling distances (GSDs) of multispectral and RGB images were 0.79 and 0.41 cm pixel^{-1}, respectively. UAV flights were conducted in the field on 6th and 20th May 2021 to collect the early season information needed for the study. RGB images

were acquired first, and then multispectral images were acquired each day. The mean forward overlap of the photographs was 80%, and the mean sidelap was 70%. The UAV observations covered the complete experimental range (**Table 2**). However, some data are missing because of weather conditions.

Image Preprocessing

Approximately 2,000 images per flight were used for the photogrammetry process using DJI Terra software (SZ DJI Technology Co., Ltd., Shenzhen, China) to obtain images of the entire experimental area. The global navigation satellite system (GNSS) real-time motion control measured seven ground control points (G) to obtain accurate geographical references. The seven GCPs were measured with a GNSS real-time kinematic (RTK) receiver (RTK GPS instrument i50, CHC Navigation Co., Ltd., Shanghai, China). The reflectance correction and radiometric calibration use a 3 m^2 carpet reference and the Spectron on software (Resonon Inc., Bozeman, MT, United States). The empirical line method was then used to convert the image's digital number (DN) value to a reflectance value (**Figure 2D**).

Development of Specific Indices Identifying Atrazine-Resistant Weeds

Canopy spectral reflectance differs between weed species, and some spectrum regions may better identify atrazine resistance status. Sample selection was based on the weed survival 14 days after application. The reflectance of susceptible and resistant biotypes of two weed species was counted in the multispectral images after 2 days of application.

TABLE 1 | Multispectral camera band specifications.

Band	Name	Center wavelength (nm)	Bandwidth (nm)
1	Blue	450	32
2	Green	560	32
3	Red	650	32
4	Near infrared	840	52
5	Red edge	730	32

TABLE 2 | Weather conditions during data collection.

Band**	Collection Date	Air Temp (°C)	Weather
BAD	2021.05.30	11∼22°C	Clear day
AD	2021.06.01	11∼22°C	Cloudy day
1 DAA	2021.06.02	13∼21°C	Cloudy day
2 DAA	2021.06.03	10∼20°C	Cloudy day
4 DAA	2021.06.05	10∼18°C	Cloudy day
5 DAA	2021.06.06	11∼21°C	Clear day
6 DAA	2021.06.07	12∼25°C	Clear day
7 DAA	2021.06.08	13∼28°C	Clear day
8 DAA	2021.06.09	18∼27°C	Cloudy day
10 DAA	2021.06.11	15∼28°C	Clear day
14 DAA	2021.06.15	18∼29°C	Cloudy day

***BAD, before atrazine application day. AD, atrazine application day; DAA, days after atrazine application.*

Figure 3 shows barnyardgrass and velvetleaf reflectance density maps for five bands extracted from multispectral images of susceptible and resistant biotype regions. Slight differences between susceptible and resistant biotypes were observed in the green, red, red edge, and near-infrared bands, and the differences between the red (650 nm) and red edge (780 nm) bands show greater stability (Jin et al., 2020). Part of the blue (450 nm) band was observed to reduce the differences in leaf surface reflectance, thereby improving the correlation between the vegetation index and leaf pigment content (Sims and Gamon, 2002). Therefore, we proposed a weed spectral resistance index named WSRI = (RE-R)/(RE-B) to calculate and evaluate actual field environmental resistant weeds and tested it in this study (**Figure 2F**).

Many VIs have similar effects when dealing with classification problems, differing in their index form expressions. Simple vegetation index forms, such as the NDVI and ratio vegetation index (RVI), are universal to the problem and reflect vegetation information well in many cases. In this study, we entered our multispectral image data into nine previously published VIs (**Table 3**) and the WSRI to evaluate and compare their weed resistance classification accuracies.

Image Fusion

The multispectral images with low spatial resolution used for classification lost almost all texture features. However, susceptible and resistant biotype differences are expressed in the texture information. The high spatial resolution of RGB images compensated for the lost texture information in the multispectral images, so image fusion using the Gram–Schmidt pan-sharpening method in ENVI 5.4.1 (EXELIS, Boulder, CO, United States) was used (**Figure 2C**). The fusion images have five bands: blue, green, red, red-edge, and near-infrared.

The Gram–Schmidt pan-sharpening method is based on Gram–Schmidt (GS) orthogonalization. GS orthogonalization is performed to orthogonalize matrix data or digital image bands (Laben and Brower, 2000). It first created a simulated low-resolution panchromatic band as a weighted linear combination of multispectral bands. Then, GS orthogonalization is performed using all bands, including the simulated panchromatic and multispectral bands. The simulated panchromatic band is the first band in GS orthogonalization. After making all bands orthogonal by using GS orthogonalization, the high-spatial resolution panchromatic band replaces the first GS band. Last, an inverse GS transform creates the pan-bands (Laben and Brower, 2000; Ehlers et al., 2010).

Background Removal and Weed Segmentation

Because of the reflectance differences between soil and plants (**Figure 2D**), Otsu's thresholding algorithm (Ostu et al., 1979) was used to separate vegetation from the soil, find an optimal value to be used for segmentation, and then adjust the threshold value, if necessary, to improve separation of the plants from the soil (**Figure 2E**; Liao et al., 2020).

Manual segmentation of maize and weeds has higher accuracy but is expensive and time-consuming. UAV multispectral and

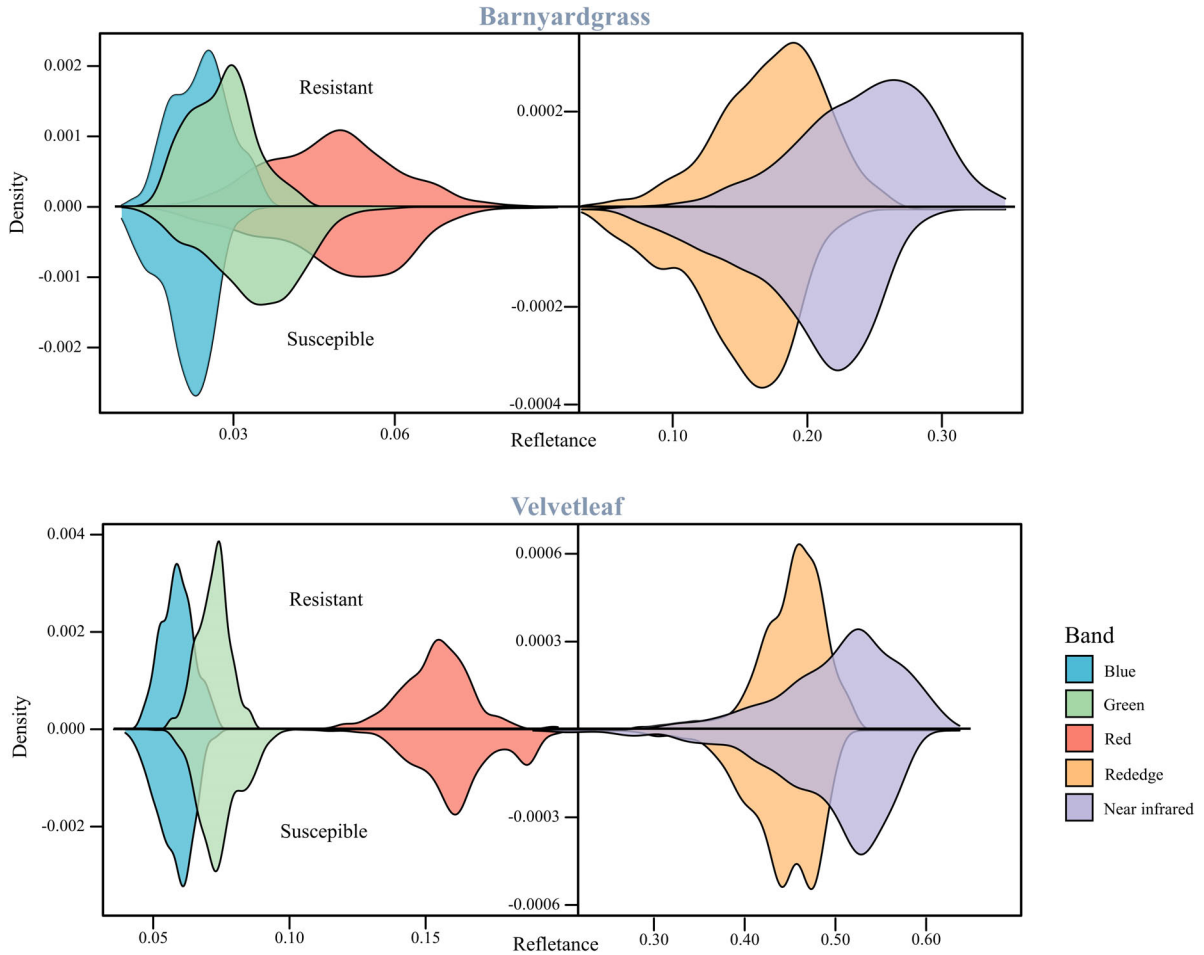

FIGURE 3 | Reflectance density maps of two weed resistant and susceptible biotypes.

RGB images were segmented for maize, barnyardgrass, and velvetleaf using the support vector machine (SVM) classifier (Cortes et al., 1995). The four-leaf stage of maize did not shade the weeds significantly and separated the maize and weeds better. A binary mask layer was created to segment the maize and the two weed types from the UAV images' extracted spectral and texture features for further processing (**Figure 2E**). The binary mask layer was generated in ENVI based on manually tagged template data.

The performance of the SVM classifier was evaluated using the confusion matrix and accuracy statistics, with the overall accuracy based on randomly selected independent test samples. The overall accuracy of SVM classification is 94.4%, which meets the experimental requirements. The zonal statistics were obtained using ArcPy and the Python 2.7 programming language to remove soil and maize and segment the barnyardgrass and velvetleaf.

Dataset Production

Different application effects were observed in the experimental area, and a training template was created for individual velvetleaf plants based on survival status 14 days after application (**Figure 4A**). The training template contained two classes: susceptible velvetleaf and resistant velvetleaf (**Figure 4B**).

Because barnyardgrass grows densely and is mostly aggregated, it is not easy to separate them into individual plants (Maun and Barrett, 1986). In this study, the resistance level was set according to the death rate of barnyardgrass in the same area 14 days after application. **Figure 4A** shows the example plants from blocks at different resistance levels (example of barnyardgrasses in high-density areas). Resistance level 1 is defined as 0–25% death of barnyardgrasses; resistance level 2 is 26–50% death of barnyardgrasses; resistance level 3 is 51–75% death of barnyardgrasses; resistance level 4 is 76–95% death of barnyardgrasses; and resistance level 5 indicates an entirely dead barnyardgrass block. Blocks with resistance levels less than or equal to 3 were considered resistant (**Figure 4B**) because these blocks exceeded the threshold for weed control in farmland weeds (Anru and Cuijuan, 2014).

The image patch of each weed plot must be cropped from the barnyardgrass WSRI fusion segmentation image to build the dataset for DCNN modeling. Thus, a region of interest (ROI) shapefile was created in ArcMap 10.3 (Esri Inc., Redlands, CA,

TABLE 3 | Vegetation indices used in this study.

Category	Features	Expression**	References
DVI	Difference vegetation index	NIR-R	Jordan, 1969
MTCI	MERIS terrestrial chlorophyll index	(NIR-RE)/(RE-R)	Dash and Curran, 2004
NDVI	Normalized differential vegetation index	(NIR-R)/(NIR + R)	Tucker et al., 1979
GNDVI	Green normalized difference vegetation index	(NIR-G)/(NIR + G)	Gitelson and Merzlyak, 1998
NDRE	Normalized difference red-edge index	(NIR-RE)/(NIR + RE)	Sims and Gamon, 2002
RENDVI	Red-edge normalized difference vegetation index	(RE-R)/(RE + R)	Sims and Gamon, 2002
RVI	Ratio vegetation index	NIR/R	Birth and Mcvey, 1968
RERVI	Red-edge ratio vegetation index	NIR/RE	Vincini and Frazzi, 2009
PSRI	Plant senescence reflectance index	(R-G)/NIR	Merzlyak et al., 1999
WSRI	Weed Spectral Resistance Index	(RE-R)/(RE-B)	This paper

***B, G, R, RE, and NIR represent blue, green, red, red-edge, and near-infrared bands, respectively.*

United States), and rectangles measuring around 0.5 m × 0.5 m were drawn. The cropped patch sizes were approximately 100 × 100 pixels. All data sets are four bands with a combination of WSRI images and RGB images.

The other UAV images throughout and after application were also processed to generate time-series image patches for dynamic weed resistance classification. Rotated image enhancement was applied to display the different shapes and directions of the weeds in the field. Four clockwise rotations (0°, the original data; 90°; 180°; and 270°) were performed for image enhancement. For the barnyardgrass dataset, the original 1,750 observations were increased four times, with 3,128 observations representing resistant blocks and 3,872 observations representing susceptible blocks for 7,000 observations each day and 28,000 total observations. For the velvetleaf dataset, the original 480 observations were increased four times, with 1,136 observations representing resistant plants and 784 observations representing susceptible plants for 1,920 observations each day and 7,680 total observations. Before the data augmentation, all data were randomly split into training and validation sets in an 8:2 ratio. The model performance was tested using a validation area (**Figure 4B**) to illustrate model's the generality and robustness.

Deep Convolutional Neural Network for Resistant Weed Classification

A DCNN (**Figure 2G**) for classifying resistant weeds was constructed using MATLAB R2021a (MathWorks Inc., Natick, MA, United States). The model was trained and tested on an NVIDIA 2080Ti GPU with 48-GB RAM and on a 64-bit Windows 10 operating system. CUDA version is 11.4.

The network was built based on the ResNet-50 model (He et al., 2016) and transfer learning (Kieffer et al., 2017). This study used the Resnet-50 model pre-trained on ImageNet (Krizhevsky et al., 2012) without fully connected (FC) layers for transfer learning. The input size was changed to 100 × 100 × 4 to match the size of the image patches. Then a convolutional layer (size of 3 × 3 × 3) was added behind the input 4-band images for reduced dimension on data. The ReLU activation layer was appended behind the convolutional layer to add non-linear characteristics. The dropout regularization method was deployed after the FC layer to reduce overfitting (Srivastava et al., 2014), and the dropout rate was set at 30%.

An Adam optimizer (Kingma and Ba, 2014) was used with a 10^{-4} learning rate and 10^{-3} decay to adaptively optimize the training process. The batch size was set to 128, and the data generator generated each batch with real-time data

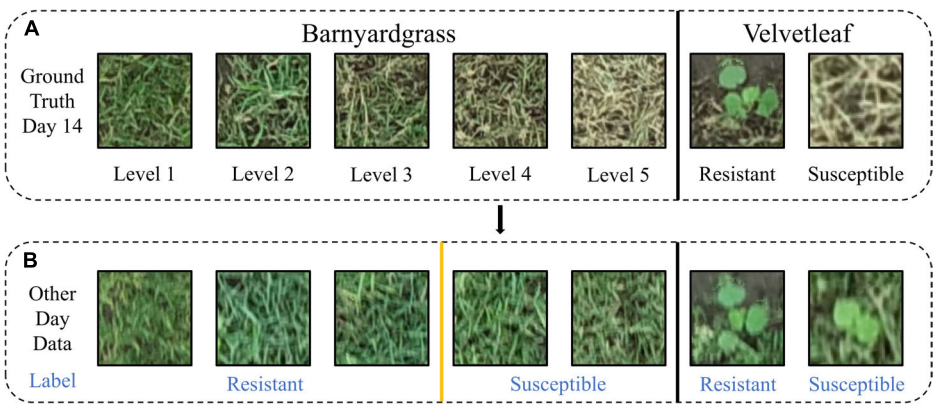

FIGURE 4 | Two weeds belonging to blocks were evaluated as susceptible and resistant. **(A)** Manual resistance level and label based on weed death coverage 14 days after atrazine application. **(B)** Visualization of the data labels on other days.

augmentation. The model was trained for 300 epochs with 10 batches per epoch. The accuracy of each classification was observed using a confusion matrix. Accuracy metrics were averaged from five repeats of randomized holdback cross-validation.

RESULTS

The DCNN was applied to classify weed resistance using the canopy spectral and textural information extracted from the UAV multispectral and RGB sensors, and the results are shown in **Table 4**.

Contribution of Spectral Bands and Vegetation Indices in the Resistant Weed Classification

The susceptible and resistant biotype reflectance densities of barnyardgrass and velvetleaf after atrazine application are shown in **Figure 3**. Spectral band differences between susceptible and resistant biotypes are related to the chlorophyll content and cell wall structure of the weed species.

Atrazine-resistant weed biotypes showed a slightly lower reflectance than susceptible weed biotypes in the visible light region. The differences between susceptible and resistant biotypes were more significant in the red edge and near-infrared regions, and the resistant biotypes showed increased spectral reflectance. These effects are related to the low chlorophyll content of susceptible biotypes, corresponding to plant stress response (Gomes et al., 2016). The main reason is that the application of atrazine reduces photosynthesis and destroys the pigments (Hess, 2000; Zhu et al., 2009). The red band is the central band of chlorophyll, which is the specific chlorophyll absorption band (Tros et al., 2021). The red edge position, which is the slope inflection point between red absorption and near-infrared reflectance, is usually used to correlate the chlorophyll content (Horler et al., 1983; Zarco-Tejada et al., 2019). Thus, the red and red edge bands are stable for the classifying atrazine-resistant weed biotypes.

This study selected the most commonly used VIs to include some stress indices and compare their results from the DCNN with the WSRI (**Table 4**). Among these, stress and pigmentation changes resulted from atrazine herbicide application. To further explore the differences in the vegetation index distributions for observing susceptible and resistant biotypes, violin plots of barnyardgrass and velvetleaf for 10 VIs 2 days after application are shown in **Figure 5**.

The results in **Figure 5** show that WSRI, DVI, NDVI, NDVI-RE, and RVI VIs distinguish between susceptible and resistant barnyardgrasses, with a common trait of these indices being that they all contain red bands. The difference vegetation index (DVI) and the RVI have little differences in susceptible and resistant biotypes because they do not integrate multi-band information well. The NDVI-RE used the red-edge bands to replace the NIR bands, resulting in a slightly better classification than the NDVI.

The WSRI retained the numerator structure of the NDVI-RE index and added the blue bands to the denominator to eliminate the spectral interference between pigments to achieve a better classification result. However, the WSRI classification of susceptible and resistant velvetleaf was very poor compared with barnyardgrass at the early stage of application, and the NDVI-RE and WSRI provided only partial classification. The WSRI makes the resistant weed data more concentrated and the susceptible weed data more dispersed, widening their differences. The average spectral response of barnyardgrass shows a more prominent separation than velvetleaf, possibly *via* lower herbicide uptake at the cuticular level, causing it to respond more slowly to herbicide stress (Couderchet and Retzlaff, 1995). In addition, velvetleaf has a higher reflectance than barnyardgrass, resulting in spectral changes that are more difficult to represent effectively.

TABLE 4 | Resistant weed classification performance summary.

Species	Feature type	Metrics	2DAA	4DAA	6DAA	8DAA
Barnyardgrass	RGB	Accuracy	0.554	0.609	0.692	0.772
	WSRI		0.571	0.634	0.724	0.796
	DVI		0.533	0.583	0.641	0.717
	MCTI		0.526	0.559	0.619	0.693
	NDVI		0.556	0.591	0.654	0.746
	GNDVI		0.548	0.570	0.635	0.712
	NDRE		0.551	0.587	0.655	0.737
	NDVI-RE		0.564	0.597	0.657	0.759
	RVI		0.559	0.584	0.681	0.755
	RVI-RE		0.543	0.576	0.646	0.722
	PSRI		0.527	0.566	0.624	0.709
	5 BANDS		0.551	0.582	0.652	0.776
	WSRI + RGB		0.602	0.665	0.761	0.811
Velvetleaf	RGB	Accuracy	0.529	0.596	0.753	0.905
	WSRI		0.541	0.604	0.767	0.914
	DVI		0.532	0.573	0.691	0.867
	MCTI		0.526	0.562	0.677	0.822
	NDVI		0.547	0.578	0.705	0.894
	GNDVI		0.539	0.567	0.686	0.875
	NDRE		0.545	0.562	0.679	0.871
	NDVI-RE		0.528	0.583	0.711	0.907
	RVI		0.539	0.571	0.700	0.891
	RVI-RE		0.537	0.576	0.694	0.898
	PSRI		0.525	0.559	0.652	0.834
	5 BANDS		0.558	0.598	0.702	0.902
	WSRI + RGB		0.551	0.634	0.798	0.924

DAA, days after application; WSRI, weed spectral resistance index.

Contribution of Spectra and RGB in Resistant Weed Classification

Spectral information with the DCNN resulted in the highest weed resistance classification accuracy when using a single sensor. The single-band WSRI vegetation information surpasses the RGB texture information, even though the RGB image resolution is about 10 times higher than that of the spectral images. The difference in accuracy between them was largest

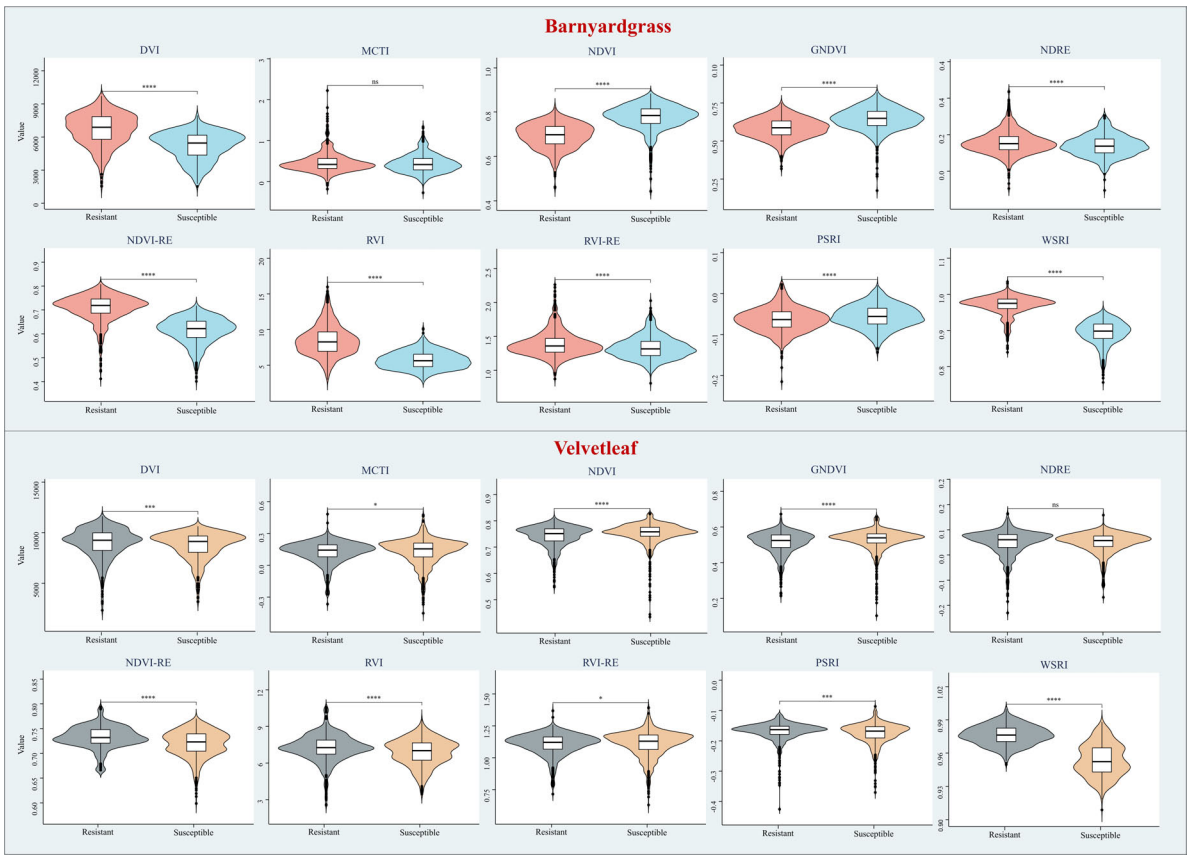

FIGURE 5 | Violin plots of different vegetation indices for susceptible and resistant biotypes of barnyardgrass and velvetleaf 2 days after application, where $*p < 0.05$; $**p < 0.01$; $***p < 0.001$; and $****p < 0.0001$ indicate significant differences between the susceptible and resistant biotypes, and *ns* indicates no significance differences.

6 days after application, while the difference was smallest 8 days after application.

As shown in **Table 4**, the combination of WSRI spectral and RGB structural information improved accuracy, compared to using only a single sensor. RGB-derived detailed texture features, such as slight leaf discoloration and rolling, are not obtained from spectral features (Rischbeck et al., 2016; Stanton et al., 2017). In addition, canopy structure information can overcome the asymptotic saturation problems inherent to spectral features to some extent (Wallace, 2013; Maimaitijiang et al., 2020). Therefore, the combination of spectral and textural information improves classification accuracy. It should be noted that the accuracy improvement was not substantial, and combining multispectral and RGB information is likely attributed to information homogeneity and redundancy among canopy spectral and textural features (Pelizari et al., 2018; Maimaitijiang et al., 2020).

Impacts of Different Times in Resistant Weed Classification

The time-series NDVI image patches of barnyardgrass and velvetleaf during the atrazine application stage are visualized in **Figure 6**. NDVI images reflect vegetation health status and nutrient information (Eide et al., 2021a). The color of the plant areas in the NDVI images represent the plant health status, where NDVI values close to 1 and redder plant regions mean healthier plants. As time increased, herbicide stress became more severe, and differences in resistance levels among weed blocks were increasingly evident. As shown in **Figure 6A** for barnyardgrass, the susceptible biotypes changed rapidly under herbicide application. About 3 days after application, the NDVI image of the leaves changed from red to yellow or even green, meaning that the vital characteristics of the susceptible biotypes gradually diminished.

By contrast, the resistant biotypes changed slowly with low amplitudes under the herbicide application. About 5 days after application, the NDVI image of the leaves changed slightly from red to yellow. The higher the resistance level, the smaller the change toward yellow. The highest resistance level showed only signs of stopping the growth and then completely recovered to normal growth about 4 days after application.

The change rate under herbicide stress conditions and the recovery speed after the application reflect resistance at different stages. The higher the resistance level of the barnyardgrass plots, the later the changes appeared. The large number of resistant

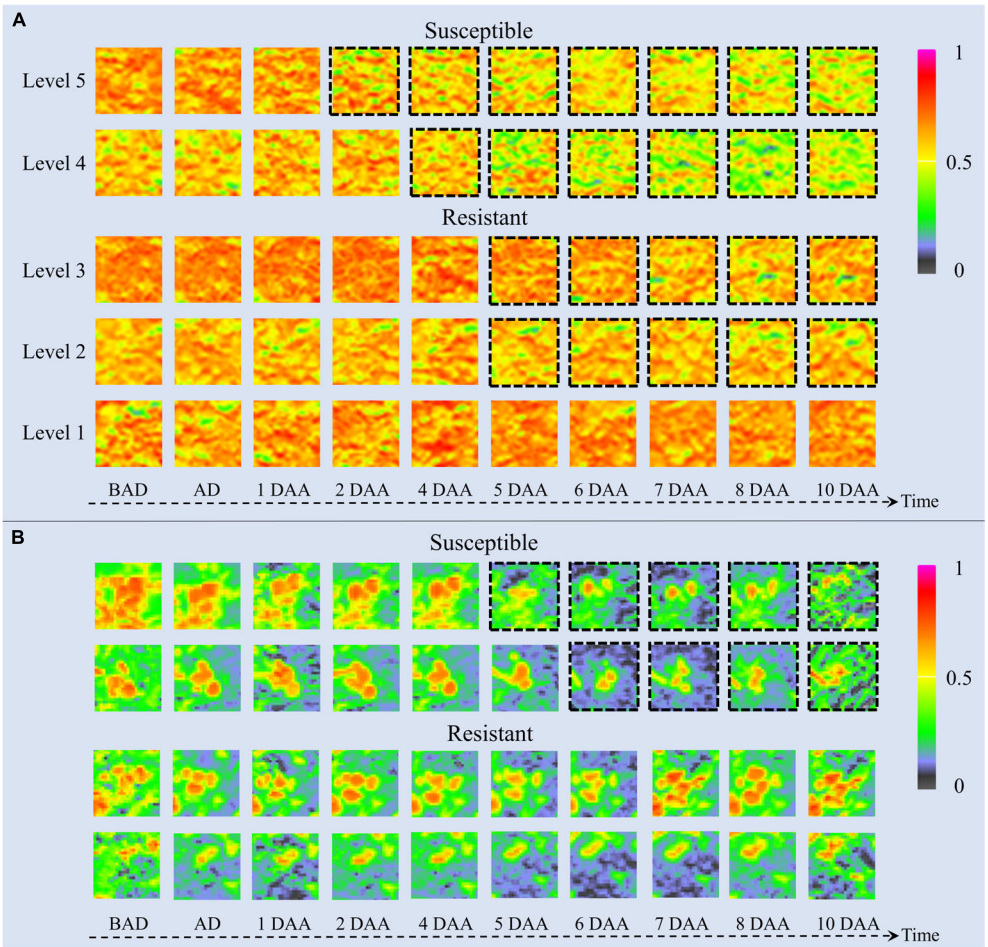

FIGURE 6 | UAV-based visualization of two weed species with dynamic changes in NDVI images. **(A)** Image patches of five resistance levels of barnyardgrass under herbicide stress, where dashed black borders around the patches indicate significant changes. **(B)** Image patches of two susceptible and two resistant velvetleaf under herbicide stress, where dashed black borders around the patches indicate significant changes. BAD is before application day; AD is application day; DAA is days after application.

barnyardgrasses surrounding susceptible barnyardgrasses made it difficult to observe changes in high-resistance level plots. A significant difference between susceptible and resistant plots in later stages is that the recovery of many resistant barnyardgrasses in the resistant plots compensated for the death of susceptible barnyardgrasses.

The dynamics of velvetleaf herbicide stress are easier to analyze because of their individual plant growth characteristics. Velvetleaf had longer herbicide stress response times than barnyardgrass, and the susceptibility and resistance of velvetleaf were not directly related to size, as shown in **Figure 6B**. The mechanism of prolonged plant death generated by sink tissue toxicity in velvetleaf may be the main reason (Fuchs et al., 2002). Atrazine caused gradual inhibition of photosynthesis in velvetleaf leaves that increased over several days and was nearly complete by 5 days (Qi et al., 2018). Therefore, the difference in the spectral response of velvetleaf is smaller than that of barnyardgrass 2 days after application.

About 5 days after application, the susceptible velvetleaf began to change significantly. The NDVI images show large red leaf area reductions with relatively little activity. By contrast, the NDVI images of the resistant velvetleaf leaves changed slightly from red to yellow about 5 days after application. However, the formerly red areas began recovering about 7 days after application, sometimes even before the herbicide application, indicating that the resistant velvetleaf had resumed growth.

Both susceptible and resistant velvetleaf biotypes showed growth inhibition at the beginning of herbicide stress, but the spectral information was still better classified by inhibition

TABLE 5 | Resistant weed classification performance summary of different densities.

Densities	Metrics	2DAA	4DAA	6DAA	8DAA
Low	Accuracy	0.617	0.649	0.725	0.821
Moderate	Accuracy	0.611	0.673	0.708	0.746
High	Accuracy	0.547	0.614	0.742	0.794

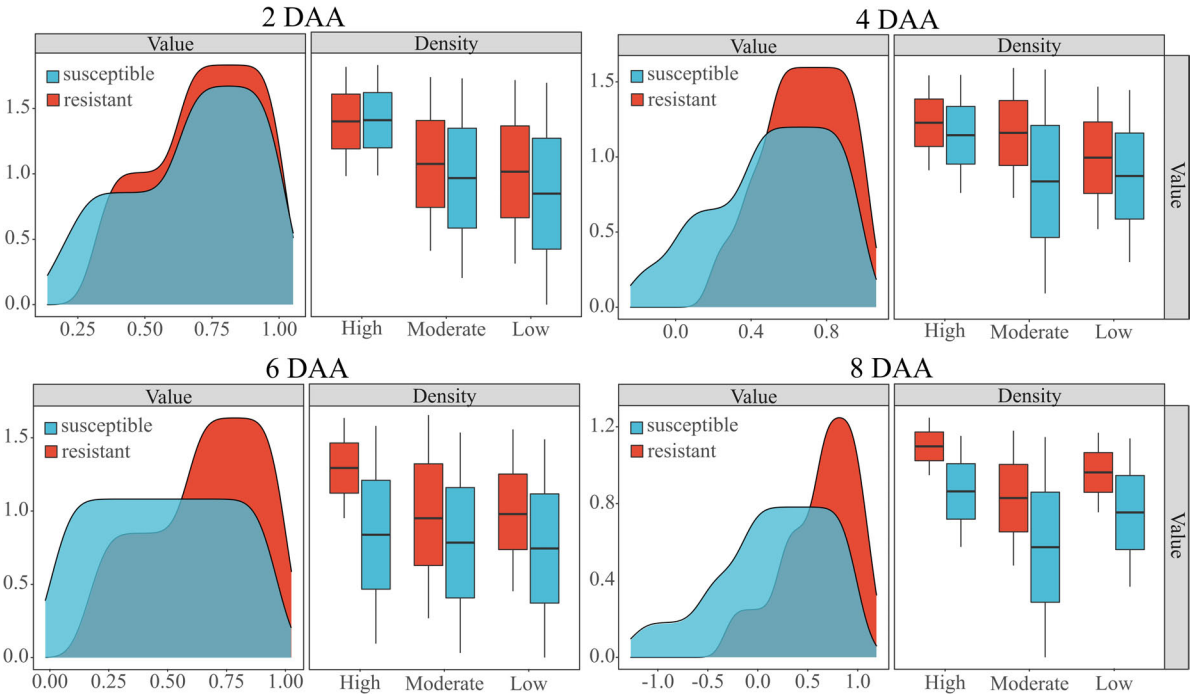

FIGURE 7 | Classification of susceptible and resistant barnyardgrass biotypes at different densities (high, moderate, low) by the WSRI. DAA is days after application.

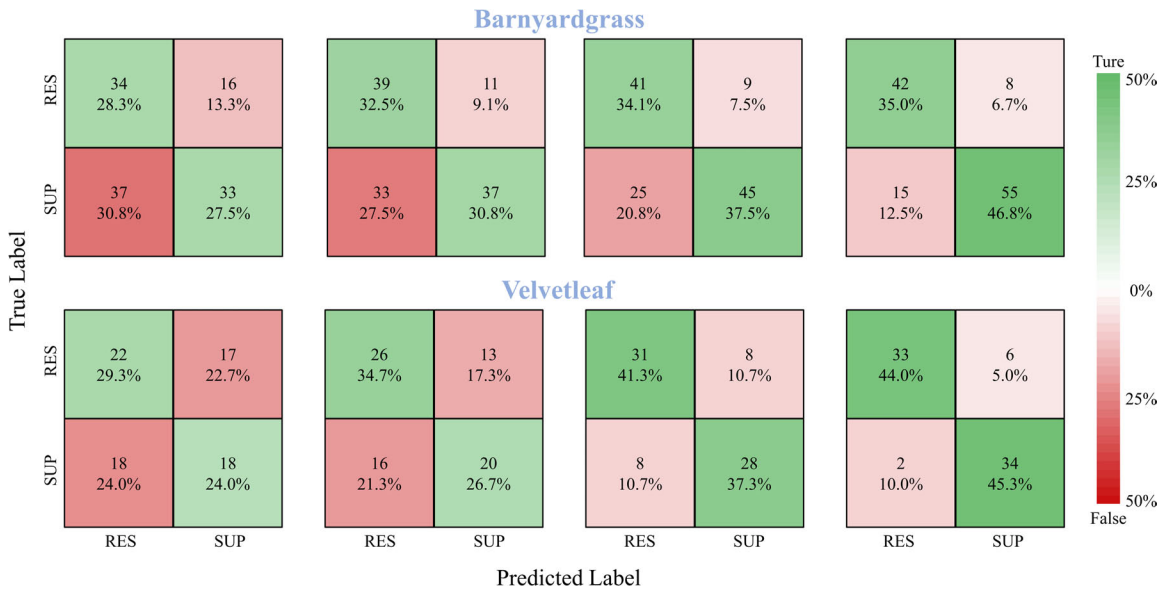

FIGURE 8 | Confusion matrices for barnyardgrass and velvetleaf in the validation area. RES are resistant weeds. SUP are susceptible weeds.

differences, demonstrating the potential of spectral information for the study of resistant weeds.

Impacts of Different Densities in Resistant Weed Classification

The distribution of barnyardgrass in a real farmland environment shows a clustered distribution (Maun and Barrett, 1986). Therefore, studies were conducted for different weed densities. The classification model was applied to different barnyardgrass densities to evaluate their reliability and adaptability. As shown in **Table 5**, the classification accuracy after herbicide application had maximum accuracies of 0.794 for low-density weeds, 0.736 for medium-density weeds, and 0.821 for high-density weeds. However, the velvetleaf distribution was rarely clustered,

and different velvetleaf densities had almost no effect on the classification model.

The performance of the WSRI was evaluated for each plot random samples on different densities. **Figure 7** shows the WSRI density plots for susceptible and resistant barnyardgrass in the sample areas at different times after application and the box plots at different weed densities. The results show gaps between susceptible and resistant biotypes at different densities, and the gaps gradually increased over time.

In summary, atrazine spraying would encounter problems such as shading and uneven spraying under high-density barnyardgrass conditions, potentially overestimating resistance levels in susceptible areas. Moreover, symbiotic areas of resistant and susceptible barnyardgrass would affect the spectral response value, resulting in a low-classification accuracy model at early application. The low- and moderate-density areas contain few weeds. Some susceptible weeds died with increasing time after application, resulting in small fluctuations in spectral response gaps and small improvements in accuracy rates. In addition, the massive death of susceptible weeds over time in high-density areas widened the gap and improved the classification accuracy.

Model Validation

A robust model should be able to generalize to new datasets and still perform well. Therefore, the model validation used the DCNN model to classify the susceptible and resistant weeds in the validation area, and the confusion matrices of the classification results are shown in **Figure 8**. At 8 days after application, the DCNN provided the highest classification accuracy, with 81.8% for barnyardgrass and 89.3% for velvetleaf. At 6 days after application, the DCNN provided better classification accuracy, with 71.6% for barnyardgrass and 78.6% for velvetleaf. The test results also confirmed the WSRI and DCNN model's robustness and generality for further application.

DISCUSSION

Impacts of Different Information in Resistant Weed Classification

Spectral information can reflect the physiological properties of the plant (Rajcan and Swanton, 2001), and physiological properties express differences between resistant and susceptible biotypes faster than appearance. Therefore, multispectral images can assess weed resistance faster and better than RGB images at the early stage of application. As reported in many previous works, spectral information such as VIs has become the primary remote sensing indicator for plant phenotypes because of their stable and superior performance (Ballester et al., 2017). RGB canopy structure information yielded slightly lower, but still comparable, performance than spectral information, indicating that canopy structure information is a promising alternative to commonly used VIs.

The results of this study indicate that the choice of the band is critical when establishing the vegetation index. The red and red edge bands had a significant influence on the classification of resistant weeds, and the reflectance changes of these two bands correlated with the degree of herbicide stress. The study results confirmed that the WSRI (RE-R)/(RE-B) performed well in classifying resistant weeds. The WSRI combines the effects of blue, red, and red-edge wavelengths to provide a comprehensive picture of weed dynamics after application and displayed better performance than other indices. Therefore, it provides powerful support for monitoring and investigating resistant weeds over a large canopy area using UAVs or satellites.

Time series of susceptible and resistant weed biotypes are dynamic expressions of herbicide stress. In this study, 4 days after application (4DAA) was the watershed timeframe for studying resistant weeds. The accurate timing of resistant weed investigation affects effective farmland time management. The rate of change and recovery after herbicide stress begins is key to classifying susceptible and resistant weed biotypes. Different weed species mean that differences in susceptible and resistant biotypes are expressed at different times. The classification effect of barnyardgrass was better than that of velvetleaf at the beginning of the application because of differences in their shape, physiology, and distribution characteristics. As the application time increased, the classification effect of velvetleaf became better than that for barnyardgrass.

Weed density is another factor influencing the research of resistant weeds. It is better to investigate the resistance of clustered weeds using different weed densities. The DCNN trained separately for different weed densities may increase the accuracy of susceptible and resistant barnyardgrass classifications. It is worth noting that higher densities mean the possibility of more resistant weeds, and untimely treatment multiplies the damage to the crop (Alipour et al., 2022).

Effectiveness and Limitations of Unmanned Aerial Vehicle Traits in Resistant Weed Investigation

This study first proposed the multispectral image-derived WSRI to classify susceptible and resistant weeds in real farmland environments. For resistant weed investigation, it took at least 2 h for three raters to manually measure the distribution of resistant weeds in 40 plots. The UAV field flights took less than 15 min, which was fast enough to capture accurate data while avoiding fluctuations in environmental factors such as cloud or wind. More importantly, the high efficiency of UAV phenotyping makes dynamic monitoring with high temporal resolution possible. Therefore, UAVs have shown great potential in the emerging study of field-resistant weeds.

However, there are some limitations for the WSRI. First, changes at the early application stage may not adequately reflect the overall weed resistance because resistant weeds grow slowly during herbicide stress conditions. This is supported by the fact that differences between susceptible and resistant biotypes were not significant at the early stages, so 4 days after herbicide application is the optimal time to investigate resistant weeds. Additionally, the WSRI is an unstable measure easily affected by temperature, humidity, and light conditions in the field.

Therefore, resistant weeds in the field should continue to be the subject of in-depth study and discussion.

CONCLUSION

The proposed UAV–WSRI phenotypic method investigates the potential of fused multispectral and RGB image data combined with deep learning for resistant weed identification in the field. Compared with imaging chambers and expensive unmanned ground vehicle platforms, the UAV platform is more flexible and efficient to deploy for high-throughput phenotyping under field conditions. In addition, the timeliness of UAVs guarantees the reliability of phenotypic traits for resistant weed identification in the field.

The WSRI introduced in this study showed better consistency than previously published spectral VIs, with actual data for atrazine-resistant weed in maize fields. The WSRI provides better classification results than high-resolution RGB data, and the fusion of the two data types further improves the results. The robust deep learning model (DCNN) makes it possible to monitor the dynamic response to resistant weeds in the field precisely, regardless of complex environmental factors.

Our results also show that time series and weed density are closely related to resistant weed identification. The UAV–WSRI phenotypic method could be extended to evaluate the resistance response of other field weeds under herbicide stress, providing a valuable step for further field weed resistance studies.

DATA AVAILABILITY STATEMENT

The raw data supporting the conclusions of this article will be made available by the authors, without undue reservation.

AUTHOR CONTRIBUTIONS

FX: conceptualization, methodology, software, formal analysis, investigation, and writing—review and editing. LQ: conceptualization, writing—review and editing, supervision, and project administration. ZL and DS: visualization. HL: data curation, conceptualization, and supervision. XL: data curation. All authors have read and agreed to the published version of the manuscript.

FUNDING

This study was supported by the National Natural Science Foundation of China (52075092) and the Provincial Postdoctoral Landing Project (LBH-Q19007).

REFERENCES

Alipour, A., Karimmojeni, H., Zali, A. G., Razmjoo, J., and Jafari, Z. (2022). Weed management in *Allium hirtifolium* L. production by herbicides application. *Ind. Crops Prod.* 177:114407. doi: 10.1016/j.indcrop.2021.114407

Anru, L., and Cuijuan, N. (2014). *Experiment of Basic Ecology*. Beijing: Higher Education Press.

Ballester, C., Hornbuckle, J., Brinkhoff, J., Smith, J., and Quayle, W. (2017). Assessment of in-season cotton nitrogen status and lint yield prediction from unmanned aerial system imagery. *Remote Sens.* 9:1149. doi: 10.3390/rs9111149

Birth, G. S., and Mcvey, G. R. (1968). Measuring the color of growing turf with a reflectance spectrophotometer. *Agron. J.* 60, 640–643. doi: 10.2134/agronj1968.00021962006000060016x

Colbach, N., Fernier, A., Le Corre, V., Messéan, A., and Darmency, H. (2017). Simulating changes in cropping practises in conventional and glyphosate-tolerant maize. I. Effects on weeds. *Environ. Sci. Pollut. Res.* 24, 11582–11600. doi: 10.1007/s11356-017-8591-7

Cortes, C., Cortes, C., Vapnik, V., Llorens, C., Vapnik, V. N., Cortes, C., et al. (1995). Support-vector networks. *Mach. Learn.* 20, 273–297. doi: 10.1007/BF00994018

Couderchet, M., and Retzlaff, G. (1995). Daily changes in the relative water content of velvetleaf (*Abutilon theophrasti* Medic.) may explain its rhythmic sensitivity to bentazon. *J. Plant Physiol.* 145, 501–506. doi: 10.1016/S0176-1617(11)81778-5

Dai, Q., Cheng, X., Qiao, Y., and Zhang, Y. (2020). Crop leaf disease image super-resolution and identification with dual attention and topology fusion generative adversarial network. *IEEE Access* 8, 55724–55735. doi: 10.1109/ACCESS.2020.2982055

Dash, J., and Curran, P. J. (2004). MTCI: the meris terrestrial chlorophyll index. *Int. J. Remote Sens.* 25, 151–161. doi: 10.1109/IGARSS.2004.1369009

Duddu, H. S. N., Johnson, E. N., Willenborg, C. J., and Shirtliffe, S. J. (2019). High-throughput UAV image-based method is more precise than manual rating of herbicide tolerance. *Plant Phenomics* 2019:6036453. doi: 10.34133/2019/6036453

Ehlers, M., Klonus, S., Åstrand, P., and Rosso, P. (2010). Multi-sensor image fusion for pansharpening in remote sensing. *Int. J. Image Data Fusion* 1, 25–45. doi: 10.1080/19479830903561985

Eide, A., Koparan, C., Zhang, Y., Ostlie, M., Howatt, K., and Sun, X. (2021a). UAV-assisted thermal infrared and multispectral imaging of weed canopies for glyphosate resistance detection. *Remote Sens.* 13:4606. doi: 10.3390/rs13224606

Eide, A., Zhang, Y., Koparan, C., Stenger, J., Ostlie, M., Howatt, K., et al. (2021b). Image based thermal sensing for glyphosate resistant weed identification in greenhouse conditions. *Comput. Electron. Agric.* 188:106348. doi: 10.1016/j.compag.2021.106348

Foyer, C. H., and Mullineaux, P. M. (1994). Causes of photooxidative stress and amelioration of defense systems in plants. *Environ. Agric.* 44, 522–538. doi: 10.1201/9781351070454

Francesconi, S., Harfouche, A., Maesano, M., and Balestra, G. M. (2021). UAV-based thermal, rgb imaging and gene expression analysis allowed detection of fusarium head blight and gave new insights into the physiological responses to the disease in durum wheat. *Front. Plant Sci.* 12:628575. doi: 10.3389/fpls.2021.628575

Fuchs, M. A., Geiger, D. R., Reynolds, T. L., and Bourque, J. E. (2002). Mechanisms of glyphosate toxicity in velvetleaf (*Abutilon theophrasti* medikus). *Pestic. Biochem. Physiol.* 74, 27–39. doi: 10.1016/S0048-3575(02)00118-9

Gitelson, A. A., and Merzlyak, M. N. (1998). Remote sensing of chlorophyll concentration in higher plant leaves. *Adv. Space Res.* 22, 689–692. doi: 10.1016/S0273-1177(97)01133-2

Gomes, M. P., Manac'H, S. G. L., Maccario, S., Labrecque, M., and Juneau, P. (2016). Differential effects of glyphosate and aminomethylphosphonic acid (AMPA) on photosynthesis and chlorophyll metabolism in willow plants. *Pestic. Biochem. Physiol.* 130, 65–70. doi: 10.1016/j.pestbp.2015.11.010

He, K., Zhang, X., Ren, S., and Sun, J. (2016). "Deep residual learning for image recognition," in *Proceeding of the 2016 IEEE Conference on Computer Vision and Pattern Recognition (CVPR)*, (Piscataway, NJ: IEEE), doi: 10.1109/CVPR.2016.90

He, Z., Wu, H., and Wu, G. (2021). Spectral-spatial classification of hyperspectral images using label dependence. *IEEE Access* 9, 119219–119231. doi: 10.1109/ACCESS.2021.3107976

Hess, F. D. (2000). Light-dependent herbicides: an overview. *Weed Sci.* 48, 160–170.

Horler, D. N. H., Dockray, M., and Barber, J. (1983). The red edge of plant leaf reflectance. *Int. J. Remote Sens.* 4, 273–288. doi: 10.1080/01431168308948546

Huan, Z.-B., Zhang, H.-J., Hou, Z., Zhang, S.-Y., Zhang, Y., Liu, W.-T., et al. (2011). Resistance level and metabolism of barnyard-grass (*Echinochloa crusgalli* (L.) Beauv.) populations to quizalofop-p-ethyl in heilongjiang province, China. *Agric. Sci. China* 10, 1914–1922. doi: 10.1016/S1671-2927(11)60192-2

Ishengoma, F. S., Rai, I. A., and Said, R. N. (2021). Identification of maize leaves infected by fall armyworms using UAV-based imagery and convolutional neural networks. *Comput. Electron. Agric.* 184:106124. doi: 10.1016/j.compag.2021.106124

Jiang, Z., Tu, H., Bai, B., Yang, C., Zhao, B., Guo, Z., et al. (2021). Combining UAV-RGB high-throughput field phenotyping and genome-wide association study to reveal genetic variation of rice germplasms in dynamic response to drought stress. *New Phytol.* 232, 440–455. doi: 10.1111/nph.17580

Jin, X., Li, S., Zhang, W., Zhu, J., and Sun, J. (2020). Prediction of soil-available potassium content with visible near-infrared ray spectroscopy of different pretreatment transformations by the boosting algorithms. *Appl. Sci.* 10:1520. doi: 10.3390/app10041520

Jordan, C. F. (1969). Derivation of leaf area index from light quality of the forest floor. *Ecology* 50, 663–666. doi: 10.2307/1936256

Kelly, S. T., Coats, G. E., and Luthe, D. S. (1999). Mode of resistance of triazine-resistant annual bluegrass (Poa annua). *Weed Technol.* 13, 747–752. doi: 10.1614/WT-03-148R1

Kieffer, B., Babaie, M., Kalra, S., and Tizhoosh, H. R. (2017). "Convolutional neural networks for histopathology image classification: training vs. using pre-trained networks," in *Proceeding of the 2017 7th International Conference on Image Processing Theory, Tools and Applications (IPTA)*, (Piscataway, NJ: IEEE), doi: 10.1109/IPTA.2017.8310149

Kingma, D., and Ba, J. (2014). Adam: a method for stochastic optimization. *Comput. Sci.* doi: 10.48550/arXiv.1412.6980

Krähmer, H., Andreasen, C., Economou-Antonaka, G., Holec, J., Kalivas, D., Kolářová, M., et al. (2020). Weed surveys and weed mapping in Europe: state of the art and future tasks. *Crop Prot.* 129:105010. doi: 10.1016/j.cropro.2019.105010

Krizhevsky, A., Sutskever, I., and Hinton, G. (2012). ImageNet classification with deep convolutional neural networks. *Adv. Neural Inf. Process. Syst.* 25, 84–90.

Laben, C. A., and Brower, B. V. (2000). *Process for Enhancing the Spatial Resolution of Multispectral Imagery Using Pan-Sharpening*. Technical Report US Patent No: 6,011,875. Rochester, NY: Eastman Kodak Company.

Liao, J., Wang, Y., Zhu, D., Zou, Y., Zhang, S., and Zhou, H. (2020). Automatic segmentation of crop/background based on luminance partition correction and adaptive threshold. *IEEE Access* 8, 202611–202622. doi: 10.1109/ACCESS.2020.3036278

Liu, Y., Tang, X., Liu, L., Zhu, J., and Zhang, J. (2018). Study on resistances of *Echinochloa crusgalli* (L.) beauv to three herbicides of corn field in Heilongjiang Province. *J. Northeast Agric. Univ.* 49, 29–39.

Maimaitijiang, M., Sagan, V., Sidike, P., Hartling, S., Esposito, F., and Fritschi, F. B. (2020). Soybean yield prediction from UAV using multimodal data fusion and deep learning. *Remote Sens. Environ.* 237:111599. doi: 10.1016/j.rse.2019.111599

Maun, M. A., and Barrett, S. (1986). The biology of canadian weeds: 77. *Echinochloa crus-galli* (L.) beauv. *Revue Canadienne De Phytotechnie* 66, 739–759. doi: 10.4141/cjps86-093

Meiyan, S., Mengyuan, S., Qizhou, D., Xiaohong, Y., Baoguo, L., and Yuntao, M. (2022). Estimating the maize above-ground biomass by constructing the tridimensional concept model based on UAV-based digital and multi-spectral images. *Field Crops Res.* 282:108491. doi: 10.1016/j.fcr.2022.108491

Merzlyak, M. N., Gitelson, A. A., Chivkunova, O. B., and Rakitin, V. Y. (1999). Non-destructive optical detection of pigment changes during leaf senescence and fruit ripening. *Physiol. Plant.* 106, 135–141. doi: 10.1034/j.1399-3054.1999.106119.x

Osco, L. P., Marcato Junior, J., Marques Ramos, A. P., de Castro Jorge, L. A., Fatholahi, S. N., de Andrade Silva, J., et al. (2021). A review on deep learning in UAV remote sensing. *Int. J. Appl. Earth Obs. Geoinf.* 102:102456. doi: 10.1016/j.jag.2021.102456

Ostu, N., Nobuyuki, O., and Otsu, N. (1979). A thresholding selection method from gray level histogram. *IEEE Trans. Syst. Man Cybern.* 9, 62–66. doi: 10.1109/TSMC.1979.4310076

Pelizari, P. A., Sprhnle, K., Gei, C., Schoepfer, E., and Taubenbck, H. (2018). Multi-sensor feature fusion for very high spatial resolution built-up area extraction in temporary settlements. *Remote Sens. Environ.* 209, 793–807. doi: 10.1016/j.rse.2018.02.025

Perotti, V. E., Larran, A. S., Palmieri, V. E., Martinatto, A. K., and Permingeat, H. R. (2020). Herbicide resistant weeds: a call to integrate conventional agricultural practices, molecular biology knowledge and new technologies. *Plant Sci.* 290:110255. doi: 10.1016/j.plantsci.2019.110255

Qi, Y., Li, J., Fu, G., Zhao, C., Guan, X., Yan, B., et al. (2018). Effects of sublethal herbicides on offspring germination and seedling growth: redroot pigweed (*Amaranthus retroflexus*) vs. velvetleaf (*Abutilon theophrasti*). *Sci. Total Environ.* 645, 543–549. doi: 10.1016/j.scitotenv.2018.07.171

Quan, L., Li, H., Li, H., Jiang, W., Lou, Z., and Chen, L. (2021). Two-stream dense feature fusion network based on RGB-D data for the real-time prediction of weed aboveground fresh weight in a field environment. *Remote Sens.* 13:2288. doi: 10.3390/rs13122288

Rajcan, I., and Swanton, C. J. (2001). Understanding maize–weed competition: resource competition, light quality and the whole plant. *Field Crops Res.* 71, 139–150. doi: 10.1016/S0378-4290(01)00159-9

Rischbeck, P., Elsayed, S., Mistele, B., Barmeier, G., Heil, K., and Schmidhalter, U. (2016). Data fusion of spectral, thermal and canopy height parameters for improved yield prediction of drought stressed spring barley. *Eur. J. Agron.* 78, 44–59. doi: 10.1016/j.eja.2016.04.013

Sher, A., Mudassir Maqbool, M., Iqbal, J., Nadeem, M., Faiz, S., Noor, H., et al. (2021). The growth, physiological and biochemical response of foxtail millet to atrazine herbicide. *Saudi J. Biol. Sci.* 28, 6471–6479. doi: 10.1016/j.sjbs.2021.07.002

Shirzadifar, A., Bajwa, S., Nowatzki, J., and Shojaeiarani, J. (2020b). Development of spectral indices for identifying glyphosate-resistant weeds. *Comput. Electron. Agric.* 170:105276. doi: 10.1016/j.compag.2020.105276

Shirzadifar, A., Bajwa, S., Nowatzki, J., and Bazrafkan, A. (2020a). Field identification of weed species and glyphosate-resistant weeds using high resolution imagery in early growing season. *Biosyst. Eng.* 200, 200–214. doi: 10.1016/j.biosystemseng.2020.10.001

Sims, D. A., and Gamon, J. A. (2002). Relationships between leaf pigment content and spectral reflectance across a wide range of species, leaf structures and developmental stages. *Remote Sens. Environ.* 81, 337–354. doi: 10.1016/S0034-4257(02)00010-X

Srivastava, N., Hinton, G., Krizhevsky, A., Sutskever, I., and Salakhutdinov, R. (2014). Dropout: a simple way to prevent neural networks from overfitting. *J. Mach. Learn. Res.* 15, 1929–1958. doi: 10.5555/2627435.2670313

Stanton, C., Starek, M. J., Elliott, N., Brewer, M., Maeda, M. M., and Chu, T. (2017). Unmanned aircraft system-derived crop height and normalized difference vegetation index metrics for sorghum yield and aphid stress assessment. *J. Appl. Remote Sens.* 11:026035. doi: 10.1117/1.JRS.11.026035

Su, J., Yi, D., Coombes, M., Liu, C., Zhai, X., McDonald-Maier, K., et al. (2022). Spectral analysis and mapping of blackgrass weed by leveraging machine learning and UAV multispectral imagery. *Comput. Electron. Agric.* 192:106621. doi: 10.1016/j.compag.2021.106621

Tros, M., Mascoli, V., Shen, G., Ho, M.-Y., Bersanini, L., Gisriel, C. J., et al. (2021). Breaking the red limit: efficient trapping of long-wavelength excitations in chlorophyll-f-containing photosystem I. *Chem* 7, 155–173. doi: 10.1016/j.chempr.2020.10.024

Tucker, C. J., Elgin, J. H., Iii, M. M., and Fan, C. J. (1979). Monitoring corn and soybean crop development with hand-held radiometer spectral data. *Remote Sens. Environ.* 8, 237–248. doi: 10.1016/0034-4257(79)90004-X

Vincini, M., and Frazzi, E. (2009). Active sensing of the N status of wheat using optimized wavelength combination: impact of seed rate, variety and growth stage. *Precision Agric.* 9, 23–30.

Vong, C. N., Conway, L. S., Zhou, J., Kitchen, N. R., and Sudduth, K. A. (2021). Early corn stand count of different cropping systems using UAV-imagery and deep learning. *Comput. Electron. Agric.* 186:106214. doi: 10.1016/j.compag.2021.106214

Wallace, L. O. (2013). "Assessing the stability of canopy maps produced from UAV-LiDAR data," in *Proceedings of the IEEE International Geoscience and Remote Sensing Symposium*, (Piscataway, NJ: IEEE), doi: 10.1109/IGARSS.2013.6723679

Wang, S., Han, Y., Chen, J., He, X., Zhang, Z., Liu, X., et al. (2022). Weed density extraction based on few-shot learning through UAV remote sensing RGB and multispectral images in ecological irrigation area. *Front. Plant Sci.* 12:735230. doi: 10.3389/fpls.2021.735230

Williams, M. M., Boydston, R. A., Peachey, R. E., and Robinson, D. (2011). Performance consistency of reduced atrazine use in sweet corn. *Field Crops Res.* 121, 96–104. doi: 10.1016/j.fcr.2010.11.020

Xia, L., Zhang, R., Chen, L., Li, L., and Xie, C. (2021). Evaluation of deep learning segmentation models for detection of pine wilt disease in unmanned aerial vehicle images. *Remote Sens.* 13:3594. doi: 10.3390/rs13183594

Yang, G., Liu, J., Zhao, C., Li, Z., Huang, Y., Yu, H., et al. (2017). Unmanned aerial vehicle remote sensing for field-based crop phenotyping: current status and perspectives. *Front. Plant Sci.* 8:1111. doi: 10.3389/fpls.2017.01111

Yang, M., Hassan, M. A., Xu, K., Zheng, C., Rasheed, A., Zhang, Y., et al. (2020). Assessment of water and nitrogen use efficiencies through UAV-based multispectral phenotyping in winter wheat. *Front. Plant Sci.* 11:927.

Zarco-Tejada, P. J., Hornero, A., Beck, P. S. A., Kattenborn, T., Kempeneers, P., and Hernández-Clemente, R. (2019). Chlorophyll content estimation in an open-canopy conifer forest with Sentinel-2A and hyperspectral imagery in the context of forest decline. *Remote Sens. Environ.* 223, 320–335.

Zhang, N., Su, X., Zhang, X., Yao, X., Cheng, T., Zhu, Y., et al. (2020). Monitoring daily variation of leaf layer photosynthesis in rice using UAV-based multispectral imagery and a light response curve model. *Agric. For. Meteorol.* 291:108098. doi: 10.1016/j.agrformet.2020.108098

Zhou, J., Zhou, J., Ye, H., Ali, M. L., Chen, P., and Nguyen, H. T. (2021). Yield estimation of soybean breeding lines under drought stress using unmanned aerial vehicle-based imagery and convolutional neural network. *Biosyst. Eng.* 204, 90–103. doi: 10.1016/j.biosystemseng.2021.01.017

Zhu, J., Patzoldt, W. L., Radwan, O., Tranel, P. J., and Clough, S. J. J. P. G. (2009). Effects of photosystem-II-interfering herbicides atrazine and bentazon on the soybean transcriptome. *Plant Genome* 2, 191–205. doi: 10.3835/plantgenome2009.02.0010

Conflict of Interest: The authors declare that the research was conducted in the absence of any commercial or financial relationships that could be construed as a potential conflict of interest.

Publisher's Note: All claims expressed in this article are solely those of the authors and do not necessarily represent those of their affiliated organizations, or those of the publisher, the editors and the reviewers. Any product that may be evaluated in this article, or claim that may be made by its manufacturer, is not guaranteed or endorsed by the publisher.

frontiers | Frontiers in Plant Science

TYPE Original Research
PUBLISHED 18 July 2022
DOI 10.3389/fpls.2022.939733

OPEN ACCESS

EDITED BY
Yiannis Ampatzidis,
University of Florida,
United States

REVIEWED BY
Vinay Vijayakumar,
University of Florida,
United States
Lucas Costa,
University of Florida,
United States

*CORRESPONDENCE
Ruirui Zhang
zhangrr@nercita.org.cn

SPECIALTY SECTION
This article was submitted to Technical Advances in Plant Science, a section of the journal Frontiers in Plant Science

RECEIVED 09 May 2022
ACCEPTED 27 June 2022
PUBLISHED 18 July 2022

CITATION
Li L, Zhang R, Chen L, Liu B, Zhang L, Tang Q, Ding C, Zhang Z and Hewitt AJ (2022) Spray drift evaluation with point clouds data of 3D LiDAR as a potential alternative to the sampling method.
Front. Plant Sci. 13:939733.
doi: 10.3389/fpls.2022.939733

Spray drift evaluation with point clouds data of 3D LiDAR as a potential alternative to the sampling method

Longlong Li[1,2,3], Ruirui Zhang[1,2,3]*, Liping Chen[1,2,3], Boqin Liu[4], Linhuan Zhang[1,2,3], Qing Tang[1,2,3], Chenchen Ding[1,2,3], Zhen Zhang[5] and Andrew J. Hewitt[6]

[1]Research Center of Intelligent Equipment, Beijing Academy of Agricultural and Forestry Sciences, Beijing, China, [2]National Research Center of Intelligent Equipment for Agriculture, Beijing, China, [3]National Center for International Research on Agricultural Aerial Application Technology, Beijing, China, [4]College of Mechanical and Electronic Engineering, Northwest A & F University, Yangling, China, [5]College of Information Science and Engineering, Shandong Agricultural University, Taian, China, [6]Centre for Pesticide Application and Safety, The University of Queensland, Brisbane, QLD, Australia

Spray drift is an inescapable consequence of agricultural plant protection operation, which has always been one of the major concerns in the spray application industry. Spray drift evaluation is essential to provide a basis for the rational selection of spray technique and working surroundings. Nowadays, conventional sampling methods with passive collectors used in drift evaluation are complex, time-consuming, and labor-intensive. The aim of this paper is to present a method to evaluate spray drift based on 3D LiDAR sensor and to test the feasibility of alternatives to passive collectors. Firstly, a drift measurement algorithm was established based on point clouds data of 3D LiDAR. Wind tunnel tests included three types of agricultural nozzles, three pressure settings, and five wind speed settings were conducted. LiDAR sensor and passive collectors (polyethylene lines) were placed downwind from the nozzle to measure drift droplets in a vertical plane. Drift deposition volume on each line and the number of LiDAR droplet points in the corresponding height of the collecting line were calculated, and the influencing factors of this new method were analyzed. The results show that 3D LiDAR measurements provide a rich spatial information, such as the height and width of the drift droplet distribution, etc. High coefficients of determination (R^2 > 0.75) were observed for drift points measured by 3D LiDAR compared to the deposition volume captured by passive collectors, and the anti-drift IDK12002 nozzle at 0.2MPa spray pressure has the largest R^2 value, which is 0.9583. Drift assessment with 3D LiDAR is sensitive to droplet density or drift mass in space and nozzle initial droplet spectrum; in general, larger droplet density or drift mass and smaller droplet size are not conducive to LiDAR detection, while the appropriate threshold range still needs further study. This study demonstrates that 3D LiDAR has the potential to be used as an alternative tool for rapid assessment of spray drift.

KEYWORDS

plant protection, droplet, spray drift, point clouds, 3D LiDAR, remote sensing

Introduction

Pesticides have significantly contributed to global agricultural development and food supplies (Oerke, 2006). Pesticide application is affected by complex environmental factors (e.g., temperature, humidity, and wind speed) and application techniques (Hilz and Vermeer, 2013). Consequently, it is estimated that 30% to 50% of the applied product drifts into non-target areas (Berg et al., 1999). Spray drift is defined by the US Environmental Protection Agency (EPA) as "the physical movement of a pesticide through the air at the time of application or soon thereafter, to any site other than the one intended for application" (EPA-United States Environmental Protection Agency, 2018). Spray drift is one of the largest sources of pollution caused by pesticides and poses significant risks to human health and the environment (Zhang et al., 2018). Many studies have investigated the effects of spray drift on ecosystems (Jong et al., 2008), water (Zhang et al., 2017), agriculture workers (Schampheleire et al., 2007), and exposure to bystanders and residents (Tsakirakis et al., 2018). Pesticides travel thousands of kilometers through air currents, eventually reaching remote areas (Stoughton et al., 1997). With the increasing awareness of the need for environmental protection, spray drift during pesticide application has attracted significant research attention globally.

Several factors such as meteorological conditions, application techniques, spray characteristics, spray equipment, target crops, and operator skills affect the degree of spray drift (Gil and Sinfort, 2005; Heidary et al., 2014). Regarding the application technology, the droplet size is widely recognized as the main factor affecting spray drift (Elliott and Wilson, 1983), and the effects of nozzle type, nozzle size, spray pressure, and additives on droplet size characteristics have been explored (Taylor et al., 2004; Nuyttens et al., 2007a). In addition, to reduce spray drift, components such as air-inclusion nozzles and low-drift nozzles with preset orifice settings have been designed to increase the droplet size (Butler Ellis et al., 2002). These specially designed nozzles can be used in harsh environments with a higher wind speed and dry conditions.

Before pesticide spraying, it is necessary to understand the anti-drift performance of the nozzle to facilitate the selection of the most appropriate nozzle (Ru et al., 2014). Based on ASAE Standard 572.1: 2009, the droplet size is divided into six classes—very fine, fine, medium, coarse, very coarse, and extra coarse (ASAE, 2009). The nozzle spray drift is commonly tested either in the field or in a wind tunnel. Field tests are complex, cumbersome, and costly, with specific requirements for the testing site and environmental stability. ISO 22866:2005 (ISO, 2005) specifies the procedures for conducting field tests, but this requires several people to work collaboratively. A series of experiments can take several hours to complete, with extremely high environmental crosswind requirements. If the wind direction changes more than 30° during the test, the measurement line must be reset (Arvidsson et al., 2011a). Wind tunnel tests were introduced to evaluate the spray drift characteristics (Southcombe et al., 1997; Herbst, 2001) by artificially controlling the temperature, humidity, wind speed, and wind direction to understand the influence of a single factor (Nuyttens et al., 2009; Zhang et al., 2015; Ferguson et al., 2016). ISO 22856:2008 standardizes the procedure for wind tunnel drift measurement (ISO, 2008).

For field and wind tunnel tests, sampling methods are mostly adopted to measure spray drift. Passive collectors, such as filter paper (Nuyttens et al., 2007b), plastic card (Carlsen et al., 2006), Petri dishes (Caldwell and Wolf, 2006), polyethylene line (Bai et al., 2013), nylon rope (Bui et al., 1998), dynamic rotating sampler (Bonds et al., 2009), and isokinetic sampler (Arvidsson et al., 2011b), were used for receiving the drift droplets, and the amount of spray deposition is quantified by discrete sampling. Each test cycle takes a long time to complete, as this method involves multiple processes, such as sample arrangement, collection, elution, and instrumental analysis. Furthermore, it is difficult to determine the spatial dispersion and evolution of spray drift clouds by point measurements. Therefore, new spray drift detection techniques or devices have been proposed and tested to develop easy and efficient alternative methods. Simulations of the transport process of spray droplets have been conducted, forming drift prediction models, such as AGDISP (Forster et al., 2012), AgDRIFT (Teske et al., 2000), RTDrift (Lebeau et al., 2011), and VALDRIFT (Allwine et al., 2010). Other studies have developed regression equations considering meteorological conditions and the drift distance to provide a reference point for the selection of nozzles and additives (Zhang et al., 2015). In addition, a mass balance system (Balsari et al., 2005) and test bench (Balsari et al., 2007) for drift measurement in an orchard and boom spraying have been developed, and were applied to measure spray drift of different types of nozzles (Gil et al., 2014; Grella et al., 2019).

With recent developments in sensor technology, the use of non-contact sensors for evaluating spray drift has become a trend. Many studies have been conducted using laser imaging (Wang et al., 2019), infrared thermal imaging (Jiao et al., 2016), and OP-FTIR (Kira et al., 2018) to assess spray drift. Compared with direct sampling, sensor detection reduces time and labor cost, providing information on the spatial variation of spray drift. Light detection and ranging (LiDAR) sensors are non-contact measurement devices that use laser beams to accurately detect the spatial position of a target. In previous studies, LiDAR sensors have been used to study droplet movement in the wingtip vortex of spraying aircraft (Hoff et al., 1989) to assess the spray aerosols drifting above orange orchards with the influence of meteorology parameters and atmospheric stability (Miller et al., 2003). Gregorio et al. (2015) developed an *ad hoc* LiDAR system for the measurement of pesticide spray drift, this system evaluates the amount of spray drift through laser signal strength. With this system, the optional spray drift reduction of hollow-cone nozzles was assessed (Gregorio et al., 2019). Currently, various types of LiDAR sensors are used for spray drift measurement. Commercial LiDAR technology is mature and highly available, exhibiting significant potential for broad and long-term applications in drift detection. Most commercial LiDAR sensors obtain plenty of distance values by scanning point clouds to construct target

contours, which provides the possibility for the detection of dispersed drift droplets in space. A commercial 2D LiDAR sensor has been used to estimate drift measurement in vineyard spraying, where the detection results were compared with passive collector experiments to demonstrate the potential of 2D LiDAR for drift measurement of air-assisted sprayer (Gil et al., 2013).

This study aims to explore the feasibility of using a commercial 3D LiDAR sensor to assess spray drift. Spray drift tests with different working parameters were conducted in a wind tunnel, and the relationship between spray drift measurements obtained with LiDAR and passive collectors was analyzed.

Materials and methods

3D LiDAR sensor

The 3D LiDAR sensor used in this study was an outdoor four-layer scanner designed for harsh environments (model LD-MRS400001, Sick, Dusseldorf, Germany), with a long range of 300 m. The sensor adopted a four-line design to simultaneously emit four laser beams to form four stacked planes, with a scanning interval angle of 0.8° and a whole scanning angle of 3.2° (−1.6° to 1.6°) in the vertical direction (Figure 1A). In the horizontal direction, the sensor had a central scanning range of 85° for four scan planes, and the scanning range was extended between +35° and +50° or −50° and −60° to a total range of 110° (Figure 1B). The droplet detection was performed with laser beams emitted by the sensor in four stacked planes, where droplets impacted with the laser to form a drift cloud. Compared to single-wire LiDAR with one laser beam, this design ensures that more data signals are acquired in a scan procedure. The sensor had scanning frequencies of 12.5, 25, and 50 Hz. The available angular resolution was dependent on the scanning frequency, set to 0.125° or 0.25° under 12.5 Hz, 0.25° under 25 Hz, and 0.5° under 50 Hz. The sensor was connected to a computer *via* Ethernet or the RS232 serial port for configuration and data transfer of measurements. The specifications of the sensor are listed in Table 1.

The sensor had the multi-echo capability to gather and evaluate up to three echoes per transmitted laser pulse. As different objects form different echo voltages, the echo signals that may interfere with the reflected objects can be filtered by setting the threshold voltage. Therefore, the system was configured with a noise filtering function. The sensor also had high scanning sensitivity for objects with transparent properties, such as rain, fog, and glass, which ensured the feasibility of using the sensor to detect drift droplets.

Data processing of drift points in space

SOPAS ET configuration software (V 02.18, Sick Sensor Intelligence) was used to manage the LiDAR sensor. Using this software, operators can configure and test measurement properties, analysis behavior, and output properties of the sensor as required. The sensor issued the original measured distance and angle information of drift droplets in reference to its coordinates. Initially, an angular coordinate system was constructed that contained each droplet spot scanned. Assuming that point A is a droplet in space (the j_{th} droplet in i-plane), its polar coordinates ($r_{ij}, \varphi_{ij}, \theta_{ij}$) are expressed as:

$$\begin{cases} r_{ij} = \left(RangeValue_i\left(j\right)\cdot scaleFactor\right)/1000 \\ \varphi_{ij} = \left(startAngle_i + j\cdot angularResolution\right)/10000 \\ \theta_{ij} = 90^{\circ} - \alpha_i \end{cases} \quad (1)$$

Where r_{ij} is the actual distance between droplet A and the sensor, m; φ_{ij} is the horizontal angle of droplet A; θ_{ij} is the vertical angle of droplet A; $RangeValue_i\left(j\right)$ is the original data output by SOPAS ET software; i represents the scan plane number between 1 ~ 4; $scaleFactor$ is the factor by which the following $RangeValue$ s can be brought to mm scale; $startAngle_i$ is the initial scan angle of the i-plane; $angularResolution$ is the angular resolution in the horizontal direction; and α_i is the angle between the four planes in the vertical direction, with values of −1.6°, −0.8°, 0.8°, and 1.6°.

The scanned droplet point, in Cartesian coordinates, was reconstructed with MATLAB (R2018a, MathWorks Inc., Massachusetts). As shown in Figure 2, the coordinates of the droplet point A $\left(x_{ij},\ y_{ij},\ z_{ij}\right)$ are given by:

$$\begin{cases} x_{ij} = r_{ij}\cdot\sin\theta_{ij}\cdot\cos\varphi_{ij} \\ y_{ij} = r_{ij}\cdot\sin\theta_{ij}\cdot\sin\varphi_{ij} \\ z_{ij} = r_{ij}\cdot\cos\theta_{ij} \end{cases} \quad (2)$$

Spray drift testing in a wind tunnel

Spray drift tests were conducted at the IEA-II wind tunnel at the National Experiment Station for Precision Agriculture, Beijing, China. A diagram of the wind tunnel is presented in Figure 3. This wind tunnel has been used in previous studies, such as Zheng et al. (2017); Zhang et al. (2019), and Tang et al. (2020). The wind tunnel consisted of an open-ended design, with a working section of 6.0 m length, 2.0 m width, and 2.0 m height. The wind tunnel applied an axial flow fan as the power source. Under the combined action of the rectifier and rectifying device, a uniform and stable wind field was generated. The adjustable range of the wind speed in the working section was 0.5 to 7 m/s; the turbulence was less than 0.3%, and the wind uniformity was less than 0.5%. The wind tunnel specifications fulfilled the requirements of the ISO 22856:2008 standard (ISO, 2008).

In this study, drift tests were conducted in strict accordance with ISO 22856:2008. A single and static nozzle was used, with the spray orientated at a right angle to the wind direction (Figure 3).

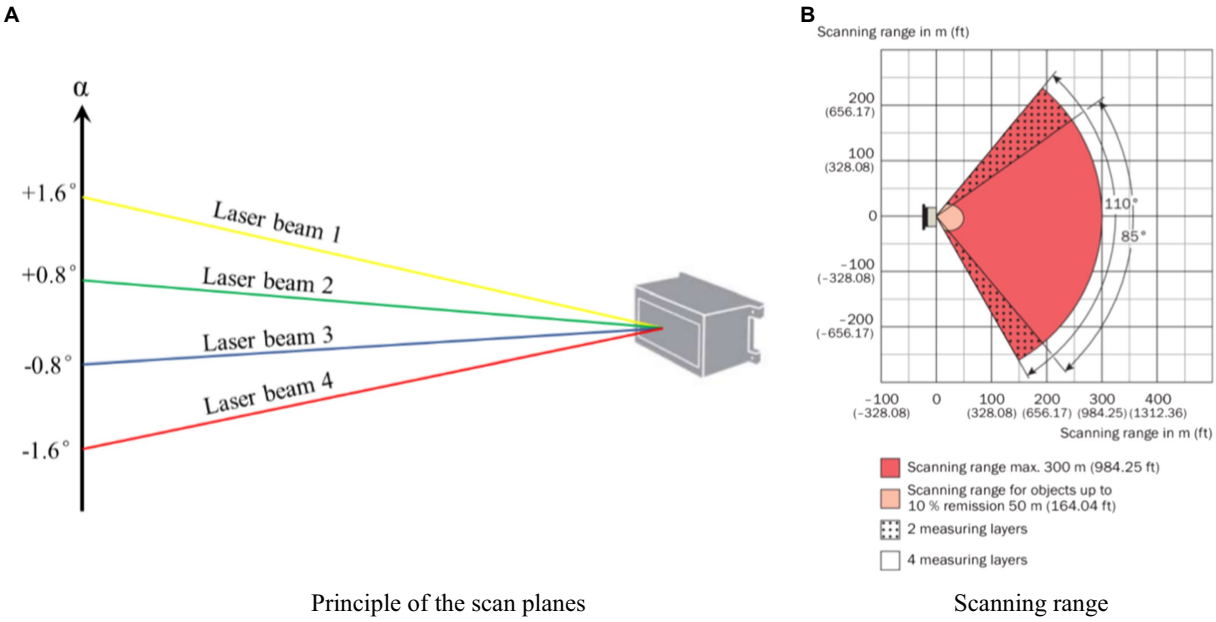

FIGURE 1
Scanning properties of the LiDAR sensor (Operation instructions of LD-MRS 3D LiDAR sensors, Sick AG, 2010). **(A)** Principle of the scan planes. **(B)** Scanning range.

TABLE 1 3D LiDAR sensor specifications.

Parameter	Technical indicators	Experiment settings
Wavelength (nm)	905	—
Laser class	1 (IEC 60825–1:2014)	—
Horizontal aperture angle (°)	110 (−60 ~ 50)	—
Vertical aperture angle (°)	3.2	—
Working range (m)	300	—
Scanning frequency (Hz)	12.5/25/50	25
Angular resolution (°)	0.125/0.25/0.5	0.25
Protection class	III	—
Enclosure rating	IP69K	—
Weight (kg)	1	—
Dimensions (mm)	94 × 165 × 88	—
Interface mode	RS-232/TCP/IP	—

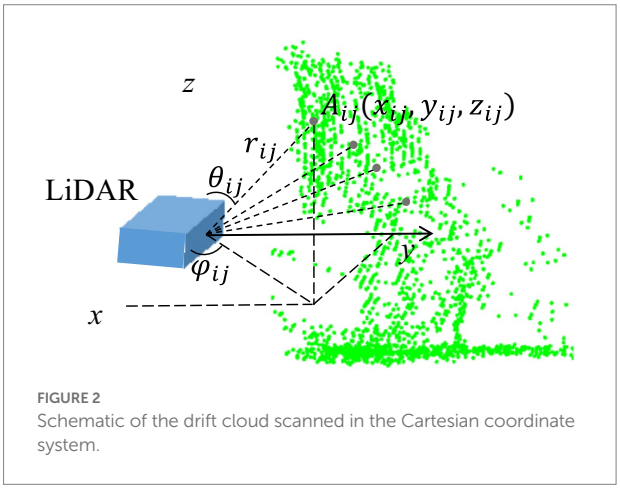

FIGURE 2
Schematic of the drift cloud scanned in the Cartesian coordinate system.

The nozzle was fixed at a height of 0.7 m from the bottom of the wind tunnel. The selected test nozzles were a standard flat-fan spray nozzle ST11002, an air-inclusion spray nozzle IDK12002, and a hollow-cone nozzle TR8002. The spray patterns of the nozzles used have representative characteristics and are widely used (Nuyttens et al., 2007a; Peter et al., 2008; Torrent et al., 2019). A mixture of a water-soluble tracer and yellow tartrazine, with a concentration of 8 g/l, was used as the spray solution. To precisely control the spraying time, a timer was equipped upstream of the nozzle. When the spray time reached the preset value, the timer automatically switched the power off, and the spray system stopped. In this study, the spraying time was set to 20 s. The spray pressure was set to 0.2, 0.3, and 0.4 MPa, and the wind speed was set to 1 to 3 m/s with an interval of 0.5 m/s. During all tests, the temperature of the wind tunnel was 25°C, and the relative humidity was 36%.

Spray drift measurements were performed with both the LiDAR sensor and the passive collectors, following ISO 22866. Before the wind tunnel tests, the flow rates of the three nozzles used were measured by the weighing method. Furthermore, the droplet spectra were tested with a laser particle analyzer (HELOS-VARIO, Sympatec GmbH, Germany). In this study, Dv_{10}, Dv_{50}, and Dv_{90} were measured, and relative span factor (RS), which represents a dimensionless indicator of the uniformity of the drop size distribution, was calculated according to equation (3); during

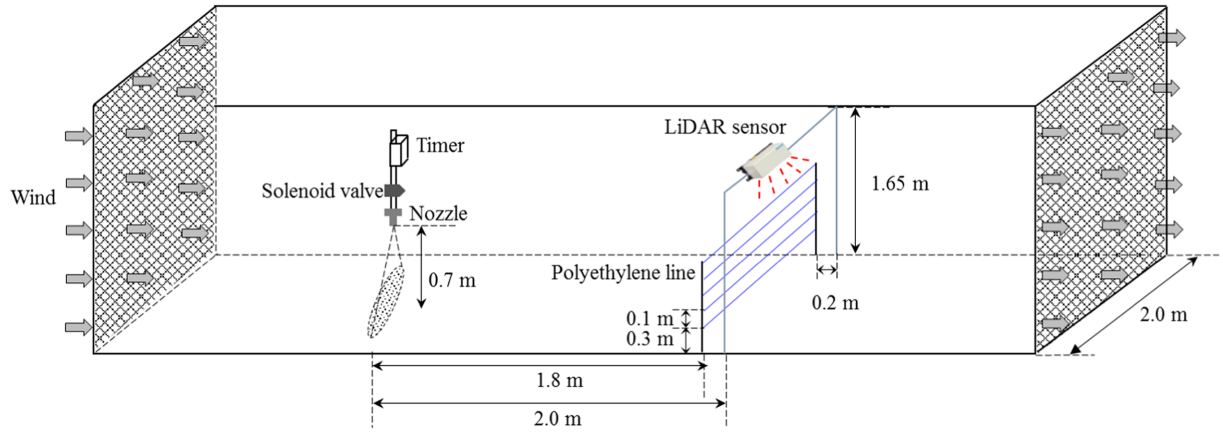

FIGURE 3
Construction of a test platform for measuring droplet drift in the wind tunnel.

TABLE 2 Flow rate and droplet spectra of nozzles.

Nozzle model	Nozzle type	Pressure/MPa	Flow rate/ L·min^{-1}	D_{v10}/μm	D_{v50}/μm	D_{v90}/μm	*RS*
ST11002	Flat-fan	0.2	0.65	71.84	159.74	279.15	1.298
		0.3	0.80	54.57	134.36	231.66	1.318
		0.4	0.92	51.05	124.97	206.76	1.246
IDK12002	Air-inclusion	0.2	0.65	142.49	327.19	594.33	1.381
		0.3	0.80	126.87	287.84	560.16	1.505
		0.4	0.92	109.04	251.20	514.90	1.616
TR8002	Hollow cone	0.2	0.65	64.70	140.88	232.12	1.188
		0.3	0.80	55.47	127.19	209.03	1.207
		0.4	0.92	47.35	115.39	196.56	1.293

the test, the nozzle was fixed at 0.5 m above the analyzer. The flow rates and droplet spectra under various working conditions are shown in Table 2. According to the experimental setup, a total of 60 spray drift tests were conducted.

$$RS = \frac{D_{v90} - D_{v10}}{D_{v50}} \quad (3)$$

Where, *RS* is the relative span factor; D_{v10}, D_{v50}, and D_{v90} are the maximum droplet diameter below which 10%, 50%, and 90% of the volume of the sample exists, respectively, μm.

Sampling process using passive collectors

As shown in Figure 3, a vertical stainless-steel bracket was placed at a horizontal distance of 1.8 m from the nozzle in the downwind direction in the wind tunnel. Five polyethylene lines with a diameter of 2.0 mm were fixed horizontally across the bracket from 0.3 to 0.7 m, at 0.1 m intervals, to sample airborne drift droplets. The minimum height of 0.3 m was fixed to eliminate the impact of droplets bouncing and ground pollution on the test results. When the spraying finished, the polyethylene lines were collected into separate Ziploc bags, and the samples were stored in a dark box. After all the tests had finished, the polyethylene lines were brought to the laboratory for quantitative analysis. Five milliliters of deionized water was added to each Ziploc bag, and it was shaken sufficiently to fully elute and dissolve the tracer on the line surface. The absorbance of the eluate was measured using a visible light spectrophotometer (752 N INESA, Shanghai, China), and the amount of tracer droplets on the passive collector surface was calculated according to:

$$\beta_{dep} = \frac{\left(Abs_{samp} - Abs_{blk}\right) \times V_{dil} \times 10^3}{Abs_{spray}} \quad (4)$$

Where, β_{dep} is the drift deposition volume on the passive collector surface in μL; Abs_{samp} is the spectrophotometer absorbance value of the sample; Abs_{blk} is the absorbance reading of the blanks; V_{dil} is the volume of dilution liquid used to solute the tracer from the passive collector in mL; and

Abs_{spray} is the spectrophotometer absorbance value of the spray mixture.

Spray drift measure algorithm using 3D LiDAR

The LiDAR sensor was fixed on the side of the wind tunnel closest to the vertical bracket. To ensure that the laser beam emitted by the sensor covered the polyethylene lines in the vertical array, the sensor was fixed 1.65 m above the wind tunnel floor, and the laser emitting surface faced downward. To prevent the passive collectors from blocking the laser beams, and considering the scanning planes of the sensor, the horizontal distance between the sensor and the vertical plane of the polyethylene line was set to 0.2 m. In the test, the scanning frequency and angular resolution of the sensor were set to 25 Hz and 0.25°, respectively. To gather more drift droplet points, four layers were used for the evaluation. The sensor was turned on before spraying, and the scanning measurements were initiated with the SOPAS ET software. The scanning time for each test was 1 min. The original data were then exported to the computer, and the drift droplet point was calculated according to equations (1) and (2).

To compare the measurements performed with the LiDAR sensor and the results obtained from the passive collectors, the number of drift points in five height intervals of 0.25–0.35, 0.35–0.45, 0.45–0.55, 0.55–0.65, and 0.65–0.75 m was calculated, corresponding to polyethylene lines at heights of 0.3, 0.4, 0.5, 0.6, and 0.7 m. Assuming the scanning point $A_{ij}(x_{ij}, y_{ij}, z_{ij})$satisfies equation (5), the cumulative number of drift points in the corresponding height interval should increase by increments of one.

$$\begin{cases} x_{\min} \le x_{ij} \le x_{\max} \\ y_0 + (k-1)\cdot\Delta d \le y_{ij} < y_0 + (k)\cdot\Delta d \\ z_{ij} \end{cases} \quad (5)$$

Where, $x_{\min}$ and $x_{\max}$ are the minimum and maximum values of the x-axis of the effective scanning area at $x_{\min} = -1.0$ m and $x_{\max}$ =1.0 m, respectively; y_0 is the minimum height of the effective scanning area, at y_0 =0.25 m; Δd is the height interval between adjacent lines, at Δd =0.1 m; and k is a constant, at $k = 1$, 2, 3, 4, and 5. The droplet points obtained by scanning in the z-axis direction are all valid; therefore, the Z_{ij} is unlimited.

Results

Distribution of drift cloud and drift deposition in a vertical profile

The number of droplet points at different height intervals scanned with the LiDAR sensor was counted, and the amount of tracer droplets deposited on the passive collectors was measured by a spectrophotometer. Figure 4 presents an overview comparison of the drift distributions obtained by the two methods. For each nozzle, a total of 15 panels were obtained under different working conditions, the left of each panel shows the drift points scanned by the LiDAR sensor, and the colored strip plot on the right side of the panel shows the deposition volume in vertical profile. The drift point cloud captured by the LiDAR sensor presents a triangular contour, where the distribution of droplets in the lower section is large and dense. As the height increases, the number of drift points tends to decrease, which is consistent with the results obtained from the passive collectors (from bottom to top, the color of the strip plot gradually fades). For the three nozzles used, the highest number of drift points was produced by the nozzle ST11002, followed by TR8002. The IDK120-02 nozzle had the least drift points, scanned under the same pressure and wind speed as the two other nozzles. The main reason for this finding is that large droplets formed in the air, limiting spray drift (Nuyttens et al., 2009; Vashahi et al., 2018). Under constant pressure, as the wind speed increases, the drifting droplets tend to be denser.

The conventional sampling method is limited by the number and arrangement of samples, making it difficult to obtain the complete spatial distribution of drift droplets. In this section, the height and width ranges of the drift cloud under various operating parameters were calculated based on droplet point coordinates. As shown in Figure 5, the width range of nozzle ST11002 is higher than 1.0 m for all test conditions, which is significantly higher than that of nozzles TR8002 and IDK12002. Despite the spray angle of nozzle IDK12002 being 120°, which is higher than the other two nozzles as it is, affected by the larger droplets produced (Table 2), the width range is smaller than that of nozzles ST11002 and TR8002. In general, for the vertical direction, as the wind speed increases, the height range also increases, and there is little difference between the nozzles.

Figure 6 presents the drift deposition volume and the corresponding scanning points for the vertical profile. In general, the spray drift obtained by the two methods decreases gradually as the height increases. Compared with the passive collector sampling method, the LiDAR technique does not exhibit high capture sensitivity, especially at greater heights. For example, at a pressure of 0.2 MPa, the drift deposition volume of nozzle ST11002 was 6.255, 20.943, and 26.405 μl for wind speeds of 1.0, 1.5, and 2.0 m/s, respectively, while the LiDAR failed to scan any droplet in the height range of 0.65 to 0.75 m. The differences may be a result of the difficulties in the laser beam impacting the low-density point cloud due to a reduced number of drift droplets.

Laser beams emitted by LiDAR sensors are in a divergent radiation mode, implying that the scanning results are affected by the frequency and angular resolution, which makes it difficult to make the actual number of droplets in the space completely consistent with the returned effective laser signal. In this study, through the comparative analysis of the drift deposition volume

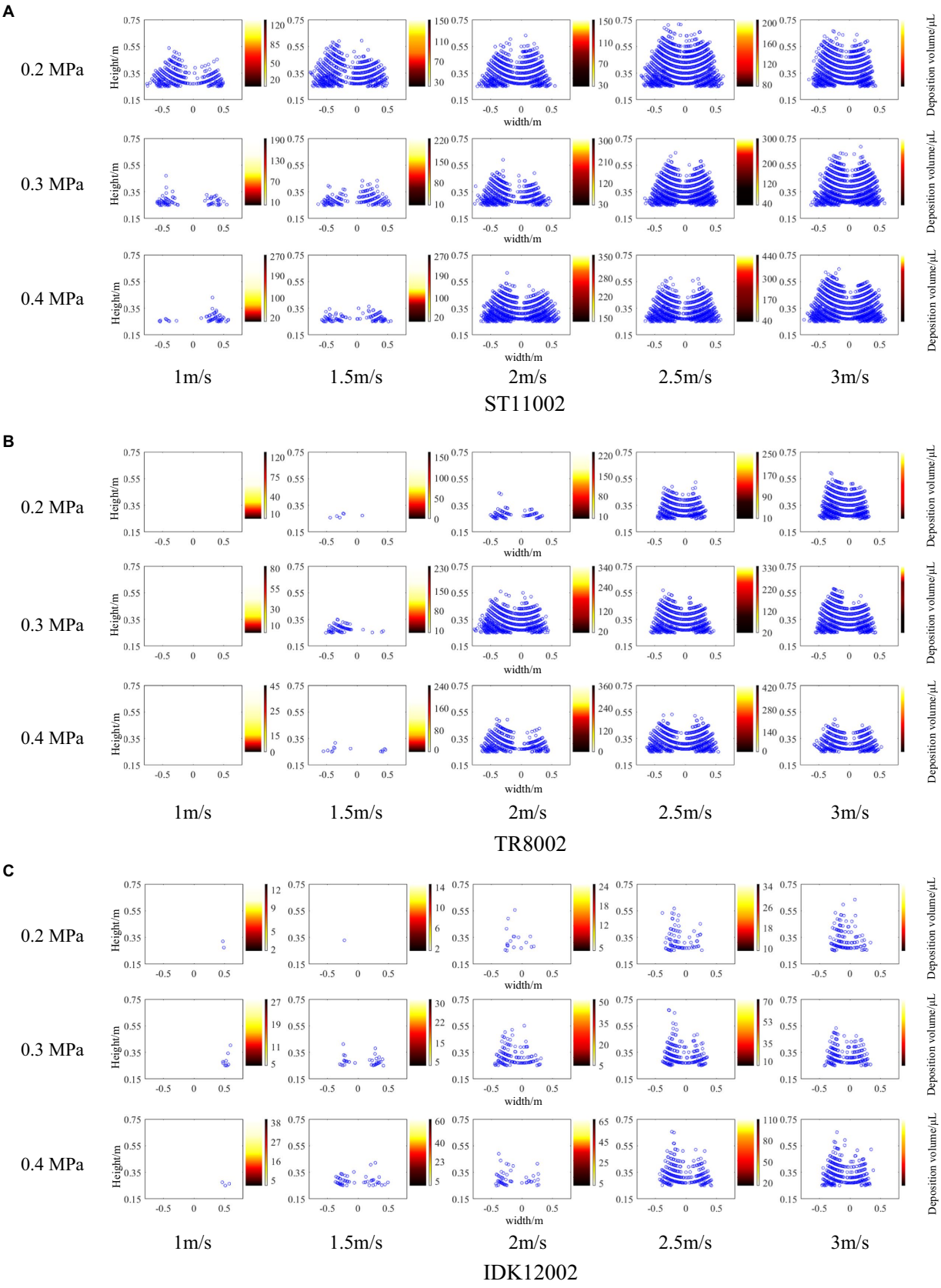

FIGURE 4
Drift points scanned by the LiDAR sensor (left of each panel) and drift deposition captured by passive collectors (right of each panel) for the three nozzles. In the strip plot for each combination, darker colors represent greater drift deposition. **(A)** ST11002. **(B)** TR8002. **(C)** IDK12002.

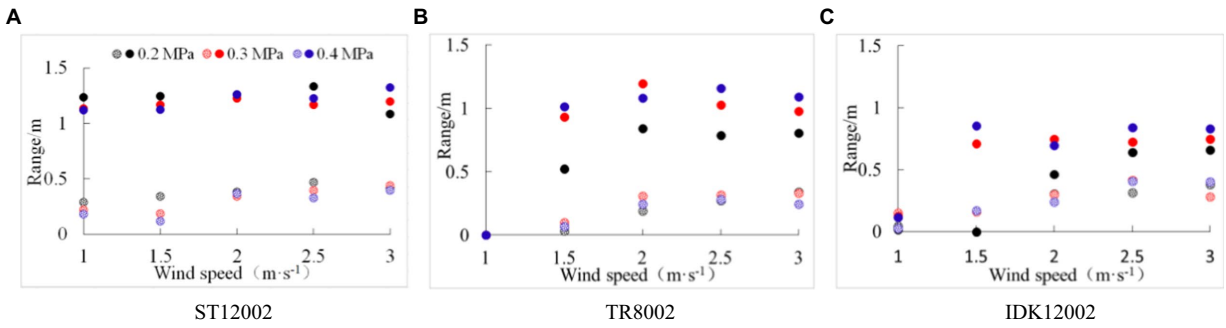

FIGURE 5
Width and height range of drift point distributions scanned by the LiDAR sensor for the three nozzles. The circles filled with solid color represent the width range in the horizontal direction and the circles filled with dotted point represent the height range in the vertical direction. **(A)** ST12002. **(B)** TR8002. **(C)** IDK12002.

and droplet points of the 60 tests, it was found that when the deposition volume was less than 50 μl, LiDAR is prone to invalid scanning, that is, it is difficult to get more feedback laser signal.

Correlation analysis between LiDAR and indirect methods

The drift deposition and the droplet points through the vertical profile were processed further, and a correlation analysis was performed (Figure 7). For the three types of nozzles used, the drift deposition volume for passive collectors gradually increased with increasing wind speed. When the wind speed exceeded 1.5 m/s, the deposition volume increased gradually with an increase in spray pressure (0.4 > 0.3 > 0.2 MPa). The drift points captured by the LiDAR sensor did not show a same regularity as the deposition volume. At 1–2 m/s, the number of drift points gradually increased with an increase in wind speed, while the point number at 2.5 m/s may be less than 3 m/s. For example, for nozzle ST12002 at a spray pressure of 0.4 MPa, the number of drift points at a wind speed of 2.5 m/s was 9,024, which is higher than 7,925 drift points at a wind speed of 3 m/s. The possible reason is that the higher movement speed of droplets affects the capture ability. The IDK12002 nozzle has significantly lower deposition and drift points than the ST11002 and TR8002 nozzles. In this case, 3D LiDAR measurement can classify the drift performance of the conventional nozzle and the anti-drift nozzle.

Through the correlation analysis of 3D LiDAR and the indirect method, it was found that the drift point number captured by 3D LiDAR generally has a good correlation with the deposition volume from passive collectors, with the coefficients of determination (R^2) of the three nozzles being greater than 0.75. Among the three nozzles, IDK122002 with less spray drift and larger droplet size has the best correlation, and the minimum R^2 is 0.80 under the three spray pressure settings. In terms of spray pressure, the R^2 of nozzles ST11002 and IDK12002 showed a decreasing trend with an increase in the spray pressure. When the spray pressure increased, the droplet size decreased (Table 2), and the amount of drifting droplets increased. The laser beam impacted the droplets directly in front of LiDAR, but a few laser beams failed to capture droplets further away from the LiDAR sensor because of the blocking effect of the droplets ahead.

Wt analysis of the influence of spray parameters on 3D LiDAR drift assessment

Changes in spray parameters can affect the drift deposition volume and drift points captured by LiDAR sensors. Through the previous analysis, it was found that the scanning accuracy of 3D LiDAR is different under different droplet size spectra, flow rates, and wind speed conditions. Understanding the influence of these factors can provide support for the rational use of 3D LiDAR to evaluate spray drift. In this study, SPSS software was used to analyze the linear relationship between drift points, deposition volume, and the coefficients of determination R^2 value of the two methods with the flow rate, D_{v50}, *RS*, and wind speed. The corresponding coefficients were calculated, as shown in Table 3. The larger the absolute value of the coefficient, the greater the influence of the parameter on the result.

The influence weights of each parameter were calculated based on the data in Table 3, as shown in Figure 8. The wind speed had the greatest influence on the sampling method by passive collectors with a ratio of 37.74%, with the flow rate, $D_{v50,}$ and relative span factor (*RS*) being equally weighted. For the drift point scanned by LiDAR, the influence of wind speed and D_{v50} accounts for a great proportion, and their influence weights are 49.62% and 42.51%, respectively. For the R^2 values of the two methods, the droplet spectrum had a greater influence, and the weight ratio of D_{v50} and *RS* was more than 80%.

Discussion

In pesticide application process, fine droplets may drift to the non-target area and cause serious environmental and public

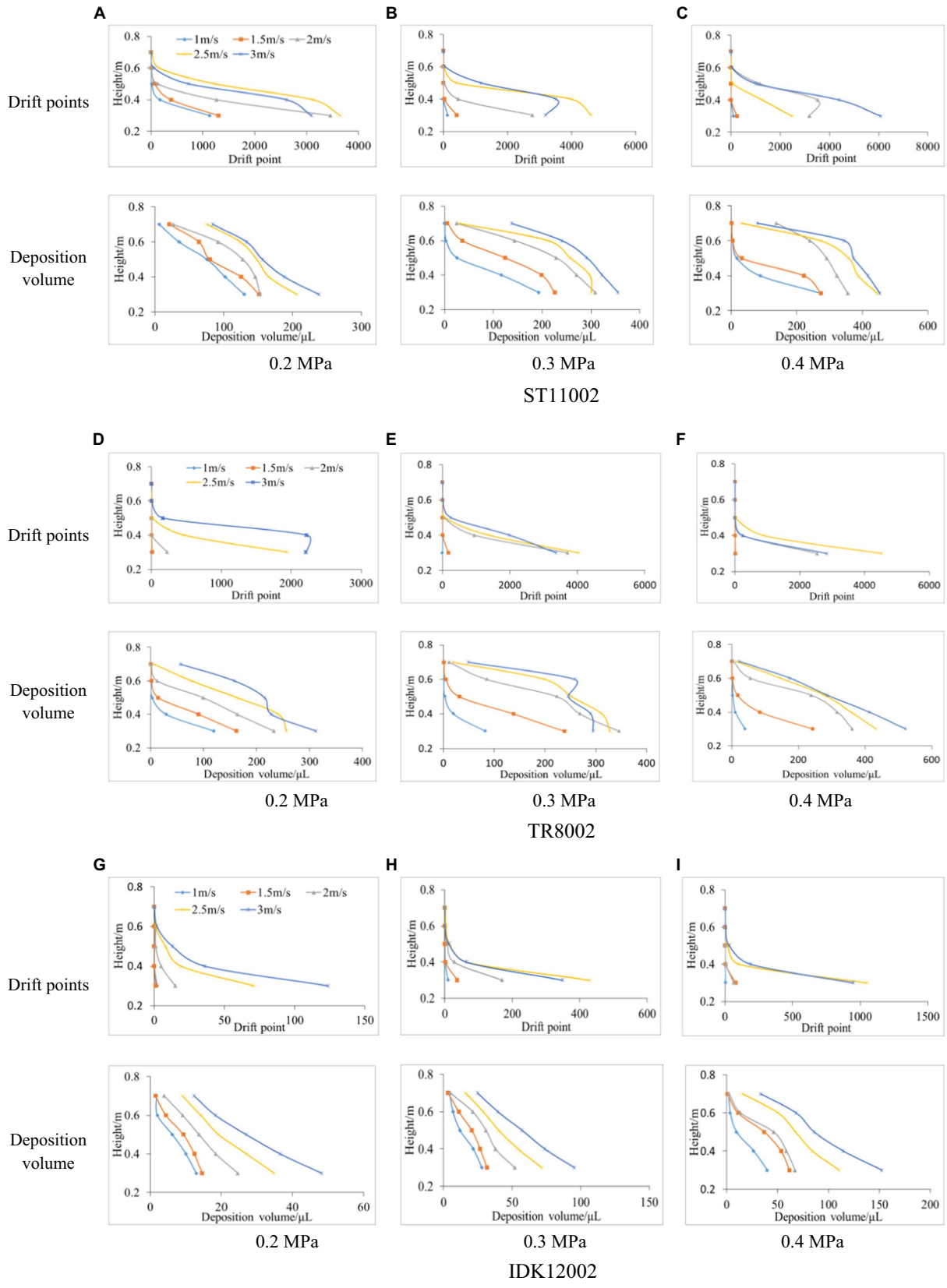

FIGURE 6
Spray drift obtained with passive collectors and LiDAR sensors at various heights for the three nozzles. **(A)** 0.2MPa. **(B)** 0.3MPa. **(C)** 0.4MPa. **(D)** 0.2MPa. **(E)** 0.3MPa. **(F)** 0.4MPa. **(G)** 0.2MPa. **(H)** 0.3MPa. **(I)** 0.4MPa.

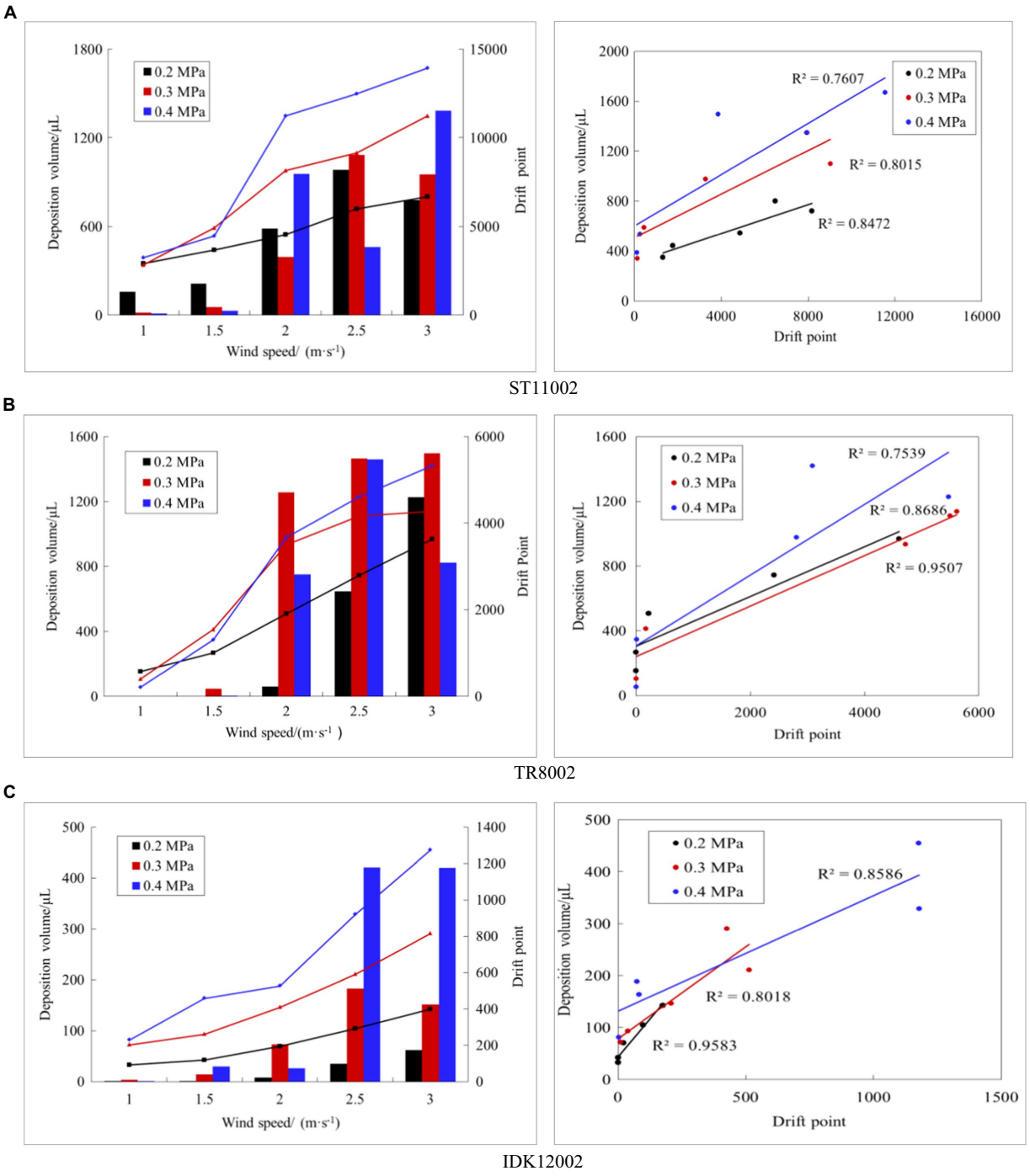

FIGURE 7
Correlation analysis of drift points and deposition volume for the three nozzles. The left panel shows the drift points and deposition under various working conditions (line represents deposition volume, column represents drift points), and the right panel shows the correlation between the two methods. **(A)** ST11002. **(B)** TR8002. **(C)** IDK12002.

health problems, including damage to the adjacent crops sensitive to chemical agents, river contamination, and risk to the health of humans and animals (Nuyttens et al., 2010). At present, spray drift is unavoidable. However, we can optimize the chemical application technology by means of drift evaluation, i.e., nozzle selection, operating parameters adjustment, and suitable working surroundings. Traditional spray drift experiments are complex, time-consuming, and labor-intensive. Therefore, there is a strong demand for an efficient and convenient alternative drift measurement method.

In this study, exploratory work was conducted to demonstrate the capacity of a commercial 3D LiDAR sensor to evaluate spray

drift generated by different nozzle types, spray pressures, and wind speeds. LiDAR measurements were compared with those obtained with the indirect method using passive collectors. Firstly, the coordinates of the drift points scanned by the LiDAR sensor were converted to obtain the point clouds in the vertical profile, intuitively observing the drift droplet distribution (Figure 4). This is difficult to achieve with traditional indirect methods. The drift width and height ranges under various working conditions were calculated through point cloud coordinates (Figure 5). The results can provide a point of reference for setting the size of anti-drift obstacles (De Schampheleire et al., 2009).

The drift points in various height intervals were counted. It was assumed that each height interval was 0.1 m (with the polyethylene line as the center, the upper and lower heights were both 0.05 m). Accordingly, the drift points and deposition volume for passive collectors were compared (Figure 6). Although the LiDAR sensor used a higher scanning frequency of 25 Hz, few droplets impacted the laser beam owing to the lower droplet density at a higher height interval (0.7 m). LiDAR sensor determines drift from the reflected signal of a laser beam impacting a droplet, while it is difficult to equate a laser feedback signal with a droplet, and laser beam impacts are sensitive to droplet density or drift mass. In addition, by correlating the drift points with the deposition volume obtained by the indirect method (Figure 7), it is observed that the nozzle IDK12002 has a better correlation between 3D LiDAR measurements and the indirect method, and the lower spray pressure with less drift appears to be more conducive to drift evaluation with 3D LiDAR. Conversely, Gil et al. (2013) conducted a study using a commercial 2D LiDAR sensor to evaluate the spray drift of orchard sprayers, the results indicate a bad ability of the 2D LiDAR sensor to evaluate spray drift in case of sparse drift cloud with air-inclusion nozzles. The droplet density or drift mass suitable for LiDAR measurement is likely to have a threshold range, beyond which the detection accuracy will be reduced. By comparing all the test data in this study, we found that when the deposition volume was less than 50 µl, 3D LiDAR is prone to invalid scanning.

The drift deposition volume from passive collectors gradually increased with increasing wind speed, while the number of drift points measured by LiDAR does not follow the same law. For example, for nozzle ST12002 at a spray pressure of 0.4 MPa, the number of drift points at a wind speed of 2.5 m/s was 9,024, which is higher than 7,925 drift points at 3 m/s (Figure 7). This phenomenon may be caused by excessive droplet density or by changes in wind speed. When the wind speed is higher, the fine droplets pass through the vertical profile at a higher speed, and either the emitted laser beam fails to perfectly impact the droplets or the high-speed droplets cause part of the energy loss, implying that the reflected signal strength cannot reach the LiDAR system identification threshold.

TABLE 3 Coefficients of spray parameters, according to the linear analysis of drift points, deposition volume, and R^2.

Spray parameter	Flow rate	D_{v50}	*RS*	Wind speed
Drift deposition volume measured by passive collector	0.303	−0.327	−0.312	0.571
Drift points scanned by LiDAR	−0.062	−0.497	0.030	0.580
R^2 of LiDAR and indirect method	−0.219	0.715	−0.519	—

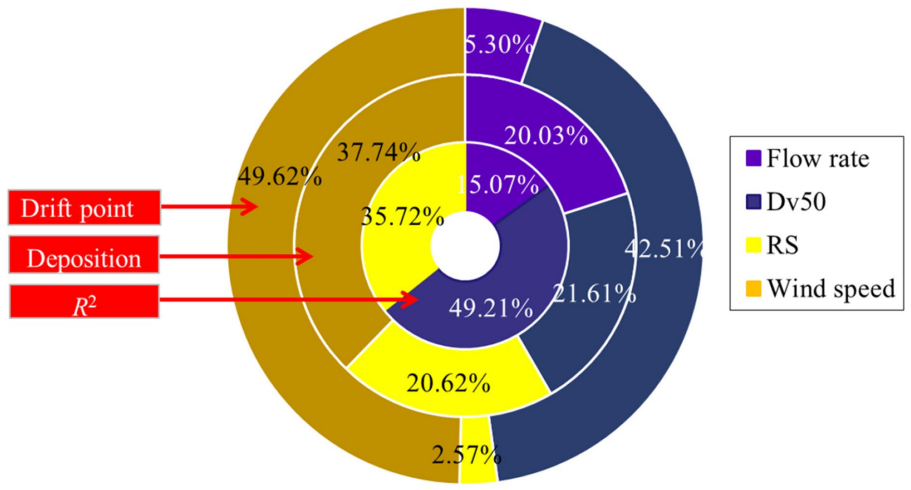

FIGURE 8
Influence weights of spray parameters on drift assessment.

Through the *wt* analysis, it was found that the D_{v50} and *RS* have a great influence on R^2 of LiDAR and indirect method (Figure 8). The droplet spectrum also indirectly affects the droplet density in the detection area. In order to reduce the detection distortion caused by laser beam occlusion and laser beam emission angle resolution, an appropriate detection area needs to be identified in advance. Although the current LiDAR sensor has a maximum detection distance of 300 meters or more, in actual spray drift evaluation, only a small plane (e.g., 1 × 1 m) close to the LiDAR may be selected as the sampling zone. This selected plane needs to be determined by experiments so that LiDAR can restore the spatial distribution of droplets most realistically.

In addition to the factors of the spray drift flux mode, the spray drift measurement with LiDAR in field maybe faces the challenges such as the impact of higher-intensity sunlight, dust suspended in the air, and ambient temperature on the performance of LiDAR. Gregorio et al. (2019) confirmed that spray drift measurement distortion maybe occured because of the presence of air-suspended dust based on the LiDAR system developed. Nowdays, the research on LiDAR detection performance in agriculture mainly focuses on sensing geometric characterization of canopy and obstacle in agricultural activities (Lee and Ehsani, 2008; Rosell and Sanz, 2021). Commercially available LiDAR sensors are expected to be a practical tool for drift assessment. However, the current research depth and breadth are not enough. It is essential to carry out subsequent research combined droplet characteristics, drift point cloud spatial distribution, application scenarios, and environmental conditions, to determine the optimal conditions for LiDAR measurements such as droplet density ranges, LiDAR Settings, and environmental conditions.

Conclusion

3D LiDAR sensors provide a fast and efficient detection method for evaluating the drift performance of different types of nozzles and spraying techniques. Through non-contact scanning, the spatiotemporal distribution plots of drifting droplets can be provided, and the influence of environmental characteristics on the spatial transport of drifting droplets can be evaluated. Compared with the traditional method of using passive collectors, LiDAR technology significantly reduces time and labor cost, as well as the operator's exposure to chemical pesticides.

In general, a good correlation was observed between the drift deposition with passive collectors and the drift points scanned by 3D LiDAR. This non-contact sensing method has shown potential for evaluating spray drift characteristics of nozzles under different working conditions. However, it is difficult to equate a laser feedback signal with a droplet, the droplet detection performance of commercially available 3D LiDAR sensors is limited by sensitivity to droplet density. It can be inferred that the effectiveness of LiDAR on droplet detection has certain threshold requirements for droplet density, knowing the optimal droplet density range can greatly improve the detection accuracy of LiDAR. Also, the droplet spectrum and movement speed may be other important factors, which affect the strength and quantity of the reflected signal of a laser beam impacting droplet. In this study, IDK12002 shows the best correlation between 3D LiDAR measurements and the indirect method, and the lower spray pressure with less drift and larger droplet size appears to be more conducive to drift evaluation with 3D LiDAR. Further research would be arranged to investigate the influence of droplet size and movement speed on detection results, and clarify the maximum and droplet density threshold range allowed by 3D LiDAR detection.

Data availability statement

The raw data supporting the conclusions of this article will be made available by the authors, without undue reservation.

Author contributions

LL: conceptualization, methodology, writing—original draft, and funding acquisition. RZ: methodology, supervision, writing—review and editing, and funding acquisition. LC: software, formal analysis, and writing—review and editing. BL: resources, software, data curation, and investigation. LZ: software and data curation. QT, CD, and ZZ: resources, validation, and investigation. AH: methodology. All authors contributed to the article and approved the submitted version.

Funding

This work was supported by National Key R&D Program of China (2019YFD1101102-3), the National Natural Science Foundation of China (32071907), and Youth Research Fund of BAAFS (QNJJ202009).

Conflict of interest

The authors declare that the research was conducted in the absence of any commercial or financial relationships that could be construed as a potential conflict of interest.

Publisher's note

References

Allwine, K. J., Thistle, W. H., Teske, E. M., and Anhold, H. (2010). The agricultural dispersal-valley spray drift modeling system compared with pesticide drift data. *Environ. Toxicol. Chem.* 21, 1085–1090. doi: 10.1002/etc.5620210526

Arvidsson, T., Bergstrom, L., and Kreuger, J. (2011a). Spray drift as influenced by meteorological and technical factors. *Pest Manag. Sci.* 67, 586–598. doi: 10.1002/ps.2114

Arvidsson, T., Bergström, L., and Kreuger, J. (2011b). Comparison of collectors of airborne spray drift. Experiments in a wind tunnel and field measurements. *Pest Manag. Sci.* 67, 725–733. doi: 10.1002/ps.2115

ASAE (2009). ASAE S572.1. Spray Nozzle Classification by Droplet Spectra. American Society of Agricultural Engineers. (MI: St. Joseph), 4.

Bai, G., Nakano, K., Mizukami, T., Miyahara, S., Ohashi, S., Kubotab, Y., et al. (2013). Characteristics and classification of Japanese nozzles based on relative spray drift potential. *Crop Prot.* 46, 88–93. doi: 10.1016/j.cropro.2012.12.017

Balsari, P., Marucco, P., and Tamagnone, M. (2005). A system to assess the mass balance of spray applied to tree crops. *Transac. ASAE* 48, 1689–1694. doi: 10.13031/2013.19997

Balsari, P., Marucco, P., and Tamagnone, M. (2007). A test bench for the classification of boom sprayers according to drift risk. *Crop Prot.* 26, 1482–1489. doi: 10.1016/j.cropro.2006.12.012

Berg, F. V. D., Kubiak, R., and Benjey, W. G. (1999). Emission of pesticides into the air. *Water Air Soil Pollut.* 115, 195–218. doi: 10.1023/A:1005234329622

Bonds, J. A., Greer, M. J., Fritz, B. K., and Hoffmann, W. C. (2009). Aerosol sampling: comparison of two rotating impactors for field droplet sizing and volumetric measurements. *J. Am. Mosq. Control Assoc.* 25, 474–479. doi: 10.2987/09-5882.1

Bui, Q. D., Womac, A. R., Howard, K. D., Mulrooney, J. E., and Amin, M. K. (1998). Evaluation of samplers for spray drift. *Trans. ASAE.* 41, 37–41. doi: 10.13031/2013.17149

Butler Ellis, M. C., Swan, T., Miller, P. C. H., Waddelow, S., Bradley, A., and Tuck, C. R. (2002). Design factors affecting spray characteristics and drift performance of air induction nozzles. *Biosyst. Eng.* 82, 289–296. doi: 10.1006/bioe.2002.0069

Caldwell, B. C., and Wolf, T. M. (2006). Measurement of long-distance particle drift using a fluorescent tracer-samplers, sensitivity, detection limits and background. *Asp. Appl. Biol.* 77, 371–378.

Carlsen, S. C. K., Spliid, N. H., and Svensmark, B. (2006). Drift of 10 herbicides after tractor spray application. 2. Primary drift (droplet drift). *Chemosphere* 64, 778–786. doi: 10.1016/j.chemosphere.2005.10.060

De Schampheleire, M., Nuyttens, D., Dekeyser, D., Verboven, P., Spanoghe, P., Cornelis, W., et al. (2009). Deposition of spray drift behind border structures. *Crop Prot.* 28, 1061–1075. doi: 10.1016/j.cropro.2009.08.006

Elliott, J. G., and Wilson, B. J. (1983). *The Influence of Weather on the Efficiency and Safety of Pesticide Application: The Drift of Herbicides*. The British Crop Protection Council: London, United Kingdom.

EPA-United States Environmental Protection Agency. (2018). Introduction to pesticide drift. Available at: https://www.epa.gov/reducing-pesticide-drift/introduction-pesticide-drift (Accessed December 28, 2021).

Ferguson, J. C., Chechetto, R. G., O'Donnell, C. C., Door, G., Moore, J. H., and Baker, G. J. (2016). Determining the drift potential of Venturi nozzles compared with standard nozzles across three insecticide spray solutions in a wind tunnel. *Pest Manag. Sci.* 72, 1460–1466. doi: 10.1002/ps.4214

Forster, W. A., Mercer, G. N., and Schou, W. C. (2012). Spray droplet impaction models and their use within AGDISP software to predict retention. *New Z. Plant Protect.* 65, 85–92. doi: 10.30843/nzpp.2012.65.5393

Gil, E., Balsari, P., Gallart, M., Llorens, J., Marucco, P., Andersen, P. G., et al. (2014). Determination of drift potential of different flat fan nozzles on a boom sprayer using a test bench. *Crop Prot.* 56, 58–68. doi: 10.1016/j.cropro.2013.10.018

Gil, E., Llorens, J., Llop, J., Fàbregas, X., and Gallart, M. (2013). Use of a terrestrial LIDAR sensor for drift detection in vineyard spraying. *Sensors* 13, 516–534. doi: 10.3390/s130100516

Gil, Y., and Sinfort, C. (2005). Emission of pesticides to the air during sprayer application: a bibliographic review. *Atmos. Environ.* 39, 5183–5193. doi: 10.1016/j.atmosenv.2005.05.019

Gregorio, E., Rocadenbosch, F., Sanz, R., and Rosell-Polo, J. R. (2015). Eye-safe lidar system for pesticide spray drift measurement. *Sensors.* 15, 3650–3670. doi: 10.3390/s150203650

Gregorio, E., Torrent, X., Planas, S., and Rosell-Polo, J. R. (2019). Assessment of spray drift potential reduction for hollow-cone nozzles: part 2. LiDAR technique. *Sci. Total Environ.* 687, 967–977. doi: 10.1016/j.scitotenv.2019.06.151

Grella, M., Marucco, P., and Balsari, P. (2019). Toward a new method to classify the airblast sprayers according to their potential drift reduction: comparison of direct and new indirect measurement methods. *Pest Manag. Sci.* 75, 2219–2235. doi: 10.1002/ps.5354

Heidary, M. A., Douzals, J. P., Sinfort, C., and Vallet, A. (2014). Influence of spray characteristics on potential spray drift of field crop sprayers: a literature review. *Crop Prot.* 63, 120–130. doi: 10.1016/j.cropro.2014.05.006

Herbst, A. (2001). "A method to determine spray drift potential from nozzles and its link to buffer zone restrictions." In: *Proceedings of the 2001 ASAE Annual International Meeting, Paper no. 01-1047*; August 1, 2001.

Hilz, E., and Vermeer, A. W. P. (2013). Spray drift review: the extent to which a formulation can contribute to spray drift reduction. *Crop Prot.* 44, 75–83. doi: 10.1016/j.cropro.2012.10.020

Hoff, R. M., Mickle, R. E., and Froude, F. A. (1989). A rapid acquisition LiDAR system for aerial spray di-agnostics. *Trans. ASABE* 32, 1523–1528. doi: 10.13031/2013.31183

ISO (2008). ISO 22856:20008. Equipment for Crop Protection d Methods for the Laboratory Measurement of Spray Drift d — Wind Tunnels.

ISO (2005). ISO 22866:2005. Equipment for Crop Protection d Methods for Field Measurement of Spray Drift. Geneva: International Standard Organization.

Jiao, L., Dong, D., Feng, H., Zhao, X., and Chen, L. (2016). Monitoring spray drift in aerial spray application based on infrared thermal imaging technology. *Comput. Electron. Agric.* 121, 135–140. doi: 10.1016/j.compag.2015.12.006

Jong, F., Snoo, G., and Zande, J. (2008). Estimated nationwide effects of pesticide spray drift on terrestrial habitats in the Netherlands. *J. Environ. Manage.* 86, 721–730. doi: 10.1016/j.jenvman.2006.12.031

Kira, O., Dubowski, Y., and Linker, R. (2018). In-situ open path FTIR measurements of the vertical profile of spray drift from air-assisted sprayers. *Biosyst. Eng.* 169, 32–41. doi: 10.1016/j.biosystemseng.2018.01.010

Lebeau, F., Verstraete, A., Stainier, C., and Destain, M. F. (2011). RTDrift: a real time model for estimating spray drift from ground applications. *Comput. Electr. Agric.* 77, 161–174. doi: 10.1016/J.COMPAG.2011.04.009

Lee, K.-H., and Ehsani, R. (2008). Comparison of two 2D laser scanners for sensing object distances, shapes, and surface patterns. *Comput. Electr. Agric.* 60, 250–262. doi: 10.1016/j.compag.2007.08.007

Miller, D. R., Salyani, M., and Hiscox, A. B. (2003). "Remote measurement of spray drift from orchard sprayers using LIDAR." In: In: *Proceedings of the 2003 ASAE Annual International Meeting, Paper NO. 031093*; July 27–30, 2003.

Nuyttens, D., Baetens, K., De Schampheleire, M., and Sonck, B. (2007a). Effect of nozzle type, size and pressure on spray droplet characteristics. *Biosyst. Eng.* 97, 333–345. doi: 10.1016/j.biosystemseng.2007.03.001

Nuyttens, D., De Schampheleire, M., Baetens, K., and Sonck, B. (2007b). The influence of operator controlled variables on spray drift from field crop sprayers. *Trans. ASABE* 50, 1129–1140. doi: 10.13031/2013.23622

Nuyttens, D., De Schampheleire, M., Verboven, P., and Sonck, B. (2010). Comparison between indirect and direct spray drift assessment methods. *Biosyst. Eng.* 105, 2–12. doi: 10.1016/j.biosystemseng.2009.08.004

Nuyttens, D., Taylor, W. A., De Schampheleire, M., Verboven, P., and Dekeyser, D. (2009). Influence of nozzle type and size on drift potential by means of different wind tunnel evaluation methods. *Biosyst. Eng.* 103, 271–280. doi: 10.1016/j.biosystemseng.2009.04.001

Oerke, E. C. (2006). Crop losses to pests. *J. Agric. Sci.* 144, 31–43. doi: 10.1017/S0021859605005708

Peter, H., Lynette, B., Christy, S., Helmut, S., and Nader, S. (2008). Flant fan and air incuction nozzles affect soybean herbicide efficacy. *Weed Biol. Manag.* 8, 31–38. doi: 10.1111/j.1445-6664.2007.00271.x

Rosell, J. R., and Sanz, R. (2021). A review of methods and applications of the geometric characterization of tree crops in agricultural activities. *Comput. Electr. Agric.* 81, 124–141. doi: 10.1016/j.compag.2011.09.007

Ru, Y., Zhu, C., and Bao, R. (2014). Spray drift model of droplets and analysis of influencing factors based on wind tunnel. *Trans. Chin. Soc. Agric. Machin.* 45, 66–72. doi: 10.6041/j.issn.1000-1298.2014.10.011

Schampheleire, D. M., Spanoghe, P., Brusselman, E., and Sonck, S. (2007). Risk assessment of pesticide spray drift damage in Belgium. *Crop Prot.* 26, 602–611. doi: 10.1016/j.cropro.2006.05.013

Sick, A. G. (2010). *Online Help-operation Instructions of LD-MRS 3D LiDAR Sensors*. Waldkirch, Germany: Sick AG.

Southcombe, E. S. E., Miller, P. C. H., Ganzelmeier, H., van de Zande, J. C., Miralles, A., and Hewitt, A. J. (1997). "The International (BCPC) Spray Classification System Including a Drift Potential Factor." in *The Brighton Crop Protection Conference Weeds Proceedings of an International Conference*; November 17–20, 1997; (Brignton, UK), 371–380.

Stoughton, T. E., Miller, D. R., Yang, X., and Ducharme, K. M. (1997). A comparison of spray drift predictions to lidar data. *Agric. Forest Meteorol.* 88, 15–26. doi: 10.1016/S0168-1923(97)00056-7

Tang, Q., Zhang, R., Chen, L., Xu, G., and Li, L. (2020). High-accuracy, high-resolution downwash flow field measurements of an unmanned helicopter for precision agriculture. *Comput. Electron. Agric.* 173:105390. doi: 10.1016/j.compag.2020.105390

Taylor, W. A., Womac, A. R., Miller, P. C. H., and Taylor, B. P. (2004). "An attempt to relate drop size to drift risk." in *Proceedings of the International Conference on Pesticide Application for Drift Management*; October 27–29; (Waikoloa, Hawaii), 210–223.

Teske, M. E., Bird, S. L., Esterly, D. M., Curbishley, T. B., Ray, S. L., and Perry, S. G. (2000). AgDRIFTt: A model for estimating near-field spray drift from aerial applications. *Environ. Toxicol. Chem.* 21, 659–671. doi: 10.1002/etc.5620210327

Torrent, X., Gregorio, E., Douzals, J. P., Tinet, C., Rosell-Polo, J. R., and Santiago, P. (2019). Assessment of spray drift potential reduction for hollow-cone nozzles: part 1. Classification using indirect methods. *Sci. Total Environ.* 692, 1322–1333. doi: 10.1016/j.scitotenv.2019.06.121

Tsakirakis, A. N., Kasiotis, K. M., Pelagia, A., Rianda, G., Richard, G., and Kyriaki, M. (2018). Determination of pesticide dermal transfer to operators & agricultural workers through contact with sprayed hard surfaces. *Pest Manag. Sci.* 74, 2858–2863. doi: 10.1002/ps.5077

Vashahi, F., Ra, S., Choi, Y., and Lee, J. K. (2018). Influence of design parameters on the air/liquid ratio of an air induction nozzle. *J. Mech.* 34, 375–385. doi: 10.1017/jmech.2017.12

Wang, Z., He, X., Li, T., Huang, M., Zhang, Y., Xu, L., et al. (2019). Evaluation method of pesticide droplet drift based on laser imaging[J]. *Trans. Chin. Soc. Agric. Eng.* 35, 73–79. doi: 10.11975/j.issn.1002-6819.2019.09.009

Zhang, H., Dorr, G., Zheng, J., Zhou, H., and Yu, J. (2015). Wind tunnel experiment and regression model for spray drift. *Trans. Chin. Soc. Agric. Eng.* 31, 94–100. doi: 10.3969/j.issn.1002-6819.2015.03.013

Zhang, R., Li, L., Fu, W., Chen, L., Yi, T., Tang, Q., et al. (2019). Spraying atomization performance by pulse width modulated variable and droplet deposition characteristics in wind tunnel. *Trans. Chin. Soc. Agric. Eng.* 35, 42–51. doi: 10.11975/j.issn.1002-6819.2019.03.006

Zhang, X., Luo, Y., and Goh, K. S. (2017). Modeling spray drift and runoff-related inputs of pesticides to receiving water. *Environ. Pollut.* 234, 48–58. doi: 10.1016/j.envpol.2017.11.032

Zhang, R., Zhang, Z., Xu, G., Chen, L., and Hewitt, A. J. (2018). Effect of spray adjuvant types and concentration on nozzle atomization. *Trans. Chin. Soc. Agric. Eng.* 34, 36–43. doi: 10.11975/j.issn.1002-6819.2018.20.005

Zheng, Y., Yang, S., Lan, Y., Hoffmann, C., Zhao, C., Chen, L., et al. (2017). A novel detection method of spray droplet distribution based on LiDARs. *Int. J. Agric. Biol. Eng.* 10, 54–65. doi: 10.25165/j.ijabe.20171004.3118

frontiers | Frontiers in Plant Science

TYPE Original Research
PUBLISHED 06 September 2022
DOI 10.3389/fpls.2022.993961

OPEN ACCESS

EDITED BY
Ruirui Zhang,
Beijing Academy of Agricultural and Forestry Sciences, China

REVIEWED BY
Lang Xia,
Institute of Agricultural Resources and Regional Planning (CAAS), China
Chunshan Wang,
Agricultural University of Hebei, China

*CORRESPONDENCE
Yuxing Han
yuxinghan@sz.tsinghua.edu.cn

†These authors have contributed equally to this work and share first authorship

SPECIALTY SECTION
This article was submitted to Technical Advances in Plant Science, a section of the journal Frontiers in Plant Science

RECEIVED 14 July 2022
ACCEPTED 12 August 2022
PUBLISHED 06 September 2022

CITATION
Wang J, Cai M, Gu Y, Liu Z, Li X and Han Y (2022) Cropland encroachment detection *via* dual attention and multi-loss based building extraction in remote sensing images. *Front. Plant Sci.* 13:993961. doi: 10.3389/fpls.2022.993961

Cropland encroachment detection *via* dual attention and multi-loss based building extraction in remote sensing images

Junshu Wang[1†], Mingrui Cai[1†], Yifan Gu[1], Zhen Liu[1], Xiaoxin Li[1] and Yuxing Han[2*]

[1]College of Electronic Engineering, College of Artificial Intelligence, South China Agricultural University, Guangzhou, China, [2]Shenzhen International Graduate School, Tsinghua University, Shenzhen, China

The United Nations predicts that by 2050, the world's total population will increase to 9.15 billion, but the per capita cropland will drop to 0.151°hm^2. The acceleration of urbanization often comes at the expense of the encroachment of cropland, the unplanned expansion of urban area has adversely affected cultivation. Therefore, the automatic extraction of buildings, which are the main carriers of urban population activities, in remote sensing images has become a more meaningful cropland observation task. To solve the shortcomings of traditional building extraction methods such as insufficient utilization of image information, relying on manual characterization, etc. A U-Net based deep learning building extraction model is proposed and named AttsegGAN. This study proposes an adversarial loss based on the Generative Adversarial Network in terms of training strategy, and the additionally trained learnable discriminator is used as a distance measurer for the two probability distributions of ground truth P_{data} and prediction P_g. In addition, for the sharpness of the building edge, the Sobel edge loss based on the Sobel operator is weighted and jointly participated in the training. In WHU building dataset, this study applies the components and strategies step by step, and verifies their effectiveness. Furthermore, the addition of the attention module is also subjected to ablation experiments and the final framework is determined. Compared with the original, AttsegGAN improved by 0.0062, 0.0027, and 0.0055 on Acc, F1, and IoU respectively after adopting all improvements. In the comparative experiment. AttsegGAN is compared with state-of-the-arts including U-Net, DeeplabV3+, PSPNet, and DANet on both WHU and Massachusetts building dataset. In WHU dataset, AttsegGAN achieved 0.9875, 0.9435, and 0.8907 on Acc, F1, and IoU, surpassed U-Net by 0.0260, 0.1183, and 0.1883, respectively, demonstrated the effectiveness of the proposed components in a similar hourglass structure. In Massachusetts dataset, AttsegGAN also

surpassed state-of-the-arts, achieved 0.9395, 0.8328, and 0.7130 on Acc, F1, and IoU, respectively, it improved IoU by 0.0412 over the second-ranked PSPNet, and it was 0.0025 and 0.0101 higher than the second place in Acc and F1.

KEYWORDS

UAV, cropland observation, building extraction, WHU building dataset, Massachusetts building dataset, multi-loss, dual attention, Sobel edge loss

Introduction

Since 1990, the trend of population migration to cities has become more pronounced, which has resulted in cities becoming the main carriers for modern human economic and social activities (Buhaug and Urdal, 2013). Statistics show that the average global cropland area loss between 1992 and 2004 was about 30,000 km^2yr^{-1}, of which 34.3% was converted to settlements, and that cropland loss was particularly pronounced in Asia in the following decade (Tan and Li, 2019). Especially in China where, even though the illegal occupation of planting land has been written into the criminal law, the occupation of cropland is still common (Xing, 2016). Due to the rapid urbanization process, the occupation of cropland is often reflected in the expansion of building areas (as shown in **Figure 1**), which has become a common phenomenon (McKittrick, 2013). Therefore, the automatic detection of buildings is crucial to the protection of cropland. On the other hand, for automated agricultural intelligent devices such as robots and UAVs, accurate identification of buildings will also provide effective reference information for their path planning and obstacle avoidance tasks.

Buildings are one of the most widely distributed and most important types of man-made objects and could be extracted by satellite or UAV (Unmanned Aerial Vehicle) remote sensing images understanding (Alshehhi et al., 2017). Currently, with the development of remote sensing technology, such as SPOT 6 of France, ZY-3, Gaofen-1 and Gaofen-2 of China, and WorldView-3 of the United States can already use meters or submeters as its spatial resolution measurement unit, and it has reached or approached the quality of aerial photography (Chen W. et al., 2017; Ghimire et al., 2020). Compared with medium and low resolution, higher resolution remote sensing images have the following characteristics:

(1) The spectral features of the ground objects are more obvious, the spectral difference between the same type of ground objects becomes larger, and the spectral difference between different types of ground objects becomes smaller;

(2) Higher spatial resolution makes the data volume of a single image larger;

(3) A single pixel often corresponds to only one type of ground object;

(4) There is more detailed information of ground objects, such as shape, brightness, texture, etc;

(5) The background of ground objects is more complex and diverse.

These distinctive features also present higher requirements for building extraction. In order to meet these various requirements of new application areas, identifying buildings in high-resolution remote sensing images is the core challenge.

Traditional remote sensing image building extraction methods mainly include knowledge-based methods using geometric knowledge and context knowledge, along with object-based image analysis (OBIA)-based methods and machine-learning-based methods using image segmentation and target classification (Cheng and Han, 2016). In these traditional methods, the extraction task often requires experts to judge and design according to the spectrum, texture, shape, spatial relationship, and other information of the building, which relies heavily on abundant human imagination, ingenuity, and experience for the design of the features. Fortunately, Hinton and Salakhutdinov (2006) demonstrated the powerful feature representation capability of deep learning models in computer vision applications. They showed that the features will be automatically obtained from the existing data by the neural network through sampling, and the more abstract features beyond human imagination can be effectively obtained by increasing the depth of the network. The burden of feature design can be shifted to model design, which is relatively simple (Ubbens and Stavness, 2017).

However, in remote sensing images, due to the increasing complexity of buildings and their backgrounds caused by progressively higher resolution, the application of deep learning to building extraction still has problems (Jun et al., 2016), such as insufficient extraction of multi-scale targets, insufficient use of image information, model overfitting, and ambiguous edges in prediction, etc. Therefore, there are still challenges with regard to accurately segmenting and characterizing buildings. In this article, to solve these deficiencies, a deep-learning-based building extraction method is proposed. The contributions of this paper can be listed as follows:

(1) The dual-attention mechanism is used, which enhances the information utilization of remote sensing imagery within

FIGURE 1
Encroachment by buildings on cropland.

both feature maps and channels, and dedicates computing resources to more critical areas.

(2) In view of the multi-scale features of modern buildings, the ASPP (atrous spatial pyramid pooling) module is added to the model, which reduces the amount of computation and parameters while increasing the receptive field of the model, enhancing its ability to extract buildings with multiple sizes and shapes.

(3) In terms of model training, to make the prediction more artificial, a learnable discriminator and adversarial loss based on the idea of generative adversarial networks are proposed, and the authenticity of the prediction is used as an auxiliary reference to guide the learning process of the model by weighted adversarial loss.

(4) In terms of loss design, an edge loss based on the Sobel operator was proposed to solve the problem of the edges of buildings being susceptible to approximate background interference.

The following sections are arranged as follows: the relevant foundations involved in this study are presented in Section "Related works"; the components, WHU dataset, multi-losses design, evaluation indexes, etc., are detailed in Section "Materials and methods"; ablation experiments and comparative experiments are presented and discussed in Section "Results and discussion"; and in Section "Conclusion," a summary of the full paper is given.

Related works

Image segmentation and semantic segmentation

The principle of building extraction is to use a building's characteristics to achieve target recognition and accurately distinguish it from the background. Previous researchers tended to identify buildings in the order of image segmentation, and then artificial characterization (Khan, 2014). The traditional image segmentation method divides an image into several regions and realizes the feature similarity within the region and the feature difference between regions.

The main methods are: (1) the threshold-based segmentation method; (2) the edge-based segmentation method; (3) the region-based segmentation method; (4) the graph-based segmentation method; and (5) the energy-based segmentation method.

However, the above methods that utilize the low-level semantics do not fully utilize the high-level semantics of remote

sensing images to qualitatively analyze the segmented regions. In practical application, especially when processing high-resolution images, the characteristics of targets will be relatively complex, and the differences between the same kinds of targets are relatively large; therefore, algorithms that only rely on low-level content information such as color, brightness, texture, etc., are insufficient to achieve a reasonable segmentation. Different from these traditional methods, the deep-learning-based semantic segmentation method can not only realize the image segmentation function, but can also achieve qualitative analysis and automatic classification for the area after clustering the pixels. In this process, abstract high-level semantic features will be fully utilized to achieve more accurate predictions.

The appearance of "semantic segmentation" as a noun can be traced back to the 1970s. Ohta et al. (1978) proposed the concept of semantic segmentation and emphasized assigning a label to each pixel in the image, thereby emphasizing the semantic meaning of the segmented region. Semantic segmentation belongs to the pixel-level scene understanding task in computer image processing, which enables a dense prediction of the input image and a label assignment for each pixel. Therefore, deep-learning-based semantic segmentation is not an isolated task, it involves image classification, target detection, target boundary division, etc., (Garcia-Garcia et al., 2017), which means it is a prediction task with high demands on image understanding.

The most meaningful models for the building extraction task in this study are fully convolutional networks (FCNs) and U-Net. In terms of task implementation, this study refers to the end-to-end idea of FCN. After the CNN (convolutional neural network) was proposed, researchers tried to apply its excellent learning performance to semantic segmentation tasks, for which the pioneering work is the FCN proposed by Long et al. (2015). FCN utilizes the powerful feature extraction capabilities of CNN to achieve end-to-end, pixel-to-pixel segmentation prediction and replaces traditional fully connected layers with convolutional layers. FCN also adapts classic network structures, such as AlexNet, VGG16, and GoogLeNet, to fully convolutional models and verifies their performance in semantic segmentation. In addition, FCN can accept input images of an arbitrary size with a fixed number and size of convolutional layers, and performs pixel-wise predictions on the input images through learnable deconvolution in terms of up-sampling.

After the performance of FCN is proved, more enlightening semantic segmentation models are proposed. Similar to U-Net in structure, PSPNet uses global pyramid pooling and deeply supervised loss as improvements, enhancing the ability of feature extraction. DenseASPP is proposed and used to solve the problem of insufficient feature resolution in the scale-axis. DANet proposes a dual-attention module that makes full use of image information and shows its performance in multi-class semantic segmentation. OCNet address the semantic segmentation task with a context aggregation scheme which focuses on enhancing the role of object information.

In this research, U-Net was referred to in the framework design. In U-Net, the contracting path performs the role of down-sampling, and the expansive path performs the role of up-sampling. It is worth noting that four connection channels were added, respectively concatenating the feature maps of four different resolutions in the down-sampling process with the corresponding layers in the up-sampling process. This operation avoids the loss of details in the down-sampling process, so that the shallow features extracted by the convolutional neural network can directly participate in the prediction.

In the process of down-sampling, the convolution calculation combined with the ReLU activation function plays a role in increasing the nonlinear relationship between pixels, and the image is shrunk by a 2×2 max pooling operation with a stride of two. After each contraction, the number of channels is doubled by a 3×3 convolution. After four contractions, U-Net starts to use a 2×2 convolution for expansion, and the number of channels will be reduced to half of the original through a 1×1 convolution and concatenated with the feature maps in contraction. Then, the number of channels of the output will be reduced by a 3×3 convolution with the ReLU function. It is worth noting that edge pixels will be lost after the convolution operation, so the corresponding feature map from the shrinking unit needs to be cropped before concatenation. Finally, U-Net will output the segmentation map according to the set size (Ronneberger et al., 2015).

Generative adversarial networks

Before the proposal of GANs (generative adversarial networks), the deep learning model often included only a generative model or a discriminative model (Goodfellow et al., 2014). The former uses a large amount of neural network parameters and their ability to fit the dataset to generate new data that does not exist in the training set, while the latter directly fits the discriminant function. Different from the traditional model, GAN, as an implicit density generative model, includes both the generative model and the discriminative model in one framework. A generative model can be likened to a counterfeiter, while a discriminative model can be likened to a policeman. The former hopes that their forgery ability is as superb as possible, so that the fake data is as similar as possible to the real data, thus the police cannot make accurate judgments. The police, on the other hand, are expected to judge the authenticity of the data as accurately as possible, and the training process is more like a competition where the competitors are alternately leading. Assuming that $P_{data}(x)$ is the distribution probability of the real data and $P_g(x)$ is the distribution probability of the generated data, when the system is in Nash equilibrium, a "smartest" generator can be obtained

to achieve more accurate fitting between $P_g(x)$ and $P_{data}(x)$ (Jabbar et al., 2021).

The advantage of GAN is that there are fewer constraints in the design, it does not need such a complex artificial qualification as that in the Markov chain or the variational boundary, but uses a learnable discriminator as an auxiliary training method to constrain the feature distribution of the generator output, which is more convenient. Moreover, the discriminator will act as a distance measurer between $P_g(x)$ and $P_{data}(x)$.

The generative adversarial networks can be expressed by the following object function:

$$\min_G \max_D V(D, G) = \mathbb{E}_{x\sim P_{data}(x)}\left[\log D(x)\right] + \mathbb{E}_{z\sim P_z(z)}\left[\log(1 - D(G(z)))\right] \quad (1)$$

where D represents the discriminator, G is the generator, $P_{data}(x)$ stands for the probability distribution of the real data, $P_z(z)$ denotes the probability distribution of random noise z, $D(x)$ represents the discrimination result on real data x, and $D(G(z))$ signifies the discrimination result of D on sample $G(z)$ generated by generator G through random noise z.

In terms of GAN training, according to the above principles, to obtain the optimal discriminator, it is necessary to let the output of $D(x)$ be 1, and let the output of $D(G(z))$ be 0, then the optimal discriminator can be expressed as:

$$\max_D V(D, G) = \mathbb{E}_{x\sim P_{data}(x)}\left[\log D(x)\right] + \mathbb{E}_{z\sim P_z(z)}\left[\log(1 - D(G(z)))\right] \quad (2)$$

To obtain the optimal generator, it is necessary to let $G(z)$ generate data as real as possible to disturb the judgment of the discriminator D. Since this process is independent of the first half of Formula (2), the optimal generator can be expressed as:

$$\min_G V(D, G) = \mathbb{E}_{z\sim P_z(z)}\left[\log(1 - D(G(z)))\right] \quad (3)$$

To provide more accurate data for the subsequent city-related evaluation tasks, the building extraction has high requirements with regard to accuracy, and researchers hope the intensive prediction performance of the model can be as close as possible to human experts. Therefore, in this study, the training of the prediction model will be aided by weighted adversarial loss.

Materials and methods

Depthwise separable convolution and atrous spatial pyramid pooling

In recent years, the difference in shape and size between different buildings has become more pronounced; therefore, in remote sensing imaging, the identification and extraction of multi-scale objects has always been a challenge (Vakalopoulou et al., 2015). In a traditional convolution-based model, to increase the receptive field, reducing the amount of computation, pooling, or convolution with a stride greater than 1 will be used, but this will reduce the spatial resolution. In this study, ResNet-50 is used in the encoder; therefore, the depth of the model is relatively deep and the amount of parameters will be large (He et al., 2016). To ensure the resolution while expanding the receptive field, ASPP (atrous spatial pyramid pooling) and a depthwise separable convolution are used to obtain multi-scale information flexibly by setting the dilation rate without introducing additional parameters, so as to better obtain multi-size buildings.

Atrous spatial pyramid pooling was formally proposed in DeepLabv2. When deep convolutional neural networks are used in semantic segmentation tasks, the input remote sensing image usually needs to undergo a down-/up-sampling process in a convolutional encoder–decoder structure. Although convolutional neural networks have a receptive field mechanism that can be used to extract multi-scale target features, its scale will be limited by the size of the convolution kernel (Chen L. C. et al., 2017). An atrous convolution can be used to cheaply increase the receptive field of output units without increasing the kernel size, which is especially effective when multiple atrous convolutions are stacked one after the other (Dai et al., 2021). Assuming that the input feature map size is $R^{in} \times R^{in}$, the output feature map size is $R^{out} \times R^{out}$, and the convolution kernel size is $K \times K$. In a traditional convolution, the receptive field range is equal to the size of the convolution kernel, which is $K \times K$. In an atrous convolution, assuming that the dilated rate is D, its receptive field will be $K' = K + (K-1)(d-1)$.

Loss function design

In this study, the overall loss is divided into three parts, namely BCE (binary cross-entropy) loss L_{bce} responsible for segmentation prediction, adversarial loss responsible for the auxiliary training of model prediction authenticity, and edge loss responsible for optimizing the accuracy of building edge prediction. The overall loss is defined as:

$$L_{sum} = L_{seg} + L_{Edge} + L_{adv} \quad (4)$$

In the first item, the predicted segmentation map $\hat{y}$ and the label map y are compared at the pixel level. For a single pixel in a remote sensing image, the building extraction task belongs to the binary classification task; therefore, this study uses binary cross-entropy as the loss, which can be expressed as:

$$L_{seg} = L_{bce}(\hat{y}, y) = -\frac{1}{n}\sum_i^n z_i \log \hat{z}_i + (1 - z_i) \quad (5)$$

where z_i and $\hat{z}_i$ denote the label value in y and the predicted value in $\hat{y}$ at the same location, respectively.

In the second item, considering that buildings often have straight boundaries with the background, in this study, a Sobel-operator-based loss was designed and added to highlight the edges. By implementing the Sobel operator in both horizontal and vertical directions, and then using it as a filter to perform convolution operations on the image to be processed, the horizontal and vertical edges on the image can be extracted. The Sobel template in the horizontal direction is:

$$f_h = \begin{bmatrix} -1 & 0 & +1 \\ -2 & 0 & +2 \\ -1 & 0 & +1 \end{bmatrix} \tag{6}$$

Meanwhile, in the vertical direction, it is:

$$f_v = \begin{bmatrix} -1 & -2 & -1 \\ 0 & 0 & 0 \\ +1 & +2 & +1 \end{bmatrix} \tag{7}$$

Specifically, two convolutional layers using the above templates are defined, and their weights are not involved in backpropagation. After the building extraction results are obtained in the forward propagation, the prediction results and the original labels are input into the two designed layers for calculation, and two dual-channel gradient maps of the edge are obtained, the values of which are between 0 and 1. Then, the mean square error (MSE) between the two gradient maps is calculated to obtain the edge loss:

$$L_{Edge} = L_{mse}\left(f_h(y), f_h(\hat{y})\right) + L_{mse}\left(f_v(y), f_v(\hat{y})\right) \tag{8}$$

In the third item, to ensure that the model prediction ability is closer to that of the experts, the idea of GAN is applied, and the extraction task is still carried out by the generator; meanwhile, an additional discriminator is trained synchronously to determine the authenticity of the pixel-level prediction results. Hence, the discriminator acts as a learnable constraint and participates in the overall training of the model by virtue of the adversarial loss, the training of which can be represented by the following function:

$$L_{adv} = L_{bce}\left(D\left(x, y\right), 1\right) + L_{bce}\left(D\left(x, G\left(x\right)\right), 0\right) \tag{9}$$

where $G(x) = \hat{y}$, G is the generator, and D represents the discriminator. In alternate iterative training of generative adversarial networks, the generator loss can be expressed as:

$$L_G = L_{bce}\left(\hat{y}, y\right) + L_{Edge} - L_{bce}\left(D\left(x, G\left(x\right)\right), 0\right) \tag{10}$$

Here, a maximized $L_{bce}\left(D\left(x, G(x)\right), 0\right)$ can be equivalent to a minimized $L_{bce}\left(D\left(x, G(x)\right), 1\right)$; furthermore, weights are added to the loss of each item, so it is easy to obtain:

$$L_G = w_1 L_{bce}\left(\hat{y}, y\right) + w_2 L_{Edge} + w_3 L_{bce}\left(D\left(x, G(x)\right), 1\right) \tag{11}$$

Dual-attention module

The aim of the attention mechanism is to obtain the difference in importance between feature maps and feature values. To realize reassignment, it causes the neural network to devote more computing resources to more important areas (Mi et al., 2020). In this building extraction task, the importance of different objects is distinct; therefore, introducing an attention module can provide more tractable and more relevant information for high-level perceptual reasoning and more complex visual processing tasks.

Generally, attention mechanisms can be divided into item-wise and location-wise, both of which can be subdivided into soft attention (differentiable), and hard attention (non-differentiable). Among them, the location-wise soft attention with feature map as an input can participate in gradient descent together with the neural network and update the weights through backpropagation (Niu et al., 2021), which is more suitable for the application scenario of deep learning, so it is also applied to this study.

In the process of building extraction, the spatial relationship between each pixel and its nearby pixels is significantly higher than the relationship with pixels far away from it; therefore, this study refers to DANet using a dual-attention module to fully capture the semantic dependencies in the spatial and channel dimensions (Fu et al., 2019).

In terms of implementation, the dual-attention module includes the position attention module [shown in **Figure 2(A)**] and the channel attention module [shown in **Figure 2(B)**], and calculates the attention matrices S and X for them, respectively.

First, the output A of the last layer after down-sampling is copied into four parts, in which B, C, and D are obtained after one convolution layer, and their size is $\{B, C, D\} \in \mathbb{R}^{C*H*W}$. Subsequently, flattening is performed within the channel, and the new dimension is $\{B, C, D\} \in \mathbb{R}^{C*N}$, where $N = H * W$. The reshaped matrix can be expressed as:

$$\begin{aligned} B_{reshape} &= C_{reshape} = D_{reshape} \\ &= \begin{bmatrix} M_{11}^1 & M_{12}^1 & \cdots & M_{ij-1}^1 & M_{ij}^1 \\ M_{11}^2 & M_{11}^2 & & M_{ij-1}^2 & M_{ij}^2 \\ \vdots & & \ddots & \vdots & \\ M_{11}^{c-1} & M_{12}^{c-1} & \cdots & M_{ij-1}^{c-1} & M_{ij}^{c-1} \\ M_{11}^c & M_{12}^c & & M_{ij-1}^c & M_{ij}^c \end{bmatrix} \end{aligned} \tag{12}$$

The matrix B is then transposed to get $B_{reshape}^T$, $B_{reshape}^T$ and C are multiplied by a matrix, and an attention matrix pam is formed with a size of $N * N$ through the SoftMax, as shown in the following formula:

$$S_{pam} = softmax\left(B_{reshape}^T \otimes C_{reshape}\right) \tag{13}$$

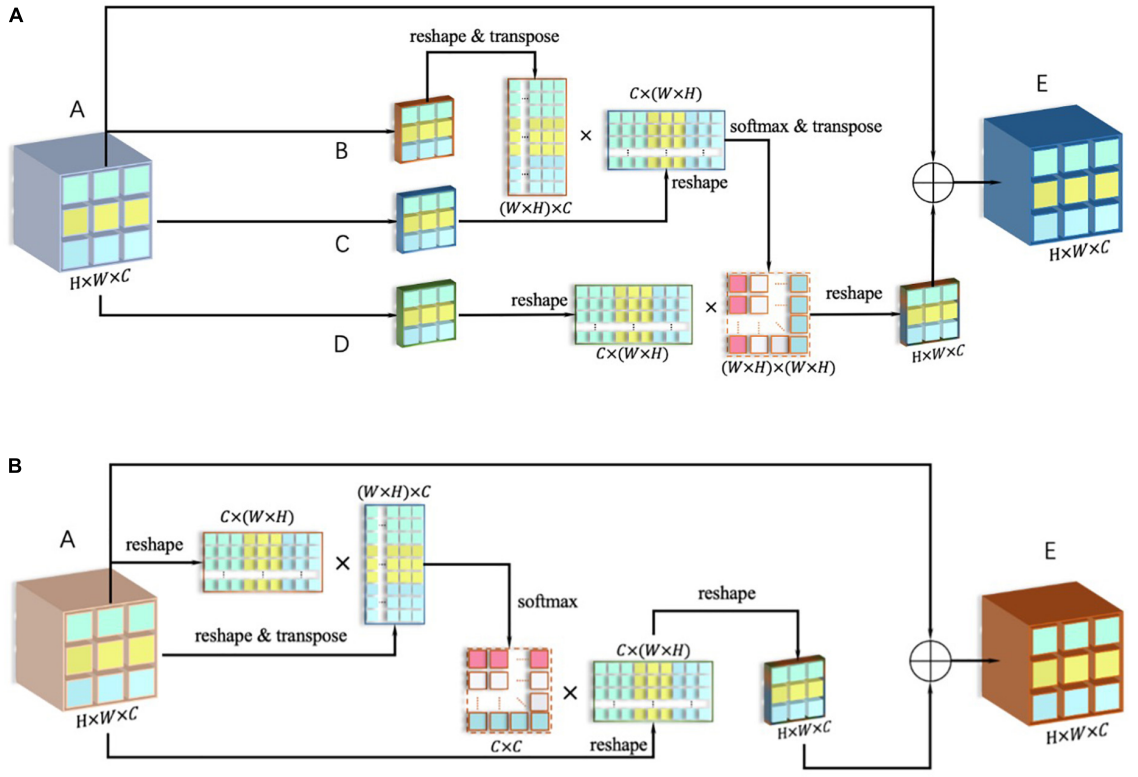

FIGURE 2
(A) Framework of position attention module; **(B)** framework of channel attention module.

It is then transposed, so that pam^T and $D_{reshape}$ are multiplied, and the *output* is then reorganized in the array dimension to make it the same as the input $A \in \mathbb{R}^{C*H*W}$, which can be expressed as:

$$output = D_{reshape} \bigotimes S_{pam}^{T} =$$

$$\begin{bmatrix} M_{11}^{1}S_{11} + \ldots + M_{ij}^{1}S_{1n} & \cdots & M_{11}^{1}S_{n1} + \ldots + M_{ij}^{1}S_{nn} \\ \vdots & \ddots & \vdots \\ M_{11}^{c}S_{11} + \ldots + M_{ij}^{c}S_{1n} & \cdots & M_{11}^{c}S_{n1} + \ldots + M_{ij}^{c}S_{nn} \end{bmatrix} \tag{14}$$

In the $output \in \mathbb{R}^{C*H*W}$ with an updated weight, each pixel in the original matrix is associated with the remaining pixels in the feature map (after being given new weight). Finally, *output* and *A* are added to get *E*, and it is used as the output of the spatial attention module.

In terms of the specific implementation of the channel attention module, the input $A \in \mathbb{R}^{C*H*W}$ is first restructured into $A \in \mathbb{R}^{C*N}$ (where $N = H * W$), and $A_{reshape}$ is multiplied by its transposed $A_{reshape}^{T}$, then a SoftMax operation is performed on the result, and the channel attention map X_{cam} can be obtained, as shown in the formula below:

$$X_{cam} = softmax\left(A_{reshape} \otimes A_{reshape}^{T}\right)$$

$$= \begin{bmatrix} S_{11} & S_{12} & \cdots & S_{1c-1} & S_{1c} \\ S_{21} & S_{22} & & S_{2c-1} & S_{2c} \\ \vdots & & \ddots & \vdots & \\ S_{c-11} & S_{c-12} & \cdots & S_{c-1c-1} & S_{c-1c} \\ S_{c1} & S_{c2} & & S_{cc-1} & S_{cc} \end{bmatrix} \tag{15}$$

Next, the attention map *X* is transposed to obtain X_{cam}^{T}, the transposed matrix is multiplied with $A_{reshape}$ [as shown in Formula (16)], and the result is then reorganized into $output \in \mathbb{R}^{C*H*W}$.

$$output = X_{cam}^{T} \bigotimes A_{reshape} =$$

$$\begin{bmatrix} S_{11}M_{11}^{1} + \ldots + S_{c1}M_{11}^{c} & \cdots & S_{11}M_{ij}^{1} + \ldots + S_{c1}M_{ij}^{c} \\ \vdots & \ddots & \vdots \\ S_{1c}M_{11}^{1} + \ldots + S_{cc}M_{11}^{c} & \cdots & S_{1c}M_{ij}^{1} + \ldots + S_{cc}M_{ij}^{c} \end{bmatrix} \tag{16}$$

It is then added to input *A* to get output *E*. It can be seen from Formula (16) that the weights have been reassigned, and

the new values are related to the values in the same position in all feature maps.

Evaluation indexes

To evaluate the predictive ability of the model comprehensively and objectively, a confusion matrix is introduced in this study, which is used to summarize the predictive performance of classification models in machine learning.

Accuracy is used to find the portion of correctly classified values, and the formula is as follows:

$$Accuracy = \frac{TP + TN}{TP + TN + FP + FN} \tag{17}$$

where TP is True Positive, FP is False Positive, FN is False Negative, and TN is True Negative. Precision is used to calculate the model's ability to classify positive values correctly, and the formula is as follows:

$$Precision = \frac{TP}{TP + FP} \tag{18}$$

Recall is used to determine the model's ability to predict positive value, and the formula is as follows:

$$Recall = \frac{TP}{TP + FN} \tag{19}$$

The $F1$ score is a comprehensive analysis of whether the TP is large enough from two perspectives, predicted and actual. The $F1$ score is the harmonic mean of precision and recall. According to the formula of harmonic mean, it can be obtained by the following formula:

$$F1 = \left(\frac{Precision^{-1} + Recall^{-1}}{2} \right)^{-1} \tag{20}$$

The formula for calculating IoU (intersection over union) is as follows:

$$IoU = \frac{TP}{TP + FP + FN} \tag{21}$$

The model framework

In the framework design of the building extraction model, a convolutional encoder–decoder structure with skip connections was designed, as referred to U-Net and ResNet-50. In the down-sampling process, two slightly different bottlenecks are used, as shown in Figure 3, with the difference being that Bottleneck 1 contains a 1 × 1 convolutional and a BN in the shortcut connection.

In the convolutional encoder, the input image goes through four bottleneck blocks, and then enters ASPP. As shown in Figure 4, the ASPP module is divided into four parts, one of which is a normal 1 × 1 convolutional layer, and the remaining three set the dilation rate D to 6, 12, and 18, respectively. The output of the four parts is then concatenated and used as the final output after a 3×3 Conv+BN+ReLU operation. In the subsequent attention module, the input is reassigned according to the attention map and used as the input of the decoder. In the decoder, up-sampling is conducted using bilinear interpolation with convolutional layers, generating a prediction for building extraction.

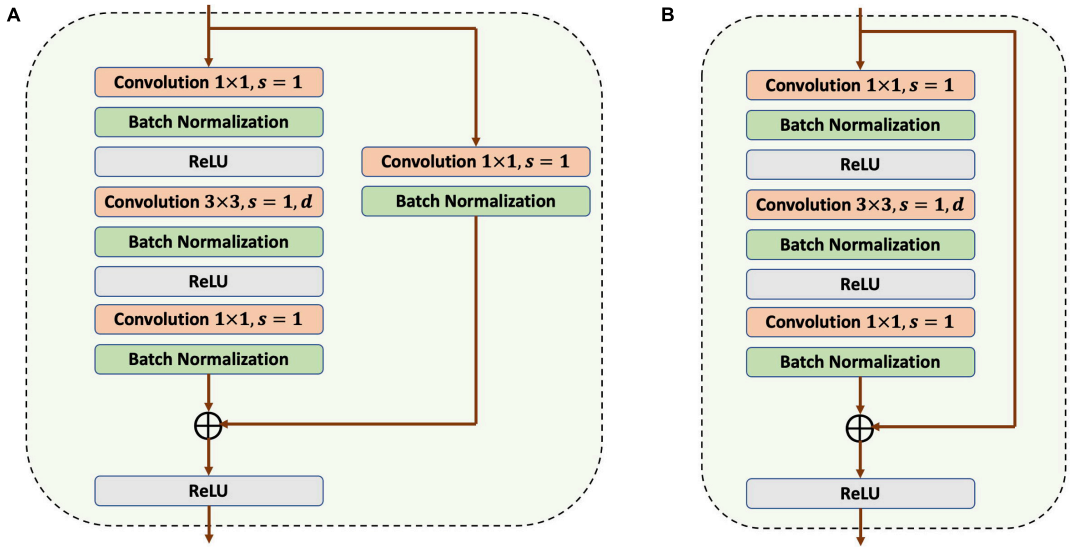

FIGURE 3
Framework of two types of bottlenecks. **(A)** Bottleneck 1. **(B)** Bottleneck 2.

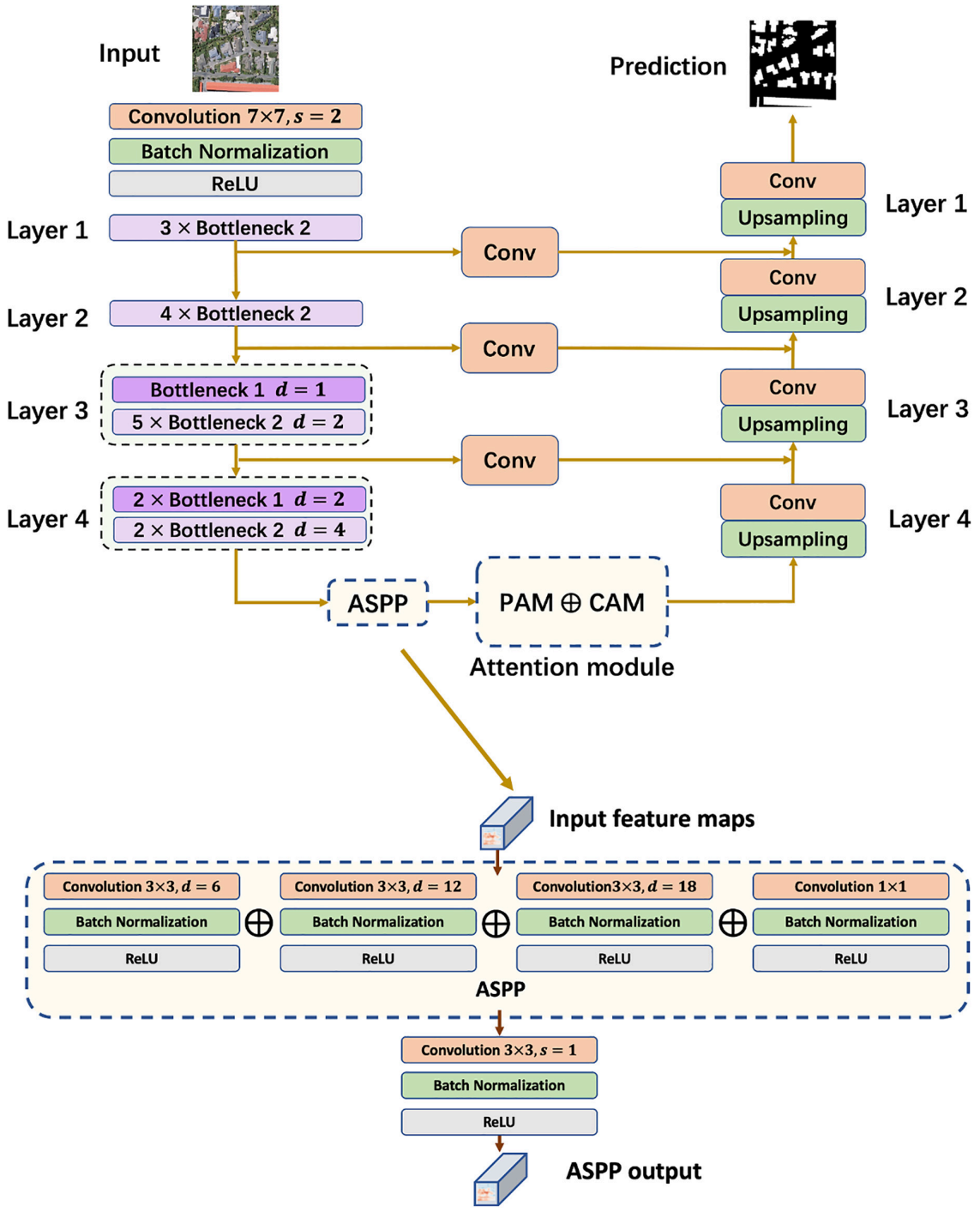

FIGURE 4
Framework of segmentation model and atrous spatial pyramid pooling.

In terms of the discriminator structure, there are two different combinations of input: the first is the original image and the prediction, and the second is the combination of the original image and the ground truth. In this study, a Markovian discriminator (also known as PatchGAN) was designed with reference to Pix2Pix (Isola et al., 2017). The output of the discriminator is not a simple 1 or 0, but a discriminant matrix that gives a separate discrimination for each part of a grided image. To better judge the high-resolution remote sensing images with dense ground

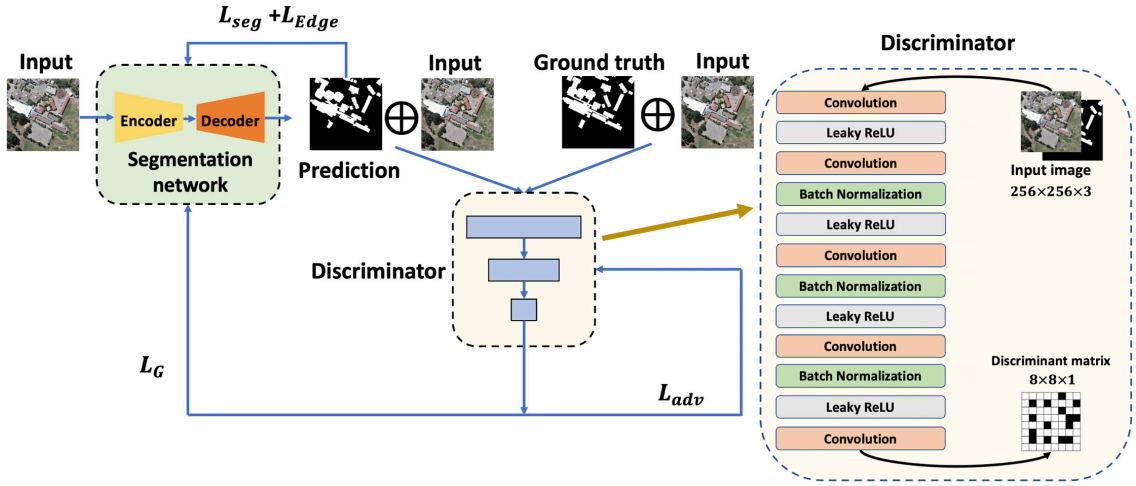

FIGURE 5
Markovian discriminator and gradient descent.

objects, the output size of the discriminator was set to 8 × 8 × 1, which is expected to output an all-zero matrix when judging the first combination, and an all-one matrix when judging the second combination. Figure 5 displays the Markovian discriminator and the process of gradient descent.

Building datasets

To verify the performance of the proposed model, two open-source building dataset was selected. WHU building dataset contains a total of 8,189 images, including 4,736 for training (containing 130,000 buildings), 1,036 for validation (containing 14,500 buildings), and 2,416 for testing (containing 42,000 buildings). This aerial dataset consists of more than 220,000 independent buildings extracted from aerial images with a 0.075°m spatial resolution covering 450°km^2 in Christchurch, New Zealand. The area is divided into 8,189 blocks with a resolution of 512°×°512 each (shown in Figure 6). The WHU dataset contains a variety of scene types, such as countryside, residential, cultural, etc. The size, purpose, and color of the buildings are also diverse, which is suitable for the training of building extraction models (Ji et al., 2018).

The Massachusetts building dataset (shown in Figure 6) has a total of 137 remote sensing images, including 137 in the training set, four in the validation set, and 10 in the test set. The dataset covers buildings of different scales in cities and suburbs, the image size is 1,500°×°1,500 and the area is 2.25 square kilometers, the dataset covers about 340 square kilometers in total (Saito et al., 2016).

Training details

The model was built in Pytorch v1.7.1, CUDA v11.1. The training equipment utilized was GeForce RTX 3090ti 24G, Adam was used as the optimizer, the learning rate was set to 0.001, and the momentum parameters were set to 0.9 and 0.999. The weights in the overall loss were set to $w_1 : w_2 : w_3 = 1 : 1 : 0.3$. In the comparative experiments, each comparative model was trained for 200 epochs. It is worth highlighting that, to prevent the segmentation model from being excessively disturbed by the meaningless discrimination generated by the random initialized discriminator in the initial stage, AttsegGAN chose to freeze the discriminator first, and let the segmentation model train separately in the training set for 1,000 iterations with a batch size of 1. The segmentation model was then frozen, letting the discriminator train separately for 800 iterations of the combined input method described above. Then, the alternate iterative training strategy of the generative adversarial network was used to complete the subsequent training. The models used for comparison were trained according to the environmental parameters provided by the authors.

Results and discussion

Ablation experiments

To improve the prediction ability of the building extraction model, this study proposes four strategies based on an "hourglass" structure: U-Net (namely ASPP),

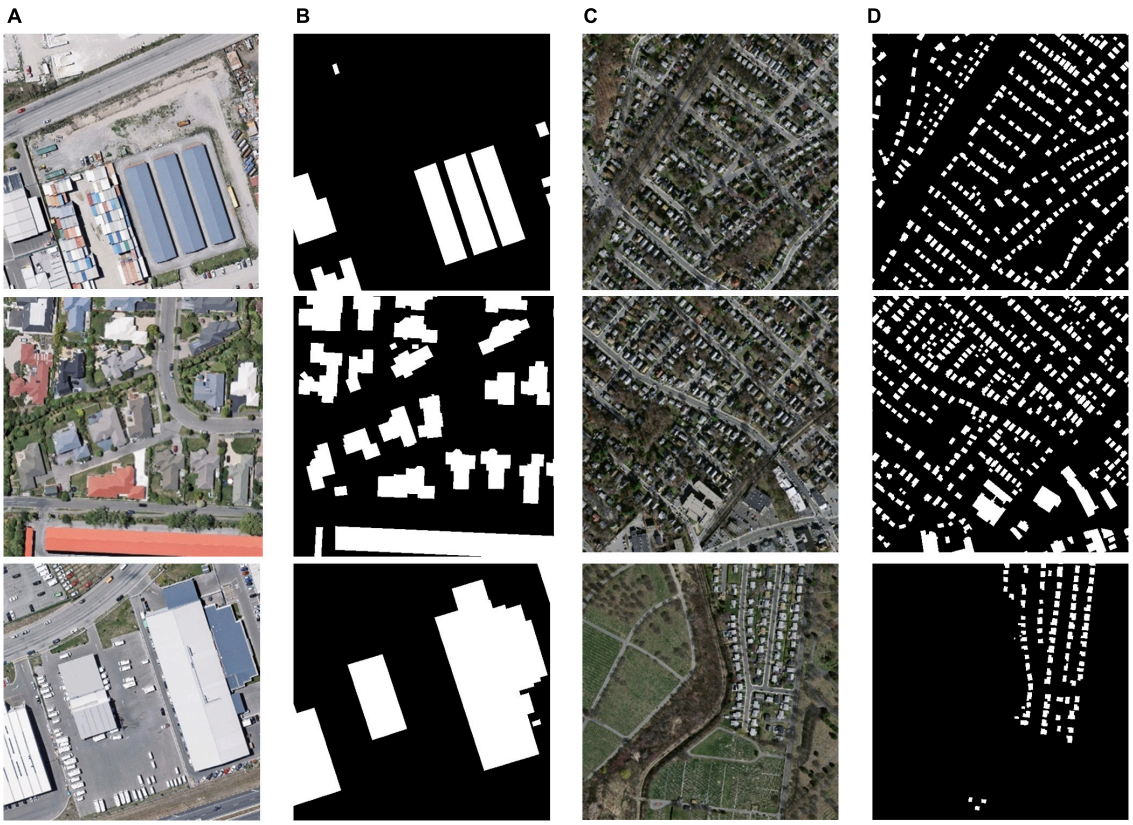

FIGURE 6
Images and labels in the WHU building dataset. **(A)** Original images in WHU dataset, **(B)** labels of WHU dataset, **(C)** original images in Massachusetts dataset, and **(D)** labels of Massachusetts dataset.

TABLE 1 Component and training strategy ablation experiments in WHU building dataset.

	Version 5 (proposed)	Version 4	Version 3	Version 2	Version 1
Sobel edge loss	✓				
Adversarial loss	✓	✓			
ASPP	✓	✓	✓		
Attention	✓	✓	✓	✓	
Acc	**0.9875**	0.9871	0.9867	0.9872	0.9813
F1	**0.9435**	0.9421	0.9400	0.9402	0.9408
IoU	**0.8907**	0.8905	0.8874	0.8862	0.8852

Bold values mean the best performing data.
The underlined value means the second best performing data.

attention mechanism, Sobel edge loss, and adversarial loss. To verify their effectiveness, this part of the experiment carried out ablation experiments in a step-by-step manner in WHU building dataset, and conducted objective evaluations through three evaluation indexes: Acc, F1, and IoU.

As shown in Table 1, after adopting the components and training strategies step by step, the prediction ability of the model was improved. Among them, the most significant improvement indicators were Acc and IoU; after adding all the improvement schemes, these two indicators were improved by 0.0062 and 0.0055, respectively, compared with the original version. The most obvious improvements to the model were adversarial loss and Sobel edge loss. After using the former, the IoU of the model was increased by 0.0038 and the F1 was increased by 0.0021, which means that the model could better predict positive values. The proposal of Sobel edge loss significantly improved

the prediction ability, with an improvement of 0.0002 to 0.0021 in the evaluation indicators other than SP, and achieving the best results in the notable Acc, F1, and IoU, reaching 0.9875, 0.9435, and 0.8907, respectively. The improvement brought by the dual-attention mechanism was more significant in Acc, with an increase of 0.0059, indicating that the performance improved after the allocation of computing resources was adjusted through the attention map. Although the overall improvement brought by ASPP was relatively insignificant, it increased by 0.0012 to 0.8874 on IoU.

Figure 7 shows the intuitive improvement brought by Sobel edge loss. It may not be able to improve the extraction of specific small-sized buildings, but it can make the lines of the extracted buildings clearer, making them closer to a straight line and to the ground truth. Although ASPP improved the extraction performance of the model in multi-size buildings while the evaluation indicators improved, it was also found that the edges of the buildings in the predicted segmentation map were obviously jagged due to the setting of the validation rate. Since semantic segmentation achieves pixel-level dense predictions, this phenomenon is not conducive to the prediction-accuracy-oriented task. However, Sobel edge loss used in conjunction with ASPP has been proven to effectively alleviate edge jaggedness.

Attention mechanism ablation experiments

According to our statistics, each time an attention module is added to the prediction model, approximately 227,000 parameters are added. Therefore, when the addition cannot effectively promote the capacity of prediction, it will increase the training cost and the risk of overfitting. In this section, the addition strategy of the attention mechanism is investigated and verified, and we propose several versions of the framework, as shown in Figure 8.

To explore the relationship between the attention module and the overfitting phenomenon, we performed the four versions on the WHU dataset and made statistics, as shown in Table 2.

From the performance on the test set, the predictive ability does not increase with the addition of the attention module, but decreases. Therefore, it is not advisable for this component to be added to the other connection channels; it works best when added only after the last down-sampling layer.

From Table 2, it can be found that Acc, F1, and IoU perform the best in the training set, indicating that after 200 epochs of training, the model can already learn enough and complete the prediction. Conversely, the indicators show a downward trend in the remaining two sets, and there is a large difference from the training set, indicating that

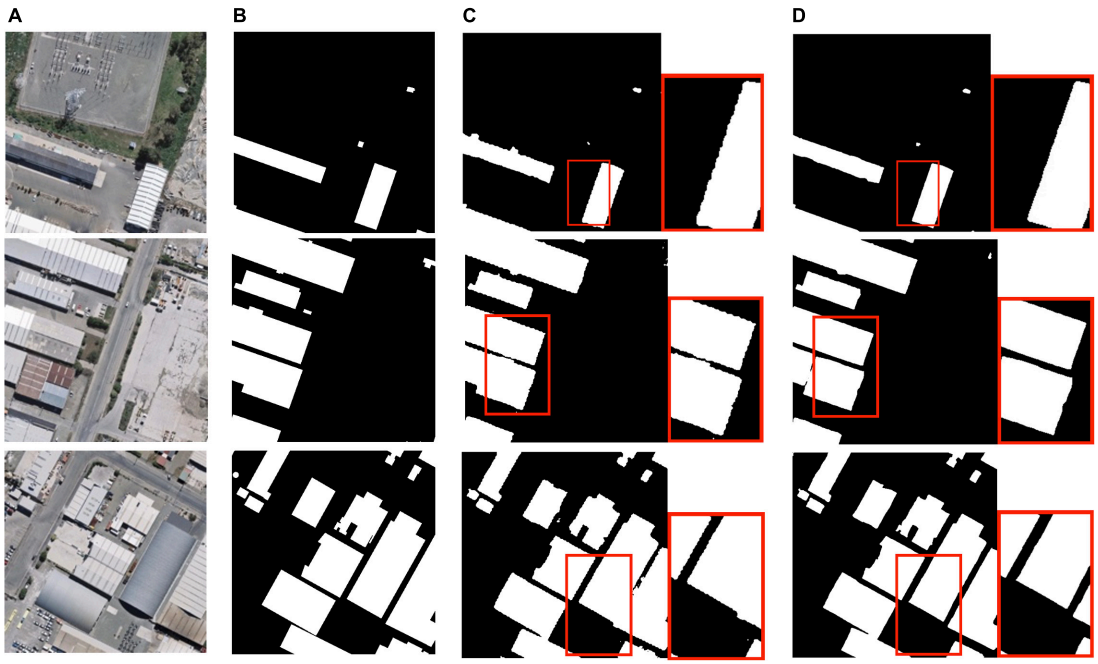

FIGURE 7
Building extraction results: **(A)** original remote sensing image; **(B)** ground truth; **(C)** prediction with atrous spatial pyramid pooling; **(D)** prediction with ASPP and Sobel edge loss.

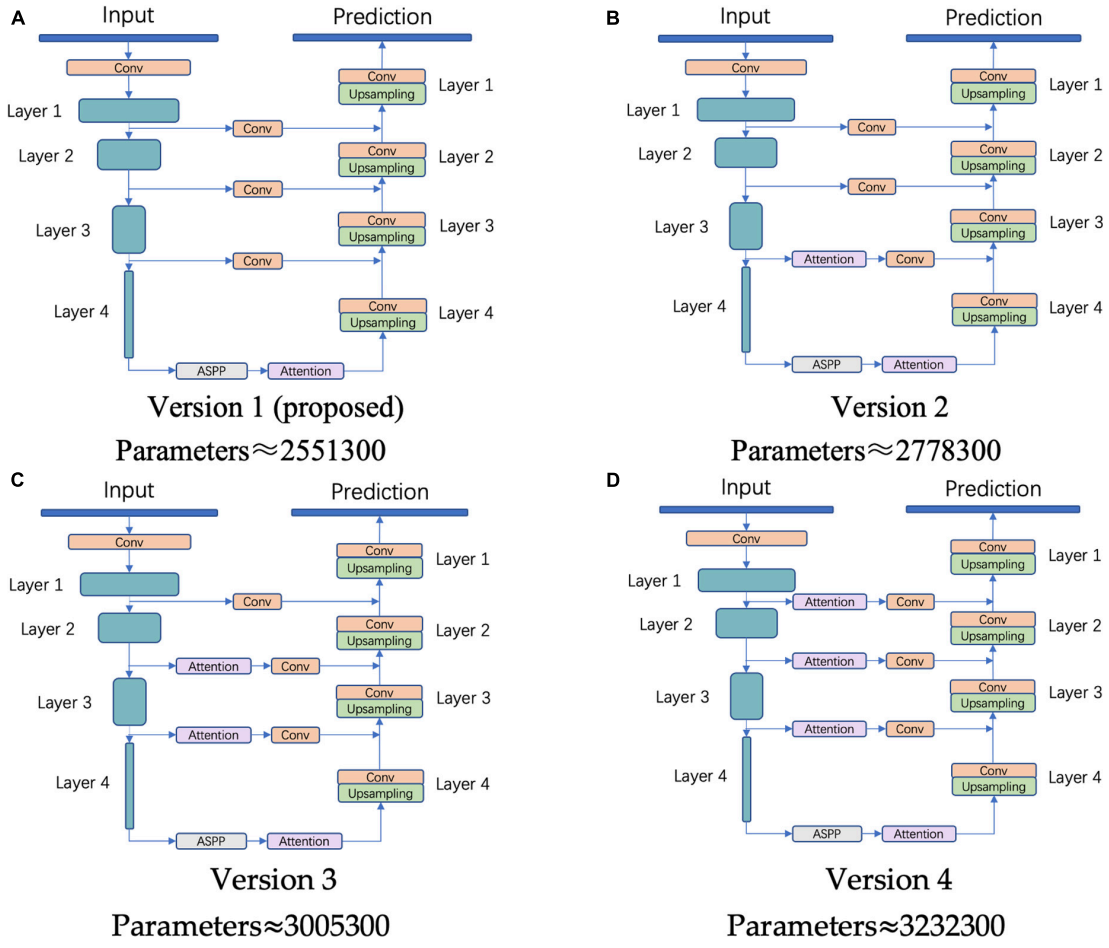

FIGURE 8
Attention mechanism ablation experiments. **(A)** Version 1 (proposed), **(B)** Version 2, **(C)** Version 3, and **(D)** Version 4.

TABLE 2 Statistics for the evaluation indicators of the three sets.

	Acc	F1	IoU
Training set			
Version 1	0.9869	0.9586	0.9107
Version 2	0.9873	0.9537	0.9119
Version 3	0.9870	0.9504	0.9039
Version 4	0.9878	0.9569	0.9153
Validation set			
Version 1	0.9883	0.8366	0.7889
Version 2	0.9879	0.8362	0.7870
Version 3	0.9889	0.8426	0.7898
Version 4	0.9883	0.8399	0.7903
Test set			
Version 1	**0.9875**	0.9435	**0.8907**
Version 2	0.9873	**0.9436**	0.8893
Version 3	0.9869	0.9421	0.8870
Version 4	0.9852	0.9397	0.8869

Bold values mean the best performing data.

these four versions have a certain degree of overfitting. This phenomenon is most obvious in Version 4, which has the largest number of parameters. Compared with the training set, the Acc, F1, and IoU of the model in the test set decreased by 0.0026, 0.0172, and 0.0284, respectively. Thus, although the attention mechanism has been proven to be an effective component, the improvement in predictive ability is not proportional to the number, and will lead to an aggravation of the overfitting, and thus performance degradation.

Comparison with state-of-the-arts on WHU building dataset

In this section, we selected four classic semantic segmentation algorithms based on deep learning that have been proven in various open-source datasets: U-Net, DeepLabv3+, DANet, and PSPNet.

As shown in Table 3, AttsegGAN is 0.1883 higher than U-Net in IoU, and 0.0260 higher in Acc, which indicates that the addition of effective components can improve the predictive ability of building extraction models in the case of similar

TABLE 3 Statistics of comparative experiment results on WHU building dataset.

	Acc	F1	IoU
U-Net	0.9615	0.8252	0.7024
DeepLabv3+ (ResNet-101)	0.9776	0.9028	0.8228
PSPNet (ResNet-101)	0.9586	0.7734	0.6434
DANet (ResNet-101)	0.9851	0.9327	0.8738
AttsegGAN	**0.9875**	**0.9435**	**0.8907**

Bold values mean the best performing data.
The underlined value means the second best performing data.

deep learning frameworks. In comparison with DeepLabv3+ and DANet, AttsegGAN also has obvious improvement in indicators: 0.0099 and 0.0024, respectively, in ACC; and 0.0697 and 0.0169 in IoU, which proves that, even if the model uses components with similar principles, the rational framework and training strategy can also significantly improve the predictive ability of the building extraction model. The visual and intuitive results are shown in Figure 9, and the predicted segmentation results are objectively represented by rendering (images are randomly selected from the test set of the WHU building dataset).

Comparison with state-of-the-arts on massachusetts building dataset

To further demonstrate the predictive ability of the proposed AttsegGAN on pixel-level binary classification task, we trained and validated it on another remote sensing image based dataset, the Massachusetts building dataset. In this section, DANet, Deeplabv3+, PSPNet, and UNet were selected to compare with AttsegGAN.

From the statistics in Table 4, it can be seen that the performance of the models on the Massachusetts building dataset is lower than that on the WHU, but still reflects the difference between the prediction ability. In the evaluation indicators, AttsegGAN is higher than other algorithms in Acc, F1, and IoU. Among them, IoU is the most obvious,

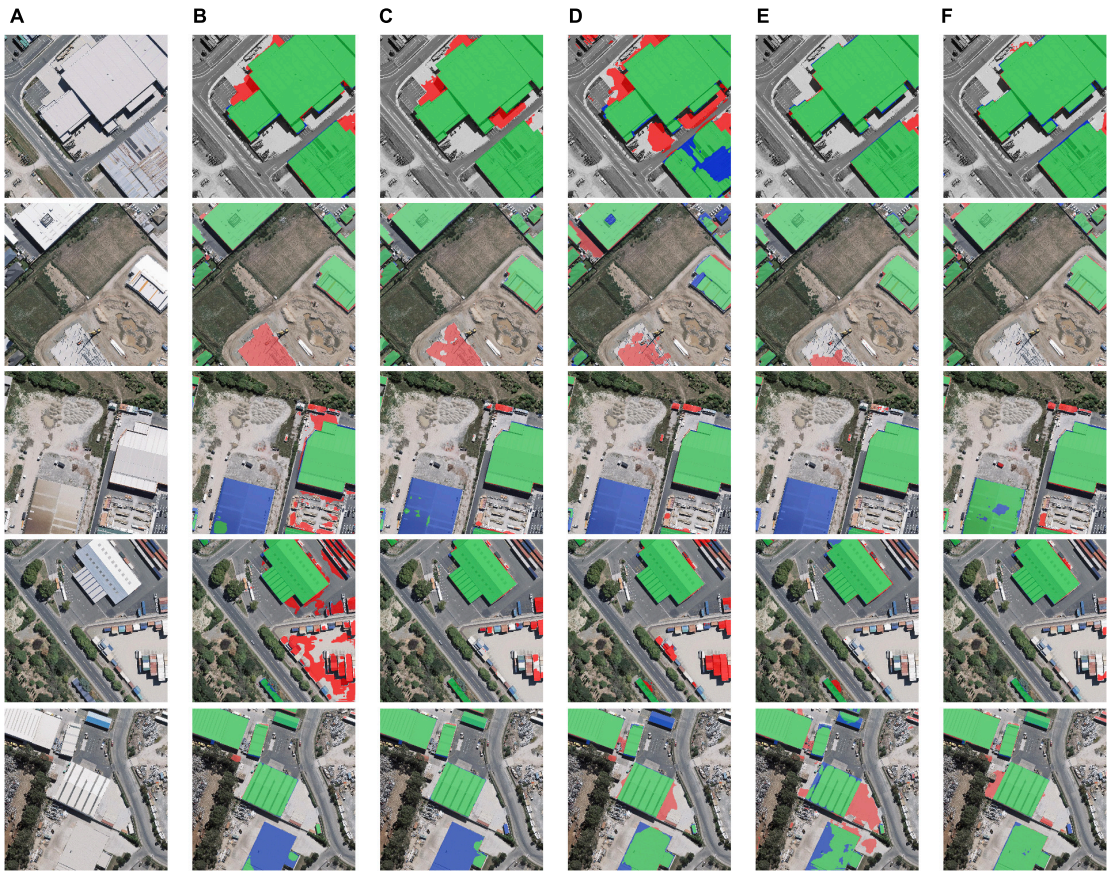

FIGURE 9
Building extraction results: **(A)** original remote sensing image; **(B)** prediction of U-Net; **(C)** prediction of DeepLabv3+; **(D)** prediction of PSPNet; **(E)** prediction of DANet; **(F)** prediction of AttsegGAN (ours). Green: true positive (tp) pixels; transparent: true negative (tn) pixels; red: false positive (fp) pixels; blue: false negative (fn) pixels.

TABLE 4 Statistics of comparative experiment results on Massachusetts building dataset.

	Acc	F1	IoU
U-Net	0.9370	0.8125	0.6930
DeepLabv3+ (ResNet-101)	0.8921	0.6929	0.5301
PSPNet (ResNet-101)	0.9317	0.8227	0.6988
DANet (ResNet-101)	0.9236	0.7989	0.6652
AttsegGAN	**0.9395**	**0.8328**	**0.7130**

Bold values mean the best performing data.
The underlined value means the second best performing data.

which is 0.0412 higher than the second-ranked PSPNet, this means that the predicted region fits the ground truth better. Meanwhile, AttsegGAN is also 0.0025 and 0.0101 higher than the second place in Acc and F1, respectively. It can be found that U-Net and AttsegGAN perform more prominently on Acc. As an earlier designed model, U-Net can outperform the newly proposed algorithm in binary classification task, indicating that the feature fusion brought by the skip connection mechanism can still effectively promote the prediction accuracy. The visual and intuitive results are shown in Figure 10, and the predicted segmentation results are objectively represented by rendering (images are randomly selected from the test set of the Massachusetts building dataset). In terms of running efficiency, when the input is a remote sensing image of size 512×512, the processing time of AttsegGAN is 0.09822s per image.

Detecting buildings in cropland

Recognition and background separation of buildings near planting land is a meaningful remote sensing image understanding task, which can provide significant reference information for planting land protection and path planning of unmanned equipment. In Figure 11, the processing performance of the proposed AttsegGAN on this task is visually displayed.

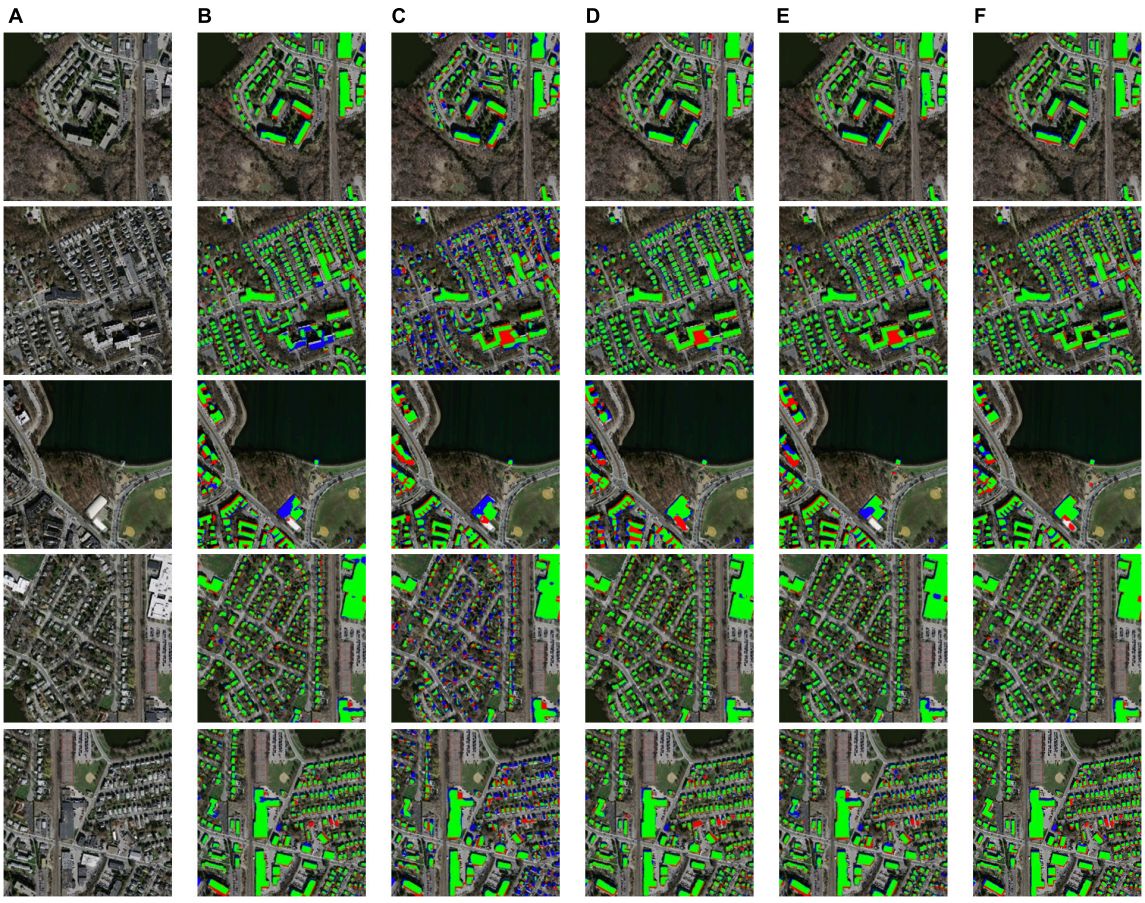

FIGURE 10
Building extraction results: **(A)** original remote sensing image; **(B)** prediction of U-Net; **(C)** prediction of DeepLabv3+; **(D)** prediction of PSPNet; **(E)** prediction of DANet; **(F)** prediction of AttsegGAN (ours). Green: true positive (tp) pixels; transparent: true negative (tn) pixels; red: false positive (fp) pixels; blue: false negative (fn) pixels.

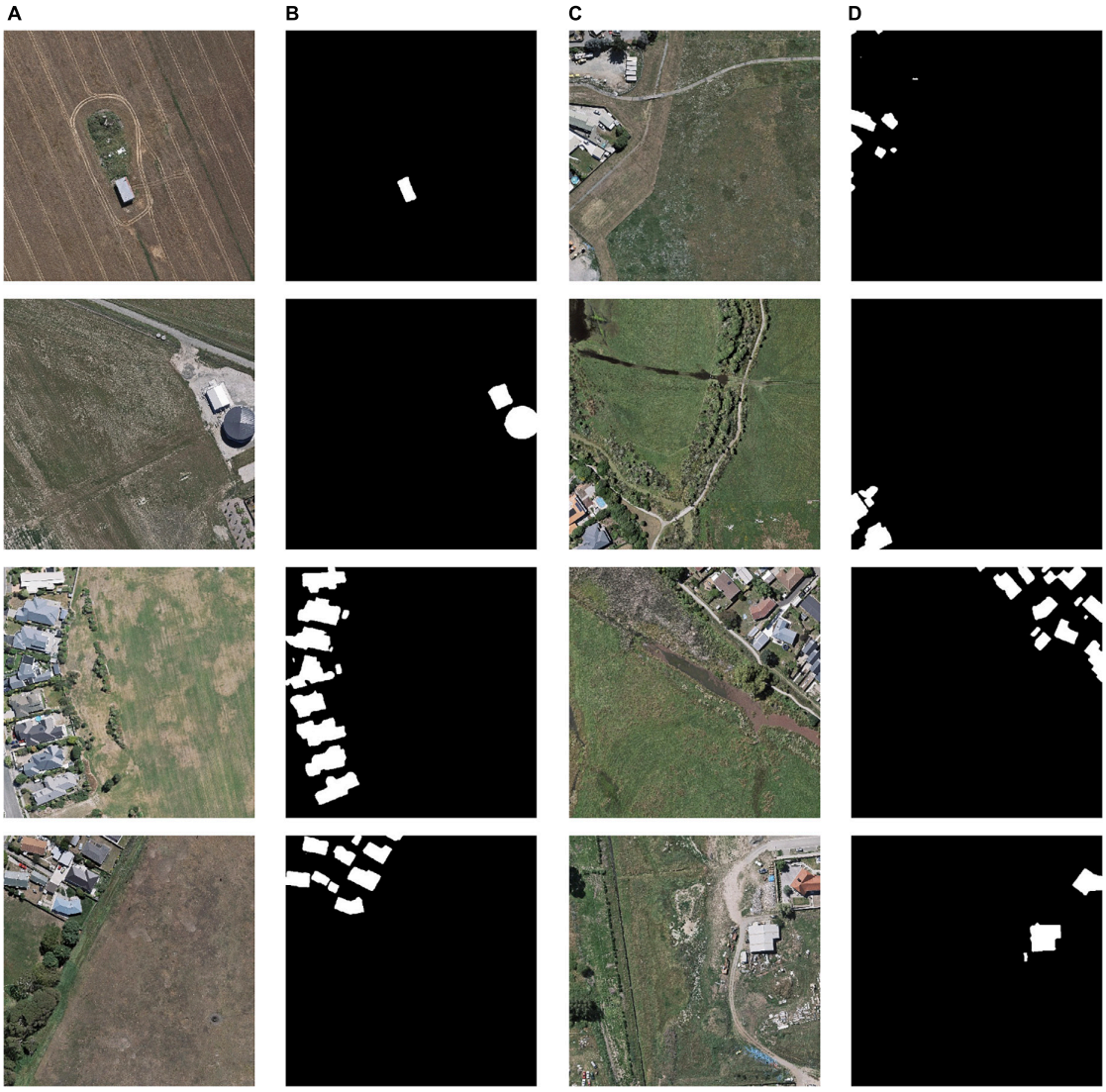

FIGURE 11
Building extraction results: **(A)** original remote sensing image; **(B)** prediction of AttsegGAN; **(C)** original remote sensing image; **(D)** prediction of AttsegGAN.

Conclusion

Aiming to provide more accurate reference information for arable land monitoring tasks, AttsegGAN is proposed in this study. AttsegGAN is a deep-learning-based building extraction model that can automatically segment and characterize buildings from high-resolution remote sensing images. This study proposes four improvements based on the U-Net structure, namely ASPP and a dual-attention mechanism with regard to model components, and adversarial loss and Sobel edge loss with regard to training strategy, with experimentation carried out on the WHU building dataset. In the ablation experiments, the improvements were added one by one, and the effectiveness was proven on the test set using three evaluation indicators, Acc, F1, and IoU, with the results showing that the improvements brought by the two losses is more obvious. In the ablation experiments for the attention module, the results show that the model prediction ability is not positively related to the number of components, but leads to overfitting. In the comparison between the final version of AttsegGAN and state-of-the-arts, AttsegGAN performed the best in comparison with U-Net, DeepLabv3+, PSPNet, and DANet, achieving 0.9875, 0.9435, and 0.8907 for Acc, F1, and IoU in the WHU test set, respectively. Meanwhile, AttsegGAN also achieved the best results on the Massachusetts test set, achieving 0.9395, 0.8328, and 0.7130 for Acc, F1, and IoU. The results

show that the proposed model could accurately complete building extraction and provide more reliable reference information for remote sensing observation tasks related to cropland.

Data availability statement

Publicly available datasets were analyzed in this study. This data can be found here: http://gpcv.whu.edu.cn/data/building_dataset.html; https://www.cs.toronto.edu/~vmnih/data/.

Author contributions

JW designed the experiments. JW and YH wrote the manuscript. MC and YH collected the data and analyzed the results. YG, ZL, and XL helped carry out the experiments. YH revised the manuscript. All authors contributed to the article and approved the submitted version.

Conflict of interest

The authors declare that the research was conducted in the absence of any commercial or financial relationships that could be construed as a potential conflict of interest.

Publisher's note

All claims expressed in this article are solely those of the authors and do not necessarily represent those of their affiliated organizations, or those of the publisher, the editors and the reviewers. Any product that may be evaluated in this article, or claim that may be made by its manufacturer, is not guaranteed or endorsed by the publisher.

References

Alshehhi, R., Marpu, P. R., Woon, W. L., and Dalla Mura, M. (2017). Simultaneous extraction of roads and buildings in remote sensing imagery with convolutional neural networks. *ISPRS J. Photogramm. Remote Sens.* 130, 139–149. doi: 10.1016/j.isprsjprs.2017.05.002

Buhaug, H., and Urdal, H. (2013). An urbanization bomb? Population growth and social disorder in cities. *Glob. Environ. Change* 23, 1–10. doi: 10.1016/j.gloenvcha.2012.10.016

Chen, L.-C., Papandreou, G., Kokkinos, I., Murphy, K., and Yuille, A. L. (2017). Deeplab: Semantic image segmentation with deep convolutional nets, atrous convolution, and fully connected crfs. *IEEE Trans. Pattern Anal. Mach. Intell.* 40, 834–848. doi: 10.1109/TPAMI.2017.2699184

Chen, W., Li, X., He, H., and Wang, L. (2017). A review of fine-scale land use and land cover classification in open-pit mining areas by remote sensing techniques. *Remote Sens.* 10:15. doi: 10.3390/rs10010015

Cheng, G., and Han, J. (2016). A survey on object detection in optical remote sensing images. *ISPRS J. Photogramm. Remote Sens.* 117, 11–28. doi: 10.1016/j.isprsjprs.2016.03.014

Dai, F., Wang, F., Yang, D., Lin, S., Chen, X., Lan, Y., et al. (2021). Detection Method of Citrus Psyllids With Field High-Definition Camera Based on Improved Cascade Region-Based Convolution Neural Networks. *Front. Plant Sci.* 12:816272. doi: 10.3389/fpls.2021.816272

Fu, J., Liu, J., Tian, H., Li, Y., Bao, Y., Fang, Z., et al. (2019). "Dual attention network for scene segmentation," in *Proceedings Of The IEEE/Cvf Conference On Computer Vision And Pattern Recognition*, (Piscataway: IEEE), 3146–3154. doi: 10.1109/TNNLS.2020.3006524

Garcia-Garcia, A., Orts-Escolano, S., Oprea, S., Villena-Martinez, V., and Garcia-Rodriguez, J. (2017). A review on deep learning techniques applied to semantic segmentation. *arXiv* [Preprint]. doi: 10.48550/arXiv.1704.06857

Ghimire, P., Lei, D., and Juan, N. (2020). Effect of image fusion on vegetation index quality—a comparative study from Gaofen-1, Gaofen-2, Gaofen-4, Landsat-8 OLI and MODIS Imagery. *Remote Sens.* 12:1550. doi: 10.3390/rs12101550

Goodfellow, I., Pouget-Abadie, J., Mirza, M., Xu, B., Warde-Farley, D., Ozair, S., et al. (2014). Generative adversarial nets. *Adv. Neural Inf. Process. Syst.* 3:27.

He, K., Zhang, X., Ren, S., and Sun, J. (2016). "Deep residual learning for image recognition," in *Proceedings Of The IEEE Conference On Computer Vision And Pattern Recognition*, doi: 10.1109/CVPR.2016.90 (Piscataway: IEEE), 770–778.

Hinton, G. E., and Salakhutdinov, R. R. (2006). Reducing the dimensionality of data with neural networks. *Science* 313, 504–507. doi: 10.1126/science.1127647

Isola, P., Zhu, J.-Y., Zhou, T., and Efros, A. A. (2017). "Image-to-image translation with conditional adversarial networks," in *Proceedings Of The IEEE Conference On Computer Vision And Pattern Recognition*, doi: 10.1109/CVPR.2017.632 (Honolulu: IEEE), 1125–1134.

Jabbar, A., Li, X., and Omar, B. (2021). A survey on generative adversarial networks: Variants, applications, and training. *ACM Comput. Surv.* 54, 1–49. doi: 10.1145/3463475

Ji, S., Wei, S., and Lu, M. (2018). Fully convolutional networks for multisource building extraction from an open aerial and satellite imagery data set. *IEEE Trans. Geosci. Remote Sens.* 57, 574–586. doi: 10.1109/TGRS.2018.2858817

Jun, W., Qiming, Q., Xin, Y., Jianhua, W., Xuebin, Q., and Xiucheng, Y. (2016). A Survey of Building Extraction Methods from Optical High Resolution Remote Sensing Imagery. *Remote Sens. Technol. App.* 31, 653–662.

Khan, M. W. (2014). A survey: Image segmentation techniques. *Int. J. Futur. Comput. Commun.* 3, 89–93. doi: 10.7763/IJFCC.2014.V3.274

Long, J., Shelhamer, E., and Darrell, T. (2015). ""Fully convolutional networks for semantic segmentation"," in *Proceedings Of The IEEE Conference On Computer Vision And Pattern Recognition*, doi: 10.1109/CVPR.2015.7298965 (Piscataway: IEEE), 3431–3440.

McKittrick, K. (2013). Plantation futures. *Small Axe* 17, 1–15. doi: 10.1215/07990537-2378892

Mi, Z., Zhang, X., Su, J., Han, D., and Su, B. (2020). Wheat stripe rust grading by deep learning with attention mechanism and images from mobile devices. *Front. Plant Sci.* 11:558126. doi: 10.3389/fpls.2020.558126

Niu, Z., Zhong, G., and Yu, H. (2021). A review on the attention mechanism of deep learning. *Neurocomputing* 452, 48–62. doi: 10.1016/j.neucom.2021.03.091

Ohta, Y.-I., Kanade, T., and Sakai, T. (1978). "An analysis system for scenes containing objects with substructures," in *Proceedings of the Fourth International Joint Conference on Pattern Recognitions*, (Piscataway: Institute of Electrical and Electronics Engineers Incorporated), 752–754.

Ronneberger, O., Fischer, P., and Brox, T. (2015). "U-net: Convolutional networks for biomedical image segmentation," in *International Conference On Medical Image Computing And Computer-Assisted Intervention*, (Berlin: Springer), 234–241. doi: 10.1007/978-3-319-24574-4_28

Saito, S., Yamashita, T., and Aoki, Y. (2016). Multiple object extraction from aerial imagery with convolutional neural networks. *Electron. Imaging* 2016, 1–9. doi: 10.2352/ISSN.2470-1173.2016.10.ROBVIS-392

Tan, M., and Li, Y. (2019). Spatial and temporal variation of cropland at the global level from 1992 to 2015. *J. Resour. Ecol.* 10, 235–245. doi: 10.5814/j.issn.1674-764x.2019.03.001

Ubbens, J. R., and Stavness, I. (2017). Deep plant phenomics: A deep learning platform for complex plant phenotyping tasks. *Front. Plant Sci.* 8:1190. doi: 10.3389/fpls.2017.01190

Vakalopoulou, M., Karantzalos, K., Komodakis, N., and Paragios, N. (2015). "Building detection in very high resolution multispectral data with deep learning features," in *2015 IEEE International Geoscience And Remote Sensing Symposium (IGARSS)*, doi: 10.1109/IGARSS.2015.7326158 (Piscataway: IEEE), 1873–1876.

Xing, L. (2016). The Judicialize the Eco-Civilization Policy in China: A Perspective of Grasslands Protection. *Kan. J. L. Pub. Pol.* 26:396.

frontiers | Frontiers in Plant Science

TYPE Original Research
PUBLISHED 08 September 2022
DOI 10.3389/fpls.2022.917462

OPEN ACCESS

EDITED BY
Ruirui Zhang,
Beijing Academy of Agricultural and Forestry Sciences, China

REVIEWED BY
Xuan Li,
Stine-Haskell Research Center, United States
Wei Fu,
Hainan University, China
Longlong Li,
Beijing Academy of Agricultural and Forestry Sciences, China

*CORRESPONDENCE
Xiaoqiang Han
hanshz@shzu.edu.cn

SPECIALTY SECTION
This article was submitted to Technical Advances in Plant Science, a section of the journal Frontiers in Plant Science

RECEIVED 14 May 2022
ACCEPTED 28 June 2022
PUBLISHED 08 September 2022

CITATION
Liu Y, Xiao Q, Han X, Zeeshan M, Fang Z and Dou Z (2022) Effect of aerial application of adjuvants on pepper defoliant droplet deposition and efficacy of defoliation sprayed by unmanned aerial vehicles. *Front. Plant Sci.* 13:917462. doi: 10.3389/fpls.2022.917462

Effect of aerial application of adjuvants on pepper defoliant droplet deposition and efficacy of defoliation sprayed by unmanned aerial vehicles

Yapeng Liu, Qinggang Xiao, Xiaoqiang Han*, Muhammad Zeeshan, Zhihao Fang and Zechen Dou

Key Laboratory of Oasis Agricultural Pest Management and Plant Protection Utilization, College of Agriculture, Shihezi University, Shihezi, China

Defoliant spraying is an important aspect of the mechanized processing of pepper harvesting. Complete and uniform spraying of defoliant could improve the quality of defoliation and reduce the impurity content in processing pepper. In this study, we assessed the effect of aerial spraying of adjuvants on physicochemical properties of defoliant solution and droplet deposition when using an unmanned aerial vehicle (UAV) for defoliation spraying. The results showed that Puliwang was a better aerial spray adjuvant suitable for spraying defoliants for processing pepper using UAVs, with a higher defoliation rate and better droplet deposition. Although the YS-20 adjuvant had a higher droplet deposition amount (0.72 $\mu g/cm^2$) in the middle layer, its performance was poor in droplet size, density, and coverage. The size and density of the droplets added with the Manniu were basically the same as the Puliwang, even the distribution uniformity was better (the CV of the upper canopy layer was only 33.6%), but the coverage rate was poor. In the treatment with AS-901N, there was no marked increase in droplet size, so evaporation and drift were not improved, eventually resulting in a lower defoliation rate. Puliwang had the highest comprehensive score, followed by AS-910N, YS-20, and Manniu.

KEYWORDS

processing pepper, defoliant, droplet deposition, aviation spray adjuvants, unmanned aerial vehicle (UAV)

Introduction

Peppers (*Capsicum annuum* L.), with a variety of nutrients, are widely used in cosmetics, food additives, and as an important pharmaceutical and industrial raw material (Baenas et al., 2019). Xinjiang is an important production and processing area for peppers in China where the land, sunlight, and heat resources are abundant. Peppers from this region are highly reputed and have market competitiveness in domestic and foreign markets (Chai et al., 2020). In 2018, the area of processing pepper in Xinjiang was 3.67×10^4 hm^2, and the annual yield contributed to 20% of the country's total production which was 25×10^4 t. At the later stage of the plant's growth, defoliants are

applied to make it ready for harvesting by shedding its leaves. As the stalks and branches of the plants are extremely fragile, the traditional boom sprayer can damage the crop by crushing the leaves as well as the mature fruit which will ultimately affect the yield and quality of the pepper (Xiao et al., 2020).

In recent years, unmanned aerial vehicles (UAVs) have made great strides in agriculture. Their spraying operations increase the deposition of pesticides on target crops and avoid physical damage to crops during ground equipment operations (Yuan et al., 2018). The distancing of humans and machines from the crops avoids pesticide poisoning and greatly improves the efficiency of pesticide spraying and the utilization rate of pesticides (Yan et al., 2021a). UAVs also have low levels of water consumption, low dilution ratios, high working heights, fast flight speeds, and high atomization abilities. UAVs have been widely used in crops such as wheat (Yan et al., 2021b), rice (Chen et al., 2020a), corn (Hussain et al., 2022), grapes (Matese and Di Gennaro, 2018), citrus (Tang et al., 2018), and cotton (Lou et al., 2018). The addition of aerial spray with adjuvants efficiently solves the drift and loss of pesticide droplets during the spraying by UAVs and improves the utilization rate of pesticides.

Extant research on the effect of UAV spraying has mainly focused on fertilization, pesticide application, and nutritional analysis (Qiu et al., 2021; Xu et al., 2021; Hafeez et al., 2022). However, UAV spraying is greatly affected by the environment, which makes it easy for the droplets to drift and evaporate, resulting in reduced pesticide utilization and environmental concerns (Wang et al., 2020). Adding adjuvants to the aerial spray is an effective method to solve the drift and loss of pesticide droplets during UAV spraying (Chen et al., 2021). Xiao et al. (2019) studied the effects of five aerial application adjuvants on droplet deposition of cotton defoliation and found that vegetable oil adjuvants had a better effect. However, limited research is available on the effects of aerial spray adjuvants on pepper defoliant processing. In this study, we studied "Honglong 18" pepper as the test material using T16 UAV as the spraying equipment and examined the efficacy of four kinds of aerial application adjuvants. The physicochemical properties of the defoliant solution were studied through laboratory experiments, and the deposition characteristics were further analyzed to assess the defoliation effect of the defoliant droplets sprayed by UAVs through field experiments. Through this study, we aim to provide theoretical guidance for the operation of the UAV spraying process in pepper defoliants.

Materials and methods

Materials

The pepper defoliant (18% glufosinate ammonium soluble concentrate) was produced by Beijing Zhongnong Honglu Technology Development Co., Ltd., Beijing, China. The tested adjuvants were YS-20 (improved vegetable oil adjuvant, Anyang Quanfeng Biotechnology Co., Ltd., Anyang, China), Manniu (vegetable oil adjuvant, Qingdao Rishengyuan Crop Nutrition Co., Ltd., Qingdao, China), Puliwang (vegetable oil adjuvant, Oro Agri. International Co., Ltd., Palmela, Portugal), and AS-910N (improved vegetable oil adjuvant Momentive Performance Materials Inc., New York, USA). Allura Red (85%) was used as a droplet tracer (Zhejiang Gigagold Pigment Technology Co., Ltd., Wenzhou, China) and ethephon aqueous solutions (40%) were used as a ripening agent (Jiangsu Anpon Electrochemical Co., Ltd., Changzhou, China).

The aviation platform used was the T16 UAV (SZ DJI Technology Co., Ltd., Shenzhen, China). The UAV was equipped with RTK/GNSS precise positioning system, and its spraying system included a little water pump, pipeline, nozzles (8 XR11001VS, located directly below the rotor), and electronic control valve. T16 UAV has six rotors with a 16.0 L water tank and a payload of 15 kg. The flight height was 2.0 m and flight speed of 5.0 m/s with a spray width of 5 m and spraying volume of 15.0 L/hm^2.

Treatments

There were five treatments in the experiment (Table 1). Treatments 1, 2, 3, and 4 were added with YS-20, Manniu, Puliwang, and AS-910N in the dosage of 225 g/hm^2. Treatment 5 was the control (CK) without adjuvant. In addition, 1,875 g/hm^2 of pepper defoliant, 300 g/hm^2 of Allura red, and 900 g/hm^2 of 40% ethephon aqueous solution were added to each treatment.

Determination of physicochemical properties of pesticide solution

Surface tension

The surface tension was measured using the ST-1510 automatic interfacial tension meter (Xuxin Instrument Equipment Co., Ltd., Beijing, China) adopting the ring method according to GB/T 6541-1986, 10s after pesticide solution preparation. Each treatment was measured three times.

Dynamic viscosity

Kinematic viscosity of pesticide solution was measured by an electronic analytical balance [Sartorius Scientific Instruments (Beijing) Co., Ltd, Beijing, China], calculated by Equation 1 (Gao et al., 2021). Each treatment was measured three times.

$$\eta = \rho \times (v_k \times 0.00947) \quad (1)$$

where η is the dynamic viscosity (mPa·s), ρ is the density (g/mL), v_k is the kinematic viscosity, and 0.00947 is the

TABLE 1 Test treatment design.

Treatment	Adjuvants	Dosage of adjuvants (g/hm^2)	Defoliant (g/hm^2)	Ethephon (g/hm^2)	Spraying volume (L/hm^2)
1	YS-20	225	1,875	900	15
2	Manniu	225	1,875	900	15
3	Puliwang	225	1,875	900	15
4	AS-910N	225	1,875	900	15
5	/	/	1,875	900	15

instrument constant for this viscometer (mm^2/s^2), given by the manufacturer.

Contact angle

Fresh pepper leaves (2 × 2 cm, avoiding leaf veins, disease spots, etc.) were fixed the on the slide, and 2 μL pesticide solution (Table 1) was dropped on the leaves, respectively. The contact angle was recorded by drop shape analyzer DSA100 (KRUSS, Hamburg, Germany). Each treatment was recorded for three replicates.

Spreading ratio

Fresh pepper leaves (2 × 2 cm, avoiding leaf veins, disease spots, etc.) were placed the on the worktable of DP74 stereomicroscope (Olympus Co., Ltd., Japan), with a magnification of 10 times. About 2 μL of pesticide solution (Table 1) was dropped on the leaves and the spreading area of the droplet was recorded. The spreading ratio was calculated by Equation 2. Each treatment was recorded for three replicates.

$$R = (S_t/S_0) \times 100\% \quad (2)$$

where R is the spreading ratio, S_t is the spreading area at t s, and S_0 is the initial area.

Field and conditions

The experiment was carried out in the Beiquan town of Xinjiang production and construction crops (44°23'11 "N, 86°6'11" E), Shihezi, Xinjiang, China, in 2019. The experimental field was fertilized to a moderate level and had planted peppers for 2 years. The peppers (Honglong 18) were sown on 13 April 2019 with a wide film model having six lines (10 ± 66 cm) and 210,000 plants/hm^2 (the actual number of plants was 12,070 plants/667 m^2), and were irrigated by drip irrigation under the film. The defoliant was sprayed from 10 am to 12 am on 12 September 2019, from an average height of 0.88 m. The average wind speed was 2.06 m/s with relative humidity of 36.90% and temperature at 22.13°C (Kestrel 5500, Nielsen-Kellerman, Boothwyn, USA).

There were three replicates of 2,700 m^2 each in every treatment, with a 10 m buffer area between each treatment (Figure 1A). A droplet information collection belt was set in the middle of each repetition and was perpendicular to the UAV route. Seven droplet information collection points were arranged in an orderly manner on the belt with a spacing of 0.5 m. A metal stick was inserted at the point, and a water sensitive paper (WSP, 26 × 76 mm) and a filter paper (d = 70 mm) were fixed at a distance of 900, 600, 100, and 50 mm from the ground through double-sided clips, in line with the upper layer, middle layer, the lower layer of pepper canopy and ground (Figure 1B). After spraying, we waited for the WSP and filter paper to dry slightly, then marked and collected them before taking them back to the lab for analysis.

Determination of droplet deposition

Droplet information

Droplet information, including droplet size, droplet density, and droplet coverage, was obtained by first scanning the collected WSP with a FileScan2500 scanner (Shanghai Zhongjing Technology Co., Ltd., Shanghai, China) at grayscale and 600 dpi parameters and then analyzing it with Image J 1.38X software (National Institutes of Health).

Droplet deposition

The droplet deposition was obtained by measuring the Allura red content on the filter paper. About 5 ml of distilled water was added to each zip lock bag with filter paper and washed with a small shaker for 10 min, then centrifuged at 4,000 rpm for 5 min (Eppendorf 5417R Centrifuge, Eppendorf Co., Ltd., Hamburg, Germany). The absorbance value (Y_i) was determined using the Infinite 200Pro ELISA instrument (Tecan, Meilen, Switzerland) at 510 nm. The Y_i was then converted to mass concentration and X_i according to the linear regression equation of the Allura red standard solution ($Y = 0.0238X + 0.0431$, $R^2 = 0.997$).

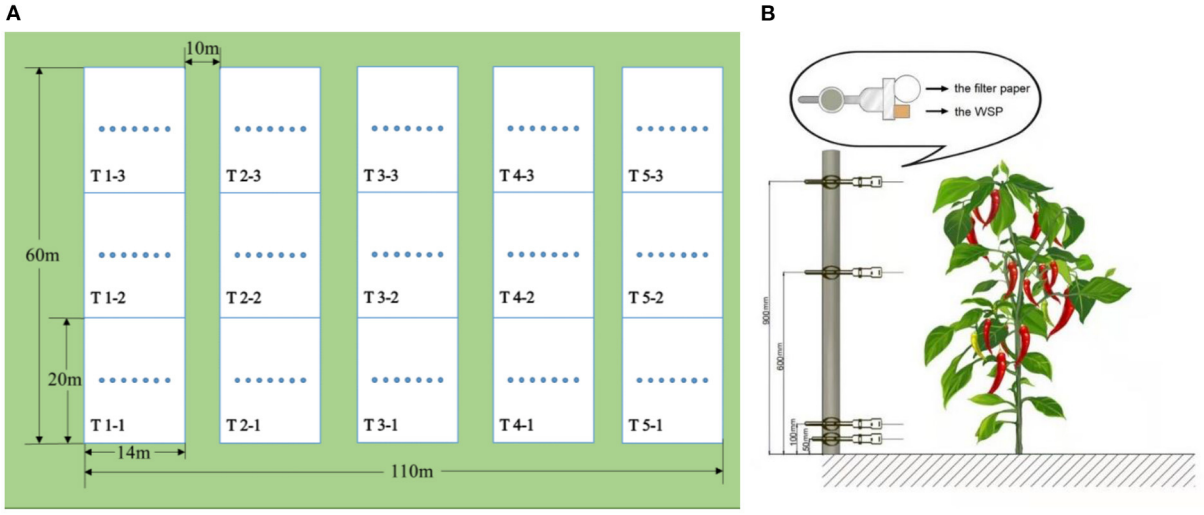

FIGURE 1
(A) The experimental layout of each treatment and **(B)** the placement of the WSP and filter papers at each sampling position within the processing pepper.

The deposition amount per unit area was calculated using Equation 3.

$$A = \frac{X_i \times V}{S} \tag{3}$$

where A is droplet deposition per unit area, X_i is the mass concentration of eluent, V is the volume of the added eluent, S is the area of droplet collector.

Droplet distribution uniformity

The uniformity of droplet distribution was calculated by the coefficient of variation (CV) of the same canopy deposition of processed peppers, and calculated using Equations 4, 5 (Lou et al., 2018).

$$s = \sqrt{\frac{1}{n-1}\sum_{i=1}^{n}(X_i - X)^2} \tag{4}$$

$$CV = \frac{s}{X} \tag{5}$$

where s is the variance, CV is the coefficient of variation, X_i is the droplet information (droplet density, DV_{50} and coverage) of each droplet captured card, X is the droplet information (droplet density, DV_{50} and coverage rate) of different parts of the pepper plant coverage, n is the total number of droplet collection cards in different parts of the pepper plant.

Spraying penetration

The spraying penetration was measured using the ratio of the deposition amount of the upper layer and lower layer of pepper canopy, as shown in Equation 6.

$$P = \frac{A_d}{A_u} \times 100\% \tag{6}$$

where P is the spraying penetration rate, A_d is the deposition amount in the lower layer of the processing pepper canopy, and A_u is the deposition amount in the upper layer of the processing pepper canopy.

Effective droplet deposition rate

After all the sample concentration values were measured, the deposition amount and deposition rate of droplets at each sampling point were calculated according to ISO22866 standard (ISO/TC 23/SC, 2005). And it was calculated using Equations 7–9 (Chen et al., 2020b).

$$D_s = \frac{F}{V \times I} \times 1.67 \tag{7}$$

$$D_d = \frac{C_e \times V}{C_s \times A} \tag{8}$$

$$R = \frac{D_d}{D_S} \times 100\% \tag{9}$$

where D_s is the deposition amount per unit area ($\mu L/cm^2$), V is the flight speed (m/s), I is the spraying interval (m), F is the spraying flow rate of the UAV (L/min), 1.67 is a constant.

D_d is the deposition amount per unit area (μL/cm^2), C_e is the concentration of the eluent (μg/mL), V is the volume of the eluent (mL); C_S is the concentration of the tracer (g/L); A is deposition sampling area (cm^2). R is the deposition rate.

Defoliation rate

Three points with consistency and representativeness were randomly selected in each replicate area. Then 10 consecutive pepper plants were selected from each point to investigate the total number of leaves before spraying. They were re-investigated 3, 5, 7, 9, and 12 d after spraying and the defoliation rate was calculated using Equation 10.

$$R_d = \frac{S_1 - S_2}{S_1} \times 100\% \quad (10)$$

where S_1 is the number of leaves investigated before spraying; S_2 is the number of leaves investigated after spraying.

Yield

At the time of harvesting the peppers (24 September 2019), three sampling sites were selected for each treatment, 15 consecutive pepper plants were selected from each site, and all their fruits were collected and the fresh fruit were weighed. After 30 days of air-drying, the harvested peppers were weighed to estimate the yield using Equation 11.

$$Y = Y \times \frac{12070}{15} \quad (11)$$

where Y is the theoretical yield (kg/667 m^2), Y is the average of fresh (dry) weight of peppers from three sampling points in each replicate (kg). With an harvest of 14,200 the planting density of the pepper field was 12,070 plants per 667 m^2.

Data analysis

All data were analyzed by OriginPro 2022b (Origin Lab, Northampton, MA, USA) and SPSS 22 (SPSS Inc., an IBM Company, Chicago, IL, USA) statistical software. Duncan's new multiple range test was selected to test the significance of differences at the level of $P < 0.05$.

Results and discussion

Effect of aerial application adjuvants on dynamic viscosity and surface tension

Reducing the surface tension of the pesticide solution can enhance the wetting performance and spreading ability of the spraying solution on the leaves. At 10 s, the surface tension of the YS-20, Manniu, Puliwang, AS910N, and CK was 45.83, 43.47, 42.57, 45.73, and 60.47 mN/m, respectively (Figure 2A). All four kinds of aerial spray adjuvants significantly reduced the surface tension of the pesticide solution to <46 mN/m. Compared with the surface tension of CK, Puliwang had the best effect on reducing the surface tension, which decreased by 29.6%. Liquid viscosity affects the atomization performance of the nozzle and also the number of satellite droplets, coalescence, viscosity dissipation in the collision process, and the spread of droplets on the leaves (Brenn and Kolobatic, 2006). As shown in Figure 2B, Puliwang and AS-910N could increase the viscosity to 1.37 and 1.34 mPa·s, respectively. The Manniu reduced the viscosity, while YS-20 had no effect on viscosity. The increase of viscosity is helpful to the deposition of droplets on leaves and avoids the bounce of droplets (Song et al., 2019). Pepper leaves are hydrophilic leaves. Increasing the viscosity of droplets, therefore, is conducive to the attachment of droplets on the leaves and improves the efficacy.

Effect of aerial application of adjuvants on contact angle

Adjuvants showed a significant effect on the contact angle of the droplet in the initial state (Figure 3). At 0 s, the contact angle without adjuvant was 83.20°, while that of YS-20, Manniu, Puliwang, and AS-910N were 60.85°, 50.22°, 60.26°, and 47.12°, respectively. The contact angle decreased rapidly within 10 s and gradually leveled off. After 5 s, the rate of contact angle slows down and tends to be stable. This indicated that the adjuvants could spread the spray solution more easily on pepper leaves, which is beneficial for the absorption of the defoliant. The adjuvant affected the contact angle by moderating the surface tension. In general, the contact angle of the leaf surface of the same crop will decrease with a decrease in surface tension (Lan et al., 2021). Xu et al. (2011) found that increasing viscosity and reducing surface tension were two main methods used to increase pesticide retention on superhydrophobic rice leaf surfaces. This was also consistent with our results, where after adding adjuvants the surface tension and contact angle of the droplets displayed the same trend. Our results showed that the surface tension and the contact angle of the pesticide solution on the pepper leaves were reduced, but the effect was different, which was based on the specific adjuvant used.

Effect of aerial spray with adjuvants on spreading ratio

The spreading of fluids over solid substrates is of great importance to pesticide applications, including defoliants. The wetting and spreading of pesticides on the leaf surface are

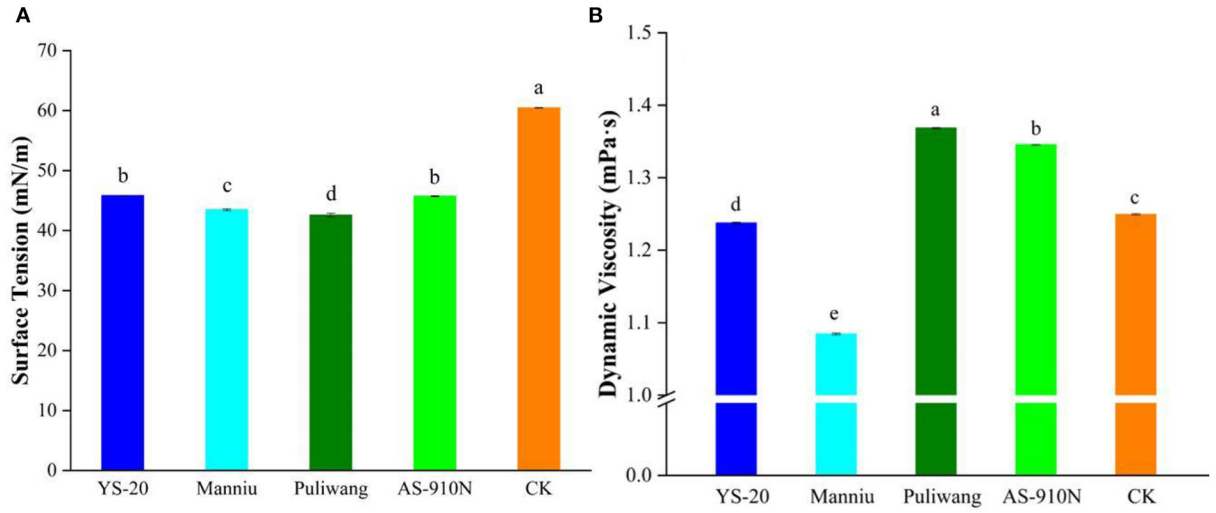

FIGURE 2
Effect of aerial spray with adjuvants on surface tension **(A)** and dynamic viscosity **(B)**. $^{a-e}$They represent the results of a significant difference analysis by Duncan's new multiple range test at the level of $P < 0.05$. Values followed by the same letter do not differ statistically.

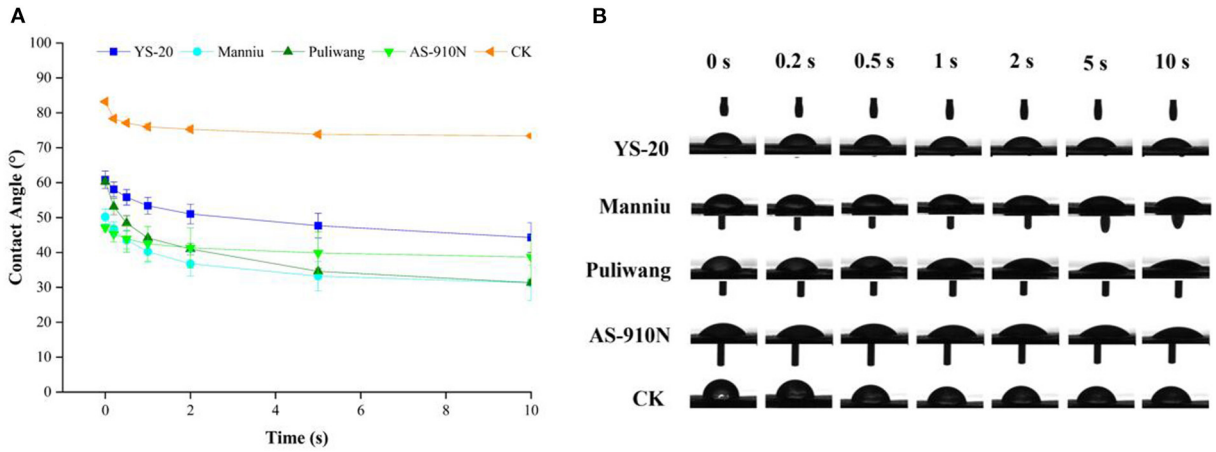

FIGURE 3
Effect of aerial spray with adjuvants on contact angle line graph **(A)** and experimental images **(B)**.

closely related to the combination of the leaf surface and the physicochemical properties of the pesticide solution. We found that adding aerial applications with adjuvants could increase the spreading ratio of defoliant droplets on the surface of pepper leaves (Figure 4). At 10 s, the spreading ratio of YS-20, Manniu, Puliwang, and AS-910N was 35.35, 34.54, 46.21, and 24.17%, respectively, which was significantly higher than that of CK (10.81%). This result was consistent with the analysis results of the contact angle. Different types of adjuvants can improve various aspects of spray dilution performance. Beacham et al. (2009) found that organosilicon adjuvants have a very prominent effect on improving the wetting of pesticide droplets on the leaf surface. However, when defoliants were used, ethephon, a strong acid ripening agent, needs to be added, which greatly destroys the stability of organosilicon adjuvants. Vegetable oil and modified vegetable oil adjuvants have been popular in recent years because of their wide tolerance. Zhou et al. (2017) found that modified seed oil slows down the evaporation rate of droplets on waxy leaves. Our experiments showed that four vegetable oil adjuvants could also effectively

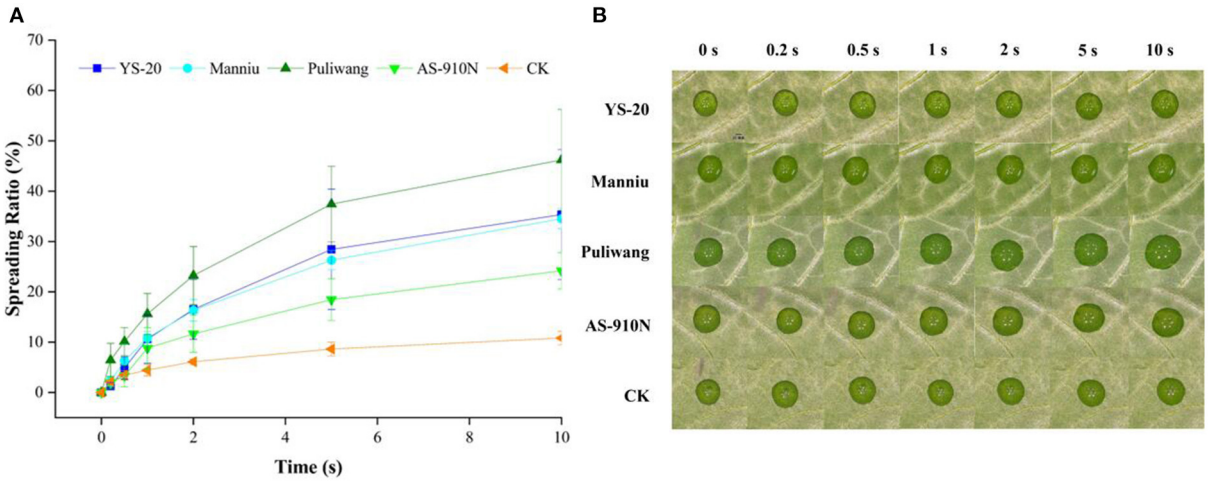

FIGURE 4
Effect of aerial spray with adjuvants on spreading ratio line graph **(A)** and experimental images **(B)**.

improve the spreading rate of defoliant droplets on pepper leaves and improve the defoliation effect.

Effect of aerial applications with adjuvants on the droplet size sprayed by UAV

Many factors, including adjuvants, pesticide formulations, and nozzles affect spray droplet size (Klein et al., 2009). The droplet size is one of the important indicators to evaluate the spraying quality when using UAVs. As shown in Table 2, the average droplet size of the treatments with adjuvants was significantly larger than that of those without adjuvants. The droplet sizes of the four adjuvants were also different. In the upper layer, the DV_{10} and DV_{50} of YS-20, Manniu, and Puliwang were larger than AS910N and CK, the DV_{90} showed no difference. In the middle and lower layers, the DV_{10} and DV_{50} of Puliwang were larger than others, but not significant. On the ground, the DV_{10} and DV_{50} of the treatments with or without adjuvants had no difference. Overall, the DV_{50} in the upper, middle, and lower layers, and ground with Puliwang was 402 ± 22.5, 377 ± 24, 365 ± 27.8, and 355 ± 28.8 μm, respectively, which was higher than other adjuvant augmented treatments. Although there is no specific droplet size range that is likely to drift under all conditions, droplets with diameters <100 μm are considered highly draftable (Nuyttens et al., 2014; Ferguson et al., 2016).

Matthews et al. reported that the optimum droplet size for herbicide spraying is 250 μm, while for fungicide, the particle size should be maintained at 50–150 μm (Matthews and Thomas, 2000). In this study, the droplet size in the treatment after adding Puliwang was between 350 and 450 μm, significantly higher than other treatments; the final defoliation rate was similarly the highest. It demonstrated that adjuvants

TABLE 2 Effect of aerial application of adjuvants on the droplet size sprayed by UAVs.

Pepper canopy	Treatment	Droplet size (μm)		
		DV_{10}	DV_{50}	DV_{90}
Upper layer	YS-20	238 ± 11.7 a	373 ± 30.4 ab	553 ± 31.5 a
	Manniu	219 ± 12.3 a	397 ± 29.6 a	650 ± 38.5 a
	Puliwang	226 ± 3.8 a	402 ± 22.5 a	628 ± 34.4 a
	AS-910N	171 ± 12.7 b	320 ± 15.3 b	523 ± 35.5 a
	CK	193 ± 17.1 b	348 ± 53.9 ab	571 ± 129 a
Middle layer	YS-20	220 ± 17.8 ab	350 ± 58.2 ab	495 ± 120.4 ab
	Manniu	208 ± 25.2 ab	368 ± 47.3 a	522 ± 83.8 ab
	Puliwang	227 ± 4.5 a	377 ± 24 a	553 ± 59.9 a
	AS-910N	153 ± 27.9 c	275 ± 34.6 b	402 ± 68.5 ab
	CK	184 ± 16.2 bc	288 ± 19.8 b	395 ± 32 b
Lower layer	YS-20	204 ± 19.4 b	311 ± 17.9 b	405 ± 37.7 b
	Manniu	205 ± 13 b	317 ± 28.3 ab	432 ± 53.4 ab
	Puliwang	235 ± 16.1 a	365 ± 27.8 a	509 ± 60.4 a
	AS-910N	179 ± 7.3 bc	292 ± 42 b	373 ± 67.7 b
	CK	163 ± 9.1 c	271 ± 18.9 b	367 ± 28.2 b
Ground	YS-20	228 ± 28.1 a	328 ± 54.5 a	437 ± 42.1 a
	Manniu	205 ± 33.1 abc	330 ± 40.9 a	446 ± 63.6 a
	Puliwang	225 ± 21.9 ab	355 ± 28.8 a	485 ± 63.7 a
	AS-910N	163 ± 43.2 c	268 ± 60.6 a	370 ± 94.6 a
	CK	167 ± 22.9 bc	291 ± 43.4 a	391 ± 90.1 a

Values followed by the same letter in the column do not differ statistically ($p < 0.05$).

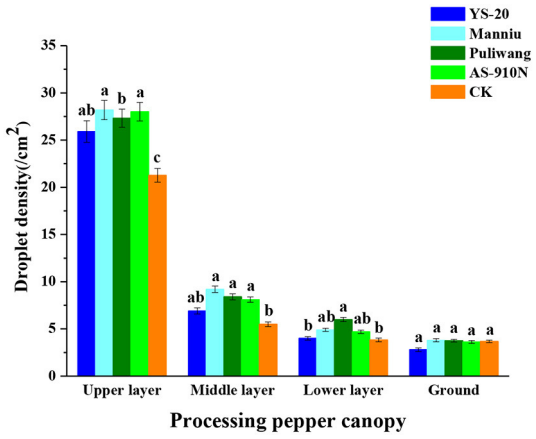

FIGURE 5
Effect of aerial spray with adjuvants on the droplet density sprayed by UAV. $^{a-c}$They represent the results of a significant difference analysis by Duncan's new multiple range test at the level of $P < 0.05$. Values followed by the same letter do not differ statistically.

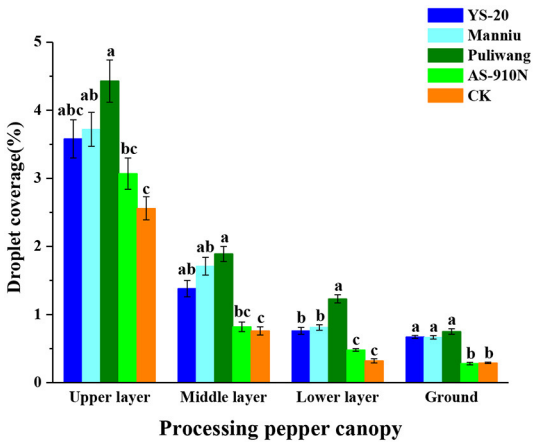

FIGURE 6
Effect of aerial spray with adjuvants on the droplet coverage sprayed by UAV. $^{a-c}$They represent the results of a significant difference analysis by Duncan's new multiple range test at the level of $P < 0.05$. Values followed by the same letter do not differ statistically.

could change droplet physicochemical properties, such as diameter and relative droplet span, thereby increasing the deposition amount on plant leaves and thus improving the utilization rate of pesticides (He et al., 2018). In addition, when the spray volume and droplet size are the same, the larger the droplet density, the higher the utilization rate of the chemical solution, and the better the control effect (Merritt, 1982). Combined with the results of contact angle and spreading rate, we found that adding spray adjuvants could increase the droplet size of the defoliant and reduce the risk of drift.

Effect of aerial application of adjuvants on the droplet density sprayed by UAVs

The droplet density of defoliants varied greatly among the layers of the pepper canopy (Figure 5). Overall, the droplet density of the upper layer of the pepper canopy was higher than that of other layers, which was due to the interception of the defoliant droplets by the upper layer with a larger leaf area in the later growth stage of pepper. In the upper and middle layers of the canopy, the average droplet densities of adjuvant-added defoliants were 27.31 and 8.11/cm^2 respectively, which were significantly higher than the CK (21.27 and 5.49/cm^2), while in the lower layer and the ground, there was no significant difference. In addition, the droplet density in the upper layer with Manniu was the highest (28.18/cm^2) among all the treatments, followed by AS-910N (28.01/cm^2) and Puliwang (27.32/cm^2), while the YS-20 (25.91/cm^2) was significantly lower than others. The droplet density of the defoliant without adjuvants was significantly lower than the aerial application with adjuvants.

Effect of aerial application with adjuvants on the droplet coverage sprayed by UAV

Meng et al. (2020) found that adding adjuvants could increase droplet coverage of the canopy, which would increase the probability of the droplets hitting the target, thereby improving its efficacy (Meng et al., 2020). As the droplets are intercepted by the upper layer of the pepper canopy, the coverage rate of the upper layer was significantly higher than other layers (Figures 6, 7). The presence (or absence), and the type of adjuvant caused a significant impact on droplet coverage. The average droplet coverage in the upper, middle, and lower layers, and ground (3.46, 1.26, 0.7, and 0.51%) of the crops treated with added adjuvant was significantly higher than CK (2.56, 0.76, 0.32, and 0.29%). When Puliwang was added, the droplet coverage of the upper, middle, and lower layers, and ground (4.44, 1.84, 1.19, and 0.76%) was significantly higher than other adjuvants. Manniu and YS-20 had the second highest coverage, and AS-910N had the least, with no significant difference from CK. In general, the defoliant droplet coverage rate for the aerial spray with adjuvants was significantly higher than that of the control (Figure 6). Previous research has shown that influenced by the wind field of the UAV rotor, the defoliant droplet coverage rate, particularly the range of spray width, varies considerably (Li et al., 2018). It should be noted that in the upper layer of the pepper crops, the droplet coverage rate was significantly different, and the adjuvant-added treatments were significantly better than the control without any adjuvant. In the middle and lower layers and the ground, there were no such differences. This may be due to the influence of drift and evaporation on the deposition of droplets in the upper layer.

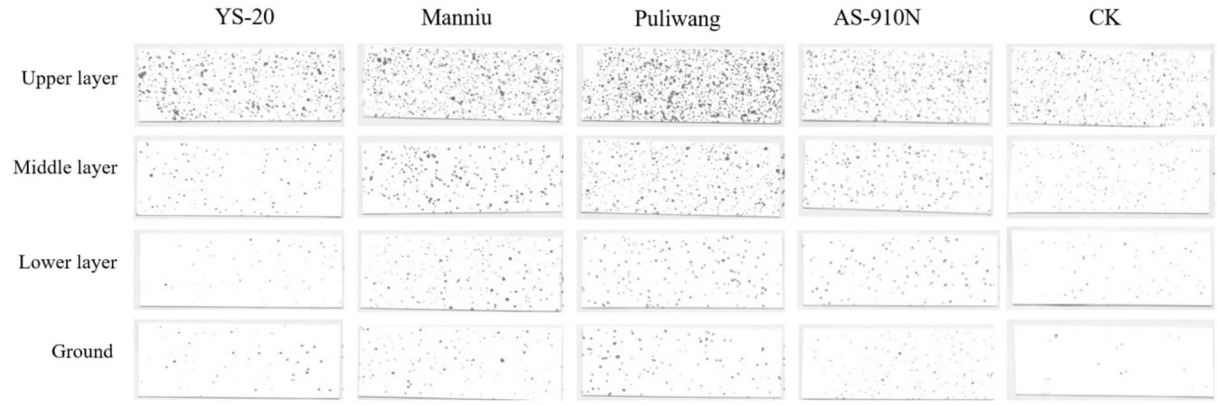

FIGURE 7
Effect of aerial spray with adjuvants on the droplet coverage sprayed by UAV (gray-scale photos of WSP).

TABLE 3 Effect of aerial spray with adjuvants on the droplet uniformity sprayed by UAV.

Treatment	Coefficient of variation (%)			Average
	Upper layer	Middle layer	Lower layer	
YS-20	57.21	67.32	73.88	66.14
Manniu	33.60	72.50	75.84	60.65
Puliwang	56.83	70.32	72.25	66.47
AS-910N	60.97	90.59	99.39	83.65
CK	64.79	84.11	107.87	82.26

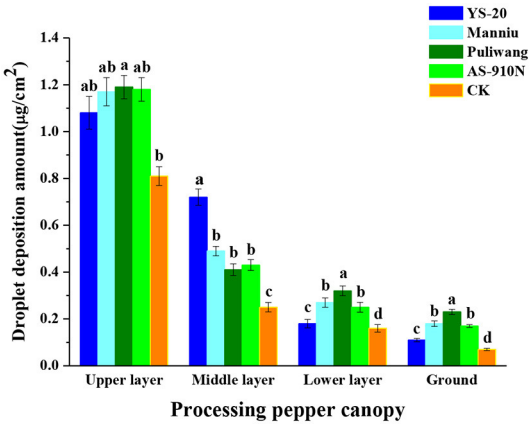

FIGURE 8
Effect of aerial spray with adjuvants on the droplet distribution sprayed by UAV. [a–d]They represent the results of a significant difference analysis by Duncan's new multiple range test at the level of $P < 0.05$. Values followed by the same letter do not differ statistically.

Effect of aerial spray with adjuvants on the droplet uniformity sprayed by UAV

The uniform distribution of droplets is expressed by the coefficient of variation (CV) of the same canopy droplet deposition. The smaller the coefficient of variation, the better the uniformity of droplet distribution (Chen et al., 2021). The field experiments were influenced by environmental conditions and the CV of droplet density and coverage rate were relatively large. The average droplet distribution uniformity of the defoliant treated with Manniu was the best (60.65%), followed by YS-20 and Puliwang (66.14 and 66.47% respectively). The results of AS-910N were the poorest (83.65%), even inferior to the CK (82.26%) (Table 3). However, most of the droplets were deposited in the upper layer due to interception, so the distribution uniformity of the upper layer was more representative. The best uniformity of droplet distribution in the upper layer was Manniu (33.60%).

The uniformity of droplet distribution was measured by the CV of the deposition in the same canopy layer of peppers (Zhan et al., 2022). According to the Chinese Civil Aviation Industry Standard, in the case of low-volume spray operation, the quality of the operation can only be guaranteed when the coefficient of variation of droplet distribution is <60%. The average variation coefficients of the whole plant droplet distribution (66.14, 60.65, 66.47, 83.65, and 82.26%) in the current study seem to be not standard. The planting density of the peppers in the experimental field reached 213,000 plants/hm^2 with an average height of about 0.88 m at the time of application. The interception effect of the upper layer was obvious, and its droplet variation coefficient (57.21, 33.60, 56.83, 60.97, and 64.79%) was more representative. Adding aerial spray adjuvants can reduce the coefficient of variation of droplet distribution which means improving the uniformity of droplet distribution, to meet the UAV operational standards.

TABLE 4 Effect of aerial spray with adjuvants on the deposition rate sprayed by UAVs.

Spraying date	Deposition rate (%)			Average
	Upper layer	Middle layer	Lower layer	
YS-20	36.4 ± 6.1 ab	23.2 ± 2.5 a	10.4 ± 3.3 a	23.33
Manniu	35.7 ± 1.2 ab	21.4 ± 2.5 a	6.2 ± 2 b	21.08
Puliwang	39.3 ± 11.5 a	17.9 ± 3.6 b	12.3 ± 5.1 a	23.13
AS-910N	30.1 ± 5.1 ab	11.5 ± 0.3 c	7.5 ± 1.3 b	16.37
CK	25 ± 1.6 b	7.2 ± 1.2 d	4 ± 0.3 c	12.07

The data in the table are averages. Values followed by the same letter in the column do not differ statistically ($p < 0.05$).

TABLE 5 Effect of aerial spray with adjuvants on the defoliation rate of processing pepper sprayed by UAVs.

Days after spraying	Defoliation rate of processing pepper (%)				CK
	YS-20	Manniu	Puliwang	AS-910N	
3	46.14 abc	47.24 ab	64.04 a	36.55 bc	20.30c
6	61.40 ab	68.33 ab	79.07 a	53.13 ab	42.31b
9	75.74 ab	75.06 ab	88.40 a	70.32 ab	62.55b
12	85.63 ab	83.19 ab	92.84 a	78.86 ab	73.04b
15	95.21 ab	95.58 ab	98.40 a	89.07 b	79.92c

The data in the table are averages. Values followed by the same letter in the column do not differ statistically ($p < 0.05$).

Effect of aerial applications with adjuvants on the droplet distribution sprayed by UAVs

The average deposition of droplets in the upper, middle, and lower layers and ground of the crops treated with adjuvants (1.15, 0.51, 0.25, 0.17 $\mu g/cm^2$) was significantly higher than the CK (0.81, 0.25, 0.15, 0.07 $\mu g/cm^2$) (Figure 8). In the upper layer, the droplet deposition amount of the Puliwang was the highest (1.19 $\mu g/cm^2$). While in the middle layer, the YS-20 was the highest (0.72 $\mu g/cm^2$). The droplet distribution penetration rates of YS-20, Manniu, Puliwang, and AS-910N were 15.51, 22.59, 27.11, and 20.97%, respectively, which were significantly higher than the CK (15.89%). The Puliwang showed a better effect in terms of penetration.

Some studies have suggested that droplets with smaller particle sizes are difficult to be intercepted by the upper layer and can penetrate better the middle and lower layers (Knoche, 1994; Wolf and Daggupati, 2009). Few other studies found that large particle-size droplets could not drift and evaporate easily and were more likely to reach the lower canopy layer (Derksen et al., 2008). In this study, we observed that the spraying penetration using Puliwang (27.11%) was better; it resulted in a larger droplet size and the DV50 reaching 402, 377, and 365 μm in the upper, middle, and lower layers. Therefore, in our study, penetration was better due to the larger droplet sizes.

Effect of aerial spray with adjuvants on the deposition rate sprayed by UAV

The effective deposition rates (23.33, 21.08, 23.13, and 16.37%) of the four treatments with adjuvants were 5–15% higher than the CK (12.07%) with a significant difference (Table 4). In the upper layer of the pepper canopy, the effective deposition rate after adding Puliwang (39.3%) was the highest. In the middle layer, the YS-20 was the highest (23.2%). In the lower layer, there was no significant difference between the effective deposition rates of YS-20 and Puliwang (10.4 and 12.3%, respectively), while being significantly higher than the other treatments.

The effective deposition rate of droplets could also be remarkably improved by adjuvants, because of the larger droplet size, the improved atomization effect, and the reduced evaporation and drift (Lan et al., 2008; Sijs and Bonn, 2020). The results of this study were similar to previous studies. In addition, adding adjuvants during pesticide spraying can change the physicochemical properties, promote the absorption of target plants or insects, and the retention of the liquid (Wang et al., 2022), thereby improving the utilization rate of pesticides.

Effect of aerial sprays with adjuvants on the defoliation rate of pepper sprayed by UAV

The addition (and absence) of adjuvants had a significant effect on the defoliation rate of pepper (Table 5). Leaf abscission began to form three days after the first spraying and the aerial spray with adjuvants had a considerable effect on the defoliation effect. Three days after spraying, the defoliation rate of crops sprayed with adjuvants was higher than that of CK, and Puliwang showed the best defoliation effect (64.04%). Between 6 and 12 days after spraying, Puliwang still showed the best defoliation rate, but there was no significant difference among the four adjuvants. Fifteen days after spraying, the defoliation rate of Puliwang treatment was 98.40%, and that of YS-20 and Manniu was more than 95%. However, the defoliation rate of AS-910N was only 89.07% and that of CK was only 79.92%. The above results showed that the addition of adjuvants to aerial applications could significantly improve the defoliation rate of pepper, and the results obtained with the use of Puliwang were the best.

TABLE 6 Effect of aerial sprays using adjuvants on the yield of pepper sprayed by UAVs.

Treatment	Fresh weight per 15 plants (g)	Dry weight per 15 plants (g)	DW/ FW ratio (%)	Theoretical yield of fresh pepper (kg/667 m^2)	Theoretical yield of dry pepper (kg/667 m^2)	Increase of dry pepper (%)
Puliwang	936.33	671.33	71.69	753.43	540.20 a	20.89
Manniu	928.67	675.33	72.72	747.27	543.42 a	21.61
YS-20	921.67	620.67	67.34	741.64	499.43 b	11.76
AS-910N	1174.33	608.00	51.77	944.94	489.24 b	9.48
CK	799.67	555.33	69.44	643.47	446.86 c	/

The data in the table are averages. Values followed by the same letter in the column do not differ statistically ($p < 0.05$).

TABLE 7 The effects of aerial application of adjuvant-enhanced defoliants on physicochemical properties, droplets deposition, and defoliation rate.

Adjuvants	Physicochemical properties				Droplet deposition						Defoliation rate (%)
	Dynamic viscosity (mPa/s)	Surface tension (mN/m)	Contact angle (°)	Spreading ratio (%)	Droplet size (μm)	Droplet density (/cm^2)	Droplet coverage (%)	Uniformity (%)	Penetration (%)	Deposition rate (%)	
YS-20	1.24	45.83	44.28	35.35	373	25.91	3.61	57.21	15.51	36.4	95.21
Manniu	1.08	43.47	31.32	34.54	397	28.18	3.70	33.60	22.59	35.7	95.58
Puliwang	1.37	42.57	31.34	46.21	402	27.32	4.44	56.83	27.11	39.3	98.4
AS-910N	1.34	45.73	38.56	24.17	320	28.01	3.15	60.97	20.97	30.1	89.07
CK	1.25	60.47	73.40	10.81	348	21.27	2.56	64.79	15.89	25.0	79.92

Effect of aerial sprays using adjuvants on the yield of pepper sprayed by UAVs

The effects of adding adjuvants to aerial applications on the yield of pepper are shown in Table 6. The average yield of pepper using adjuvants (518.00 kg/666.7 m^2) was significantly higher than that of the CK (446.85 kg/666.7 m^2). The yield of adding Puliwang (540.19 kg/666.7 m^2) was slightly lower than Manniu (543.41 kg/666.7 m^2), but significantly higher than other treatments. Puliwang and Manniu could significantly improve the yield of peppers; their yield increase rate exceeded 20%.

To sum up, the aerial applications using adjuvants had varying degrees of effects on the physicochemical properties, droplet deposition, and defoliation rate of the pesticide solution (Table 7). The performance of adjuvants could be evaluated based on these effects as indicators. Pearson correlation analysis was used to study the relationship between these indicators (Figure 9). The results showed that surface tension was significantly positively correlated with contact angle ($r = 0.987$, $p < 0.01$), and significantly negatively correlated with spreading ratio and defoliation rate ($r = -0.883$ and -0.937, $p < 0.05$). This indicates that the addition of adjuvants could effectively reduce the surface tension, thereby promoting the spreading of the droplets. In addition, the spreading rate was significantly positively correlated with droplet coverage ($r = 0.989$, $p < 0.01$), deposition rate ($r = 0.992$, $p < 0.05$), and defoliation rate ($r = 0.980$, $p < 0.05$). The droplet coverage was also significantly positively correlated with deposition rate ($r = 0.966$, $p < 0.01$) and defoliation rate ($r = 0.946$, $p < 0.05$). It could be seen that the adjuvants improved the spreading ratio of the droplets, the coverage rate, and the deposition rate, so that the contact between the defoliant and the pepper leaves was increased, which finally enhanced the defoliation effect. Furthermore, although not significant, there was a positive correlation between droplet size and droplet distribution penetration ($r = 0.494$), which supports the previous observation. In addition, the dynamic viscosity had a certain effect on the droplet size ($r = -0.335$). Specifically, the higher the viscosity, the smaller the droplets produced by the UAV spray, which was consistent with previous studies (Jamalabadi et al., 2017).

Through the correlation analysis, we found that the correlation between the indicators caused obstacles to the comprehensive evaluation of different adjuvants. Therefore, principal component analysis (PCA) was used to comprehensively evaluate the adjuvants. We selected two principal components whose cumulative contribution rate of eigenvalue reached 85.16% (Figure 10A). The variance contribution rates of principal components 1 and 2 were 66.97 and 18.19% respectively, indicating that it could effectively reflect the original data in the auxiliary indicators. The loading plot for principal components was used to measure the contributions of the principal components. Specifically, a larger

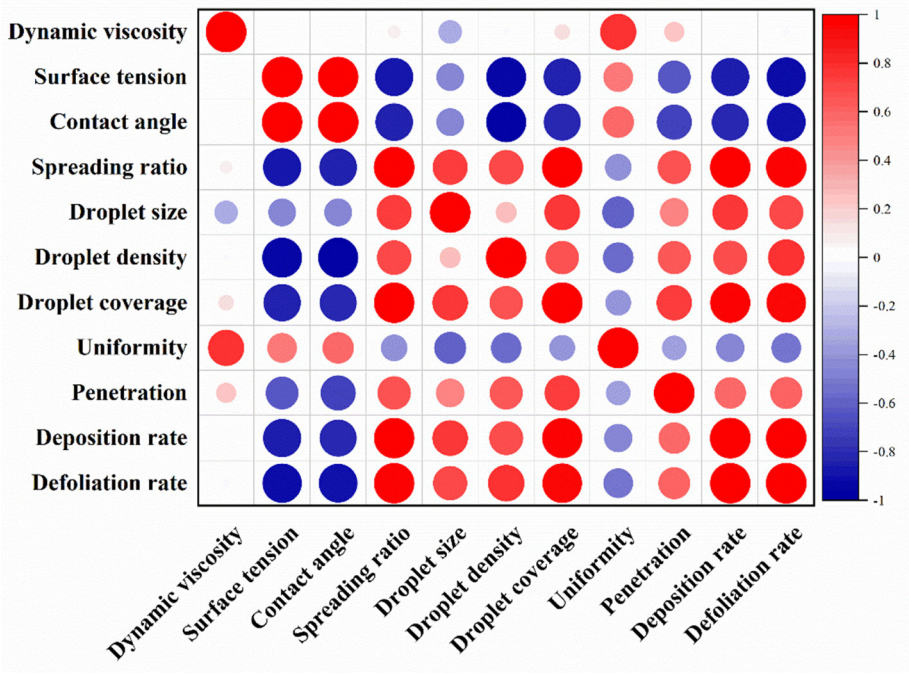

FIGURE 9
Heat map for the pearson correlation coefficients. The color and size of the circles represent the *r* and *p*-values. Deep and large circle signal a significant correlation.

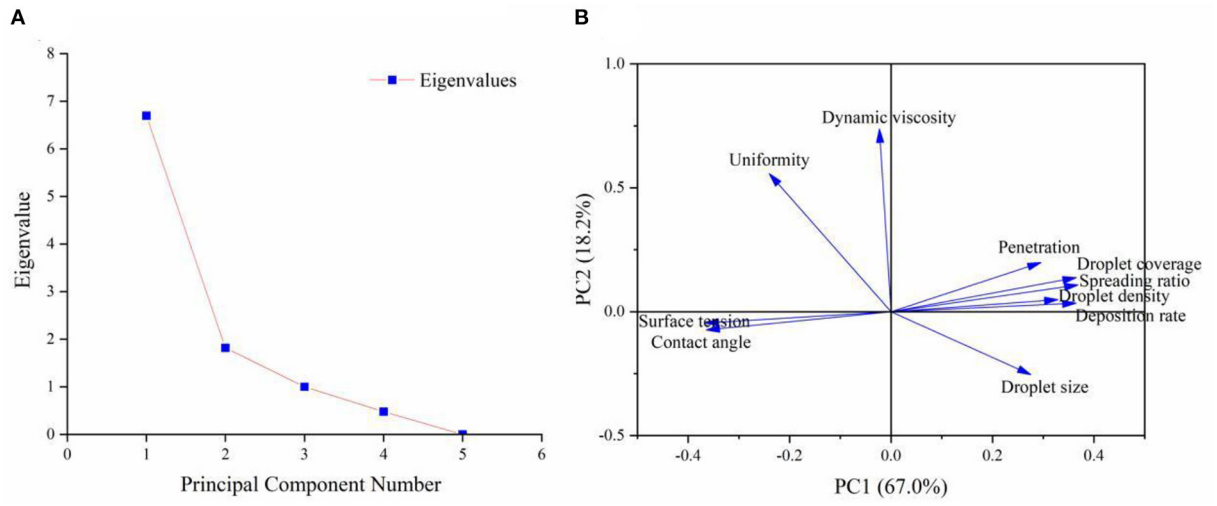

FIGURE 10
Scree plot of eigenvalues for principal components **(A)** and loading plot for principal components 1 and 2 **(B)**.

absolute value of the load means that the contribution of the corresponding principal component is larger (Karytsas and Choropanitis, 2017). Principal component 1 had a large to small load in terms of spreading ratio, contact angle, droplet coverage, surface tension, deposition rate, droplet density, penetration, and droplet size (Figure 10B). Principal component 2 had a large load in terms of uniformity and dynamic viscosity (Figure 10B). These results showed that except for uniformity and dynamic viscosity, other indicators could reflect the performance of the aerial application of adjuvants to a large extent, especially

TABLE 8 Comprehensive score of adjuvant performance.

Adjuvant	Scores of first principal components (F1)	Scores of second principal components (F2)	Comprehensive score (F)
YS-20	0.0303	−0.1078	0.0008
Manniu	0.3163	−1.6467	−0.1023
Puliwang	1.2190	0.6833	1.1046
AS-910N	−0.0123	0.8793	0.1781
CK	−1.5533	0.191966.	−1.1806

spreading ratio, contact angle, droplet coverage, surface tension, deposition rate, and droplet density.

Based on the mathematical model of PCA, we found that the comprehensive score for evaluating the performance of adjuvants (Table 8). Puliwang had the highest comprehensive score among the four adjuvants, followed by AS-910N, YS-20, and Manniu. The score of CK without additives was only 1.1806, far lower than the other four treatments. Therefore, it can be established that Puliwang had the best performance.

Conclusion

In this study, pepper processing and aerial spray adjuvants were selected as research objects, and the type of adjuvant that could effectively improve the defoliation effect of the pepper when sprayed by UAV was determined. Specifically, we studied the effects of aerial spray adjuvants on the physicochemical properties of the pepper defoliants. On that basis, the effects of various adjuvants on droplet deposition and defoliation of pepper crops were determined by spraying adjuvant enhanced defoliants using UAVs. The results of correlation analysis and principal component analysis show that Puliwang had the best effect as an adjuvant for aerial application of defoliants.

Data availability statement

The original contributions presented in the study are included in the article/supplementary material, further inquiries can be directed to the corresponding author.

Author contributions

XH conceived and designed the experiments and wrote the paper. YL, QX, ZF, and ZD performed the field experiments. YL, QX, and XH analyzed the data. MZ conceived the research and revised the manuscript. All authors contributed to the article and approved the submitted version.

Funding

This research was funded by Xinjiang Production and Construction Corps Major Scientific and Technological Projects, grant number 2018AA010-03 and the National Key Research and Development Program of China, grant number 2016YFD0200700.

Acknowledgments

The authors are grateful to SZ DJI Technology Co., Ltd., for providing plant protection for the unmanned aerial vehicle. We thank Yao Zhaoqun for his help in data analysis.

Conflict of interest

The authors declare that the research was conducted in the absence of any commercial or financial relationships that could be construed as a potential conflict of interest.

Publisher's note

All claims expressed in this article are solely those of the authors and do not necessarily represent those of their affiliated organizations, or those of the publisher, the editors and the reviewers. Any product that may be evaluated in this article, or claim that may be made by its manufacturer, is not guaranteed or endorsed by the publisher.

References

Baenas, N., Belović, M., Ilic, N., Moreno, D., and GarcíaViguera, C. (2019). Industrial use of pepper (*Capsicum Annum* L.) derived products: technological benefits and biological advantages. *Food Chem.* 274, 872–885. doi: 10.1016/j.foodchem.2018.09.047

Beacham, D. R., Matar, O. K., and Craster, R. V. (2009). Surfactant-enhanced rapid spreading of drops on solid surfaces. *Langmuir* 25, 14174–14181. doi: 10.1021/la9019469

Brenn, G., and Kolobatic, V. (2006). Satellite droplet formation by unstable binary drop collisions. *Phys. Fluids* 18, 87–101. doi: 10.1063/1.2225363

Chai, A. L., Chen, L. D., Xu, S., Patiguli, A., Wang, L. L., Shi, Y. X., et al. (2020). Molecular identification of co-infection of pepper mild mottle virus and Cucumber mosaic virus on Pepper in Kashgar, Xinjiang. *Acta Agri. Boreali-Sinica* 35, 332–337. doi: 10.7668/hbnxb.20191552

Chen, P. C., Lan, Y. B., Huang, X. Y., Qi, H. X., Wang, G. B., Wang, J., et al. (2020a). Droplet deposition and control of planthoppers of different nozzles in two-stage rice with a quadrotor unmanned aerial vehicle. *Agronomy* 10, 303. doi: 10.3390/agronomy10020303

Chen, S. D., Lan, Y. B., Zhou, Z. Y., Deng, X. L., and Wang, J. (2021). Research advances of the drift reducing technologies in application of agricultural aviation spraying. *Int. J. Agri. Biol. Eng.* 14, 1–10. doi: 10.25165/j.ijabe.20211405.6225

Chen, S. D., Lan, Y. B., Zhou, Z. Y., Ouyang, F., Wang, G. B., Huang, X. Y., et al. (2020b). Effect of droplet size parameters on droplet deposition and drift of aerial spraying by using plant protection UAV. *Agronomy* 10, 195. doi: 10.3390/agronomy10020195

Derksen, R. C., Zhu, H., Ozkan, H. E., Hammond, R. B., Dorrance, A. E., and Spongberg, A. L. (2008). Determining the influence of spray quality, nozzle type, spray volume, and air-assisted application strategies on deposition of pesticides in soybean canopy. *Trans. ASABE* 51, 1529–1537. doi: 10.13031/2013.25301

Ferguson, J. C., Chechetto, R. G., and Hewitt, A. J. (2016). Assessing the deposition and canopy penetration of nozzles with different spray qualities in an oat (*Avena sativa* L.) canopy. *Crop Protect.* 81, 14–19. doi: 10.1016/j.cropro.2015.11.013

Gao, X., Li, M., Zhang, H., Tang, X. N., and Chen, K. L. (2021). Fabrication of regenerated cellulose films by DMAc dissolution using parenchyma cells *via* low-temperature pulping from Yunnan-endemic bamboos. *Indus. Crops Products* 160, 113116. doi: 10.1016/j.indcrop.2020.113116

Hafeez, A., Husain, M. A., Singh, S. P., Chauhan, A., Khan, M. T., Kumar, N., et al. (2022). Implementation of drone technology for farm monitoring & pesticide spraying: a review. *Inform. Proces. Agri.* 2, 2. doi: 10.1016/j.inpa.2022.02.002

He, L., Wang, G. B., Hu, T., Meng, Y. H., Yan, X. J., and Yuan, H. Z. (2018). Influences of spray adjuvants and spray volume on the droplet deposition distribution with unmanned aerial vehicle (UAV) spraying on rice. *Plant Protect.* 44, 1046–1052. doi: 10.13802/j.cnki.zwbhxb.2017.2016147

Hussain, M., Wang, Z., Huang, G. M., Mo, Y., Kaousar, R., Duan, L. S., et al. (2022). Comparison of droplet deposition, 28-homobrassinolide dosage efficacy and working efficiency of the unmanned aerial vehicle and knapsack manual sprayer in the maize field. *Agronomy* 12, 385. doi: 10.3390/agronomy,12020385

ISO/TC 23/SC (2005). *Equipment for Crop Protection-Methods for the Field Measurement of Spray Drift: ISO 22866*. Paris: ISO Copyright Office.

Jamalabadi, M. Y. A., DaqiqShirazi, M., Kosar, A., and Shadloo, M. S. (2017). Effect of injection angle, density ratio, and viscosity on droplet formation in a microfluidic T-junction. *Theoret. Appl. Mechanics Lett.* 7, 243–251. doi: 10.1016/j.taml.2017.06.002

Karytsas, S., and Choropanitis, I. (2017). Barriers against and actions towards renewable energy technologies diffusion: a Principal Component Analysis for residential ground source heat pump (GSHP) systems. *Renew. Sustain. Energy Rev.* 78, 252–271. doi: 10.1016/j.rser.2017.04.060

Klein, R. N., Golus, J. A., and Nelms, K. L. (2009). The effect of adjuvants, pesticide formulation and spray nozzle tips on spray droplet size. *J ASTM Int.* 6, 1–7. doi: 10.1520/JAI102156

Knoche, M. (1994). Effect of droplet size and carrier volume on performance of foliage-applied herbicides. *Crop Protect.* 13, 163–178. doi: 10.1016/0261-2194(94)90075-2

Lan, Y. B., Hoffmann, W. C., Fritz, B. K., Martin, D. E., and Lopez, J. D. (2008). Spray drift mitigation with spray mix adjuvants. *Appl. Eng. Agri.* 24, 5–10. doi: 10.13031/2013.24157

Lan, Y. B., Shan, C. F., Wang, Q. Y., Liu, Q., Yang, C. L., Xie, Y. J., et al. (2021). Effects of different spray additives on droplet deposition characteristics during plant protection UAV spraying operations. *Trans. Chinese Soc. Agri. Eng.* 37, 31–38. doi: 10.11975/j.issn.1002-6819.2021.16.005

Li, J. Y., Lan, Y. B., and Shi, Y. Y. (2018). Research progress on airflow characteristics and field pesticide application system of rotary-wing UAV. *Trans. Chinese Soc. Agri. Eng.* 34, 104–118. doi: 10.11975/j.issn.1002-6819.2018.12.013

Lou, Z. X., Xin, F., Han, X. Q., Lan, Y. B., Duan, T. Z., and Fu, W. (2018). Effect of unmanned aerial vehicle flight height on droplet distribution, drift and control of cotton aphids and spider mites. *Agronomy* 8, 187. doi: 10.3390/agronomy8090187

Matese, A., and Di Gennaro, S. F. (2018). Practical applications of a multisensor UAV platform based on multispectral, thermal and RGB high resolution images in precision viticulture. *Agriculture* 8, 116. doi: 10.3390/agriculture8070116

Matthews, G. A., and Thomas, N. (2000). Working towards more efficient application of pesticides. *Pest Manag. Sci.* 56, 974–976. doi: 10.1002/1526-4998(200011)56:11<974::AID-PS231>3.0.CO;2-4

Meng, Y. H., Su, J. Y., Song, J. L., Chen, W. H., and Lan, Y. B. (2020). Experimental evaluation of UAV spraying for peach trees of different shapes: effects of operational parameters on droplet distribution. *Comput. Electr. Agri.* 170, 105282. doi: 10.1016/j.compag.2020.105282

Merritt, C. R. (1982). The influence of form of deposit on the phytotoxicity of mcpa, paraquat and glyphosate applied as individual drops. *Ann. Appl. Biol.* 101, 527–532. doi: 10.1111/j.1744-7348.1982.tb00854.x

Nuyttens, D., Zwertvaegher, I., and Dekeyser, D. (2014). Comparison between drift test bench results and other drift assessment techniques. *Aspects Appl. Biol.* 122, 293–301.

Qiu, Z. C., Ma, F., Li, Z. W., Xu, X. B., Ge, H. X., and Du, C. W. (2021). Estimation of nitrogen nutrition index in rice from UAV RGB images coupled with machine learning algorithms. *Comput. Electr. Agri.* 189, 106421. doi: 10.1016/j.compag.2021.106421

Sijs, R., and Bonn, D. (2020). The effect of adjuvants on spray droplet size from hydraulic nozzles. *Pest Manag. Sci.* 76, 3487–3894. doi: 10.1002/ps.5742

Song, Y. Y., Cao, C., Xu, B., Ran, G. C., Cao, L. D., Li, F. M., et al. (2019). Research progress on bouncing behavior and control technology of pesticide droplets at plant leaf surface. *Chinese J. Pesticide Sci.* 21, 895–907. doi: 10.16801/j.issn.1008-7303.2019.0110

Tang, Y., Hou, C. J., Luo, S. M., Lin, J. T., Yang, Z., and Huang, W. F. (2018). Effects of operation height and tree shape on droplet deposition in citrus trees using an unmanned aerial vehicle. *Comput. Electr. Agri.* 148, 1–7. doi: 10.1016/j.compag.2018.02.026

Wang, G. B., Han, Y. X., Li, X., Andaloro, J., Chen, P. C., Hoffmann, W. C., et al. (2020). Field evaluation of spray drift and environmental impact using an agricultural unmanned aerial vehicle (UAV) sprayer. *Sci. Tot. Environ.* 737, 139793. doi: 10.1016/j.scitotenv.2020.139793

Wang, S. L., Li, X., Zeng, A. J., Song, J. L., Xu, T., Lv, X. L., et al. (2022). Effects of adjuvants on spraying characteristics and control efficacy in unmanned aerial application. *Agriculture* 12, 138. doi: 10.3390/agriculture12020138

Wolf, R. E., and Daggupati, N. P. (2009). Nozzle type effect on soybean canopy penetration. *Appl. Eng. Agri.* 25, 23–30. doi: 10.13031/2013.25426

Xiao, Q. G., Du, R., Yang, L., Han, X. Q., Zhao, S. F., Zhang, G. Q., et al. (2020). Comparison of droplet deposition control efficacy on phytophthora capsica and aphids in the processing pepper field of the unmanned aerial vehicle and knapsack sprayer. *Agronomy* 10, 215. doi: 10.3390/agronomy10020215

Xiao, Q. G., Xin, F., Lou, Z. X., Zhou, T. T., Wang, G. B., Han, X. Q., et al. (2019). Effect of aviation spray adjuvants on defoliant droplet deposition and cotton defoliation efficacy sprayed by unmanned aerial vehicles. *Agronomy* 9, 217. doi: 10.3390/agronomy9050217

Xu, L., Zhu, H., Ozkan, H. E., Bagley, W. E., and Krause, C. R. (2011). Droplet evaporation and spread on waxy and hairy leaves associated with type and concentration of adjuvants. *Pest Manag. Sci.* 67, 842–851. doi: 10.1002/ps.2122

Xu, M., Liu, M. J., Liu, F., Zheng, N., Tang, S., Zhou, J. J., et al. (2021). A safe, high fertilizer-efficiency and economical approach based on a low-volume spraying UAV loaded with chelated-zinc fertilizer to produce zinc-biofortified rice grains. *J. Clean. Prod.* 323, 129188. doi: 10.1016/j.jclepro.2021.129188

Yan, X. J., Wang, M., Zhu, Y. X., Shi, X., Liu, X. H., Chen, Y. X., et al. (2021b). Effect of aviation spray adjuvant on improving control of fusarium head blight and reducing mycotoxin contamination in wheat. *Agriculture* 11, 1284. doi: 10.3390/agriculture11121284

Yan, X. J., Zhu, S. H., Yang, D. B., and Yuan, H. Z. (2021a). Agriculture on the wings of science and technology: plant protection unmanned aerial vehicle (UAV) low-volume spraying technology reduces pesticide use and boosts control efficacy. *J. Plant Protect.* 48, 469–476. doi: 10.13802/j.cnki.zwbhxb.2021.2021835

Yuan, H. Z., Guo, Y. W., Xue, X. Y., Yan, X. J., Chen, X., Kong, X., et al. (2018). The role of the popularization and appli-cation of plant protection unmanned aircraft in improving the utilization rate of pesticides in China. *Agri. Eng. Technol.* 38, 46–50. doi: 10.16815/j.cnki.11-5436/s.2018.09.008

Zhan, Y. L., Chen, P. C., Xu, W. C., Chen, S. D., Han, Y. F., Lan, Y. B., et al. (2022). Influence of the downwash airflow distribution characteristics of a plant protection UAV on spray deposit distribution. *Biosyst. Eng.* 216, 32–45. doi: 10.1016/j.biosystemseng.2022.01.016

Zhou, Z. L., Cao, C., Cao, L. D., Zheng, L., Xu, J., and Li, F. M. (2017). Evaporation kinetics of surfactant solution droplets on rice (*Oryza sativa*) leaves. *PLoS ONE* 12, e0176870. doi: 10.1371/journal.pone.0176870

frontiers | Frontiers in Plant Science

TYPE Original Research
PUBLISHED 30 September 2022
DOI 10.3389/fpls.2022.1009630

OPEN ACCESS

EDITED BY
Ruirui Zhang,
Beijing Academy of Agricultural and Forestry Sciences, China

REVIEWED BY
Wei Fu,
Hainan University, China
Jiangtao Qi,
Jilin University, China

*CORRESPONDENCE
Qing Zhang
zhangqing202017@aircas.ac.cn
Yubin Lan
ylan@scau.edu.cn

SPECIALTY SECTION
This article was submitted to Technical Advances in Plant Science, a section of the journal Frontiers in Plant Science

RECEIVED 02 August 2022
ACCEPTED 29 August 2022
PUBLISHED 30 September 2022

CITATION
Lu J, Qiu H, Zhang Q, Lan Y, Wang P, Wu Y, Mo J, Chen W, Niu H and Wu Z (2022) Inversion of chlorophyll content under the stress of leaf mite for jujube based on model PSO-ELM method.
Front. Plant Sci. 13:1009630.
doi: 10.3389/fpls.2022.1009630

Inversion of chlorophyll content under the stress of leaf mite for jujube based on model PSO-ELM method

Jianqiang Lu[1,2,3], Hongbin Qiu[1,2,3,4], Qing Zhang[4]*, Yubin Lan[1,2,3]*, Panpan Wang[5], Yue Wu[4], Jiawei Mo[1,2,3], Wadi Chen[1,2,3], HongYu Niu[1,2,3] and Zhiyun Wu[1,2,3]

[1]College of Electronic Engineering, College of Artificial Intelligence, South China Agricultural University, Guangzhou, China, [2]National Center for International Collaboration Research on Precision Agricultural Aviation Pesticide Spraying Technology (NPAAC), Guangzhou, China, [3]Guangdong Laboratory for Lingnan Modern Agriculture, Guangzhou, China, [4]Key Laboratory of Digital Earth Science, Aerospace Information Research Institute, Chinese Academy of Sciences, Beijing, China, [5]The 14th Division of Xinjiang Production and Construction Corps, Institute of Agricultural Sciences, Kunyu, China

During the growth season, jujube trees are susceptible to infestation by the leaf mite, which reduces the fruit quality and productivity. Traditional monitoring techniques for mites are time-consuming, difficult, subjective, and result in a time lag. In this study, the method based on a particle swarm optimization (PSO) algorithm extreme learning machine for estimation of leaf chlorophyll content (SPAD) under leaf mite infestation in jujube was proposed. Initially, image data and SPAD values for jujube orchards under four severities of leaf mite infestation were collected for analysis. Six vegetation indices and SPAD value were chosen for correlation analysis to establish the estimation model for SPAD and the vegetation indices. To address the influence of colinearity between spectral bands, the feature band with the highest correlation coefficient was retrieved first using the successive projection algorithm. In the modeling process, the PSO correlation coefficient was initialized with the convergent optimal approximation of the fitness function value; the root mean square error (RMSE) of the predicted and measured values was derived as an indicator of PSO goodness-of-fit to solve the problems of ELM model weights, threshold randomness, and uncertainty of network parameters; and finally, an iterative update method was used to determine the particle fitness value to optimize the minimum error or iteration number. The results reflected that significant differences were observed in the spectral reflectance of the jujube canopy corresponding with the severity of leaf mite infestation, and the infestation severity was negatively correlated with the SPAD value of jujube leaves. The selected vegetation indices NDVI, RVI, PhRI, and MCARI were positively correlated with SPAD, whereas TCARI and GI were negatively correlated with SPAD. The accuracy of the optimized PSO-ELM model (R^2=0.856, RMSE=0.796) was superior to that of the ELM model alone (R^2=0.748, RMSE=1.689). The PSO-ELM model for remote sensing estimation of relative leaf chlorophyll content of jujube shows high fault tolerance and improved data-processing efficiency. The results provide

a reference for the utility of UAV remote sensing for monitoring leaf mite infestation of jujube.

KEYWORDS

SPAD, PSO-ELM, SPA, hyperspectral, jujube, damage severity, leaf mite

Introduction

The jujube tree (*Zizyphus jujuba*), which plays a significant role in the ecological and economic development of the Xinjiang oasis, is a key component of agricultural growth in southern Xinjiang. One of the primary pests that endanger the health of jujube is the leaf mite (*Tetranychus truncatus Ehara*), and when it infests the jujube during the growth season, it can lower the quality of the jujube by more than 35%. Therefore, efficient pest control and early detection are crucial for jujube orchard management.

Remote sensing monitoring using low-altitude unmanned aerial vehicles (UAVs), such as UAVs equipped with multispectral and hyperspectral cameras, addresses the above issues. In addition to low-altitude UAVs, measurements using satellites are also available for remote sensing to monitor the growth of crop plants. In recent years, agricultural pest and disease monitoring has increasingly utilized remote sensing monitoring technology (Adao et al., 2017; Bai et al., 2020; Jiang et al., 2021). With its rapid, real-time, large-area, and non-destructive qualities, the technology has demonstrated benefits that cannot be matched by standard pest and disease monitoring approaches. Large-scale monitoring of crops, including crop area, pest and early warning, and growth conditions, may be accomplished by satellite remote sensing (Bai et al., 2019). However, throughout the imaging process, satellite remote sensing optical images are frequently influenced by inclement weather such as clouds, rain, and fog. Compared with satellite remote sensing, UAV remote sensing platforms have the characteristics of low operating cost, high flexibility, and fast data acquisition in real time, which is a unique advantage in the field of crop pest and disease detection. As an essential component of low-altitude remote sensing (Zhang et al., 2021), UAV remote sensing platforms have unique advantages for crop pest and disease monitoring, which considerably expands the scope of remote sensing use in crop monitoring (Dehkordi et al., 2020; Xu et al., 2022). Satellite remote sensing is primarily used for monitoring broad areas, but it cannot provide images with sufficient spatial resolution and the images are susceptible to weather conditions (Bendig et al., 2015; You et al., 2022). In addition, the progressive improvement of UAV technology has made feasible its combination with hyperspectral and multispectral technology for agricultural disease monitoring, providing a reference for accurate crop disease monitoring and to guide remedial management (Adao et al., 2017; Li et al., 2021). For instance, UAV hyperspectral remote sensing can monitor a broad area with high precision, efficiency, and continuity, and accomplish the fusion of UAV multisource remote sensing imagery and target extraction. In previous studies (Liu et al., 2020), UAV hyperspectral remote sensing has been utilized to perform pertinent research on a variety of agricultural diseases, such as citrus Huanglongbing (Garcia-Ruiz et al., 2013; Deng X.L. et al., 2020), wheat yellow rust (Dehkordi et al., 2020; Guo et al., 2021), and pine wilt disease (Deng X. et al., 2020; Qin et al., 2021; Xia et al., 2021), etc.

UAV hyperspectral remote sensing facilitates information extraction in image and spectral dimensions, and is frequently employed for monitoring agricultural growth conditions, and pest and disease stress in the field. Photosynthesis is an essential reference for evaluation of plant development (Hunt et al., 2013, Sun Q. et al., 2021), and chlorophyll content is an indication of plant photosynthetic capacity; hence, chlorophyll content can effectively reflect the growth status of a crop (Ji et al., 2021; Kaivosoja et al., 2021; Lei et al., 2021). The variation of the chlorophyll content of crops is important for monitoring the growth of crops. On the one hand, chlorophyll content absorption reflects the strength of photosynthesis, the growth stage and health status of crops; on the other hand, pests and diseases also directly affect the chlorophyll content of plants. Therefore, monitoring chlorophyll content effectively reflects the growth condition of crops. Variations in grayscale values on hyperspectral scanning recordings are caused on a broad scale when the crop is damaged by pests or disease, resulting in considerable variances in spatial, spectral, and temporal phases (Liu et al., 2017; Ahmad et al., 2018). The introduction of fused hyperspectral data and chlorophyll feature content approaches by analyzing local spectral differences of crops may also enhance remote sensing research on the monitoring of pests and diseases (Vanegas et al., 2018). It may be used for monitoring vegetation production, controlling crop resources, and monitoring pests and diseases by calculating the chlorophyll content of the crop canopy. Consequently (Wang et al., 2015), monitoring of crop chlorophyll content indicators might assist in reflecting the severity or incidence of agricultural pests and diseases to a certain extent.

A key biochemical indicator of crop development is chlorophyll content, and when jujube trees are infected with leaf mites, the amount of chlorophyll varies according to the degree of the disease. Hyperspectral has rich spectral information, which provides the possibility for the construction of chlorophyll inversion models. The severity of leaf mite infestation was correlated with chlorophyll content, which can be indirectly

reflected by measuring the chlorophyll content of jujube. The majority of current research on crop chlorophyll inversion with hyperspectral data is based on statistical regression models, which may be broadly classified into two types: vegetation index models and direct spectrum models. In the vegetation index models, the hyperspectral data are first utilized to generate several vegetation indices (Sun Q. et al., 2021), which are then used to develop numerous linear or nonlinear regression methods to produce an inversion model between these indices and chlorophyll content in the vegetation index models (Guo et al., 2021; Ji et al., 2021; Sun J. et al., 2021). It is easy to build the inversion model using vegetation indices, but a single vegetation index cannot adequately characterize the entire hyperspectral information. The direct spectrum models rely on the modeling of the entire hyperspectral bands, which is usually a high-dimension vector. Using the whole hyperspectral band directly may result in excessive model complexity or model overfitting. Dimension reduction approaches like as principal component analysis (PCA) or partial least squares (PLS) may assist in addressing this issue in part.

Most of the current research on the relationship between hyperspectral data and chlorophyll content focuses on the changes in chlorophyll content of crops under different nutrient stresses and different growth periods, while the hyperspectral inversion research on chlorophyll content of crops infected by diseases and insect pests is relatively less. The main performance is that the research pays more attention to the spectral characteristics of crop diseases and less attention to the physiological and biochemical changes in plants caused by diseases and insect pests. In addition, the research on crop diseases and insect pests using remote sensing technology is mostly aimed at grain crops such as wheat and rice, as well as economic crops such as cotton, soybean, and rapeseed, which pay less attention to pests and diseases of jujube plants.

Therefore, the aim of this study was to estimate SPAD values for leaf mite infestation of jujube based on UAV hyperspectral images. The estimation performance of the model based on VIs and selected feature bands was also analyzed. The relationship between the degree of leaf mite infestation and canopy leaf SPAD values was investigated based on the best estimates of SPAD values obtained. More specifically, the following points were noted in our study:

(1) Based on the experimental data, the correlation between the hyperspectral characteristic parameters of the jujube canopy and chlorophyll content was analyzed.
(2) Establishment of jujube SPAD estimation model under stress of leaf mite based on VI alone by using a linear regression model.
(3) To improve the accuracy of the inversion of the chlorophyll content of jujube infested with leaf mites. A proposed method employs a successive projection algorithm (SPA) to extract the characteristic bands from the high-dimensional hyperspectral vector, reducing model complexity and avoiding model overfitting. With the extracted characteristic bands as input, by building a PSO-ELM inversion model for the chlorophyll content of jujube.

Materials and methods

Study areas

The 224th regiment, the study area selected for this experiment, is located north of National Highway 315 at the crossroads of Pishan County and Moyu County in Hotan Region, on the southern edge of the Great Taklamakan Desert in Xinjiang, China (Li et al., 2021). The total land area is 234,751 km^2 and the terrain slopes from the southwest to the northeast. Jujube predominates in the study area, which comprises a planting area of 74,057 ha, a sizable landmass, an abundance of light and heat resources, drought, low rainfall, high evaporation, low relative humidity, and significant diurnal temperature differences—all of which are unique natural conditions that have aided the explosive growth of the jujube industry in Xinjiang. The 14th division's 224th regiment began planting jujube in 2003, according to investigations by the Xinjiang Production and Construction Corps. jujube orchards have expanded by more than 90 km^2 since approximately 2019, and constitute 72% of all arable land and 83% of all orchard land (Liu et al., 2015).

At the three designated study areas, a total of 90 sample survey sites were selected, where communities of healthy jujube plants and plants infested with leaf mites were clearly separated. Taking into consideration the features of pest infestation and the distinguishability of remote sensing images, the infestation severity was divided into four classes: healthy, mild damage, moderate damage, and severe damage. Based on an investigation of the effects of environmental changes on leaf mite infestation of jujube trees in Xinjiang, it was determined that the peak incidence of leaf mites occurs annually from June to August (Zhang et al., 2013; Li H. et al., 2020). By clustering, leaf mites mostly suck sap on the underside of leaves, causing grayish white or yellowish fine patches on the leaves, decreasing the leaf chlorophyll content, and impairing the development and growth of jujube plants. In light of this, the present experiment chose the aforementioned period to conduct the research and employed an UAV-mounted hyperspectral sensor and ground acquisition for data collection in the field trial. The study area shown in Figure 1.

Data acquisition

UAV hyperspectral remote sensing image acquisition and data processing

The experiment employed a M600Pro UAV (Shenzhen DJI, Shenzhen, China) equipped with a hyperspectral camera (Rikola, Oulu, Finland) and the SPAD-502Plus (Konica Minolta, Osaka,

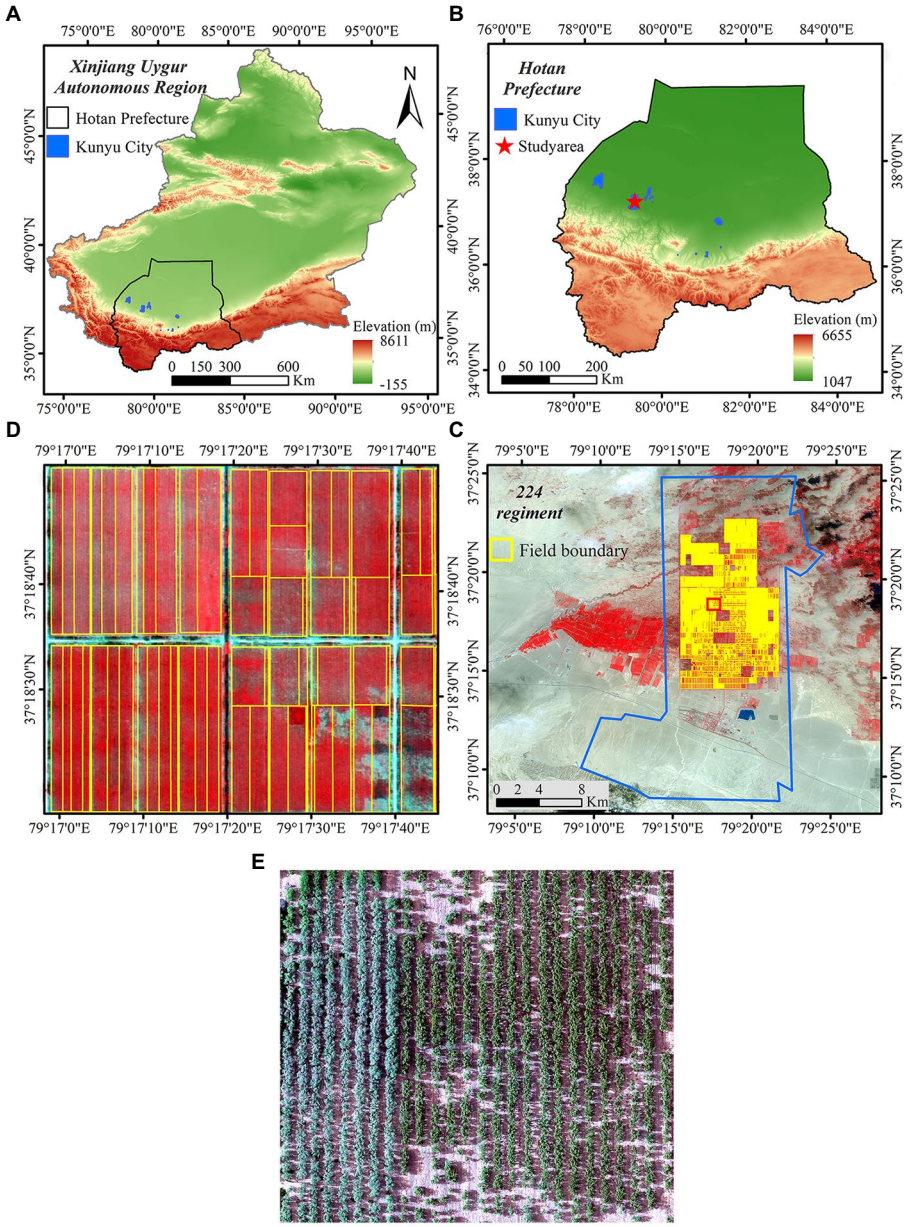

FIGURE 1
Study area. **(A)** Xinjiang Uygur Autonomous Region; **(B)** Hotan area; **(C)** 224th regiment; **(D)** and **(E)** Image of the study area.

Japan). Supplementary Figure 1 depicts the experimental instruments and the scene diagrams. The acquisition period ranged from 11:00 to 15:00 (the sun altitude angle was >45°) under bright, clear, or partially overcast conditions. In anticipation of flight photography, radiation correction was conducted on the hyperspectral camera. Four 50 cm × 50 cm diffuse reflectance gray plates (reflections of 3%, 22%, 48%, and 64%, respectively.) were placed on a level surface in the test location, and the surface of the calibration plate was devoid of interfering objects and shadows. In accordance with the features of the hyperspectral imagers provided by Rikola, system correction and post-processing correction were conducted on the hyperspectral images after image acquisition was completed.

Correcting the system

In the course of capturing hyperspectral images, the UAV platform creates inevitable systematic inaccuracies owing to the instrument's inherent constraints and the measurement technique, which must be addressed. Radiation calibration, dark current correction, and lens vignetting correction are the primary components.

The feature information of the original jujube tree orchard hyperspectral image was expressed as the digital number (DN). However, because the systematic error DN cannot accurately reflect the spectral characteristics of the feature, the DN of the original image must be converted to the feature reflectance using the information for the calibration plate representing the specific

reflectance obtained at the same time as the experiment, as shown in Equation (1).

$$\rho_t = \frac{DN_t - DN_1}{DN_2 - DN_1}(\rho_2 - \rho_1) + \rho_1 \quad (1)$$

where ρ_t and DN_t are the reflectance and DN of the original image target element, ρ_1 and ρ_2 are the reflectance of different calibration plates, and DN_1 and DN_2 denote the DN value of different calibration plates, respectively.

Post-processing refinement

In this work, the UAV images were captured using frame-wide imaging. Owing to the imaging principle and environment, there are small changes in position and attitude between the bands, resulting in hyperspectral cube bands that do not totally overlap. The flight time of the UAV is ~20–30 min, and the radiation brightness gradient difference between different bands will be affected by the change of solar illumination conditions, resulting in inhomogeneous color and DN. The irradiance can be effectively corrected to the normal level using Equations (2), (3).

$$L_{jc}(\lambda)_{at\_sensor} = L_j(\lambda)_{at_{sensor}} \times C_j(\lambda) \quad (2)$$

$$C_j(\lambda) = E_j(\lambda) / E_{ref}(\lambda) \quad (3)$$

where $L_{jc}(\lambda)_{at\_sensor}$ is the irradiance consistency corrected image; $L_{jc}(\lambda)_{at_{sensor}}$ is the jth original image; $C_j(\lambda)$ is the jth image multiplicative correction factor; $E_j(\lambda)$ is the irradiance value recorded for the jth image; and $E_{ref}(\lambda)$ is the irradiance value of the reference image.

The UAV flew at a height of 60 m, at a speed of 5 m s^{-1}, with overlap and side overlap of the images of 75%, a baseline distance of 25.9 m, a route spacing of 34.5 m. The Agisoft PhotoScan program was used to import photographs and the position and orientation system data, define the coordinate system, align the images, produce point clouds, grids, and textures, construct a digital elevation model, and produce orthophotos. The stitched orthophoto was geometrically corrected using GPS point data collected in the field to reduce the accuracy between the hyperspectral image features and the actual feature positions. The projection coordinate system was set to the Universal Transverse Mercator and the final correction error was controlled within 0.5 m. Within 0.5 m is the ultimate correcting error. Even after radiation correction, a variety of random disturbances remain in the picture reflectance, including impulse noise and Gaussian noise. Using Savitzky–Golay filtering, the spectral curve was considered to be polished, ensuring that the noise was efficiently smoothed with the same form and width as the signal.

Measurement of SPAD at ground sampling points

The collection environment is shown in Supplementary Figure 2. A handheld chlorophyll absorbance meter, the SPAD-502Plus, was used to estimate the chlorophyll content of leaves swiftly and non-destructively. On the same day as the UAV flight, the SPAD properties of jujube trees were assessed. The field sampling points were arranged in the shape of a 'S', each of the three chosen blocks comprised 30 sampling points. Four classes of jujube trees were selected with the same spatial distribution. Thus, 90 sets of samples were gathered, consisting of a total of 1,200 samples. Following the sample allocation concept, 20 of the 90 groups of samples were utilized as test samples, while the measured SPAD values of the remaining 70 groups were randomly chosen as modeling samples. To minimize sampling error, canopy leaves of comparable size, color, and shape were chosen for the sampling procedure (Han et al., 2021). The measurements were performed at the leaf tip, center, and base, and the mean value was used to represent the leaf's SPAD characteristic parameter.

Classification of plant pest severity

This study was carried out in experimental plots with leaf mite occurrence in the field, and field leaf mite surveys were conducted by hand to collect samples. At the time of sampling, the degree of leaf damage and the latitude and longitude information of the sampling site were recorded based on GPS positioning, the 90 sample points were sited evenly throughout the jujube tree planting area. According to the Code of Practice of Prevention and Control Techniques for Pests and Diseases of Jujube (National Standard of the People's Republic China), the severity levels of jujube tree mite infestation was divided into four classes in Supplementary Table 1. Healthy leaves were assigned a value of I, mild damage a value of II, moderate damage a value of III, and severe damage a value of IV. The four categories leaves are shown in Figure 2.

Vegetation index

A vegetation index may be subdivided into several vegetation index parameters based on various monitoring and computation methodologies (Torres-Sanchez et al., 2014; Liu et al., 2020; Ji et al., 2021). A vegetation index incorporates linear or nonlinear combinations of reflectance in distinct spectral bands to produce correlated spectral signals so as to simplify the spectral information and enhance vegetation-related features. For identification of agricultural pests and diseases, the visible red band, which is highly absorptive in green plants, and the near-infrared band, which is highly reflective and transmissive in green plants, are often selected. The spectral response of these two bands

to the same biophysical phenomena provides a strong contrast that changes with the leaf canopy structure and coverage; hence, their ratio, difference, or linear combination may be utilized to augment or disclose the implicit vegetation information (Lei et al., 2021). In the present study, the normalized difference vegetation index (NDVI), ratio vegetation index (RVI), physiological reflex vegetation index (PhRI), modified chlorophyll absorption ratio index (MCARI), transformed chlorophyll absorption ratio index (TCARI), and green index (GI) were chosen. Information on the vegetation indices is presented in Table 1.

Statistical analysis

Regarding the accuracy of the parameter estimates, the coefficient of determination (R^2) and root mean square error (RMSE) were employed to assess the model accuracy. The R^2 value represents the degree of fit, whereas RMSE measures the accuracy of data measurement. In general, it is believed that the closer the R^2 value is to 1, the better it indicates a strong goodness of fit, and conversely, a low value indicates a poor goodness of fit. The smaller the RMSE, the better it indicates a small error, whereas a high value indicates the inaccuracy is large. The calculation of these statistics is shown in Equations (4), (5):

$$R^2 = \frac{\sum_{i=1}^{n}\left(x_i - \hat{x}\right)^2\left(y_i - \hat{y}\right)^2}{\sum_{i=1}^{n}\left(x_i - \hat{x}\right)^2\sum_{i=1}^{n}\left(y_i - \hat{y}\right)^2} \quad (4)$$

$$RMSE = \sqrt{\frac{\sum_{i=1}^{n}\left(y_i - \hat{y}\right)^2}{n}} \quad (5)$$

where n denotes the number of samples for estimation or validation of the model; x_i, $\hat{x}$, y_i, and $\hat{y}$ denote: measured value, measured mean value, estimated value, and estimated mean value, respectively.

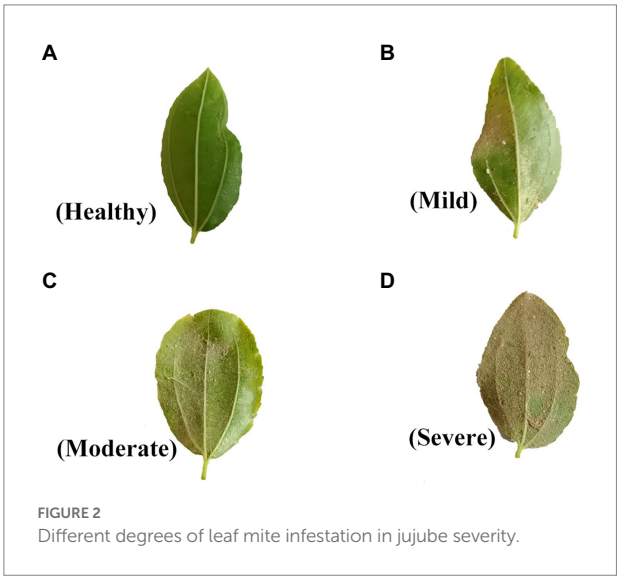

FIGURE 2
Different degrees of leaf mite infestation in jujube severity.

Results

Characteristics of SPAD variation

From 90 sample points, a total of 1,200 ground SPAD values were obtained, Table 2 summarizes the statistical properties of the sampled data. The modeling sample and the validation sample differed except for the data samples. The variation range of SPAD values for the modeling set of samples was 20.80–66.90,

TABLE 1 Vegetation index information.

Name	Formula	Comprehensive embodiment	Application	Reference
NDVI	$\frac{NIR - R}{NIR + R}$	Integrated crop growth variability	Diseases detection	Mahlein et al. (2013)
RVI	$\frac{NIR}{R}$	Crops growth sensitivity	Chlorophyll estimation	Birth and McVey (1968)
PhRI	$\frac{(R_{550} - R_{531})}{(R_{550} + R_{531})}$	Crop growth pattern	Chlorophyll estimation	Daughtry et al. (2000)
MCARI	$\frac{((R_{701} - R_{671}) - 0.2(R_{701} - R_{549}))}{\left(\frac{R_{701}}{R_{671}}\right)}$	Crops chlorophyll variations	LAI and chlorophyll estimation	Zhang et al. (2019)
TCARI	$3\left((R_{700} - R_{675}) - \frac{0.2(R_{700} - R_{500})}{\left(\frac{R_{700}}{R_{670}}\right)}\right)$	Crops growth sensitivity	Chlorophyll estimation	Haboudane et al. (2002)
GI	$\left(\frac{R_{554}}{R_{677}}\right)$	Crops green variability	Leaf rust detection	Ashourloo et al. (2014)

TABLE 2 Statistical characteristics of chlorophyll content.

Sample set	No. of samples	Min.	Max.	Mean.	Std. deviation	C.V/%
Overall	1,200	20.80	67.50	46.17	9.66	20.93
Modeling Set	800	20.80	66.90	46.21	9.71	21.01
Validation Set	400	21.50	67.50	45.97	9.68	21.06

the mean was 46.21, and the coefficient of variation was 21.01%. The variation range of SPAD values for the validation set of samples was 21.50–67.50, the mean was 45.97, and the CV was 21.06%. Considering the impact of leaf mites on the leaf chlorophyll content, the CV of the SPAD values was more than 10%, suggesting that the chlorophyll content was more variable. The discrepancies between the modeling and validation sets were negligible, there were no significant differences within the modeling and validation sets ($p = 0.678$), as determined by an independent samples t-test. Therefore, the sample sets were appropriate for modeling and validation.

Analysis of SPAD and spectral characteristics of jujube under infestation of leaf mite

Chlorophyll content is an indicator of the biochemical parameters of the crop and reflects the growth of the crop (Qi et al., 2021). Pest infestation causes changes in the chlorophyll content of the crop. Thus, measuring chlorophyll content reveals the health and vigor of the crop. When jujube plants are infected with leaf mites, the mean SPAD value of their canopy leaves decreases gradually with an increase in the severity of leaf mite infestation (Figure 3). The results demonstrated that the SPAD value of jujube trees was negatively associated with the severity of leaf mite infestation.

With the more severe leaf mite infestation, the SPAD values of jujube chlorophyll content gradually decreased, thus causing changes in the spectral characteristics of the canopy of jujube, showing a trend of decreasing spectral reflectance step by step with the increase of leaf mite infestation. Figure 4 depicts the average spectral reflectance curves of jujube trees at the canopy scale under different severities of leaf mite infestation. The spectral band features of jujube plants differ notably with the severity of leaf mite infestation. Considering the phenomena of "green peaks" owing to decreased chlorophyll absorption, the spectral characteristic curves of healthy jujube trees exhibited modest reflectance peaks in the green band between 520 and 570 nm. Because of the intense absorption of chlorophyll for photosynthesis, a red wavelength absorption trough, termed a "red valley," forms in the red wavelength range of 620–690 nm. As the chlorophyll concentration rises, so does the photosynthetic capability. The "green peak" and "red valley" in the green light spectrum progressively diminish between 680 and 750 nm. Given light scattering within the leaf, the reflectance in the near-infrared

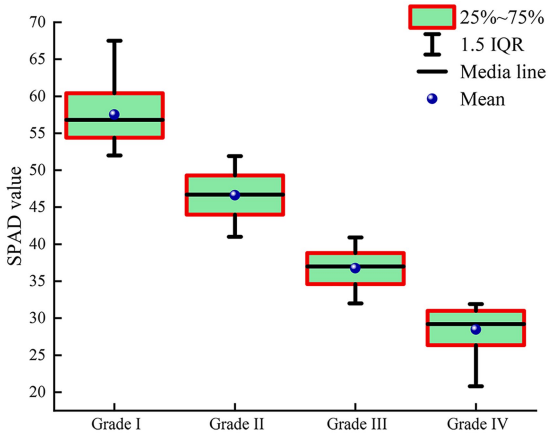

FIGURE 3
Variations in SPAD values of jujube leaves for different leaf mite infestation levels.

range exhibits conspicuous peaks of high reflectance, which constitute the spectrum's largest peak and generate a highly reflective platform. The variation in spectral reflectance of leaf mite damage of jujube trees was increasingly evident with an increase in the severity of infestation, which led to a decline in chlorophyll content and severe damage to the cellular structure and tissues of the leaf.

Correlation between SPAD value and vegetation indices of jujube trees

To facilitate an understanding of the relationship between vegetation indices and the chlorophyll content of jujube, a correlation coefficient matrix map is presented in Figure 5. Positive correlations are represented by numbers greater than zero, whereas negative correlations are represented by values less than zero (Yang et al., 2021). The absolute values of the correlation coefficients between SPAD and NDVI, RVI, PhRI, MCARI, TCARI, and GI ranged from 0.64 to 0.82. The NDVI, RVI, PhRI, and MCARI were positively correlated with SPAD, whereas TCARI and GI were negatively correlated with SPAD. As can be seen in Figure 5, the six selected vegetation indices were significantly correlated with SPAD, among which the correlation coefficient between leaf SPAD value and PhRI reached a maximum of 0.82, which was higher than the correlation coefficient between SPAD value and other vegetation indices. Further, by taking SPAD of jujube leaves as the dependent variable, and using NDVI, RVI, PhRI, MCARI, TCARI, and GI as independent variables, a remote sensing estimation model for the relative chlorophyll content of jujube canopy leaves was constructed. Table 3 shows the statistical regression modeling of vegetation indices to inversion chlorophyll content. The modeling determination coefficient of the SPAD-PhRI estimation model was 0.702, which was higher than the modeling accuracy of SPAD value and other vegetation indices.

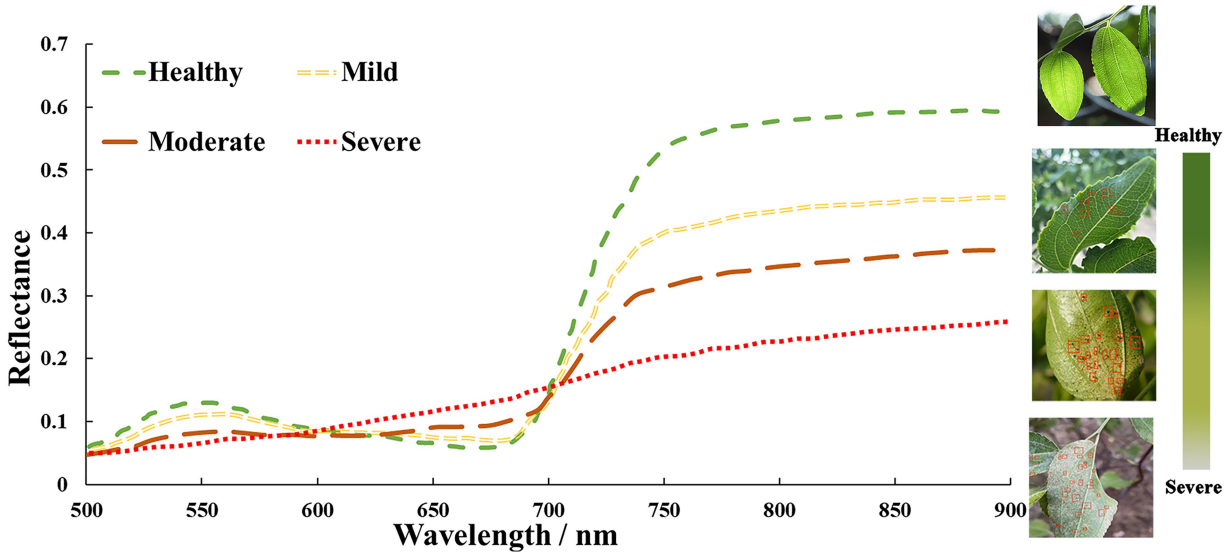

FIGURE 4
Spectral curves of jujube trees for different leaf mite damage indices.

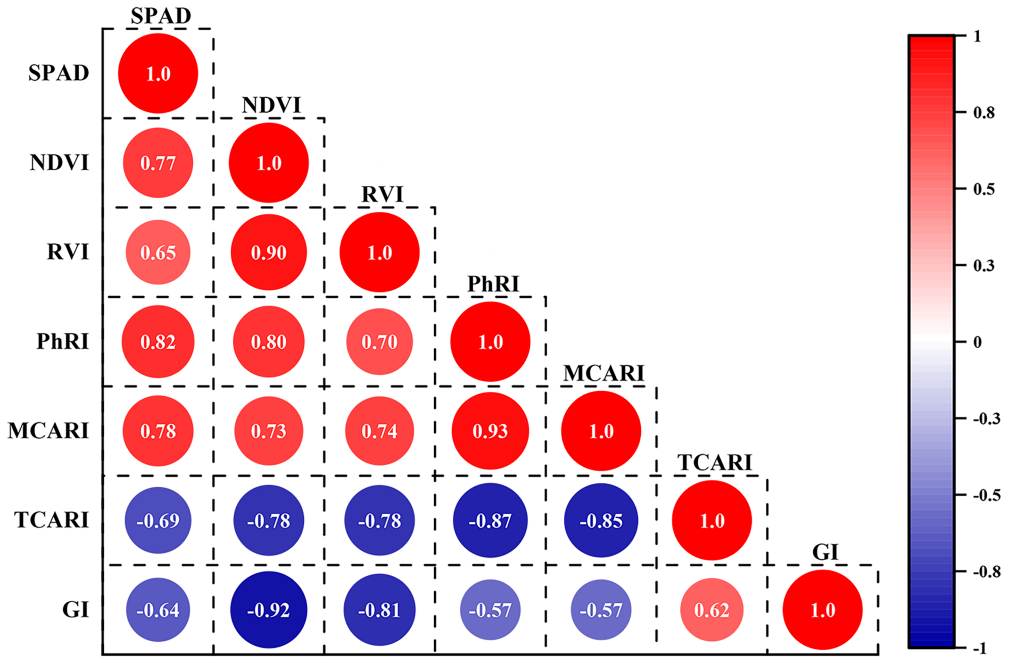

FIGURE 5
Correlation analysis between SPAD and vegetation index.

Correlation between SPAD value and spectral reflectance

As the chlorophyll content of jujube trees infected by leaf mites will change, as illustrated in Figure 6, chosen chlorophylls significantly associated with leaf mite infection were correlated with the raw and first-order derivative spectra for the analysis. The correlation coefficients between the original spectra and the SPAD value were negative at 500–749 nm and positive above 750 nm (Figure 6A). The absolute value of the correlation between the original spectrum and the chlorophyll content is mostly between 0.5 and 0.65, and the curve changes are relatively flat. When the original spectrum is transformed by the first derivative, the correlation with the chlorophyll content of jujube leaves is significantly enhanced in some wavelength bands, among which it reaches a very significant positive correlation at 660, 685, 735, and 754 nm, and at 550, 588, 633, and 702 nm highly significant negative correlation. The maximum correlation

coefficients between the first-order derivative spectra and the SPAD value were −0.75 and 0.70 at 702 and 754 nm (Figure 6B), respectively. It is evident that the chlorophyll of jujube leaves strongly affects the first-order differential spectrum under the leaf mite infestation. The curve of the correlation coefficient between the first-order derivative spectrum and chlorophyll content fluctuates obviously. Considering that the spectral derivative enhances the slight change in the slope of the spectral curve, the reason for this change is related to the biochemical absorption characteristics of crops. It can be seen that the chlorophyll of jujube trees is damaged by the infection of leaf mites, and the first derivative spectrum has a strong sensitivity to the chlorophyll content of jujube. Consequently, hyperspectral remote sensing technology may be used to quantify the chlorophyll content of jujube under the stress of leaf mite infestation.

TABLE 3 Correlation between SPAD values of canopy leaves and vegetation index of jujube trees.

VI	Model	R^2	RMSE
NDVI	$y = 2.04x + 65.36$	0.668	1.062
RVI	$y = 18.14x + 101.76$	0.585	0.951
PhRI	$y = 15.61x + 94.95$	0.702	0.886
MCARI	$y = 2.0x + 65.3$	0.657	0.869
TCARI	$y = -0.53x + 80.20$	0.632	0.896
GI	$y = 2.74x + 72.55$	0.608	0.787

SPA feature band selection

Hyperspectral data are abundant in volume and wavelength information, but the correlation between wavelengths is excessively high and contains a substantial quantity of duplicated information,

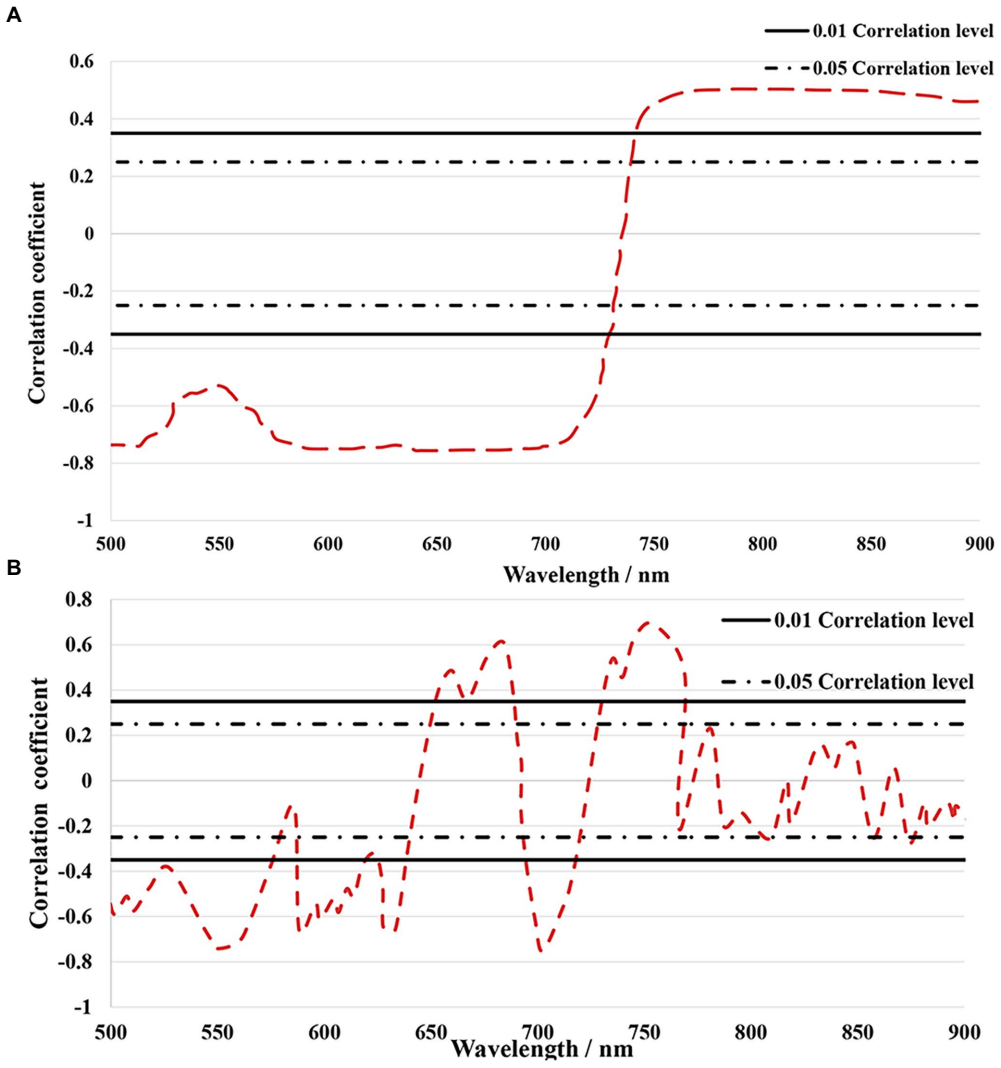

FIGURE 6
(A) Raw spectra with SPAD correlation analysis; (B) First-order derivative spectra with SPAD correlation analysis.

which poses a barrier to the storage and processing of huge amounts of data for practical applications (Liu et al., 2021). However, duplicate information in the spectral can be avoided by using a successive projection algorithm (SPA) for analysis to select the wavelengths of interest. The RMSE is calculated as the square root of the sum of the square of the departure of the observed value from the actual value divided by the number of observations and is used to assess the deviation between the observed and true values (de Sousa Fernandes et al., 2016). Given that the objective of feature wavelength extraction is to accurately categorize healthy and unhealthy plants, the fewest possible feature wavelengths should be used. In the present study, the RMSE decreased with an increase in the number of feature bands extracted (Figure 7A). The RMSE was smallest (0.451) with five feature wavelengths; the minimum RMSE value is attained when the number of bands contained in the corresponding optimal band set, which is the optimal subset of bands for the period, attains its minimum. Therefore, five characteristic wavelengths were chosen as the optimal outcome. The selected characteristic bands comprised 512.1, 628.8, 674.2, 736.6, and 773.2 nm (Figure 7B).

Model building and prediction

An ELM is a feed-forward neural network with a single or multiple hidden layers. Unlike in conventional neural networks with back propagation (BP), the parameters of the nodes in the hidden layers of ELM are randomly assigned and never tuned. It solves the shortcomings of classic neural networks, such as sluggish training rate, local optimum instability, and sensitivity to learning rate (Li W. et al., 2020). However, the conventional ELM architecture is considered to have drawbacks (Zhang et al., 2022), such as the unpredictability of weights and thresholds, and the uncertainty of network parameters, which make it less effective at processing data and result in overfitting phenomena that reduce the accuracy of the prediction model. To optimize the parameters, such as weights and thresholds, of the ELM model in order to increase the prediction accuracy of the model, PSO was implemented (Kaloop et al., 2019). The position and velocity of the particles were updated according to Equations (6), (7), the particle fitness value was recalculated, the individual extremes and population extremes were determined with each update, and iterations were repeated in order to conduct an optimization search in the solution space.

$$V_{kd}(t+1) = \omega V_{kd} + c_1 r_1 \left[Pbest_{kd}(t) - X_{kd}(t) \right] + c_2 r_2 \left[Gbest_{kd}(t) - X_{kd}(t) \right] \tag{6}$$

$$X_{kd}(t+1) = X_{kd}(t) + V_{kd}(t+1) \tag{7}$$

where $V_{kd}(t+1)$ is the velocity of particle k in the d th dimension in the $t+1$ th iteration; ω is the inertia weight, generally taken to be 0.9; c_1 and c_2 are learning factors; r_1 and r_2 are random numbers in the range [0, 1]; and $Pbest_{kd}(t)$ and $Gbest_{kd}(t)$ denote the extreme positions of particle k in the individual and the population.

In the present study, PSO was used to improve the input weights and thresholds of the ELM model, and each particle may be considered to be an ELM model for the prediction of chlorophyll content. The location information of the particles is utilized to represent the input weights and thresholds of the ELM model (as shown in Figure 8), whereas the particle dimension D and the kth particle k are represented as follows:

$$D = t(n+1) \tag{8}$$

$$\theta^k = \begin{bmatrix} \omega_{11}^k, \omega_{12}^k, \cdots \omega_{1t}^k, \omega_{21}^k, \omega_{22}^k, \cdots \omega_{2t}^k, \cdots, \\ \omega_{n1}^k, \omega_{n2}^k, \cdots \omega_{nt}^k, b_1^k, b_2^k, \cdots b_t^k \end{bmatrix} \tag{9}$$

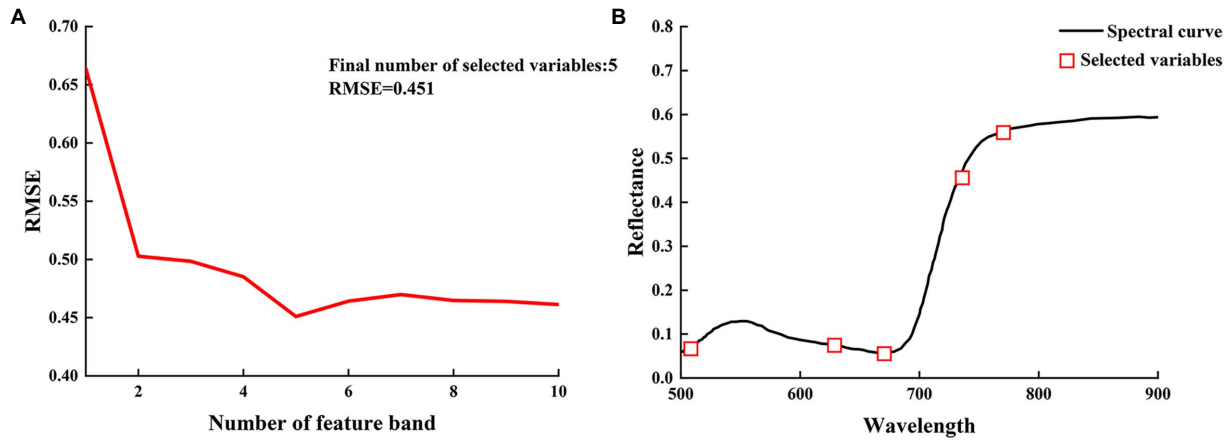

FIGURE 7
(A) Number of the best spectral variable for sample model; (B) Selection of characteristic hyperspectral bands.

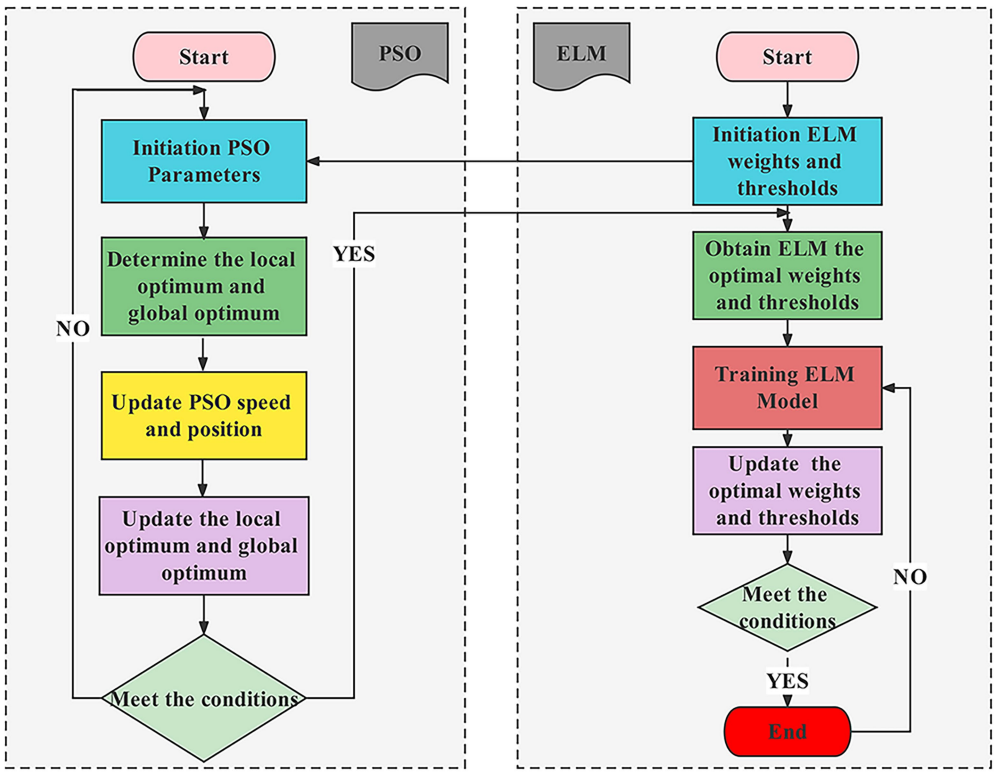

FIGURE 8
Flow chart of the PSO-ELM algorithm.

where n and t are the number of neurons in the input and hidden layers, respectively; ω_{ij}^{k} and b_{j}^{k} are the input weights and hidden layer thresholds, respectively, and both are random numbers within the range [−1, 1], $1 < i < n$, and $1 < j < t$.

The PSO-ELM employs the SPA extracted characteristic bands as the independent variable and the leaf chlorophyll content of the jujube canopy as the dependent variable. Initially, the PSO parameters were initialized and the ideal fitness function value was chosen based on the performance of the PSO-ELM model. The inertia weights were set to 0.90, the maximum number of iterations was set to 100, and the learning factors were set to 1.40. Subsequently, the input weights and thresholds corresponding to each particle were substituted into the ELM model, and the predicted and measured values of RMSE were used for adaptation of the PSO to calculate the individual and global extremes. Lastly, the particle positions and velocities were updated by iterative comparison, and the particle adaptation values were calculated, and the particle extremes and global extremes were updated until the minimum error was achieved or until the maximum number of iterations was attained.

Using the 512.1, 628.8, 674.2, 736.6, and 773.2 nm bands as independent variables and the chlorophyll content as a dependent variable with ELM and PSO-ELM, respectively, the SPA method was utilized to create models for prediction of the chlorophyll content of jujube trees (as shown in Figure 9). The unoptimized ELM and PSO-ELM prediction values were utilized to compare and evaluate the actual measured data in order to confirm the prediction accuracy of the suggested models. Table 4 shows the prediction results of the PSO-ELM inversion model of jujube tree chlorophyll content used in this study were superior to those of the inversion model built with the simple extreme learning method, and the PSO-ELM model of chlorophyll content inversion ($R^2 = 0.856$, RMSE = 0.796) was superior to that of the chlorophyll content inversion built with the single ELM ($R^2 = 0.748$, RMSE = 1.689).

Given that the absolute value of the correlation between reflectance and chlorophyll content in the 500–900 nm band is generally between 0.5 and 0.65, and that there is a connection between distinct bands in this range, extracting and establishing the chlorophyll content inversion is complicated. SPA is used in this study to extract the distinctive bands of chlorophyll content inversion in order to reduce the complexity of spectral data. The number of bands is decreased to 5 after screening the contribution value, and the spectral wavenumber is lowered by 88.89%. The RMSE is 0.451. The correlation coefficients for the ELM and PSO-ELM inversion models were found to be 0.748 and 0.856, respectively. The preferential selection of five feature band

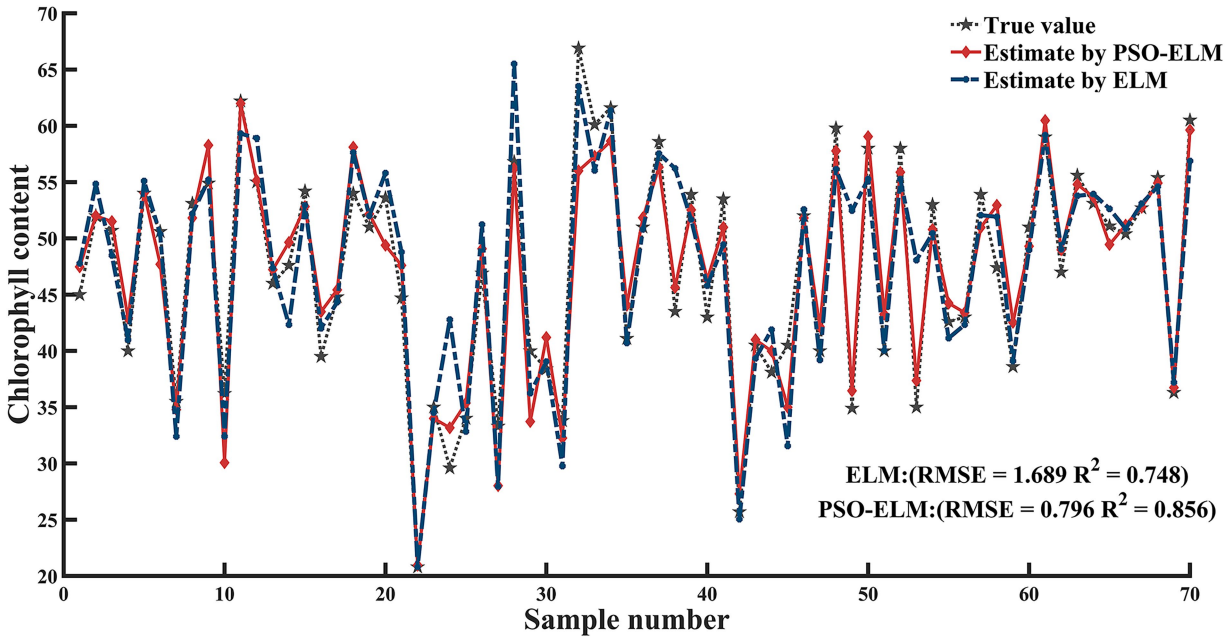

FIGURE 9
ELM and PSO-ELM models Chlorophyll content inversion model.

TABLE 4 Model comparison.

Model	Modeling set		Validation set	
	R^2	RMSE	R^2	RMSE
ELM	0.748	1.689	0.681	1.566
PSO-ELM	0.856	0.796	0.825	0.862

parameters of SPA reduces the problem of redundancy among spectral data, improves modeling efficiency and operational efficiency, and reduces the effect of covariance of input data parameters, indicating that SPA is a more effective method for feature wavelength extraction. The sensitive bands of chlorophyll content response of jujube were selected by using SPA, and an extreme learning machine inversion model based on particle swarm optimization was established with a view to achieving rapid, accurate, and nondestructive diagnosis of canopy chlorophyll content under leaf mite infestation and improving inversion accuracy.

The spatial distribution of jujube leaf mites in the research region was determined， using ArcGIS software based on the disease grading criteria for leaf mite severity (I–IV; as shown in Figure 10). The map displays the range of SPAD values that correlate to the severity of each mite infestation. While other portions of the plot were less damaged and could be mildly treated for prevention to fulfill the demands of normal jujube tree development, the left area of the plot required concentrated spraying of pesticides since it was more heavily infested. The results demonstrated that the outcomes of the ground survey and the UAV images are similar.

Discussion

Analysis of the correlation between spectral reflectance and chlorophyll content

Using hyperspectral spectra the benefit of "image-spectrum integration," we acquired hyperspectral images of the jujube tree, sought to inversion of chlorophyll content under the stress of leaf mite for jujube. Recent studies have focused greater attention on the spectral properties of crop diseases, and less on the physiological and biochemical alterations imposed by the diseases. The present results revealed that leaf mite infestation influences the spectral reflectance of the jujube tree canopy, and that SPAD values are strongly associated with the leaf mite infestation index. Given the relative decrease in chlorophyll content caused by insect damage, the spectral properties of jujube plants varied significantly with severity of insect damage. As the population of leaf mites peaks, the chlorophyll content in the leaves declines, resulting in a reduction in the photosynthetic activity of the leaves and a considerable decrease in spectral reflectance. The "white patches" or yellowing of branches caused by mite feeding on the leaves decreased the leaf area index and leaf chlorophyll content of jujube. In addition, it was demonstrated that crop pests and chlorophyll are strongly associated, and that spectral data can reflect changes in chlorophyll content caused by agricultural pests. Future work will focus on transferring such an integrative methodology presented here to other agronomic parameters estimation.

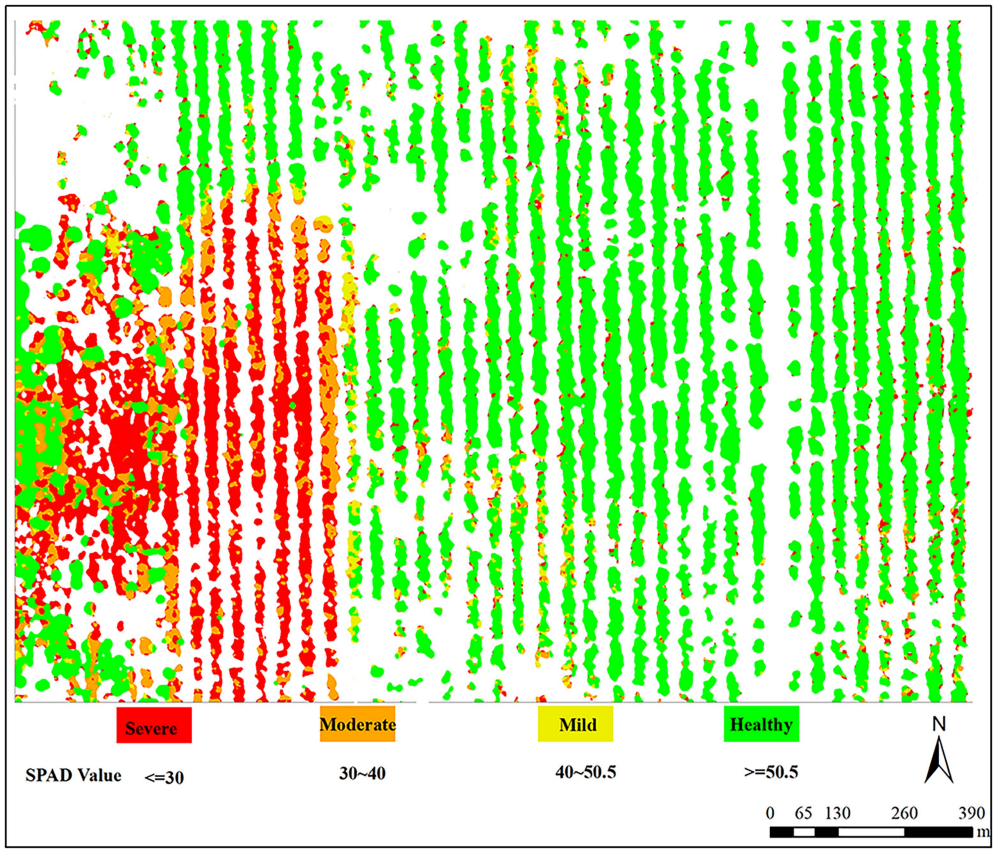

FIGURE 10
Inversion spatial distribution map of infestation severity of jujube mites.

Spectral-based inversion model of chlorophyll content

In recent years, the link between reflectance spectral characteristics and pest parameters has been investigated using spectral data, and the sensitive wavebands following pest damage have been screened to enable pest monitoring and identification by classification. In the present study, we estimated the relative chlorophyll content of jujube trees under leaf mite infestation using UAV hyperspectral inversion and proposed a model for prediction of the chlorophyll content of jujube using PSO-ELM. The influence of random parameters of the ELM model on prediction accuracy and its weak generalization performance were effectively compensated. In addition, the inversion accuracy of jujube tree chlorophyll content was improved. The present results serve as a reference for the utility of UAV remote sensing for diagnosis and monitoring of leaf mite infestation in jujube.

Challenges and prospective research

Collaborative "air–sky–ground" building of pest and disease monitoring research. In studies utilizing UAV remote sensing to monitor crop development, pests, and diseases, the determination coefficients (inversion accuracy) of the parameter inversion findings are typically greater than those of satellite remote sensing (Adao et al., 2017). However, the essential research methodologies and fundamental concepts of both are identical or comparable (Aasen et al., 2018). The essence of the higher inversion accuracy of UAV remote sensing is as follows. First, given the lower altitude of aerial photography, the distance to the crop canopy is shorter, hence there is less distortion and sensitivity of the acquired information (e.g., image texture features, spectral features, and thermal radiation features), which more accurately reflect small changes in the crop phenotypes. Second, the small spatial scale of UAV remote sensing not only objectively excludes heterogeneous factors (such as climate variation, soil conditions, moisture conditions, crop varieties, pest and disease stress, and human management practices) that affect the inversion of crop growth, pests, and diseases at medium and large scales, but also allows for the precise control of variable factors required for the experiment. However, this advantage of UAV remote sensing is also a constraint to its application (Delavarpour et al., 2021; Wang et al., 2022). Although the combination of ground-based data with UAV remote sensing data may provide point-to-point inversion of crop growth, pests, and diseases, a number of

limitations remain. The geographical extent is confined to the field size, and the consequent localization and individual variability in crop phenotypes limit the portability of monitoring models based on UAV remote sensing (Rezwan and Choi, 2022), so it is impossible to duplicate the inversion laws observed at larger scales or other sites. It is challenging to overcome regional disparities in numerous elements, such as crop types, natural environmental conditions, and human management practices, using satellite remote sensing (Messina and Modica, 2020; Zhou et al., 2020). It is also challenging for satellite remote sensing to overcome the impact of the diverse inversion influences on the inversion precision. Given the restricted geographical extent, UAV remote sensing is able to effectively screen diverse information. While employing satellite remote sensing techniques, we provide UAV remote sensing data as a crucial correction index for satellite remote sensing inversion agricultural growth, pest and disease studies to aid in the development of crop models. This may provide jujube pests monitor new ideas for follow-up studies.

Conclusion

In this study, leaf mite damage was monitored using an UAV platform equipped with a hyperspectral sensor. By acquiring hyperspectral images of jujube orchards with varying severities of leaf mite infestation, hyperspectral inversion was investigated to assess the relative chlorophyll content of jujube trees under the stress of leaf mite infestation. The results confirmed that the SPAD values of jujube plants were negatively correlated with severity of leaf mite infestation and leaf damage. Significant spectral variation was observed, with SPAD values diminished in the green peaks and red troughs of the spectral band with an increase in the severity of leaf damage. The differences in spectral reflectance among leaf mite-infested jujube plants were more pronounced. A strong correlation was observed between the SPAD value of jujube trees and the original and first-order derivative spectral reflectance of the canopy of jujube trees infested with leaf mites. It is therefore possible to quantify the leaf chlorophyll content of jujube trees under the stress of leaf mite infestation using hyperspectral remote sensing, thus providing a theoretical foundation for monitoring leaf mite infestation of jujube trees using hyperspectral remote sensing. Five feature bands were extracted using SPA: 512.1, 628.8, 674.2, 736.6, and 773.2 nm. The PSO-ELM model was developed using the extracted characteristic bands as input variables and the chlorophyll content of jujube trees as the output variable. The superior performance of the PSO-optimized ELM model demonstrated the viability of UAV deployment to perform hyperspectral inversion of the chlorophyll content of jujube plants infested with leaf mites. Thus, the variation in leaf chlorophyll content may be utilized to examine the categorization of jujube plants by severity of leaf mite infestation based on the variation in spectral characteristics.

Data availability statement

The original contributions presented in the study are included in the article/Supplementary material, further inquiries can be directed to the corresponding author.

Author contributions

HQ conceptualized the experiment, selected the algorithms, collected and analyzed the data, and wrote the manuscript. JM, YW, and WC trained the algorithms. HN, ZW, and PW collected and analyzed data, and wrote the manuscript. QZ, JL, and YL supervised the project. All authors contributed to the article and approved the submitted version.

Funding

This study was supported by Laboratory of Lingnan Modern Agriculture Project (NT2021009), Basic and Applied Basic Research Project of Guangzhou Basic Research Plan in 2022 (grant no. 202201010077), The 111 Project (D18019), Intelligent agriculture integration demonstration (Y951050), and Construction of Geological Big Data of Mountain-Building Zone Along the Silk Road (E2D6050100).

Acknowledgments

The authors wish to thank the Regiment 224 of the Xinjiang Production and Construction Corps 14th Division for the help in the collection of the ground data and field data.

Conflict of interest

The authors declare that the research was conducted in the absence of any commercial or financial relationships that could be construed as a potential conflict of interest.

Publisher's note

Supplementary material

The Supplementary material for this article can be found online at: https://www.frontiersin.org/articles/10.3389/fpls.2022.1009630/full#supplementary-material

References

Aasen, H., Honkavaara, E., Lucieer, A., and Zarco-Tejada, P. J. (2018). Quantitative remote sensing at ultra-high resolution with UAV spectroscopy: a review of sensor technology, measurement procedures, and data correction workflows. *Remote Sens.* 10:1091. doi: 10.3390/rs10071091

Adao, T., Hruska, J., Padua, L., Bessa, J., Peres, E., Morais, R., et al. (2017). Hyperspectral imaging: a review on UAV-based sensors, data processing and applications for agriculture and forestry. *Remote Sens.* 9:1110. doi: 10.3390/rs9111110

Ahmad, M. N., Shariff, A. R. M., and Moslim, R. (2018). Monitoring insect pest infestation via different spectroscopic techniques. *Appl. Spectrosc. Rev.* 53, 836–853. doi: 10.1080/05704928.2018.1445094

Ashourloo, D., Mobasheri, M. R., and Huete, A. (2014). Developing two spectral disease indices for detection of wheat leaf rust (Pucciniatriticina). *Remote Sens.* 6, 4723–4740. doi: 10.3390/rs6064723

Bai, T. C., Wang, T., Zhang, N. N., Chen, Y. Q., and Mercatoris, B. (2020). Growth simulation and yield prediction for perennial jujube fruit tree by integrating age into the WOFOST model. *J. Integr. Agric.* 19, 721–734. doi: 10.1016/s2095-3119(19)62753-x

Bai, T. C., Zhang, N., Mercatoris, B., and Chen, Y. Q. (2019). Jujube yield prediction method combining Landsat 8 vegetation index and the phenological length. *Comput. Electron. Agric.* 162, 1011–1027. doi: 10.1016/j.compag.2019.05.035

Bendig, J., Yu, K., Aasen, H., Bolten, A., Bennertz, S., Broscheit, J., et al. (2015). Combining UAV-based plant height from crop surface models, visible, and near infrared vegetation indices for biomass monitoring in barley. *Int. J. Appl. Earth Obs. Geoinf.* 39, 79–87. doi: 10.1016/j.jag.2015.02.012

Birth, G. S., and McVey, G. R. (1968). Measuring the color of growing turf with a reflectance spectrophotometer 1. *Agron. J.* 60, 640–643. doi: 10.2134/agronj1968.00021962006000060016x

Daughtry, C. S. T., Walthall, C. L., Kim, M. S., de Colstoun, E. B., and McMurtrey, J. E. (2000). Estimating corn leaf chlorophyll concentration from leaf and canopy reflectance. *Remote Sens. Environ.* 74, 229–239. doi: 10.1016/S0034-4257(00)00113-9

de Sousa Fernandes, D. D., Almeida, V. E., Pinto, L., Veras, G., Harrop Galvao, R. K., Gomes, A. A., et al. (2016). The successive projections algorithm for interval selection in partial least squares discriminant analysis. *Anal. Methods* 8, 7522–7530. doi: 10.1039/c6ay01840h

Dehkordi, R. H., El Jarroudi, M., Kouadio, L., Meersmans, J., and Beyer, M. (2020). Monitoring wheat leaf rust and stripe rust in winter wheat using high-resolution UAV-based red-green-blue imagery. *Remote Sens.* 12:18. doi: 10.3390/rs12223696

Delavarpour, N., Koparan, C., Nowatzki, J., Bajwa, S., and Sun, X. (2021). A technical study on UAV characteristics for precision agriculture applications and associated practical challenges. *Remote Sens.* 13:1204. doi: 10.3390/rs13061204

Deng, X., Tong, Z., Lan, Y., and Huang, Z. (2020). Detection and location of dead trees with pine wilt disease based on deep learning and UAV remote sensing. *AgriEngineering* 2, 294–307. doi: 10.3390/agriengineering2020019

Deng, X. L., Zhu, Z. H., Yang, J. C., Zheng, Z., Huang, Z. X., Yin, X. B., et al. (2020). Detection of citrus Huanglongbing based on multi-input neural network model of UAV Hyperspectral remote sensing. *Remote Sens.* 12:2678. doi: 10.3390/rs12172678

Garcia-Ruiz, F., Sankaran, S., Maja, J. M., Lee, W. S., Rasmussen, J., and Ehsani, R. (2013). Comparison of two aerial imaging platforms for identification of Huanglongbing-infected citrus trees. *Comput. Electron. Agric.* 91, 106–115. doi: 10.1016/j.compag.2012.12.002

Guo, A. T., Huang, W. J., Dong, Y. Y., Ye, H. C., Ma, H. Q., Liu, B., et al. (2021). Wheat yellow rust detection using UAV-based Hyperspectral technology. *Remote Sens.* 13:22. doi: 10.3390/rs13010123

Haboudane, D., Miller, J. R., Tremblay, N., Zarco-Tejada, P. J., and Dextraze, L. (2002). Integrated narrow-band vegetation indices for prediction of crop chlorophyll content for application to precision agriculture. *Remote Sens. Environ.* 81, 416–426. doi: 10.1016/s0034-4257(02)00018-4

Han, X., Wei, Z., Chen, H., Zhang, B. Z., Li, Y. N., and Du, T. S. (2021). Inversion of winter wheat growth parameters and yield under different water treatments based on UAV multispectral remote sensing. *Front. Plant Sci.* 12:13. doi: 10.3389/fpls.2021.609876

Hunt, E. R., Doraiswamy, P. C., McMurtrey, J. E., Daughtry, C. S. T., Perry, E. M., and Akhmedov, B. (2013). A visible band index for remote sensing leaf chlorophyll content at the canopy scale. *Int. J. Appl. Earth Obs. Geoinf.* 21, 103–112. doi: 10.1016/j.jag.2012.07.020

Ji, Z. L., Pan, Y. Z., Zhu, X. F., Wang, J. Y., and Li, Q. N. (2021). Prediction of crop yield using Phenological information extracted from remote sensing vegetation index. *Sensors* 21:16. doi: 10.3390/s21041406

Jiang, Y. F., Zhang, L., Yan, M., Qi, J. G., Fu, T. M., Fan, S. X., et al. (2021). High-resolution mangrove forests classification with machine learning using worldview and UAV Hyperspectral data. *Remote Sens.* 13:21. doi: 10.3390/rs13081529

Kaivosoja, J., Hautsalo, J., Heikkinen, J., Hiltunen, L., Ruuttunen, P., Nasi, R., et al. (2021). Reference measurements in developing UAV Systems for Detecting Pests, weeds, and diseases. *Remote Sens.* 13:1238. doi: 10.3390/rs13071238

Kaloop, M. R., Kumar, D., Samui, P., Gabr, A. R., Hu, J. W., Jin, X., et al. (2019). Particle swarm optimization algorithm-extreme learning machine (PSO-ELM) model for predicting resilient modulus of stabilized aggregate bases. *Appl. Sci.-Basel* 9:3221. doi: 10.3390/app9163221

Lei, S. H., Luo, J. B., Tao, X. J., and Qiu, Z. X. (2021). Remote sensing detecting of yellow leaf disease of Arecanut based on UAV multisource sensors. *Remote Sens.* 13:22. doi: 10.3390/rs13224562

Li, W., Li, B., Guo, H. L., Fang, Y. X., Qiao, F. J., and Zhou, S. W. (2020). The ECG Signal Classification Based On Ensemble Learning Of PSO-ELM algorithm. *Neural Network World* 30, 265–279. doi: 10.14311/nnw.2020.30.018

Li, H., Li, Q., Wang, D., Liu, J., Zhang, J., and Lu, Y. (2020). Effect of a cotton intercrop on spider mite populations in jujube trees. *J. Asia Pac. Entomol.* 23, 167–171. doi: 10.1016/j.aspen.2019.12.004

Li, X. R., Yang, C. H., Zhang, H. R., Wang, P. P., Tang, J., Tian, Y. Q., et al. (2021). Identification of abandoned jujube fields using multi-temporal high-resolution imagery and machine learning. *Remote Sens.* 13:19. doi: 10.3390/rs13040801

Liu, L. Y., Dong, Y. Y., Huang, W. J., Du, X. P., and Ma, H. Q. (2020). Monitoring wheat Fusarium head blight using unmanned aerial vehicle Hyperspectral imagery. *Remote Sens.* 12:19. doi: 10.3390/rs12223811

Liu, W.-Y., Peng, J., Dou, Z.-J., Chen, B., Wang, J.-Q., Xiang, H.-Y., et al. (2017). Estimation models for jujube leaf pigment concentration with Hyperspectrum data at canopy scale. *Spectrosc. Spectr. Anal.* 37, 156–161. doi: 10.3964/j.issn.1000-0593(2017)01-0156-06

Liu, J., Xie, J., Meng, T., and Dong, H. (2021). Organic matter estimation of surface soil using successive projection algorithm. *Agron. J.* 114, 1944–1951. doi: 10.1002/agj2.20934

Liu, Y. B., Zhang, L. L., and Liu, Q. Z. (2015). Changes of nematode community under monoculture wheat and wheat/jujube intercropping system in Xinjiang, Northwest China. *Helminthologia* 52, 123–129. doi: 10.1515/helmin-2015-0022

Mahlein, A.-K., Rumpf, T., Welke, P., Dehne, H.-W., Plümer, L., Steiner, U., et al. (2013). Development of spectral indices for detecting and identifying plant diseases. *Remote Sens. Environ.* 128, 21–30. doi: 10.1016/j.rse.2012.09.019

Messina, G., and Modica, G. (2020). Applications of UAV thermal imagery in precision agriculture: state of the art and future research outlook. *Remote Sens.* 12:1491. doi: 10.3390/rs12091491

Qi, S., Quanjun, J., Xiaojin, Q., Liangyun, L., Xinjie, L., and Huayang, D. (2021). Improving the retrieval of crop canopy chlorophyll content using vegetation index combinations. *Remote Sens.* 13:470. doi: 10.3390/rs13030470

Qin, J., Wang, B., Wu, Y., Lu, Q., and Zhu, H. (2021). Identifying pine wood nematode disease using UAV images and deep learning algorithms. *Remote Sens.* 13:162. doi: 10.3390/rs13020162

Rezwan, S., and Choi, W. (2022). Artificial intelligence approaches for UAV navigation: recent advances and future challenges. *IEEE Access* 10, 26320–26339. doi: 10.1109/access.2022.3157626

Sun, Q., Jiao, Q. J., Liu, L. Y., Liu, X. J., Qian, X. J., Zhang, X., et al. (2021). Improving the retrieval of Forest canopy chlorophyll content from MERIS dataset by introducing the vegetation clumping index. *IEEE J. Sel. Top. Appl. Earth Observations Remote Sen.* 14, 5515–5528. doi: 10.1109/jstars.2021.3082621

Sun, J., Yang, L., Yang, X., Wei, J., Li, L., Guo, E., et al. (2021). Using spectral reflectance to estimate the leaf chlorophyll content of maize inoculated with Arbuscular Mycorrhizal fungi under water stress. *Front. Plant Sci.* 12:646173. doi: 10.3389/fpls.2021.646173

Torres-Sanchez, J., Pena, J. M., de Castro, A. I., and Lopez-Granados, F. (2014). Multi-temporal mapping of the vegetation fraction in early-season wheat fields using images from UAV. *Comput. Electron. Agric.* 103, 104–113. doi: 10.1016/j.compag.2014.02.009

Vanegas, F., Bratanov, D., Powell, K., Weiss, J., and Gonzalez, F. (2018). A novel methodology for improving plant Pest surveillance in vineyards and crops using UAV-based Hyperspectral and spatial data. *Sensors* 18:260. doi: 10.3390/s18010260

Wang, J., Jiang, C., and Kuang, L. (2022). High-mobility satellite-UAV communications: challenges, solutions, and future research trends. *IEEE Commun. Mag.* 60, 38–43. doi: 10.1109/mcom.001.2100850

Wang, J., Jing, Y. S., Huang, W. J., Zhang, J. C., Zhao, J., Zhang, Q., et al. (2015). Comparative research on estimating the severity of yellow rust in winter wheat.

Spectrosc. Spectr. Anal. 35, 1649–1653. doi: 10.3964/j.issn.1000-0593(2015)06-1649-05

Xia, L., Zhang, R., Chen, L., Li, L., Yi, T., Wen, Y., et al. (2021). Evaluation of deep learning segmentation models for detection of pine wilt disease in unmanned aerial vehicle images. *Remote Sens.* 13:3594. doi: 10.3390/rs13183594

Xu, Z., Zhang, Q., Xiang, S., Li, Y., Huang, X., Zhang, Y., et al. (2022). Monitoring the severity of Pantana phyllostachysae Chao infestation in Moso bamboo forests based on UAV multi-spectral remote sensing feature selection. *Forests* 13:418. doi: 10.3390/f13030418

Yang, M., Gao, P., Zhou, P., Xie, J., Sun, D., Han, X., et al. (2021). Simulating canopy temperature using a random Forest model to calculate the crop water stress index of Chinese brassica. *Agronomy-Basel* 11:2244. doi: 10.3390/agronomy11112244

You, J., Zhang, R. R., and Lee, J. (2022). A deep learning-based generalized system for detecting pine wilt disease using RGB-based UAV images. *Remote Sens.* 14:20. doi: 10.3390/rs14010150

Zhang, J. J., Cheng, T., Guo, W., Xu, X., Qiao, H. B., Xie, Y. M., et al. (2021). Leaf area index estimation model for UAV image hyperspectral data based on wavelength variable selection and machine learning methods. *Plant Methods* 17:49. doi: 10.1186/s13007-021-00750-5

Zhang, M. Z., Su, W., Fu, Y. T., Zhu, D. H., Xue, J. H., Huang, J. X., et al. (2019). Super-resolution enhancement of Sentinel-2 image for retrieving LAI and chlorophyll content of summer corn. *Eur. J. Agron.* 111:125938. doi: 10.1016/j.eja.2019.125938

Zhang, W., Teng, G., and Wang, C. (2013). Identification of jujube trees diseases using neural network. *Optik* 124, 1034–1037. doi: 10.1016/j.ijleo.2013.01.014

Zhang, X., Zhao, D., Wang, T., Wu, X., and Duan, B. (2022). A novel rainfall prediction model based on CEEMDAN-PSO-ELM coupled model. *Water Supply* 22, 4531–4543. doi: 10.2166/ws.2022.115

Zhou, Y., Rao, B., and Wang, W. (2020). UAV swarm intelligence: recent advances and future trends. *IEEE Access* 8, 183856–183878. doi: 10.1109/access.2020.3028865

frontiers | Frontiers in Plant Science

TYPE Original Research
PUBLISHED 20 October 2022
DOI 10.3389/fpls.2022.1040923

OPEN ACCESS

EDITED BY
Ruirui Zhang,
Beijing Academy of Agricultural and Forestry Sciences, China

REVIEWED BY
Longzhe Quan,
Anhui Agricultural University, China
Qinghui Lai,
Kunming University of Science and Technology, China

*CORRESPONDENCE
Huiming Zhang
994330@hainanu.edu.cn
Wei Fu
994026@hainanu.edu.cn

SPECIALTY SECTION
This article was submitted to Technical Advances in Plant Science, a section of the journal Frontiers in Plant Science

RECEIVED 09 September 2022
ACCEPTED 03 October 2022
PUBLISHED 20 October 2022

CITATION
Zhang B, Wang R, Zhang H, Yin C, Xia Y, Fu M and Fu W (2022) Dragon fruit detection in natural orchard environment by integrating lightweight network and attention mechanism. *Front. Plant Sci.* 13:1040923. doi: 10.3389/fpls.2022.1040923

Dragon fruit detection in natural orchard environment by integrating lightweight network and attention mechanism

Bin Zhang[1,2], Rongrong Wang[2], Huiming Zhang[1,2*], Chenghai Yin[3], Yuyang Xia[2], Meng Fu[2] and Wei Fu[1,2*]

[1]School of Information and Communication Engineering, Hainan University, Haikou, China, [2]Mechanical and Electrical Engineering College, Hainan University, Haikou, China, [3]College of Mechanical and Electrical Engineering, Shihezi University, Shihezi, China

An improved lightweight network (Improved YOLOv5s) was proposed based on YOLOv5s in this study to realise all-weather detection of dragon fruit in a complex orchard environment. A ghost module was introduced in the original YOLOv5s to realise the lightweight of the model. The coordinate attention mechanism was joined to make the model accurately locate and identify the dense dragon fruits. A bidirectional feature pyramid network was built to improve the detection effect of dragon fruit at different scales. SIoU loss function was adopted to improve the convergence speed during model training. The improved YOLOv5s model was used to detect a dragon fruit dataset collected in the natural environment. Results showed that the mean average precision (*mAP*), precision (*P*) and recall (*R*) of the model was 97.4%, 96.4% and 95.2%, respectively. The model size, parameters (Params) and floating-point operations (FLOPs) were 11.5 MB, 5.2 M and 11.4 G, respectively. Compared with the original YOLOv5s network, the model size, Params and FLOPs of the improved model was reduced by 20.6%, 18.75% and 27.8%, respectively. Meanwhile, the *mAP* of the improved model was improved by 1.1%. The results prove that the improved model had a more lightweight structure and better detection performance. Moreover, the average precision (*AP*) of the improved YOLOv5s for dragon fruit under the front light, back light, side light, cloudy day and night was 99.5%, 97.3%, 98.5%, 95.5% and 96.1%, respectively. The detection performance met the requirements of all-weather detection of dragon fruit and the improved model had good robustness. This study provides a theoretical basis and technical support for fruit monitoring based on unmanned aerial vehicle technology and intelligent picking based on picking robot technology.

KEYWORDS

dragon fruit, object detection, YOLOv5s, lightweight network, mechanism of attention

1 Introduction

People love Dragon fruit because of its high nutritional value, constipation prevention, detoxification, blood glucose reduction, antioxidants and other effects (Attar et al., 2022). The field management of this tropical fruit is labour-intensive. Thus, studying disease and pest monitoring for the fruit based on unmanned aerial vehicle (UAV) technology and intelligent picking based on picking robot technology is very important. Fruit and vegetable object detection in the natural orchard environment is a key technology for monitoring and picking fruit pests and diseases (Tang et al., 2020; Zheng et al., 2021). Given the complex environmental information, such as uneven light intensity and overlapping occlusion between branches and leaves and fruits in dragon fruit orchards (Jiang et al., 2012; Chu and Chang, 2020), studying a method that can accurately detect dragon fruit in complex environments for efficient and automatic all-weather fruit monitoring and picking of dragon fruit is of great research value and practical significance.

Researchers at home and abroad have recently achieved certain results in the field of fruit and vegetable object detection, and a variety of object detection methods proposed have been applied to fruit and vegetable detection tasks in natural scenarios (Behera et al., 2018; Jiang et al., 2019; He et al., 2020; Yu et al., 2021; Jiang et al., 2022). These methods are mainly based on traditional image processing methods and deep learning algorithms (Saleem et al., 2021). Traditional image processing methods are mainly based on the colour, shape and texture of fruits and vegetables, which have been widely used to recognise citrus (Kurtulmus et al., 2011; Lu et al., 2018), apple (Rakun et al., 2011; Linker et al., 2012; Sun et al., 2019), pineapple (Chaivivatrakul and Dailey, 2014) and mango (Payne et al., 2013). However, these methods have high environmental requirements. When the orchard light is uneven and occlusions are found between fruits, recognition accuracy is significantly reduced. With the rapid development of deep learning, a convolutional neural network (CNN) algorithm has been applied to fruit and vegetable object detection, achieving good results. Typical studies are as follows: Sun et al. (2018) proposed an improved Faster-RCNN for tomato recognition, which adopted ResNet50 as the feature extraction network and used the k-means clustering method to adjust the preselected box, effectively improving the recognition accuracy but slowing down the detection speed. Fu et al. (2020) used the Faster-RCNN to identify apples. Before model establishment, a depth filter was used to remove the background of fruit trees in the image, improving recognition accuracy by 2.5% compared with the original network model. Tian et al. (2019) proposed an improved YOLO-V3 model to detect apples at different growth stages in orchards, and the average time of detection model was 0.304 s for images with 3000×3000 resolution. Li et al. (2021) identified occlusion and small object green pepper based on the deep learning object detection algorithm of Yolov4-tiny combining the attention mechanism and multi-scale prediction. The average precision value of the model reached 95.11%, the accuracy rate was 96.91%, and the recall rate was 93.85%. Zhang et al. (2021) proposed a recognition and positioning method for cherry tomatoes based on a lightweight neural network improved YoloV4-Lite, and the recognition accuracy and *AP* were improved by 8.29% and 0.15%, respectively, compared with the original network model. Xiong et al. (2020) added residual network to YOLOv3 model for night citrus recognition, and the recognition accuracy and the recognition speed was increased by 2.27% and 26%, respectively, compared with the original network model. Cecotti et al. (2020) used transfer learning to pre-train the network and data enhancement to increase the number of samples. They also used a modified Resnet network to identify grapes and perform yield estimates, which achieved good accuracy. Giang et al. (2022) rapidly detected tomatoes based on semantic segmentation neural network of RGB-D image, and the detection accuracy rate was 80.2%. Huang et al. (2022) applied the YOLOv5 algorithm to detect the citrus data set collected by UAV, and the detection accuracy rate was 93.32%. Yan et al. (2021) proposed a lightweight apple object detection method using improved YOLOv5s to identify grasping and ungrasping apples in apple tree images automatically, and the recognition recall rate, accuracy, *AP* and F_1 were 91.48%, 83.83%, 86.75% and 87.49%, respectively. Zhang et al. (2022) applied the YOLOX object detection algorithm to carry out the counting detection of Holly fruit and tested the counting efficiency under different distances and scenarios. Zhou et al. (2022) proposed an enhanced YOLOX-s object detection algorithm. Compared with the original YOLOX-s, the enhanced model improved the detection *AP* of kiwifruit images by 6.52%, reduced the number of model parameters by 44.8% and upgraded the model detection speed by 63.9%. Miao et al. (2022) developed an efficient tomato picking robot based on traditional image processing methods and YOLOv5 object detection algorithm, which had high detection accuracy under different lighting conditions, with an average deviation of 2 mm and a picking time of 9 s/cluster. Wang et al. (2022) proposed an improved YOLOv4 model for pear detection in the natural environment. The *AP* of the model was 96.71%, the model size was reduced by approximately 80%, and the average detection speed was 0.027 s. Many researchers have researched fruit target detection based on CNN and achieved good results, but they mainly realised fruit detection under daytime conditions. During the growth of dragon fruits, supplemental light is carried out at night, providing an advantageous condition for the all-weather picking of dragon fruits. Few reports have focused on target detection for picking dragon fruits in all weather.

Thus, this study constructed a lightweight neural network model to reduce the size of the network model and improve the detection accuracy, which was used for the all-weather real-time detection task of dragon fruit picking robots in complex scenes.

The main innovations and contributions are summarised as follows:

1. To establish data sets of dragon fruits under different lighting conditions. Through data enhancement, the image dataset was diversified, and the anti-interference ability under complex conditions was enhanced.
2. The lightweight ghost module was adopted in the model, replacing the conventional convolution of the original YOLOv5s network by combining a small number of convolution kernels and linear change operations to achieve the lightweight improvement of the model. The coordinate attention mechanism (CAM) was added to the original YOLOv5s network to make the model more accurate in locating and identifying dense dragon fruit. The feature fusion of different scales was strengthened by constructing a bidirectional feature pyramid network (BiFPN). The SIoU loss function was used to replace the original loss function to improve the convergence speed during model training.

The rest of the paper was structurally organised as follows: The second section presents the data material, including dragon fruit growth characteristics, image acquisition and dataset construction. The third section introduces the improved YOLOv5s dragon fruit detection model, which mainly includes the lightweight improvement of the model, the introduction of CAM and BiFPN, and the improvement of the loss function. The fourth section introduces the training and testing of the model, including the training platform information, parameter setting of the training network and evaluation index. The fifth section presents the test results and discussion. The final section illustrates the conclusions and prospects of the study.

2 Data materials

2.1 Growth characteristics of dragon fruit

Dragon fruit is a plant of the cactus family. Its branches are mostly triangular, and its edge width is generally 3–8 cm. It has many branches and is mainly cultivated by dense trellis planting (Figure 1). As a typical tropical and subtropical fruit, the shape of dragon fruit is generally spherical, the length of the fruit is 7–12 cm, and the diameter of the fruit is 5–10 cm. Fruits of the dragon fruit are distributed on branches. Given that fruits are blocked by branches and overlap with each other, accurately identifying dragon fruit, counting and measuring production, monitoring fruit diseases and insect pests and accurately picking fruit using picking robots in the field are difficult.

2.2 Image acquisition

This study took the red dragon fruit cultivated by dense trellis planting in modern standard orchards as the research object. The dragon fruit images were collected from the dragon fruit planting base in Yazhou, Sanya City, Hainan Province (latitude: 18.20.45, longitude: 109.12.14). Nikon SLR cameras and intelligent mobile phones were used to collect images of dragon fruits. Multi-scale dragon images were acquired during the three periods of sunny day, cloudy day and night. In the

FIGURE 1
Planting pattern of dragon fruit.

shooting process, the operation process of the picking robot was simulated, and the shooting angle and distance were constantly changed. A total of 1987 images were collected. Among them, shooting conditions on sunny days included front light, side light and back light. The collected images included varying maturity, attitude, size, lighting, background and fruit overlap occlusion. The image resolution is 4,288×2,848 pixels, and the format is JPEG. Figure 2 shows the dragon fruit images collected under different lighting conditions.

2.3 Construction of data set

The collected data were clipped and compressed to 640×640 pixels to improve the training efficiency of the network model and shorten the training time in the training stage of the deep learning model. The LabelImg annotation tool was used to annotate the rectangular box of the dragon fruit in the image manually. During annotation, all mature dragon fruits fully exposed in the image were labelled in a rectangular frame, the exposed part of overlapping or occluded mature dragon fruits were labelled, and the mature dragon fruits with occlusion degrees less than 5% in the image were not labelled. A total of 1,987 images were labelled, and the number of labelled mature dragon fruits was 5,123. After annotation, the.xml file containing the ground truth was obtained. To avoid the phenomenon of sample imbalance and overfitting of model training, data enhancement technology was used to expand the size of dragon fruit data sets and improve the robustness and generalisation ability of the model. Under different lighting conditions, for the original dragon fruit images with obvious features, defocus blur, motion blur, pixelation and cloud were used to enrich the data features, increase the number of training data and reduce the unbalanced proportion of samples and the sensitivity of the model to the image to improve the model robustness. Table 1 shows the basic information of the specifically constructed dragon fruit data sets.

The constructed dragon fruit data sets were divided into the training and testing sets according to the ratio of 8:2, and the number of dragon fruit image samples in the train and test sets was 4,000 and 1,000, respectively. There were no duplicate images between the training set and testing set.

3 Improvement of detection model for dragon fruit based on YOLOv5s

3.1 The network structure of YOLOv5s

The network structure of the YOLOv5s model is a classical one-stage structure, as shown in Figure 3, which is composed of four parts: input, backbone, neck and prediction head. Mosaic data enhancement, adaptive anchor frame calculation, adaptive image scaling and other methods are used at the input. The backbone part integrates Conv, C3, SPPF and other feature extraction modules for feature extraction. The neck part adopts the PANet structure for multi-scale feature fusion to strengthen feature extraction and greatly improve the model effect. Compared with other Faster-RCNN, SSD and YOLO series models, this model has fewer parameters, a small weight file and the advantages of fast reasoning speed and high detection accuracy. Therefore, the detection model for dragon fruit was designed based on the YOLOv5s deep convolutional network, which was conducive to the embedded development of the dragon fruit picking robot vision system.

3.2 Improved YOLOv5s detection model for dragon fruit

Given the multi-scale and multi-mode characteristics of all-weather picking and recognition of dense trellis planting fruit in a natural environment, a lightweight neural network model with high recognition accuracy based on YOLOv5s network structure was proposed, which is suitable for all-weather real-time detection task of dragon fruit picking robot in complex scenes. Firstly, the lightweight ghost module was used to replace the conventional convolution of the original YOLOv5s backbone network by combining a small number of convolution kernels and linear change operations, which effectively realised the lightweight improvement of the YOLOv5s network model. Secondly, CAM was added to the original YOLOv5s network, which could capture the cross-channel information and the information of direction perception and position perception, so that the model could accurately locate and identify the dense dragon fruit. Thirdly, the PANet feature fusion network was

FIGURE 2
Dragon fruit images under different lighting conditions. **(A)** Front light. **(B)** Back light. **(C)** Side light. **(D)** Cloudy day. **(E)** Night.

TABLE 1 Basic information of dragon fruit data sets.

Category	Daytime					
	Sunny day			Cloudy day	Night	Sum
	Front light	Back light	Side light			
The number of original image	390	310	440	347	500	1987
The number of enhancement of data	1000	1000	1000	1000	1000	5000
The number of marked dragon fruit	2930	2814	3070	3035	2883	14732

improved, and the BiFPN was built to enhance the transmission of feature information between different network layers, realise two-way feature fusion of deep and shallow layers and improve the detection effect of dragon fruit at different scales. Finally, the SIoU loss function was used to replace the original loss function to improve the convergence speed of model training.

3.2.1 Network lightweight improvement

Ghost module is a method to realise a lightweight neural network (Han et al., 2020), which can make the deep neural network transplant the network to some mobile devices with relatively weak computing power on the basis of ensuring the performance ability of the algorithm. The overall direction is to reduce the number of network model Params and FLOPs.

As shown in Figure 4, the ghost module uses a simple linear operation Φ instead of the original convolution operation to generate ghost graphs. Suppose that the size of the input feature graph is h × w × c convolved with n sets of convolution kernels of size k×k, and the size of the output feature graph is h′×w′×n. In the ghost model, m groups of k×k kernels are convolved with input to generate the intrinsic graph intrinsic of m×h′×w′, after which the intrinsic graph is linearly transformed Φ to produce the Ghost graph, and intrinsic and ghost together are used as output. Compared with ordinary convolution, after the ghost module is adopted, the model acceleration ratio r_s and compression ratio r_c are obtained, as shown in Equations (1) and (2).

$$r_s = \frac{n \cdot h' \cdot w' \cdot c \cdot k \cdot k}{\frac{n}{s} \cdot h' \cdot w' \cdot c \cdot k \cdot k + (s-1) \cdot \frac{n}{s} \cdot h' \cdot w' \cdot c \cdot d \cdot d} \approx s \quad (1)$$

$$r_c = \frac{n \cdot c \cdot k \cdot k}{\frac{n}{s} \cdot c \cdot k \cdot k + (s-1) \cdot \frac{n}{s} \cdot c \cdot d \cdot d} \approx s \quad (2)$$

These equations reveal that, compared with ordinary convolution, the ghost module reduced the calculation amount and the number of parameters in the convolution process to a certain extent. A large number of Conv and C3 modules in the original YOLOv5 network model are found, resulting in a large calculation amount and parameter volume of the model. The lightweight improvement of the network model is completed by using the ghost module to replace the Conv modules of layers 1, 3, 5, 7, 10, 14, 18 and 21 of the original network model with GhostConv and the C3 modules of layers 2, 4, 6 and 8 with C3Ghost module for calculation.

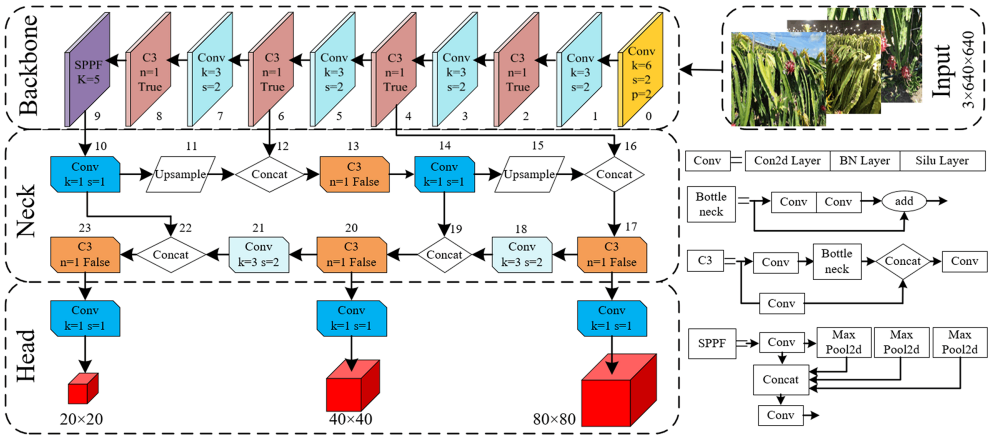

FIGURE 3
Network structure diagram of YOLO V5 model.

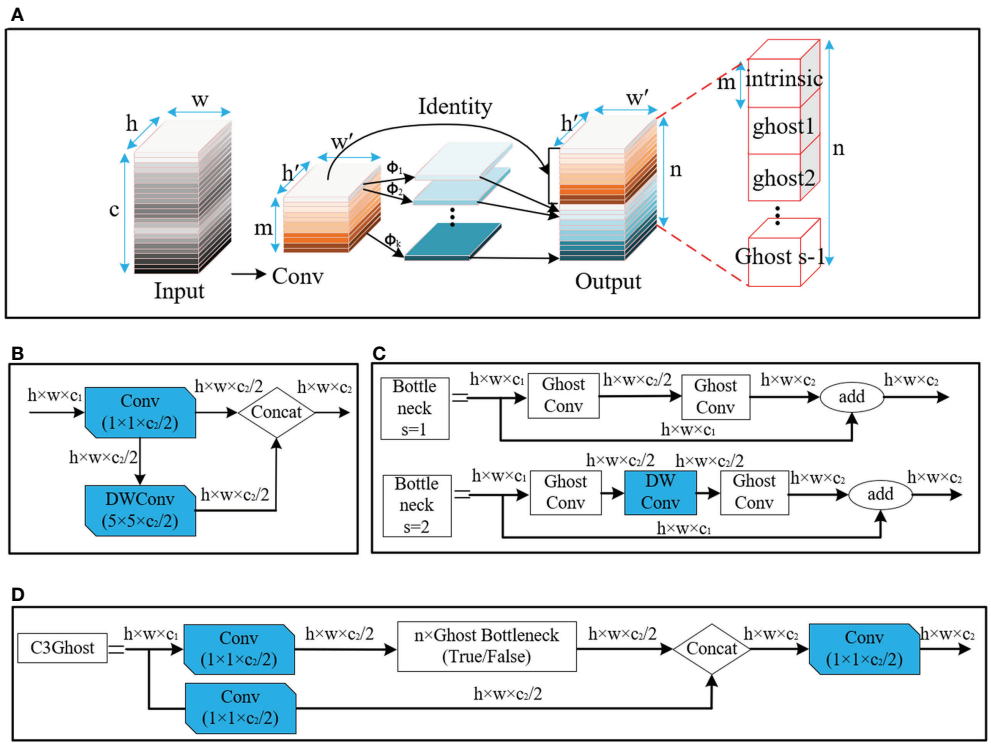

FIGURE 4
Structure of ghost. **(A)** Diagram of ghost module. **(B)** Ghost Conv. **(C)** GhostBottleneck. **(D)** C3 Ghost.

3.2.2 Coordinate attention mechanism (CAM)

The detection of small dense objects in densely planted dragon fruit orchards is easily influenced by different lighting conditions, especially in the night scene, when the detection is difficult. The original YOLOv5 network model easily loses the feature information of dense objects and small objects in the reasoning process, and the detection effect of small dense objects is poor. As shown in Figure 5, CAM is a novel mobile network attention mechanism proposed by embedding location information into channel attention (Hou et al., 2021). To alleviate the problem of location information loss caused by two-dimensional global pooling proposed by previous attention mechanisms, such as SENet (Hu et al., 2018) and CBAM (Woo et al., 2018), CAM decomposed channel attention into two one-dimensional feature coding processes, which aggregated features along two spatial directions respectively.

A CAM block can be viewed as a computational unit that can take any intermediate feature tensor $X=[x_1,x_2,\cdots,x_c]\in R^{C\times H\times W}$ as input and output with the same size as the intermediate feature tensor $Y=[y_1,y_2,\cdots,y_c]$. Meanwhile, it has the effect of enhancing representation.

Therefore, CAM was inserted in this study after layers 4, 6, 8, 9, 17, 20 and 23 of the original YOLOv5 network model. After data enhancement, the dragon fruit images entered the main network for feature extraction and then entered the neck part of the model through the CAM connected between the main part and the neck part (layers 4, 6 and 9 of the original network). In the neck part, the dragon fruit image feature fusion of different scales was carried out. Finally, CAM, after the 17th, 20th and 23rd layers of the original network, entered the prediction head part of the model, so that the network model can more accurately notice the dense small dragon fruit objects. It improved the detection ability of the network.

3.2.3 Construction of the bidirectional feature pyramid network (BiFPN)

The neck part of the original YOLOv5 network model uses PANet for multi-scale feature fusion, and the three effective feature layers of different scales obtained in the backbone part continue to extract features in the neck part. When fusing different input features, PANet adds the features without distinction. However, because these different input features have different resolutions, their contributions to the fused output features tend to be unequal. BiFPN is a new feature fusion method proposed by the Google Brain team, which realises the two-way fusion of top-down and bottom-up deep and shallow features and enhances the transmission of feature

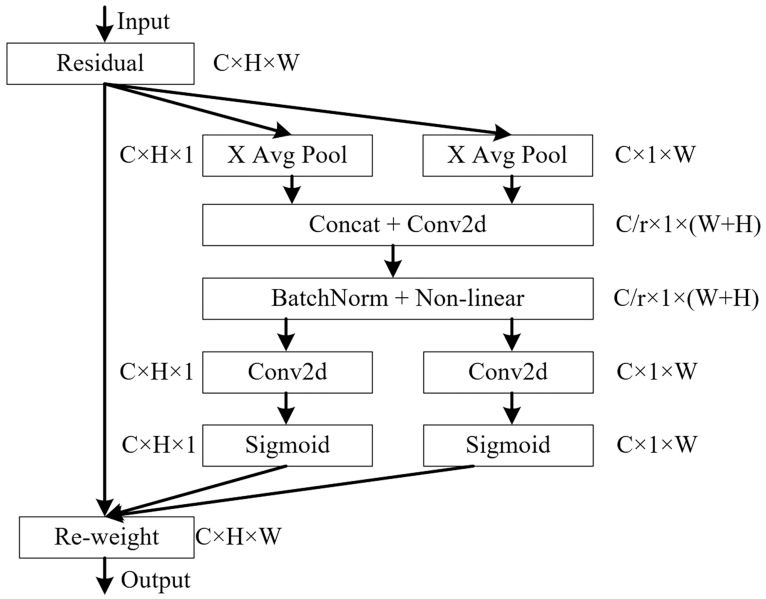

FIGURE 5
Structure diagram of Coordinate Attention module.

information between different network layers. The PANet and BiFPN structures are shown in Figure 6.

In this study, the PANet in YOLOv5 structure is replaced by BiFPN, and the Concat of layer 16, 20, 24 and 28 in the network structure is renamed as BiFPN_Concat. To fuse more image features without consuming more computational cost, the image features output from the 8th layer network were fused to the 24th layer network by concatenation, and the image features output from the 11th layer network are fused to the 28th layer network by concatenation, so as to achieve a higher level of feature fusion. BiFPN used the fast normalised fusion, which is normalised by dividing the use-right value by the sum of the ownership value. It normalises the weights to between 0 and 1 to improve the detection speed.

3.2.4 Improvement of loss function

The traditional object detection loss function relies on the aggregation of bounding box regression indicators, such as the distance, overlap region and aspect ratio of the predicted box and real box (i.e. GIoU, DIoU and CIoU). The original YOLOv5 network model used the CIoU loss function, but it did not consider that the situation of required direction does not match between the real box and predict box. It led to a slower and less efficient convergence of the network model during training. At the same time, the predicted box may "wander around" during training and produce worse models. To solve the above problems, SIoU loss function was used to replace the original loss function, which could introduce the vector angle between the real box and the predicted box (Gevorgyan, 2022). It includes four parts: angle cost, distance cost, shape cost and IoU cost.

Angle cost is shown in Equation (3). Figure 7 shows that, when α is $\pi/2$ or 0, the angle cost is 0. In the training process, if α is less than $\pi/4$, α is minimised; otherwise, β is minimised.

$$\Lambda = \cos[2 \times \sin^2(\arcsin\frac{c_h}{\sigma} - \frac{\pi}{4})] \tag{3}$$

Among them,

$$\sigma = \sqrt{(b_{c_x}^{gt} - b_{c_x})^2 + (b_{c_y}^{gt} - b_{c_y})^2} \tag{4}$$

$$c_h = \max(b_{c_y}^{gt}, b_{c_y}) - \min(b_{c_y}^{gt}, b_{c_y}) \tag{5}$$

where, c_h is the height difference between the centre points of the real box and the predicted box, σ is the distance between the centre points of the real box and the predicted box, $(b_{c_x}^{gt}, b_{c_y}^{gt})$ is the centre coordinates of the real box and (b_{c_x}, b_{c_y}) is the centre coordinates of the predicted box.

Distance cost Δ is shown in Equation (6),

$$\Delta = 2 - e^{-(2-\Lambda)(\frac{b_{c_x}^{gt} - b_{c_x}}{c_{w1}})^2} - e^{-(2-\Lambda)(\frac{b_{c_y}^{gt} - b_{c_y}}{c_{h1}})^2} \tag{6}$$

where, (c_{w1}, c_{h1}) is the width and height of the minimum outer rectangle of the real box and the predicted box.

The shape cost Ω is shown in Equation (7),

$$\Omega = (1 - e^{-\frac{|w - w^{gt}|}{\max(w, w^{gt})}})^{\theta} + (1 - e^{-\frac{|h - h^{gt}|}{\max(h, h^{gt})}})^{\theta} \tag{7}$$

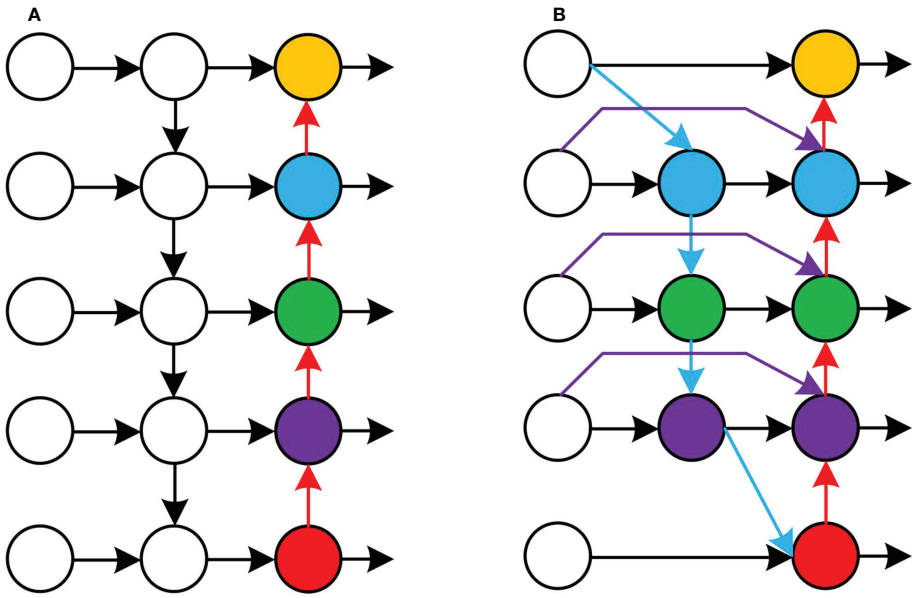

FIGURE 6
Structures of PANet and BiFPN. **(A)** Structure of PANet. **(B)** Structure of BiFPN.

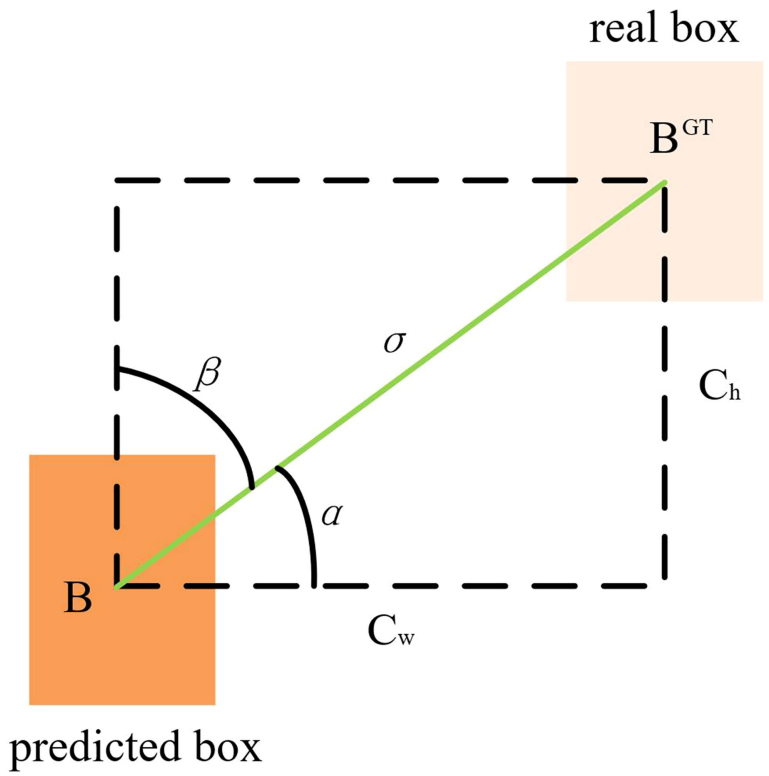

FIGURE 7
The scheme for calculating the contribution of the Angle cost to the loss function.

where, (w, h) is the width and height of the predicted box, (w^{gt}, h^{gt}) is the width and height of the real box and θ is the degree of attention to shape loss.

To sum up, the SIoU loss function is defined as Equation (8).

$$\text{Loss}_{\text{SIoU}} = 1 - \text{IoU} + \frac{\Delta + \Omega}{2} \tag{8}$$

3.2.5 Improved detection model for dragon fruit

The overall structure of the improved detection model network for dragon fruit is shown in Table 2. The from column in the table indicates which layer the input comes from, −1 represents the output from the previous layer, −2 represents the output from the upper layer. The params column represents the size of the argument, module is the name of the module, and the arguments are the information about the module argument, including the number of input channels and output channels, the size of the convolution kernel and the step size information.

4 Model training and testing

4.1 Training processing platform

This study built a deep learning framework based on PyTorch 1.7.1 to train and test the dragon fruit detection model. The relevant configurations of the test platform are as follows: Intel(R) Core(TM) i9-10900X CPU and NVIDIA

TABLE 2 The overall structure of the improved network.

Number	From	Params	Module	Arguments
0	-1	3520	Conv	[3, 32, 6, 2, 2]
1	-1	10144	Ghost Conv	[32, 64, 3, 2]
2	-1	12072	C3Ghost	[64, 64, 3]
3	-1	38720	Ghost Conv	[64, 128, 3, 2]
4	-1	47040	C3Ghost	[128, 128, 4]
5	-1	6704	CAM	[128, 128]
6	-2	151168	Ghost Conv	[128, 256, 3, 2]
7	-1	186976	C3Ghost	[256, 256, 5]
8	-1	13360	CAM	[256, 256]
9	-2	597248	Ghost Conv	[256, 512, 3, 2]
10	-1	679680	C3Ghost	[512, 512, 4]
11	-1	51296	CAM	[512, 512]
12	-1	656896	SPPF	[512, 512, 5]
13	-1	51296	CAM	[512, 512]
14	-1	69248	Ghost Conv	[512, 256, 1, 1]
15	-1	0	Upsample	[None, 2, 'nearest']
16	[-1,8]	2	BiFPN	[1]
17	-1	361984	C3	[512, 256, 1, False]
18	-1	18240	Ghost Conv	[256, 128, 1, 1]
19	-1	0	Upsample	[None, 2, 'nearest']
20	[-1,5]	2	BiFPN	[1]
21	-1	90886	C3	[256, 128, 1, False]
22	-1	6704	CAM	[128, 128]
23	-2	75584	Ghost Conv	[128, 128, 3, 2]
24	[-1,16,8]	3	BiFPN	[1]
25	-1	460288	C3	[896, 256, 1, False]
26	-1	13360	CAM	[256, 256]
27	-2	298624	Ghost Conv	[256, 256, 3, 2]
28	[-1,14,11]	3	BiFPN	[1]
29	-1	1444864	C3	[1024, 512, 1, False]
30	-1	51296	CAM	[512, 512]
31	[22,26,30]	26970	Detect	[nc, anchors]

GeForce RTX 3090 GPU (Dual Cards). The operating system is Windows 10. The acceleration environment is CUDA 11.3 and CUDNN 8.2.0. The development environment is PyCharm 2021.2.2 and Python 3.7. Other Python libraries are Numpy 1.21.6 and Opencv 4.6.0. The model input image size is 640×640 pixels. The training parameters are as follows: a batch size of 64, 300 training iterations, momentum of 0.937, initial learning rate of 0.001, attenuation coefficient of 0.9.

4.2 Evaluation indicators

This study used precision (*P*) to measure the accuracy of dragon fruit prediction. Recall (*R*) measures the detection of positive samples in all dragon fruit. Average precision (*AP*) measures the performance of the detector in each category. Mean average precision (*mAP*) is the average of all class *AP*s. *P*, *R*, *AP* and *mAP* are defined as (9)–(12). The complexity of the algorithm or model is measured by the number of parameters (Params) and floating-point operations (FLOPs).

$$P = \frac{\mathrm{TP}}{\mathrm{TP} + \mathrm{FP}} \times 100\,\% \tag{9}$$

$$R = \frac{\mathrm{TP}}{\mathrm{TP} + \mathrm{FN}} \times 100\,\% \tag{10}$$

$$AP = \int_0^1 P(R)dR \times 100\,\% \tag{11}$$

$$mAP = \frac{\sum_{i=1}^{k} AP}{k} \tag{12}$$

where, TP is the number of correctly predicted positive samples, TN is the number of correctly predicted negative samples, FP is the number of negative samples divided into positive samples, FP is the number of positive samples divided into negative samples, and *k* is the number of categories.

5 Results and discussion

The training process of the original YOLOv5s model and the improved YOLOv5s model used the same data set and the same parameters. According to the log files saved in the training process, the training loss curves of the two models were drawn, as shown in Figure 8.

Figure 8A is the positioning loss curve, which was used to represent the error between the predicted box and the labelled box. After 10 rounds of iteration, the decline rate of positioning loss value started to become gentle. After 200 rounds of iteration, the positioning error tended to the stable state. At this point, the localisation loss of the improved YOLOv5s model was reduced by 0.01 compared with the original YOLOv5s. The model's performance improved after the SIoU loss function was adopted. Figure 8B is the confidence loss curve, which calculates the network's confidence in the iterative process. The confidence loss curves of the two models were consistent before and after the improvement. Figure 8C is the classification loss curve, which is used to show whether the aiming frame and the corresponding calibration classification are correct. After 100 rounds of iteration, the classification error of the model tended to the stable state, where the classification error of the improved YOLOv5s model was significantly reduced compared with the original YOLOv5s. Figure 8 shows that, compared with the original YOLOv5s model, the improved YOLOv5s model has faster convergence and smaller loss value. The results showed that the convergence ability of the network was improved after modifying the original loss function.

5.1 Comparison of different algorithms

To compare the accuracy of different models in dragon fruit detection, eight representative network models of YOLOv3, YOLOv3-Tiny, YOLOv4-CSP, YOLOv4-Tiny, YOLOv5s, YOLOX-s, YOLOv7 and YOLOv7-Tiny, were selected to

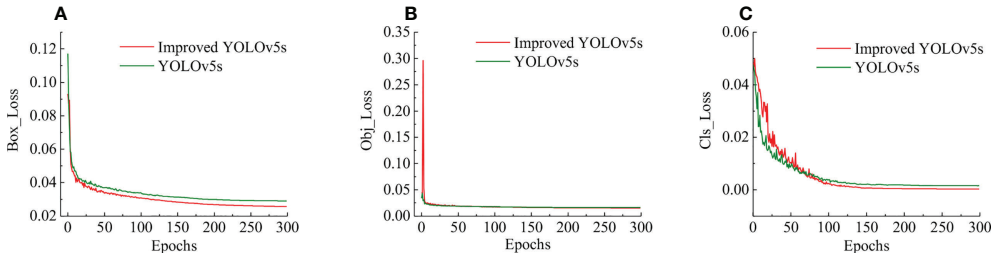

FIGURE 8
Comparison of Loss curves for model training. **(A)** The positioning loss curve. **(B)** The confidence loss curve. **(C)** The classification loss curve.

compare and test with the improved YOLOv5s. All models used the same data set of dragon fruit for training and testing. The value of *mAP*, *P*, *R*, model size, Params and FLOPs were selected as model evaluation indicators. Table 3 shows the detection results of dragon fruit for a different model.

Table 3 shows that, compared with YOLOv3, YOLOv3-Tiny, YOLOv4-CSP, YOLOv4-Tiny, YOLOv5s, YOLOX-s, YOLOv7 and YOLOv7-Tiny, the improved YOLOv5s model has the highest *P*, *R* and *mAP* values of 96.4%, 95.2% and 97.4%, respectively. The model size, Params and FLOPs of the Improved YOLOv5s were larger than those of YOLOV4-Tiny, but they were smaller than other networks, which were 11.5 MB, 5.2 M and 11.4 G, respectively. Compared with the above eight network models, *mAP* of the improved YOLOv5s model was enhanced by 0.3%, 2.1%, 3.1%, 4.5%, 1.1%, 3.9%, 1.8% and 1.4% respectively, *P* was improved by 0.4%, 3.4%, 4.8%, 4.1%, 1.7%, 6.3%, 2.5% and 5.6% respectively, and *R* was improved by 0.6%, 3.4%, 7.9%, 7.1%, 1.5%, 8.7%, 5.6% and 2.4%, respectively. Compared with the lightweight YOLOV3-Tiny, YOLOv5s, YOLOX-s and YOLOV7-Tiny, the model size was reduced by 34.3%, 20.69%, 66.5% and 6.5%, Params was reduced by 37.3%, 18.7%, 42.2%, 8.8%, respectively, FLOPs was reduced by 12.3%, 27.8%, 57.3% and 13.6%, respectively. The results showed that the improved YOLOv5s model ensured good detection accuracy and realised the lightweight improvement of the network model. The improved YOLOv5s model could be embedded into the vision system of the dragon fruit picking robot to realise the automatic picking operation of dragon fruits.

5.2 Analysis of ablation experiment results

The ablation experiment is to verify the optimisation effect of each improved module, and the experimental results are shown in Table 4. Improved model 1 represents the introduction of the ghost module in the original network. Improved model 2 represents the modification of the pyramid structure of the original network. Improved model 3 represents the addition of CAM in the original network. Improved model 4 represents the modification of the loss function. Improved model 5 represents the addition of all the above improvement methods in the original network.

Table 4 shows that, after the ghost module was used to lightweight the original YOLOv5s network structure, the Params was reduced by 28%, and the FLOPs was reduced by 34.8% compared with the original network model, but the *mAP* of the model increased by 0.4%. The main reason was that after the ghost module was used to replace the ordinary convolution in the original network, more feature maps were generated through linear operation, and this rich or even redundant information usually ensured a comprehensive understanding of the input dragon fruit features. Therefore, the lightweight network structure of the ghost module introduced into the original YOLOv5s network in this study could still ensure the detection accuracy of the model. When the CAM was added to the model, compared with the original model, the *mAP* of the model was improved by 0.5 percentage points, but the Params and the FLOPs of the model were increased by 2.4 M and 5.2 G, respectively. After replacing the PANet structure in the YOLOv5s network with BiFPN, the *mAP* of the model was improved by 0.9 percentage points, the Params and the FLOPs increased by 0.2 M and 0.7 G, respectively. After the loss function of the model was modified, the *mAP* of the model was improved by 0.5%. When these four improvements were combined into the model, compared with the original YOLOv5s network model, the *mAP* was increased by 1.1%, the Params was reduced by 18.7%, and the FLOPs was reduced by 27.8%. The results showed that improved YOLOv5s had better detection performance for dragon fruit objects, and the complexity of the model was reduced by using a lightweight module.

5.3 Analysis of detection results in different scenarios

To verify the feasibility of the improved YOLOv5s model, the dragon fruit images collected in different scenes were tested,

TABLE 3 Identification results of dragon fruit for different model.

Model	*mAP*/%	*P*/%	*R*/%	Model size/MB	Params/M	FLOPs/G
YOLOv3	97.1	96.0	94.6	123.6	58.7	155.3
YOLOv3-Tiny	95.3	93.0	91.8	17.5	8.3	13.0
YOLOv4-CSP	94.3	91.6	87.3	105.5	50.1	119.7
YOLOv4-Tiny	92.9	92.3	88.1	6.3	2.9	6.4
YOLOv5s	96.3	94.7	93.7	14.5	6.4	15.8
YOLOX-s	93.5	90.1	86.5	34.3	9.0	26.7
YOLOv7	95.6	93.9	89.6	74.9	35.5	105.2
YOLOv7-Tiny	96.0	90.8	92.8	12.3	5.7	13.2
Improved YOLOv5s	97.4	96.4	95.2	11.5	5.2	11.4

10.3389/fpls.2022.1040923

TABLE 4 Results of ablation experiment.

Model	Lightweight	Modifying the feature pyramid	Add attention mechanism	Modify the loss function	*mAP*/%	Params/M	FLOPs/G
YOLOv5s	×	×	×	×	96.3	6.4	15.8
Improved model 1	√	×	×	×	96.7	4.6	10.3
Improved model 2	×	√	×	×	97.2	6.8	16.2
Improved model 3	×	×	√	×	96.8	8.8	21.0
Improved model 4	×	×	×	√	96.8	6.4	15.8
Improved model 5	√	√	√	√	97.4	5.2	11.4

"√" Indicates that the current improvement method is used in the model, while "×" indicates that the current improvement method is not used in the model.

TABLE 5 Test results of dragon fruit recognition in different lighting scenes by the YOLOv5s model before and after improvement.

Model	*mAP*	*AP*				
		Front light	Back light	Side light	Cloudy day	Night
YOLOv5s	96.3	99.0	96.7	98.4	93.8	93.6
Improved YOLOv5s	97.4	99.5	97.3	98.5	95.5	96.1

including the scenes of front light, back light, side light, cloudy day and night. The results are shown in Table 5.

Table 5 shows that both models before and after improvement had the best recognition effect for dragon fruit in the scenes of the front light. The *AP* of the before and after improvement model in detecting dragon fruit under front light was 99.0% and 99.5%, respectively, and the *AP* of the improved model was improved by 0.5%. The *AP* of the before and after improvement model in detecting dragon under the backlight was 96.7% and 97.3%, respectively. The performance of the improved model was improved by 0.6%. The *AP* of the before and after improvement model in detecting dragon fruit under side light was 98.4% and 98.5%, respectively, and the performance of the improved model was improved by 0.1%. The *AP* of the model before and after the improvement under cloudy day was 93.8% and 95.5%, respectively, and the detection performance of the improved model was improved by 1.7%. The *AP* of the model before and after improvement at night is 93.6% and 96.1%, and the detection performance of the improved model is improved by 2.5%. According to Table 5, under different lighting conditions, the maximum deviation of the YOLOv5s model before improvement in detecting dragon fruit was 5.4%, and the maximum deviation after improvement was 3.4%, which was 2% lower than before the improvement. The improved model had the greatest improvement for the situation that was difficult to detect at night, indicating that the improved model was more robust to all-weather dragon fruit detection.

TABLE 6 Visual results of dragon fruit object detection on sunny days.

Front light	The original image	Visual result of YOLOv5s		Visual result of Improved YOLOv5s	
Single fruit big object			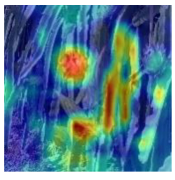		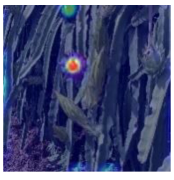
Many fruits in the goal			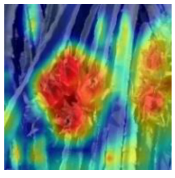		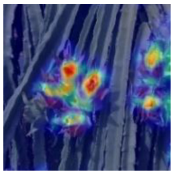

(Continued)

10.3389/fpls.2022.1040923

TABLE 6 Continued

Front light	The original image	Visual result of YOLOv5s		Visual result of Improved YOLOv5s	
Dense small object			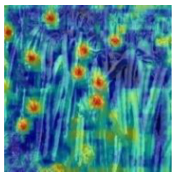		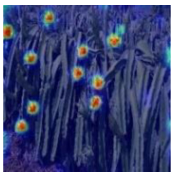
Back light	**The original image**	**Visual result of YOLOv5s**		**Visual result of Improved YOLOv5s**	
Single fruit big object			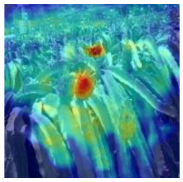		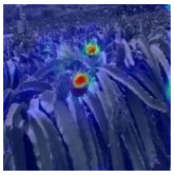
Many fruits in the goal			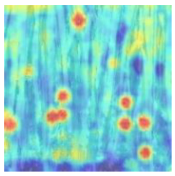		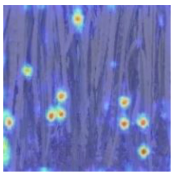
Dense small object			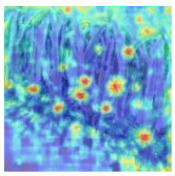		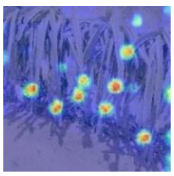
Side light	**The original image**	**Visual result of YOLOv5s**		**Visual result of Improved YOLOv5s**	
Single fruit big object			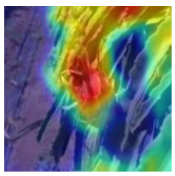		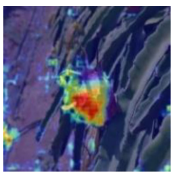
Many fruits in the goal			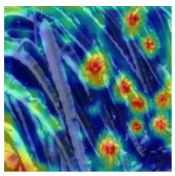		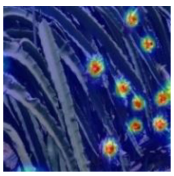
Dense small object			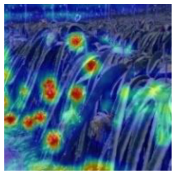		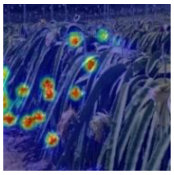

Tables 6, 7 show the detection visualisation results of the YOLOv5s model in different lighting scenes before and after the improvement. According to the visualisation results, the improved detection model had a better detection effect and stronger robustness in detecting dragon fruit objects of different scales under different lighting environments. The positioning was more accurate, and the model had a strong anti-interference ability in dense small object detection.

Video images of the dragon fruit orchard taken by UAV were used for detection to test further the real-time detection performance of the improved model on dragon fruit. UAV (model: Phantom 4 RTK) was used to shoot video images of the dragon fruit orchard at a low altitude of 1 meter in the daytime and night, with a resolution of 1280×720. The proposed improved model was used to detect the dragon fruits in video images. The results showed that the dragon fruits in the video

10.3389/fpls.2022.1040923

TABLE 7 Visual results of dragon fruit object detection on cloudy and night days.

Cloudy	The original image	Visual result of YOLOv5s		Visual result of Improved YOLOv5s	
Single fruit big object			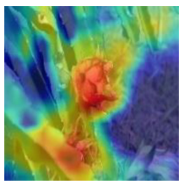		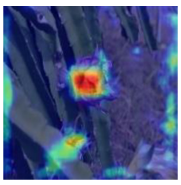
Many fruits in the goal			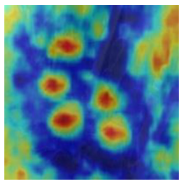		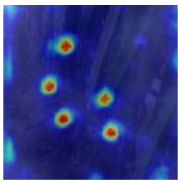
Dense small object		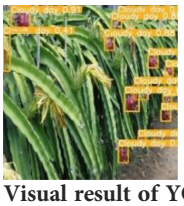	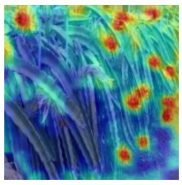		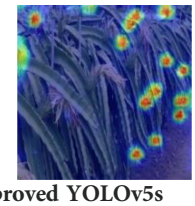
Night	**The original image**	**Visual result of YOLOv5s**		**Visual result of Improved YOLOv5s**	
Single fruit big object	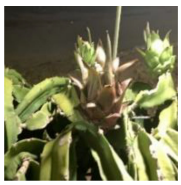		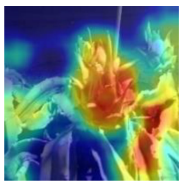		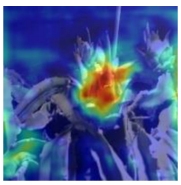
Many fruits in the goal		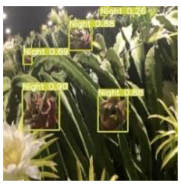	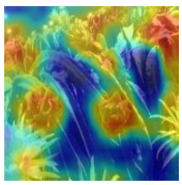		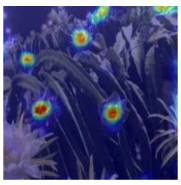
Dense small object			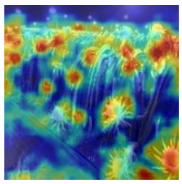		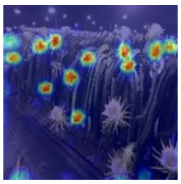

images could be effectively detected. The image pre-processing time of single frame video is 0.6 ms, the reasoning time is 17.0 ms, and the post-processing time is 1.9 ms. The results further verify the strong robustness of the improved algorithm and provide technical support and research basis for deploying the algorithm on mobile devices and developing the vision system of orchard monitoring and picking equipment in the later stage.

Conclusions

Aiming at the all-weather object detection of dense trellis planting of dragon fruit in a complex environment, a detection method that integrated a lightweight network and attention mechanism was proposed in this study. Firstly, dragon fruit data sets were constructed in complex natural environments. Second, the lightweight ghost module and CAM were integrated into the YOLOv5s network structure, while a bidirectional weighted feature pyramid network was constructed in the neck part of the network. Finally, the SIoU loss function was used to replace the loss function of the original network model to improve the convergence speed during model training.

The *mAP* value of the testing sets for dragon fruit detection by this method was 97.4%, *P* was 96.4%, *R* was 95.2%, model size was 11.5 MB, Params was 5.2 M, and FLOPs was 11.4 G. Compared with the original YOLOv5s network, the model

size, Params and FLOPs of the model were reduced by 20.6%, 18.75% and 27.8%, respectively, and the *mAP* of the model improved by 1.1%. The improved model has a lighter structure and better detection performance. Using this model, the *AP* of dragon fruit was 99.5%, 97.3%, 98.5%, 95.5% and 96.1% under front light, backlight, side light, cloudy day and night, respectively. The detection performance could meet the requirements of all-weather detection of dragon fruit and had good robustness. The model was used to test video images with a resolution of 1280×720. The results showed that the pre-processing time of a single frame video image was 0.6 ms, the reasoning time was 17.0 ms, and the post-processing time was 1.9 ms. The model had good application potential in intelligent operations, such as orchard counting and yield measurement, fruit disease and insect pest monitoring by low-altitude UAV and precise picking in the field based on the picking robot.

The next research will mainly apply the existing model to practical tasks, such as orchard counting and yield measurement, fruit disease and insect pest monitoring by low-altitude UAV and precise picking in the field based on the picking robot. The data enhancement method and model detection performance will continue to be optimised to improve the detection accuracy of the model further.

Data availability statement

The original contributions presented in the study are included in the article/supplementary material. Further inquiries can be directed to the corresponding authors.

Author contributions

BZ designed and performed the experiment, selected the algorithm, analyzed the data, trained the algorithms, and wrote the manuscript. BZ, RW, CY, YX, and MF collected data. HZ monitored the data analysis. WF and HZ conceived the study and participated in its design. All authors contributed to this article and approved the submitted version.

Funding

This work was supported by the Key R&D Projects in Hainan Province (Grant No. ZDYF2022XDNY231), the National Natural Science Foundation of China (Grant No. 32160424) and the Key R&D Projects in Hainan Province (Grant No. ZDYF2020042).

Acknowledgments

The authors would like to thank their schools and colleges, as well as the funding of the project. All support and assistance are sincerely appreciated. Additionally, we sincerely appreciate the work of the editor and the reviewers of the present paper.

Conflict of interest

The authors declare that the research was conducted in the absence of any commercial or financial relationships that could be construed as a potential conflict of interest.

Publisher's note

References

Attar, S. H., Guendesli, M. A., Uruen, I., Kafkas, S., Kafkas, N. E., Ercisli, S., et al. (2022). Nutritional analysis of red-purple and white-fleshed pitaya (Hylocereus) species. *Molecules* 27, 808. doi: 10.3390/molecules27030808

Behera, S. K., Mishra, N., Sethy, P. K., and Rath, A. K. (2018). On-tree detection and counting of apple using color thresholding and CHT. *Proc. 2018 IEEE Int. Conf. Communication Signal Process. (Iccsp)* 224-228. doi: 10.1109/ICCSP.2018.8524363

Cecotti, H., Rivera, A., Farhadloo, M., and Pedroza, M. A. (2020). Grape detection with convolutional neural networks. *Expert. Syst. Appl.* 159, 113588. doi: 10.1016/j.eswa.2020.113588

Chaivivatrakul, S., and Dailey, M. N. (2014). Texture-based fruit detection. *Precis. Agric.* 15, 662–683. doi: 10.1007/s11119-014-9361-x

Chu, Y. C., and Chang, J. C. (2020). Regulation offloral bud development and emergence by ambient temperature under a long-day photope-riod in white-fleshed pitaya (Hylocereus undatus). *Sci. Hortic.* 271, 109479. doi: 10.1016/j.scienta.2020.109479

Fu, L. S., Majeed, Y., Zhang, X., Karkee, M., and Zhang, Q. (2020). Faster r-CNN-based apple detection in dense-foliage fruiting-wall trees using RGB and depth features for robotic harvesting. *Biosyst. Eng.* 197, 245–256. doi: 10.1016/j.biosystemseng.2020.07.007

Gevorgyan, Z. (2022). SIoU loss: More powerful learning for bounding box regression. *arXiv preprint arXiv.* 2205, 12740. doi: 10.48550/arXiv.2205.12740

Giang, T. T. H., Khai, T. Q., Im, D. Y., and Ryoo, Y. J. (2022). Fast detection of tomato sucker using semantic segmentation neural networks based on RGB-d images. *Sensors* 22, 5140. doi: 10.3390/s22145140

Han, K., Wang, Y. H., Tian, Q., Guo, J. Y., Xu, C. J., and Xu, C. (2020). GhostNet: More features from cheap operations. *Proc. Cvpr IEEE* 2020, 1577–1586. doi: 10.1109/CVPR42600.2020.00165

He, Z. L., Xiong, J. T., Chen, S. M., Li, Z. X., Chen, S. F., Zhong, Z., et al. (2020). A method of green citrus detection based on a deep bounding box regression forest. *Biosyst. Eng.* 193, 206–215. doi: 10.1016/j.biosystemseng.2020.03.001

Hou, Q. B., Zhou, D. Q., and Feng, J. S. (2021). Coordinate attention for efficient mobile network design. *Proc. Cvpr IEEE* 2021, 13713–13722. doi: 10.1109/CVPR46437.2021.01350

Huang, H. Q., Huang, T. B., Li, Z., Lyu, S. L., and Hong, T. (2022). Design of citrus fruit detection system based on mobile platform and edge computer device. *Sensors* 22, 59. doi: 10.3390/s22010059

Hu, J., Shen, L., and Sun, G. (2018). Squeeze-and-Excitation networks. *Proc. Cvpr IEEE* 2018, 7132–7141. doi: 10.1109/CVPR.2018.00745

Jiang, B., He, J., Yang, S., Fu, H., Li, T., Song, H., et al. (2019). Fusion of machine vision technology and AlexNet-CNNs deep learning network for the detection of postharvest apple pesticide residues. *Artif. Intel. Agric.* 1, 1–8. doi: 10.1016/j.aiia.2019.02.001

Jiang, Y. L., Liao, Y. Y., Lin, T. S., Lee, C. L., Yen, C. R., and Yang, W. J. (2012). The photoperiod-regulated bud formation of red pitaya (Hylocereus sp.). *Hortscience* 47, 1063–1067. doi: 10.21273/HORTSCI.47.8.1063

Jiang, M., Song, L., Wang, Y. F., Li, Z. Y., and Song, H. B. (2022). Fusion of the YOLOv4 network model and visual attention mechanism to detect low-quality young apples in a complex environment. *Precis. Agric.* 23, 559–577. doi: 10.1007/s11119-021-09849-0

Kurtulmus, F., Lee, W. S., and Vardar, A. (2011). Green citrus detection using 'eigenfruit', color and circular gabor texture features under natural outdoor conditions. *Comput. Electron. Agric.* 78, 140–149. doi: 10.1016/j.compag.2011.07.001

Linker, R., Cohen, O., and Naor, A. (2012). Determination of the number of green apples in RGB images recorded in orchards. *Comput. Electron. Agric.* 81, 45–57. doi: 10.1016/j.compag.2011.11.007

Li, X., Pan, J. D., Xie, F. P., Zeng, J. P., Li, Q., Huang, X. J., et al. (2021). Fast and accurate green pepper detection in complex backgrounds *via* an improved Yolov4-tiny model. *Comput. Electron. Agric.* 191, 106503. doi: 10.1016/j.compag.2021.106503

Lu, J., Lee, W. S., Gan, H., and Hu, X. W. (2018). Immature citrus fruit detection based on local binary pattern feature and hierarchical contour analysis. *Biosyst. Eng.* 171, 78–90. doi: 10.1016/j.biosystemseng.2018.04.009

Miao, Z. H., Yu, X. Y., Li, N., Zhang, Z., He, C. X., Li, Z., et al. (2022). Efficient tomato harvesting robot based on image processing and deep learning. *Precis. Agric.* 23, 1–34. doi: 10.1007/s11119-022-09944-w

Payne, A. B., Walsh, K. B., Subedi, P. P., and Jarvis, D. (2013). Estimation of mango crop yield using image analysis - segmentation method. *Comput. Electron. Agric.* 91, 57–64. doi: 10.1016/j.compag.2012.11.009

Rakun, J., Stajnko, D., and Zazula, D. (2011). Detecting fruits in natural scenes by using spatial-frequency based texture analysis and multiview geometry. *Comput. Electron. Agric.* 76, 80–88. doi: 10.1016/j.compag.2011.01.007

Saleem, M. H., Potgieter, J., and Arif, K. M. (2021). Automation in agriculture by machine and deep learning techniques: A review of recent developments. *Precis. Agric.* 22, 2053–2091. doi: 10.1007/s11119-021-09806-x

Sun, J., He, X. F., Ge, X., Wu, X. H., Shen, J. F., and Song, Y. Y. (2018). Detection of key organs in tomato based on deep migration learning in a complex background. *Agriculture* 8, 196. doi: 10.3390/agriculture8120196

Sun, S. H., Jiang, M., He, D. J., Long, Y., and Song, H. B. (2019). Recognition of green apples in an orchard environment by combining the GrabCut model and ncut algorithm. *Biosyst. Eng.* 187, 201–213. doi: 10.1016/j.biosystemseng.2019.09.006

Tang, Y. C., Chen, M. Y., Wang, C. L., Luo, L. F., Li, J. H., Lian, G. P., et al. (2020). Recognition and localization methods for vision-based fruit picking robots: A review. *Front. Plant Sci.* 11, 510. doi: 10.3389/fpls.2020.00510

Tian, Y. N., Yang, G. D., Wang, Z., Wang, H., Li, E., and Liang, Z. Z. (2019). Apple detection during different growth stages in orchards using the improved YOLO-V3 model. *Comput. Electron. Agric.* 157, 417–426. doi: 10.1016/j.compag.2019.01.012

Wang, C. L., Wang, Y. W., Liu, S. C., Lin, G. C., He, P., Zhang, Z. G., et al. (2022). Study on pear flowers detection performance of YOLO-PEFL model trained with synthetic target images. *Front. Plant Sci.* 13. doi: 10.3389/fpls.2022.911473

Woo, S., Park, J., Lee, J. Y., and Kweon, I. S. (2018). CBAM: convolution block attention module. *Proc. Cvpr IEEE* 2018, 3–19. doi: 10.1007/978-3-030-01234-2_1

Xiong, J., Zheng, Z., Liang, J. E., Zhong, Z., Liu, B., and Sun, B. (2020). Citrus detection method in night environment based on improved YOLO v3 network. *Trans. Chin. Soc Agric. Mach.* 51, 199–206. doi: 10.6041/j.issn.1000-1298.2020.04.023

Yan, B., Fan, P., Lei, X. Y., Liu, Z. J., and Yang, F. Z. (2021). A real-time apple targets detection method for picking robot based on improved YOLOv5. *Remote Sens.* 13, 1619. doi: 10.3390/rs13091619

Yu, L. Y., Xiong, J. T., Fang, X. Q., Yang, Z. G., Chen, Y. Q., Lin, X. Y., et al. (2021). A litchi fruit recognition method in a natural environment using RGB-d images. *Biosyst. Eng.* 204, 50–63. doi: 10.1016/j.biosystemseng.2021.01.015

Zhang, F., Chen, Z., Bao, R., Zhang, C., and Wang, Z. (2021). Recognition of dense cherry tomatoes based on improved YOLOv4-LITE lightweight neural network. *Trans. Chin. Soc Agric. Eng.* 37, 270–278. doi: 10.11975/j.issn.1002-6819.2021.16.033

Zhang, Y. C., Zhang, W. B., Yu, J. Y., He, L. Y., Chen, J. N., and He, Y. (2022). Complete and accurate holly fruits counting using YOLOX object detection. *Comput. Electron. Agric.* 198, 107062. doi: 10.1016/j.compag.2022.107062

Zheng, T. ,. X., Jiang, M. Z., and Feng, M. C. (2021). Vision based target recognition and location for picking robot: A review. *Chine. J. Scien. Instru.* 42, 28–51. doi: 10.19650/j.cnki.cjsi.J2107650

Zhou, J., Hu, W., Zou, A., Zhai, S., Liu, T., Yang, W., et al. (2022). Lightweight detection algorithm of kiwifruit based on improved YOLOX-s. *Agriculture* 12, 993. doi: 10.3390/agriculture12070993

frontiers | Frontiers in Plant Science

TYPE Original Research
PUBLISHED 31 October 2022
DOI 10.3389/fpls.2022.1040808

OPEN ACCESS

EDITED BY
Ruirui Zhang,
Beijing Academy of Agricultural and Forestry Sciences, China

REVIEWED BY
Xiaoqiang Du,
Zhejiang Sci-Tech University, China
Feng Kang,
Beijing Forestry University, China

*CORRESPONDENCE
Yongjun Zheng
zyj@cau.edu.cn
Xingxing Liu
liuxingxing@cau.edu.cn

†These authors have contributed equally to this work and share first authorship

SPECIALTY SECTION
This article was submitted to Technical Advances in Plant Science, a section of the journal Frontiers in Plant Science

RECEIVED 09 September 2022
ACCEPTED 11 October 2022
PUBLISHED 31 October 2022

CITATION
Jiang S, Chen B, Li W, Yang S, Zheng Y and Liu X (2022) Stereoscopic plant-protection system integrating UAVs and autonomous ground sprayers for orchards.
Front. Plant Sci. 13:1040808.
doi: 10.3389/fpls.2022.1040808

Stereoscopic plant-protection system integrating UAVs and autonomous ground sprayers for orchards

Shijie Jiang[1†], Bingtai Chen[1†], Wenwei Li[1], Shenghui Yang[1], Yongjun Zheng[1,2*] and Xingxing Liu[1*]

[1]College of Engineering, China Agricultural University, Beijing, China, [2]Yan Tai Institute, China Agricultural University, Yan Tai, China

For orchard plant protection, conventional large machines and small sprayers are practically restricted by either narrow planting intervals with dense leaves or their inadequate penetration power, which leads to an unsatisfactory effect of spray. This paper proposes a stereoscopic plant-protection strategy that integrates unmanned air and ground sprayers to spray different parts of canopies to improve uniformity. In order to verify the proposal, a stereoscopic plant-protection system (SPS) was developed, consisting of a small swing-arm sprayer and a T16 plant-protection Unmanned Aerial Vehicle (UAV). Then, optimal operation parameters were determined by Computational Fluid Dynamics (CFD) and orthogonal experiments, and the uniformity was finally quantified by trials. CFD and orthogonal experiments showed that a swing-arm angle of 60° and a forward speed of 0.4 m/s were optimal for the ground sprayer, whilst a height of 2.0 m from the top of canopies and a forward speed of 1.0 m/s were appropriate for the UAV. The trial results showed that the density of vertical droplet deposition varied from 90 to 107 deposits/cm^2 in canopies, and the uniformity was 38.3% higher than conventional approaches. The uniformity of top, bottom, inside and outside canopies was significantly improved. Meanwhile, the density of droplet deposition on both sides of leaves in all test points exceeded 25 deposits/cm^2, able to meet the standard of spray. This study provides a practical approach for uniform pesticide spray to large-canopy fruit trees. Moreover, the high flexibility of plant-protection UAVs and the significant trafficability of small swing-arm sprayers can solve the problem of large machine entering and leaving orchards.

KEYWORDS

orchard, stereoscopic plant-protection, uniform spraying, UAV, UGV, computational fluid dynamics (CFD)

1 Introduction

Plant protection is important in the orchard production process to promote fruit production (Zhao et al., 2017; Jiang et al., 2021), while the current means still relies on chemical spray (Zhai et al., 2018; Rehberg et al., 2020; Zheng et al., 2020a). It is ideal for the entire canopy of fruit trees to be uniformly covered by droplets. However, due to topographical characteristics (such as undulating terrain, slope and unevenness) and narrow row intervals (especially row interval closure by canopies during tree branching and foliage densifying), large plant-protection machinery cannot enter orchards, while small one cannot achieve full-canopy spray. Thus, it faces serious difficulties for orchard plant protection to achieve expected effect (especially in hilly mountainous orchards) (Hołownicki et al., 2017; Zheng et al., 2020b).

Manual spray presents strong randomness, which is hard for droplets to cover targets uniformly, so using mechanised and intelligent equipment has played a key role in achieving uniform fruit-tree spray in developed regions such as Europe, the United States, Japan and Korea. In Japan and Korea, orchard terrain is mainly hilly and mountainous (Jin et al., 2017). Plant-protection machines mostly utilise miniaturised design with levelling and anti-tipping mechanisms and other safety devices to improve the application efficiency and adaptability to the terrain. However, there are still problems like the imperviousness of dense canopies and the non-uniform distribution of droplets in canopies. In Europe and the United States, the topography of orchards is significantly different from China and Japan. Farm and large-scale planting patterns were generally adopted with deep integration of agronomy and agricultural machinery (Grella et al., 2020), providing the possibility of large plant-protection machinery operations. Among them, air-assisted sprayers are the most widely used devices (Miranda-Fuentes et al., 2017). Although large plant-protection machines show the convenience for plant protection in orchards and have significant application effects compared to manual spray (Liu et al., 2012), they present noticeable problems (Salcedo et al., 2017), such as pesticide overuse, fruit pesticide residues, soil pesticide residues and water pollution (Kira et al., 2018; Kasner et al., 2020). Since the end of the 20th century, many corresponding environmental policies have been promulgated in Europe and the United States, and the use of pesticides has become more stringent. For example, safety quarantine zones must be set up for spray, and pesticides are severely restricted. Therefore, it has been more challenging to develop spray technology to reduce drift and improve the uniformity of droplet distribution. In the 21st century, the target-directional air delivery method gradually replaced the diffuse air delivery method that causes serious drift. The target-directional implement shows a noticeable effect on fruit trees with narrow canopy and uniform height (Song et al., 2012; Niu et al., 2019). However, it is limited by its large size and is only adapted to small canopies and wide row-spacing orchards.

With the advancement of technology, variable spray techniques based on the characteristics of fruit tree canopies have been rapidly developed (He et al., 2011; Cai et al., 2017; Manandhar et al., 2020), and sensors such as LiDAR (Fessler et al., 2020) and depth cameras (Xiao et al., 2017) have been used to acquire fruit tree canopy features (Rosell and Sanz, 2012; Yandún Narváez et al., 2016). Applying pesticides on demand can effectively reduce chemical waste (Miranda-Fuentes et al., 2016). However, there are serious problems. Firstly, in terms of orchard adaptability, after acquiring the characteristics of fruit trees based on sensors, the spray mechanism needs to reach a certain position to deliver droplets onto target locations, which further increases the overall size of the sprayers. (Chen et al., 2011; Liu et al., 2013; Liu et al., 2016) so that they become less adaptable to the orchard environment. In addition, for most large-canopy orchards, canopy closure between rows can directly affect the accuracy of feature sense, even leading to no acquisition of expected canopy features. Inspired by the successful application of plant-protection Unmanned Aerial Vehicles (UAVs) in fields (Zhang et al., 2016), there have been many studies related to plant-protection UAVs in orchard conditions (Wang et al., 2017; Liu et al., 2020; Meng et al., 2020). UAVs can avoid the terrain restrictions that ground sprayers have to suffer but present the disadvantages of the spray for large-canopy fruit trees. The distribution of droplets at the top and bottom of canopies varies highly. With serious row closure, the droplet deposition in the lower part of canopies does not even reach the spraying standard (25 deposits/cm^2), which still cannot meet the demand for uniform spray in canopies.

Our team conducted preliminary experiments in two apple orchards in Shanxi Province and Beijing, a mango orchard in Guangxi Province and a citrus orchard in Chongqing Province from June 2018 to April 2021. Typical sprayers for orchards were selected for the experiment, including a ring-shape air-assisted sprayer (model SSA-E541, Wuxi Yifeng Wanshan Technology Co., Ltd.), a tower-shaped air-assisted sprayer (model G6S, Shandong Guohaha Agricultural Machinery Co., Ltd.), a single-rotor plant-protection UAV (model Z-3N, Nanjing Institute of Simulation Technology, Jiangsu Province) and a six-rotor plant-protection UAV (model 3WWDZ-10, Beijing Viga UAV Technology Co., Ltd.). The results in Figure 1 show that droplets were not uniformly distributed at the top, bottom, inside and outside canopies during single equipment spraying. In particular, during the six-rotor plant-protection UAV spraying, the droplet deposition density in the top layers of canopies was high and uniform, while that in the bottom was poor. Meanwhile, the droplet distribution of the air-assisted sprayer was non-uniform in the top layers and was better in the

bottom layers. (Chen et al., 2020; Jiang et al., 2022). These pre-test results were highly consistent with the issue on the basis of the literature review above.

This study proposes a stereoscopic plant-protection method with a corresponding Stereoscopic Plant-protection System (SPS) to improve the uniformity of canopy spray. Numerical simulations using Computational Fluid Dynamics (CFD) and orchard experiments were conducted to determine the optimal operation parameters for the SPS. Then, the experiments of the SPS were conducted. It is a new idea for orchard plant protection, especially for closure orchards, and provides a technical solution to improve the spray uniformity in the canopy of fruit trees.

2 Materials and methods

2.1 Development of SPS

2.1.1 SPS scheme

As shown in Figure 1, the plant-protection UAV and the ground air-assisted sprayer present complementary characteristics for canopy spray. Thus, they were combined to cover the entire tree canopies (Figure 2). Plant-protection UAVs were in charge of the upper part of canopies, while small ground sprayers (air-assisted sprayers) focused on the middle and bottom parts.

The plant-protection UAV adopted the canopy top-seeking operation mode (Zhang et al., 2019). It flew directly above the fruit tree canopies, and the spray swath mainly covered the top half of the canopies. The small ground sprayer travelled between the rows of trees, and the spraying range mainly covered the bottom half of the canopies. To prevent the wind fields by the two devices from affecting each other and reducing the spraying effect, the system could select the following three operation modes:

1. sequential independent spraying. One of the devices firstly sprayed. After it was completed, the other one sprayed.
2. simultaneous following spraying. The plant-protection UAV operated first and was followed by the ground sprayer after flying a certain distance (≥spraying width).

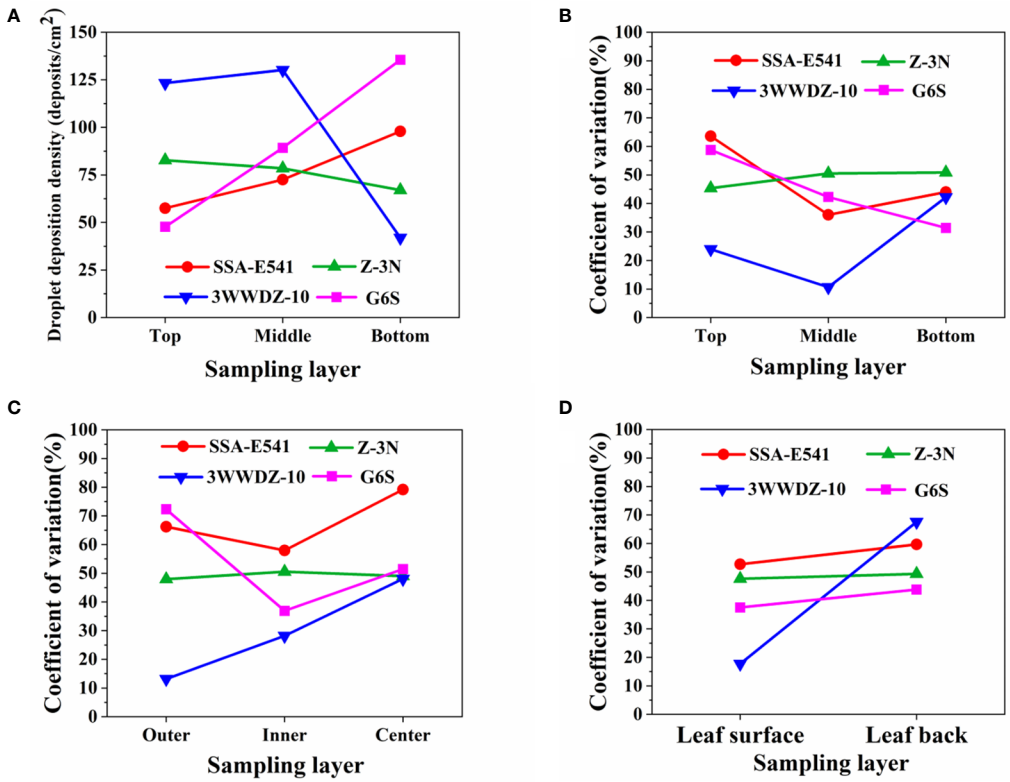

FIGURE 1
Typical equipment canopy droplet deposition experimental results. **(A)** Vertical longitudinal sampling layer droplet deposition density. **(B)** Vertical longitudinal sampling layer droplet distribution uniformity. **(C)** Horizontal radial sampling layer droplet distribution uniformity. **(D)** Uniformity of droplet distribution on leaf surface and leaf back.

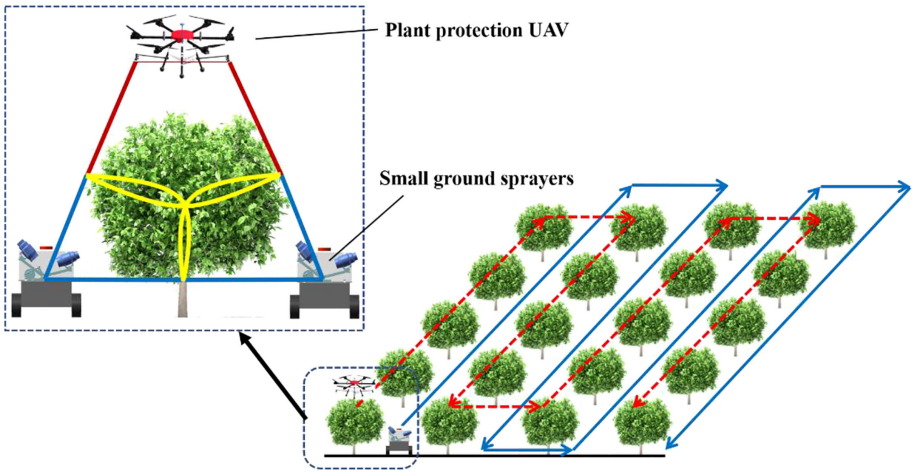

FIGURE 2
Schematic of stereoscopic plant protection. The dashed line indicates the operation route of the plant-protection UAV, while the solid line is that of the ground sprayer.

3. simultaneous free spraying. The plant-protection UAV and the ground sprayer simultaneously sprayed but did not spray one fruit tree at the same time.

2.1.2 Plant-protection UAV

According to the previous study results (Chen et al., 2020), it is known that the droplet deposition density and distribution uniformity of the six-rotor plant-protection UAV on canopies is better than that of the single-rotor one. Therefore, the T16 six-rotor plant-protection UAV (Figure 3) produced by Shenzhen DJI Innovation Technology Co., Ltd was exploited for this study. It has a terrain-following function and wide spraying performance, which could ensure a similar spray effect in most cases. Its main parameters are shown in Table 1.

2.1.3 Small swing-arm sprayer

According to the preliminary investigation of orchard characteristics, a small swing-arm sprayer (Figure 4A) was specially developed to spray the lower and middle canopy of fruit trees. The main components consisted of a crawler chassis, a swing-arm air-assisted spraying mechanism, a booster renewal mechanism

FIGURE 3
T16 six-rotor plant-protection UAV.

TABLE 1 Main parameters of T16 plant-protection UAV.

Categories	Values	Categories	Values
Weight of the whole machine (without battery)	18.50 kg	Medicine tank volume	16.00 L
Nozzle type	SX11001VS	Number of nozzles	8
Operating height (height above the canopy)	1.50~3.00 m	Maximum spray flow	3.60 L/min
Maximum operating speed	7.00 m/s	Spraying width	4.00~6.50 m

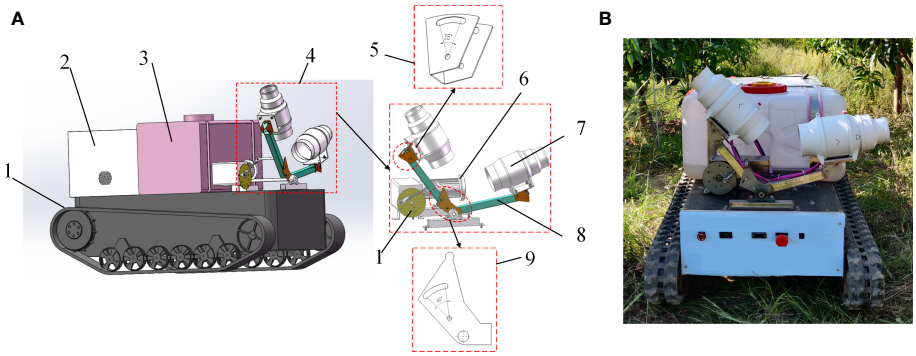

FIGURE 4
Small swing-arm sprayer. **(A)** Small swing-arm sprayer 3D model. **(B)** Small swing-arm sprayer prototype. 1. Crawler type walking chassis 2. Booster renewal mechanism 3. Liquid tank 4. Swing-arm air-assisted spraying mechanism 5. Angle adjustment parts 6. Direct current reducer motor 7. Piping fan 8. V-shaped swing-arm support bar 9. Driving fan blade.

and a liquid tank. The crawler chassis and the swing-arm air-assisted spraying mechanism were developed earlier, which could autonomously navigate in rows by electrical driving (Liu et al., 2021) and follow spray targets (Jiang et al., 2021), respectively.

The swing-arm air-assisted spraying mechanism was V-shaped and was driven by a DC motor with a drive mechanism to do the swing-arm action. Small pipe fans were installed at the end of each V-shaped swing-arm support bar through the angle adjustment parts. The fans on both sides were controlled independently. Two fan-shaped nozzles were installed at the exit of the fans, respectively. The V-shaped swing-arm support bar was connected by driving fan blades. The angle adjustment parts and the driving fan blade were set with a circular slot, which could adjust the opening and closing angle of the bar. The angle adjustment parts and the driving fan blade were adjustable from 0 to 40° and 0 to 35°, respectively.

In this study, the air-assisted system of the small swing-arm sprayer consisted of small pipe fans. The air volume of the fan was determined according to the displacement principle (Dekeyser et al., 2013). The air-assisted system could effectively reduce the loss of both air volume and energy and enhance the duration of operation.

On the basis of 3D model construction and theoretical parameter calculation, the prototype was developed as shown in Figure 4B. Its main technical parameters are shown in Table 2.

2.2 Parameter optimisation of SPS based on CFD

In terms of the SPS, the operating parameters of both the UAV and the swing-arm sprayer are essential to improve the spraying performance, whilst the wind fields from these two devices are the key factors affecting the deposition of droplets in canopies (Xu et al., 2017). Thus, CFD was applied to investigate the airflow distribution patterns of these two types of wind fields with fruit trees. The optimal combination of operating parameters with a uniform canopy spraying performance was determined. Based on ANSYS Fluent 18.2, the wind fields of the six-rotor plant-protection UAV and the swing-arm sprayer were numerically simulated.

2.2.1 CFD geometric model construction

Compared with high computational costs of using entire 3D fruit tree canopy models, using porous medium models to replace fruit tree canopies (Duga et al., 2015; Hong et al., 2018a) has been confirmed by numerous studies for its reliability (Endalew et al., 2009; Salcedo et al., 2015; Duga et al., 2016; Hong et al., 2018b). In this study, fruit tree canopies were represented by a porous medium model, and the hindrance effect of the canopy on airflow was simulated by adding a momentum loss source term in the porous media region. Moreover, the canopy sparseness was

TABLE 2 The main parameters of the small swing-arm sprayer.

Categories	Values	Categories	Values
Overall dimensions (length × width × height)	2.05 m × 1.10 m × 1.00 m	Maximum spraying width	≤5.50 m
Overall machine mass	500 kg (empty)	Maximum operating speed	0.70 m/s
Power	48V lead battery pack (45Ah)	Maximum fan speed	2500 r/min
Medicine tank volume	150L	Maximum air volume of fan	2304 m^3/h
Number of nozzles	2	Maximum flow rate of the pump	12 L/min
Nozzle category	Fan spray nozzle	Maximum pressure of the pump	4.50 MPa

characterised by defining different pressure loss coefficients because canopies had various degrees of sparseness and it has different drag magnitudes. The final model is shown in Figure 5A, where the full-leaf stage fruit tree was represented by an ellipsoidal canopy and a cylindrical branch trunk. Meanwhile, on the basis of preliminary fruit tree measurements, the canopy pressure loss coefficient, the plant height, the trunk height and the crown width were set as 10.0, 3.5 m, 0.8m and 2.8m, respectively.

In terms of the plant-protection UAV, rotors are the core to generate downwash airflow. Thus, the 3D model of the UAV was appropriately simplified. Only the six rotors were kept, which is acceptable for the simulation (Zhang et al., 2019; Yang et al., 2020). The simplified model of the UAV is shown in Figure 5B, where the rotational diameter of the rotor was 609mm.

In terms of the swing-arm sprayer, a similar simplification was conducted. Only the fans were used for simulation, and other components were not considered. The simplified model of the swing-arm sprayer is shown in Figure 5C, where the right fan was taken as an example, and the diameter of the wind outlet was 247mm.

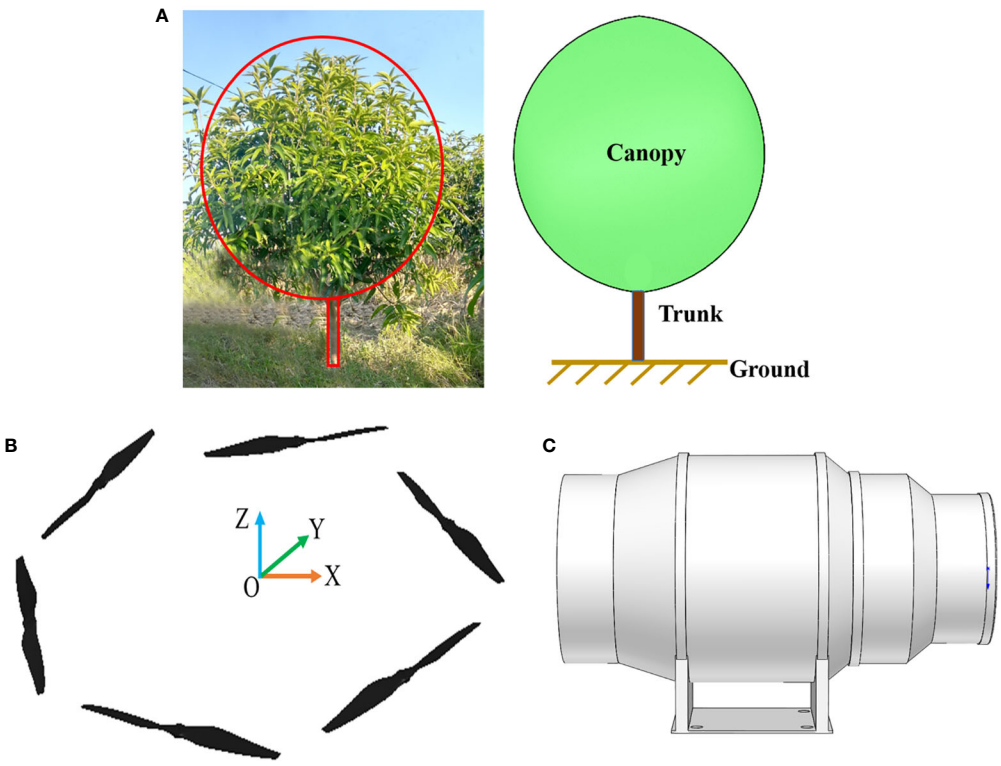

FIGURE 5
CFD geometric model construction. **(A)** Simplified model of fruit tree. **(B)** Simplified model of plant-protection UAV. **(C)** Simplified model of swing-arm sprayer.

2.2.2 Setting of computational areas and boundary conditions

It is required that numerical simulation conditions should be similar to the actual spraying ones so that simulation results are reliable. In this study, a virtual orchard model was constructed based on the parameters of orchard investigations, the model calculation area was 20.0 m × 15.0 m (long ×wide) with a height of 13.0 m (Figure 6), so airflow could be fully developed. The model included the fruit tree canopy subdomain and a branch subdomain. The fruit tree branch subdomain did not need to be solved, so it was removed during preprocessing and set as the wall boundary. Only the outlet boundary was kept.

The air sub-domain and rotor rotation sub-domains were included in the simulation of the six-rotor plant-protection UAV. The 'interface' boundary condition was applied for the interface between the air sub-domain and the rotor rotation sub-domains. The rotor rotation (rotational speed 2500 r/min) sub-domain was processed by slip grids. Meanwhile, the upper boundary of the air sub-domain was the pressure inlet, the lower boundary of the ground was set to the non-slip wall boundary, and the other boundaries were the pressure outlets. The rotor was 2.0m away from the top of the fruit tree canopies.

The air sub-domain and fan sub-domains were included in the simulation of the swing-arm sprayer. The fan was located at the central line of the row spacing, about 2.0 m from the tree trunk and 0.6 m above the ground. For the setting of the solution parameters, only the external flow field of the fans was concerned. Moreover, the no-slip wall boundary was used for the air subdomain, and the rest of the boundaries were set as pressure outlets.

Meshing was conducted after the geometric model and the computational areas were determined. Non-structural tetrahedral meshes applicable to complex entities were used for gridding. The mesh numbers for the plant-protection UAV and swing-arm sprayer simulation were 8112602 and 4694187, respectively. No negative meshes and left-hand meshes existed, so the meshes were used for calculation.

In terms of solution, the renormalization group (RNG) κ-ε turbulence model was selected, and the control equations were discretised by the finite volume method. The pressure-velocity coupling was chosen from the Pressure-Implicit with Splitting of Operators (PISO) algorithm. The pressure interpolation format was chosen from the PRESTO! format for high-speed rotating and porous media. The second-order windward pair momentum, turbulent kinetic energy and turbulent dissipation rate were discretised in the spatial domain.

2.3 Orchard experiments of SPS

2.3.1 Experimental site and sprayers

The experiment was conducted in August 2020 in mango orchards in Tianyang District, Baise City, Guangxi Zhuang Autonomous Region (Figure 7). The environmental temperature during the experiment was about from 28°C to 32°C, and the humidity was about from 45% to 49%. The orchards were planted in the conventional mode. The row spacing was 4.5 m, the plant interval was 3.5 m, and the tree height was about 4.5 m. The trees were about 30 years old, and the canopies were large and closed in some areas. The UAV (Figure 3) and the sprayer (Figure 5) were employed in the experiments.

In addition, the wind speed and volume meter, AR856 produced by Shenzhen Franken Electronics Co., Ltd., and temperature and humidity meter produced by Deloitte Group Co., Ltd. were used to monitor and record meteorological parameters such as wind speed, wind direction, temperature and humidity.

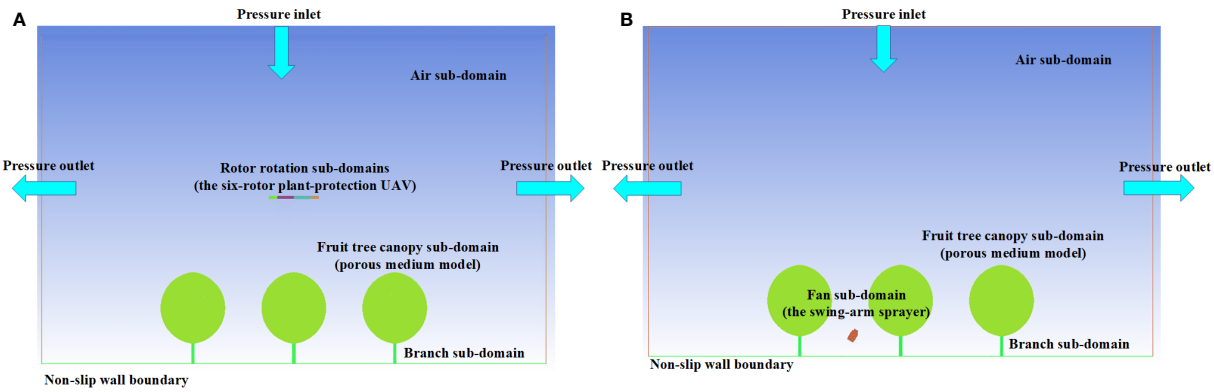

FIGURE 6
The model calculation area. **(A)** Plant-protection UAV model calculation area. **(B)** Swing-arm sprayer model calculation area.

FIGURE 7
Experimental scenarios.

2.3.2 Experimental scheme

The experiments were conducted according to the standards NY/T 992-2006, 'The operation quality for air-assisted orchard sprayer', and JB/T 9782-2014, 'Equipment for crop protection - General test methods'.

1) Sampling point arrangement

The experimental scheme is shown in Figure 8. Three fruit trees with similar shape, height and canopy size were selected as target fruit trees in the experimental area (Figure 8A). The target fruit trees were far from the start and end of rows to reduce the errors caused by the devices slowing down and turning.

The scheme of canopy droplet sampling points is shown in Figure 8B. In the canopy, according to the height and shape of each target tree, vertical sampling was divided into top, middle and bottom layers, and horizontal radial sampling was divided into the centre, inner and outer layers relative to the location of the trunk. One sampling point was placed in the centre layer of canopies and marked as O. Four sampling points were placed in the inner and outer layers of canopies, marked as e, s, w, n and E, S, W, N, respectively. Thus, there were 27 sampling points in canopies. On the ground, 9 sampling points were set with the trunk of the tree as the centre.

Water-sensitive papers (76 mm × 26 mm) were exploited to collect droplets, laid on both sides of leaves on each sampling point, so 54 pieces were used in total. Each ground sampling point arranged a water-sensitive paper and made the water-sensitive paper face up. The spray solution was water without solids in suspension at the normal temperature.

2) Optimization of operational parameters based on orthogonal experiment

The previous CFD simulation had determined both the proper operation height of the six-rotor plant-protection UAV and the appropriate swing-arm angle of the swing-arm sprayer. Hence, a three-factor with three-level orthogonal experiment was conducted to find the optimal operation speed. The factor level of the orthogonal experiment is shown in Table 3.

The sequential independent mode was used for the experiment. After setting water-sensitive paper, the swing-arm sprayer was firstly enrolled in the test. When the sprayer completed the test, the T16 UAV started.

3) Effect verification of the SPS based on trials

Based on the CFD simulation and the orthogonal experiment, the optimal operating parameters of the SPS were determined. They were selected for the effect verification of the

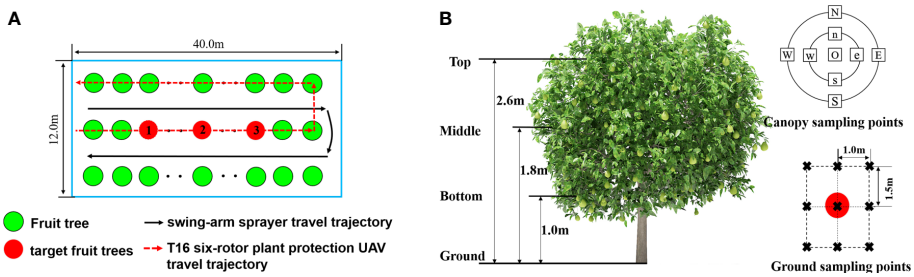

FIGURE 8
Sampling scheme. **(A)** Selection of target fruit trees. **(B)** Sampling point layout scheme.

TABLE 3 Three-factor with three-level orthogonal experiment table for the SPS.

Experimental group	Factor A: Swing-arm sprayer operating speed (m/s)	Factor B: T16 plant-protection UAV operating height (m)	Factor C: T16 plant-protection UAV operating speed (m/s)
1	0.40 (1)	2.00 (1)	1.00 (1)
2	0.40 (1)	2.50 (2)	1.50 (2)
3	0.40 (1)	3.00 (3)	2.00 (3)
4	0.50 (2)	2.00 (1)	1.50 (2)
5	0.50 (2)	2.50 (2)	2.00 (3)
6	0.50 (2)	3.00 (3)	1.00 (1)
7	0.60 (3)	2.00 (1)	2.00 (3)
8	0.60 (3)	2.50 (2)	1.00 (1)
9	0.60 (3)	3.00 (3)	1.50 (2)

A1 refers to the first level of factor A, that is, A1 is 0.40m/s; B1 refers to the first level of factor B, that is, B1 is 2.00 m; other factor levels are expressed in the same way, e.g., B2, C3, etc.

SPS, comparing the spraying effect of the SPS with that of the T16 plant-protection UAV and the swing-arm sprayer. The operation parameters for the single-device experiment were the same as that for two-device one.

2.3.3 Data analysis

All the water-sensitive paper was processed by the following steps:.

- All the water-sensitive paper was scanned with LASERJET PRO MFP M132 to obtain the corresponding scan images. Then, the images were read by DepositScan ™ droplet analysis software to get indices such as droplet deposition, deposition density and coverage. All the data were recorded in an Excel table.
- The coefficient of variation was calculated by using the equations from (1) to (3) to analyse the droplet distribution uniformity. SPSS 21.0 and Origin 9.1 software were used for data processing and graph plotting.

$$\bar{q} = \frac{\Sigma q_i}{n} \quad (1)$$

$$S = \sqrt{\frac{\Sigma(q_i - \bar{q})^2}{n-1}} \quad (2)$$

$$CV(\%) = \frac{s}{\bar{q}} \times 100 \quad (3)$$

where, q_i is the i-th sampling point droplet deposition density, deposits/cm^2; $\bar{q}$ is the average value of sampling point droplet deposition density, deposits/cm^2; n is the number of sampling points; S is the standard deviation of droplet deposition density, deposits/cm^2, and CV (%) is the coefficient of variation.

3 Results and discussion

3.1 Results and analysis of CFD simulation

3.1.1 Wind field distribution of the six-rotor plant-protection UAV

(1) Time-dependent characteristics of wind field speed

Figure 9 shows the speed distribution of the rotor wind field at different moments, respectively. It can be seen that the rotor airflow kept extending downward with increasing time. At 0.5 s, the rotor airflow approximately reached canopies. At 1.0s, the rotor airflow covered the top of canopies. At 5.0 s, the wind field had not yet reached spreading along the ground, although some of it touched the ground. Therefore, a six-rotor plant-protection UAV was used for fruit tree spraying, the height from the top of the canopy was 2.0m. Meanwhile, the plant-protection UAV stayed at least 4.0s after take-off and then started operation.

(2) Wind speed distribution of different locations in canopies

The simulated fruit trees were divided into top, middle and bottom layers at a distance of 2.3m, 3.4m and 4.5m from the center of the plant-protection UAV, and 9 sample points were selected uniformly in each layer (the sample point distribution scheme was the same as the foliar sampling point layout scheme in Section 2.1) to obtain the maximum airflow velocity in the vertical direction (Z direction) at each sample point (Table 4).

As shown in Table 4, the average speeds of the top, middle and bottom layers inside canopies were 3.22 m/s, 0.51 m/s and 0.10 m/s, respectively, with a decreasing trend from top to bottom. The average wind speed in the bottom layers was minimal, which could hardly carry and transport droplets.

3.1.2 Wind field distribution law of the swing-arm sprayer

Figure 10 shows the wind field velocity distribution of the fan at different moments, indicating that canopies had an

10.3389/fpls.2022.1040808

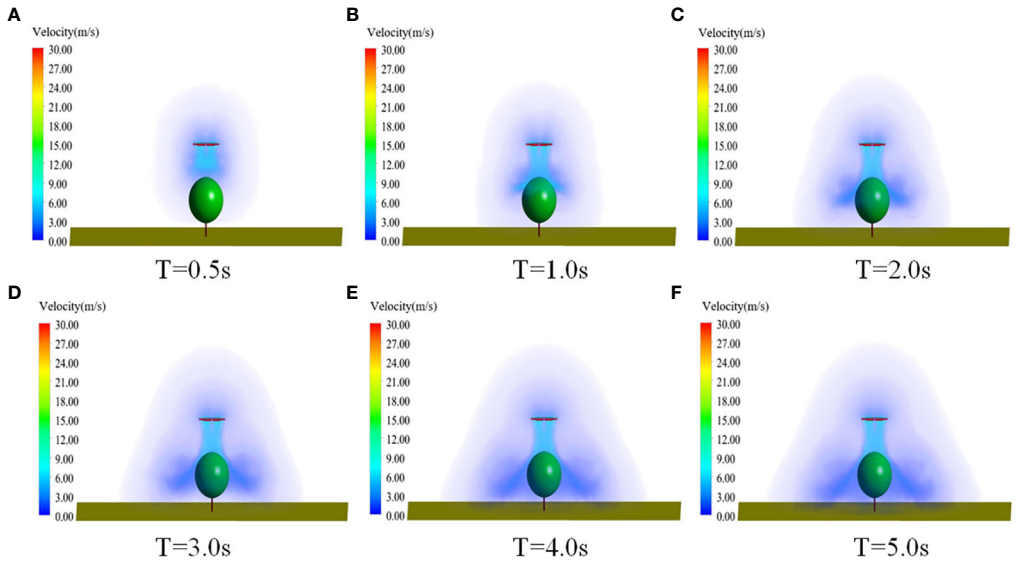

FIGURE 9
Wind field speed distribution of six-rotor plant-protection UAV at different times. **(A)** T=0.5s. **(B)** T=1.0s. **(C)** T=2.0s. **(D)** T=3.0s. **(E)** T=4.0s. **(F)** T=5.0s.

TABLE 4 Velocity distribution of each layer within the canopy.

Location	Sample point speed (m/s)									Average speed (m/s)
	1	2	3	4	5	6	7	8	9	
Top layer	3.11	5.05	3.88	5.14	2.02	2.23	3.03	2.36	2.18	3.22
Middle layer	0.42	0.41	0.37	0.35	0.61	0.57	0.59	0.57	0.68	0.51
Bottom layer	0.10	0.09	0.09	0.10	0.10	0.10	0.10	0.10	0.11	0.10

obvious blocking effect on the fan airflow. It can be seen that at 0.5 s, the fan airflow reached canopies. At 1.0 s, the airflow appeared to roll up around canopies because of the blocking effect. The rolled-up airflow gradually increased and kept stable at about 2.5 s. Therefore, the swing-arm sprayer could start spraying after the fan was turned on for 2.5 s.

3.1.3 Optimal operation parameters of the SPS

Figure 11 shows the velocity distribution of the stable wind field of the UAV rotors at different operating heights (height to the top of the canopy). The rotor airflow reached the canopy surface in a centrosymmetric pattern, and the operating height caused the change of the airflow to the target. The airflow area to targets gradually decreased as the operating height increased. In the range from 1.5 m to 2.0 m, the airflow velocity changes in the canopy were not obvious, and the optimal operation height should be selected in this range.

Figure 12 shows the velocity distribution of the stable wind field of the sprayer fan at different swing-arm angles. During spraying, the area covered by the airflow from the fan to the target gradually increased gradually with the swing-arm angle started from 0°. When the swing-arm angle was certain, the airflow velocity inside canopies gradually decreased as the canopy depth increased. It basically covered the lower half side (left side) of canopies, and the airflow mostly spread uniformly in the range from 1.5 m/s to 3.5 m/s, which is beneficial to the uniform distribution of droplets.

Based on the above simulation results, the comparative effect of the wind field coupling in the stereoscopically applying canopy with different operating parameters is given in Figure 13. When the operation height of the UAV was 2.0 m, the rotor airflow speed was between 0.50 m/s and 1.00 m/s in the range of canopy height from 2.0 m to 2.4 m, the rotor airflow speed was between 1.00 m/s and 1.50 m/s in the range of canopy height from 2.4 m to 2.7 m, the rotor airflow speed was above 1.5 m/s in the range of canopy height

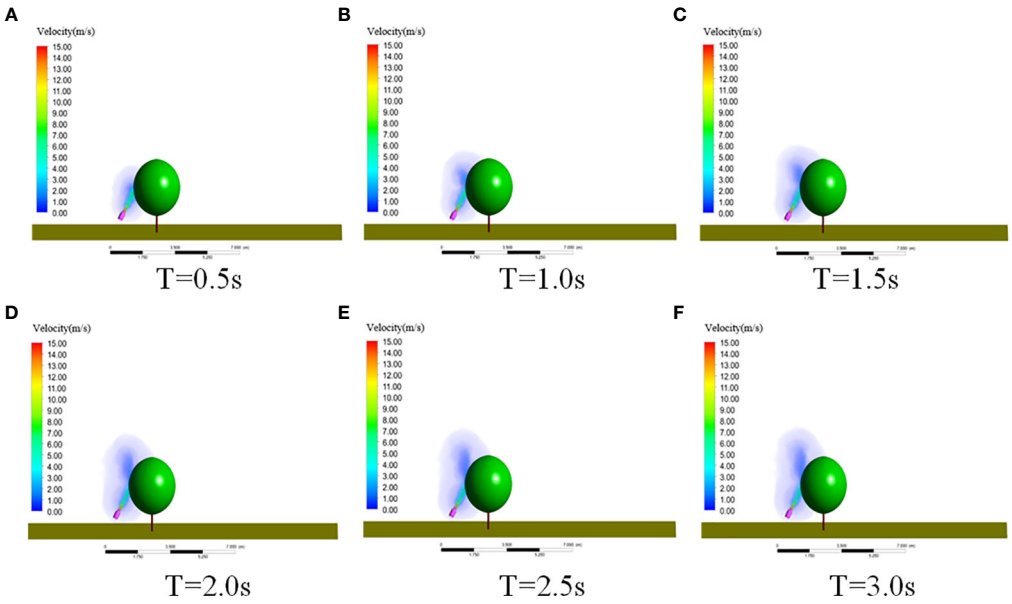

FIGURE 10
Wind speed distribution of the swing-arm sprayer at different times. **(A)** T=0.5s. **(B)** T=1.0s. **(C)** T=1.5s. **(D)** T=2.0s. **(E)** T=2.5s. **(F)** T=3.0s.

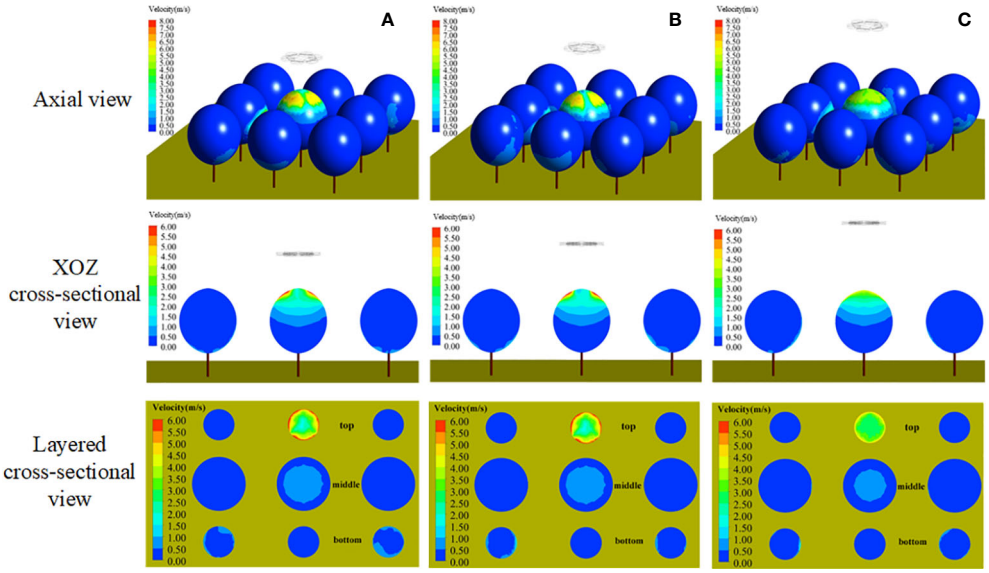

FIGURE 11
Air speed distribution of plant-protection UAV at different heights. **(A)** Operating height 1.5m. **(B)** Operating height 2.0m. **(C)** Operating height 3.0m.

from 2.7 m, the rotor airflow speed was above 1.5 m/s in the range of canopy height from 2.7 m. When the swing-arm angle of the swing-arm sprayer was 60°, the fan airflow speed of canopy height below 2.6 m was above 1.5 m/s, the fan airflow speed between 2.6 m and 2.7 m was from 1.00 m/s to 1.50 m/s, and the fan airflow speed of canopy height above 2.7m rapidly became smaller.

Therefore, when the maximum swing-arm angle of the swing-arm sprayer was 60° and the operation height of the

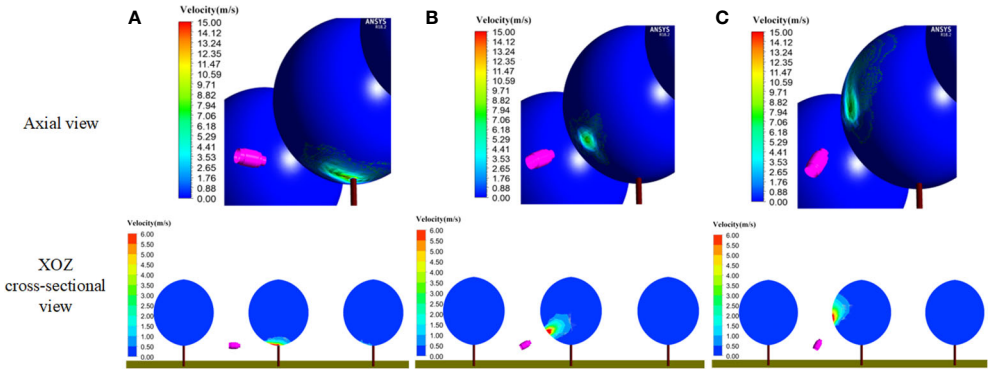

FIGURE 12
Fan air speed distribution under different swing-arm angles. **(A)** Swing-arm angle 0°. **(B)** Swing-arm angle 30°. **(C)** Swing-arm angle 60°.

plant-protection UAV was 2.0 m, the wind fields of the two devices could be coupled enough.

3.2 Results and analysis of the orthogonal experiment

The orthogonal test results are shown in from Table 5 to Table 7.

In terms of droplet deposition density, deposition uniformity and range analysis (Tables 5–7), it is known that the results of experiment group 1 (A1B1C1 group) were better than the others, demonstrating an optimal spraying performance.

According to Table 6, the factors affecting the droplet deposition density in order of priority were the speed of the swing-arm sprayer, the operating height and the operating speed of the T16 UAV.

According to Table 7, for the top of canopies, the order of factors affecting the uniformity of droplet distribution was T16

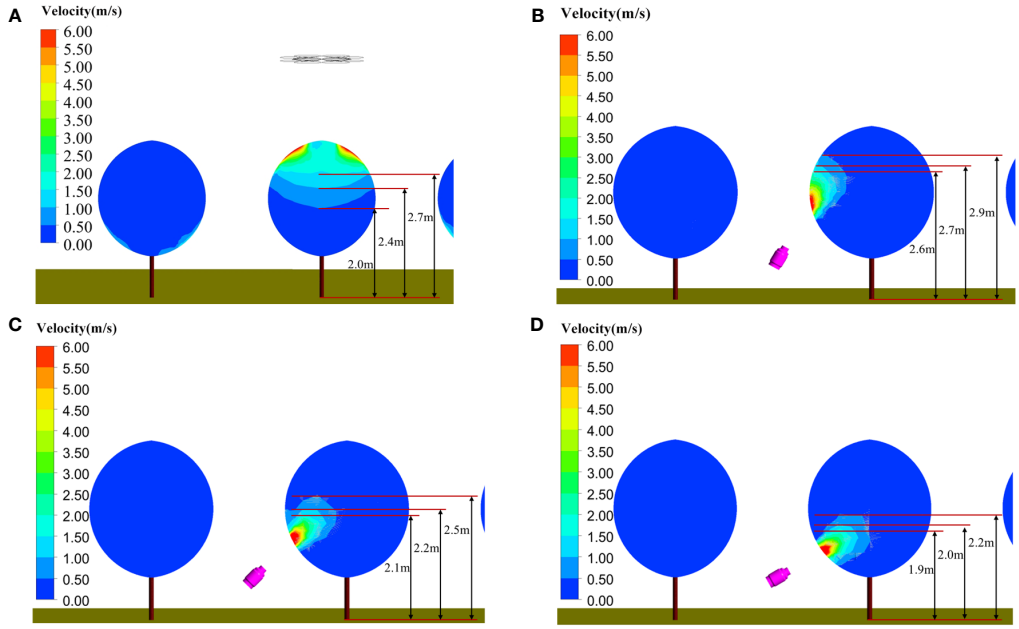

FIGURE 13
Comparison of canopy wind field coupling under different operating parameters. **(A)** Plant-protection UAV operation height 2.0 m. **(B)** Swing-arm angle of swing-arm sprayer 60°. **(C)** Swing-arm angle of swing-arm sprayer 45°. **(D)** Swing-arm angle of swing-arm sprayer 30°.

TABLE 5 Results of vertical longitudinal droplet deposition distribution in the canopy.

Experimental group	Droplet deposition density (deposits/cm^2)			Coefficient of variation/%		
	Top layer	Middle layer	Bottom layer	Top layer	Middle layer	Bottom layer
1	90.10	99.60	106.80	43.75	16.08	10.54
2	73.80	91.90	95.40	44.82	31.39	32.79
3	65.60	103.90	95.20	82.25	31.90	45.13
4	49.50	61.30	79.60	87.00	95.00	39.00
5	63.20	53.30	70.30	53.58	17.94	33.16
6	52.90	80.60	88.50	61.75	34.28	28.25
7	66.80	91.10	94.20	42.03	33.23	39.85
8	58.90	101.10	65.90	39.84	25.60	25.91
9	78.00	56.20	52.90	61.22	76.59	64.88

TABLE 6 Canopy vertical longitudinal droplet deposition density range analysis.

Indicators	Factor A			Factor B			Factor C		
	Top layer	Middle layer	Bottom layer	Top layer	Middle layer	Bottom layer	Top layer	Middle layer	Bottom layer
K_1	229.50	295.40	297.40	206.40	252.00	280.60	201.90	281.30	261.20
K_2	165.60	195.20	238.40	195.90	246.30	231.60	201.30	209.40	227.90
K_3	203.70	248.40	213.00	196.50	240.70	236.60	195.60	248.30	259.70
$\overline{K_1}$	76.50	98.50	99.10	68.80	84.00	93.50	67.30	93.80	87.10
$\overline{K_2}$	55.20	65.10	79.50	65.30	82.10	77.20	67.10	69.80	76.00
$\overline{K_3}$	67.90	82.80	71.00	65.50	80.20	78.90	65.20	82.80	86.60
Range	21.30	33.40	28.10	3.50	3.80	16.30	2.10	24.00	11.10

K_i indicates the sum of the experimental results corresponding to each factor at level i, $\overline{K_i}$ indicates the mean of the experimental results corresponding to each factor at level i.

plant-protection UAV operation height, swing-arm sprayer speed and T16 plant-protection UAV operation speed. For the middle and lower part of canopies, that was UAV operation speed, UAV operation height and swing-arm sprayer travel speed.

According to the analysis of the above experimental results, the optimal operation parameters of SPS were: a speed of 0.4 m/s and 1.0 m/s for the swing-arm sprayer and the T16 plant-protection UAV, respectively, and an operating height of 2.0 m for the UAV.

3.3 Results and analysis of the verification trials

The results of the verification trials are shown in Figure 14.

The SPS could significantly increase droplet deposition density. When the T16 plant-protection UAV operated independently, the canopy droplet deposition density decreased from top to bottom. The maximum droplet deposition density was 101 deposits/cm^2 at the top layers, and its range was nearly 61 deposits/cm^2. When the swing-arm sprayer operated independently, it was less than 10 deposits/cm^2, and the density in the middle and lower layers was closer and reached the spray quality requirements. The maximum density range was 24 deposits/cm^2. When the SPS operated, the density range was from 90 to 107 deposits/cm^2, and the maximum density range was only 17 deposits/cm^2.

The uniformity of droplet distribution of the SPS was generally better than that of the T16 UAV and the swing-arm sprayer. It was only weaker than the T16 UAV in the upper canopy layer. The coefficient of variation was 16.1% and 10.5% in the middle and lower canopy layers, 38.3% higher than that of the conventional air-assisted sprayer in the corresponding positions. The horizontal radial droplet distribution of the SPS was better than that of both the T16 UAV and the swing-arm sprayer. The variation coefficients of each canopy layer of the SPS from the outside to the inside were 29.8% 34.2% and 15.8%.

The SPS performed better than the T16 plant-protection UAV and swing-arm sprayer in terms of droplet deposition

TABLE 7 Canopy vertical longitudinal fog droplet distribution uniformity range analysis.

Indicators	Factor A			Factor B			Factor C		
	Top layer	Middle layer	Bottom layer	Top layer	Middle layer	Bottom layer	Top layer	Middle layer	Bottom layer
K_1	170.82	79.37	88.46	172.78	144.31	89.39	145.34	75.96	64.70
K_2	202.33	147.22	100.41	138.24	74.93	91.86	193.04	202.98	136.67
K_3	143.09	135.42	130.64	205.22	142.77	138.26	177.86	83.07	118.14
$\overline{K_1}$	56.94	26.46	29.49	57.59	48.10	29.80	48.45	25.32	21.57
$\overline{K_2}$	67.44	49.07	33.47	46.08	24.98	30.62	64.35	67.66	45.56
$\overline{K_3}$	47.70	45.14	43.55	68.41	47.59	46.09	59.29	27.69	39.38
Range	19.74	22.61	14.06	22.33	23.12	16.29	15.90	42.34	23.99

K_i indicates the sum of the experimental results corresponding to each factor at level i, $\overline{K_i}$ indicates the mean of the experimental results corresponding to each factor at level i.

density on the front and back of the leaves. The droplet density on both sides was higher than the theoretical application requirement of 25 deposits/cm^2.

The ground loss of the SPS and the SSA-E541 air-assisted sprayer were compared. As shown in Figure 15, the ground loss of the SPS reduced significantly.

According to the analysis above, it is indicated that the spraying performance of the SPS was obviously improved. The SPS could be a new way for mechanisation of orchard plant protection, especially for the orchards in hilly areas.

3.4 Discussions

The trafficability of the miniaturised sprayers and the high flexibility of plant-protection UAVs could effectively solve the

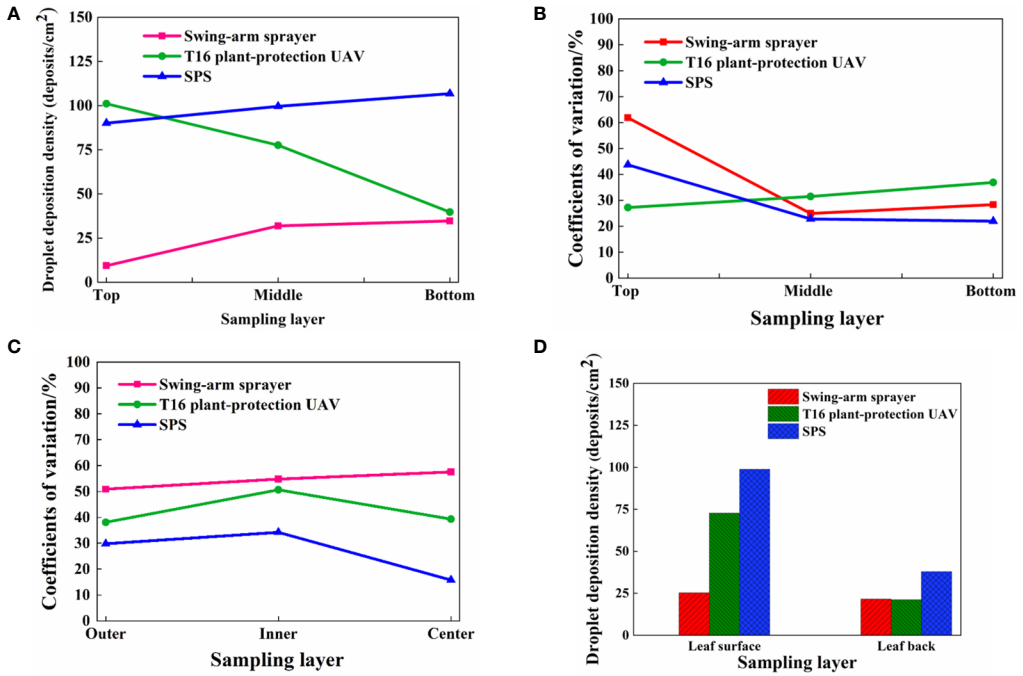

FIGURE 14
Results of the validation experiment of the SPS. **(A)** Vertical longitudinal sampling layer droplet deposition density. **(B)** Vertical longitudinal sampling layer droplet distribution uniformity. **(C)** Horizontal radial sampling layer droplet distribution uniformity. **(D)** Density of droplet deposition on leaf surface and leaf back. The values in the figure are the average values of the sampling points when not stated. For example, the density of droplet deposition in the top of canopies was the means of the values of all the corresponding positions.

FIGURE 15
Comparison of ground loss.

difficulties of a) large machines entering and leaving and b) the non-uniform application of small machines.

Compared with field crops, fruit trees have the characteristics of large canopies. The phenomenon of depression between rows is common, especially in mature fruit trees and traditional orchards. There is the problem of impermeable and uneven canopies during spraying, and it is difficult for sprayers to be applied in such orchards. To solve the above issues, this study proposes a layered spraying method, using a plant-protection UAV and a small ground sprayer to spray different locations of canopies, respectively. This method ensures good passability in orchards and improves spray uniformity in canopies. The feasibility of this method was further verified through actual orchard trials.

However, there are still some shortcomings:

1. this study obtained the optimal parameters of SPS by using CFD and orthogonal tests. Nonetheless, the parameter selection took a lot of time, and the subsequent experiments can be performed to further optimization of the best parameter determination method and improve the efficiency.
2. In this study, the experiments were conducted in mango orchards (big canopy). The reliability of application parameters needs to be further verified for orchards with vertical planting patterns (high canopies).
3. precision application methods (such as target application and variable application) can be combined to improve pesticide use further and reduce waste and environmental pollution.

4 Conclusion

To solve the problems that the spray droplet distribution of plant-protection UAV on the canopy is 'more on top and less on the bottom', while the ground sprayer is 'less on top and more on the bottom', an asynchronous stratified stereoscopic plant-protection method combining small ground sprayer and a plant-protection UAV is proposed. The main conclusions are as follows:

1. The overall scheme of stereoscopic plant-protection was defined based on the spraying requirements. The plant-protection UAV was selected and a small swing-arm sprayer was designed. The SPS consisting of a T16 six-rotor plant-protection UAV and a small swing-arm sprayer was developed.
2. The CFD-based optimisation of the operational parameters of the SPS was conducted. The wind field distribution characteristics of the plant-protection UAV and the swing-arm sprayer were clarified, and the

coupling effects of the canopy wind field of stereoscopic spraying were analyzed. The theoretical operating parameters of the SPS for uniform application to the canopy of fruit trees were identified. The operating height of the plant-protection UAV was 2.0 m, and the swing-arm angle of the swing-arm sprayer was 60°.

3. Based on CFD numerical simulation, a three-factor with three-level orthogonal experiment was conducted to identify the optimal parameters of the SPS. The speed of the swing-arm sprayer was 0.4 m/s, the operating height of the T16 plant-protection UAV was 2.0 m, and the operating speed was 1.0 m/s, respectively. They were selected for the verification experiments of the SPS. The results showed that the SPS had a vertical longitudinal droplet deposition density of 90-107 deposits/cm^2 in canopies, and the coefficients of variation of uniformity in the top, middle and lower layers were 43.7%, 16.1% and 10.5%, respectively, and the uniformity was 38.3% higher than conventional air-assisted sprayers. The coefficient of uniformity variation of the horizontal radial canopy from outer to central layers was 29.8%, 34.2% and 15.8%, respectively. The uniformity of application of the SPS in the upper, lower, inner and outer canopies of fruit trees were significantly improved, while the density of droplets deposited on both sides of the leaves was more than 25 deposits/cm^2, and could meet the spray requirements.

The SPS proposed in this paper can provide an adequate technical means and solution for uniform application to large canopy fruit trees. Meanwhile, the high mobility of plant-protection UAVs and the high trafficability of small swing-arm sprayers between orchard rows can solve the problem of the difficulty of entering and leaving the orchard when using large plant-protection equipment.

Data availability statement

The raw data supporting the conclusions of this article will be made available by the authors, without undue reservation.

Author contributions

SJ: Data curation, tests, and writing- original draft. BC: Formal analysis, data curation, visualization, tests. WL: Tests and validation. SY: Methodology, writing - review & editing. YZ: Supervision, methodology and resources. XL: Methodology and writing - review & editing. All authors contributed to the article and approved the submitted version.

Funding

This study is supported and funded by the Yantai Locality and University Cooperation Development Project (2021XDRHXMPT29), the National Key R&D Program of China (2018YFD0700603), and the National Natural Science Foundation of China (NSFC) (32171901).

Acknowledgments

Appreciation to Guangxi Agricultural Machinery Research Institute Co., Ltd. for their help in the experiment process.

Conflict of interest

The authors declare that the research was conducted in the absence of any commercial or financial relationships that could be construed as a potential conflict of interest.

Publisher's note

References

Cai, J., Wang, X., Song, J., Wang, S., Yang, S., and Zhao, C. (2017). Development of real-time laser-scanning system to detect tree canopy characteristics for variable-rate pesticide application. *Int. J. Agric. Biol. Eng.* 10, 155–163. doi: 10.25165/j.ijabe.20171006.3140

Chen, B., Zheng, Y., Jiang, S., Yang, S., Lv, H., and Kang, F. (2020). Resource consumption evaluation model of orchard spray machinery. *Trans. Chin. Soc. Agric. Machinery*. 51, 289–297. doi: 10.6041/j.issn.1000-1298.2020.S2.034

Chen, Y., Zhu, H., and Ozkan, H. E. (2011). "Development of LiDAR-guided sprayer to synchronize spray outputs with canopy structures," in *2011 ASABE annual international meeting sponsored by ASABE* Kentucky, US: Louisville. 11–24. doi: 10.13031/2013.37206

Dekeyser, D., Duga, A., Verboven, P., Endalew, A., Hendrickx, N., Nuyttens, D., et al. (2013). Assessment of orchard sprayers using laboratory experiments and computational fluid dynamics modelling. *Biosyst. Eng.* 114, 157–169. doi: 10.1016/j.biosystemseng.2012.11.013

Duga, A., Dekeyser, D., Ruysen, K., Bylemans, D., Nuyttens, D., Nicolai, B., et al. (2015). Numerical analysis of the effects of wind and sprayer type on spray distribution in different orchard training systems. *Boundary-Layer. Meteorol.* 157, 517–535. doi: 10.1007/s10546-015-0064-2

Duga, A., Delele, M., Ruysen, K., Dekeyser, D., Nuyttens, D., Bylemans, D., et al. (2016). Development and validation of a 3D CFD model of drift and its application to air-assisted orchard sprayers. *Biosyst. Eng.* 154, 62–75. doi: 10.1016/j.biosystemseng.2016.10.010

Endalew, A., Hertog, M., Delele, M., Baetens, K., Persoons, T., Baelmans, M., et al. (2009). CFD modelling and wind tunnel validation of airflow through plant canopies using 3D canopy architecture. *Int. J. Heat. Fluid. Flow* 30, 356–368. doi: 10.1016/j.ijheatfluidflow.2008.12.007

Fessler, L., Fulcher, A., Lockwood, D., Wright, W., and Zhu, H. (2020). Advancing sustainability in tree crop pest management: refining spray application rate with a laser-guided variable-rate sprayer in apple orchards. *Hortscience* 55, 1522–1530. doi: 10.21273/HORTSCI15056-20

Grella, M., Miranda Fuentes, A., Marucco, P., and Balsari, P. (2020). Field assessment of a newly-designed pneumatic spout to contain spray drift in vineyards: evaluation of canopy distribution and off-target losses. *Pest Manage. Sci.* 76, 4173–4191. doi: 10.1002/ps.5975

He, X., Zeng, A., Liu, Y., and Song, J. (2011). Precision orchard sprayer based on automatically infrared target detecting and electrostatic spraying techniques. *Int. J. Agric. Biol. Eng.* 4, 35–40. doi: 10.3965/j.issn.1934-6344.2011.01.035-040

Hołownicki, R., Doruchowski, G., Świechowski, W., Godyń, A., and Konopacki, P. J. (2017). Variable air assistance system for orchard sprayers; concept, design and preliminary testing. *Biosyst. Eng.* 163, 134–149. doi: 10.1016/j.biosystemseng.2017.09.004

Hong, S., Zhao, L., and Zhu, H. (2018a). CFD simulation of airflow inside tree canopies discharged from air-assisted sprayers. *Comput. Electron. Agric.* 149, 121–132. doi: 10.1016/j.compag.2017.07.011

Hong, S., Zhao, L., and Zhu, H. (2018b). CFD simulation of pesticide spray from air-assisted sprayers in an apple orchard: Tree deposition and off-target losses. *Atmospheric. Environ.* 175, 109–119. doi: 10.1016/j.atmosenv.2017.12.001

Jiang, S., Ma, H., Yang, S., Zhang, C., Su, D., Zheng, Y., et al. (2021). Target detection and tracking system for orchard spraying robots. *Trans. Chin. Soc. Agric. Eng.* 37, 31–39. doi: 10.11975/j.issn.1002-6819.2021.09.004

Jiang, S., Yang, S., Xu, J., Li, W., Zheng, Y., Liu, X., et al. (2022). Wind field and droplet coverage characteristics of air-assisted sprayer in mango-tree canopies. *Pest Manage. Sci.* 78, 4892–4904. doi: 10.1002/ps.7110

Jin, N., Lee, Y., Kim, Y., Kim, H., Hur, Y., Kim, Y., et al. (2017). The optimal dose and spraying method of chemical pesticides for pest control effects in apple orchards. *Kyushu Univ. Inst. Repository* 62, 393–402. doi: 10.5109/1854012

Kasner, E. J., Fenske, R. A., Hoheisel, G. A., Galvin, K., Blanco, M., Seto, E., et al. (2020). Spray drift from three airblast sprayer technologies in a modern orchard work environment. *Ann. Work. Exposures. Health* 64, 25–37. doi: 10.1093/annweh/wxz080

Kira, O., Dubowski, Y., and Linker, R. (2018). *In-situ* open path FTIR measurements of the vertical profile of spray drift from air-assisted sprayers. *Biosyst. Eng.* 169, 32–41. doi: 10.1016/j.biosystemseng.2018.01.010

Liu, X., Li, Y., Li, M., Yuan, J., Fang, Q., Hou, J., et al. (2016). Design and test of smart-targeting spraying system on boom sprayer. *Trans. Chin. Soc. Agric. Machinery.* 47, 37–44. doi: 10.6041/j.issn.1000-1298.2016.03.006

Liu, Y., Ru, Y., Chen, Q., Chen, X., and Liu, B. (2020). Design and test of real-time monitoring system for UAV variable spray. *Trans. Chin. Soc. Agric. Machinery.* 51, 91–99. doi: 10.6041/j.issn.1000-1298.2020.07.011

Liu, X., Yuan, J., Zhang, X., Liu, F., and Li, S. (2012). Development and experiment on 3MQ-600 type air-assisted boom sprayer with air-deflector. *Trans. Chin. Soc. Agric. Eng.* 28, 8–12. doi: 10.3969/j.issn.1002-6819.2012.10.00

Liu, X., Zhang, C., Zhang, H., Yang, S., Jiang, S., Zheng, Y., et al. (2021). Inter-row automatic navigation method by combining least square and SVM in forestry. *Trans. Chin. Soc. Agric. Eng.* 37, 157–164. doi: 10.11975/j.issn.1002-6819.2021.09.018

Liu, H., Zhu, H., Shen, Y., Chen, Y., and Ozkan, H. E. (2013). "Evaluation of a laser scanning sensor for variable-rate tree sprayer development," in *2013 ASABE annual international meeting sponsored by ASABE* Kansas City, MO, US. 1689–1700.

Manandhar, A., Zhu, H., Ozkan, E., and Shah, A. (2020). Techno-economic impacts of using a laser-guided variable-rate spraying system to retrofit conventional constant-rate sprayers. *Precis. Agric.* 21, 1156–1171. doi: 10.1007/s11119-020-09712-8

Meng, Y., Su, J., Song, J., Chen, W., and Lan, Y. (2020). Experimental evaluation of uav spraying for peach trees of different shapes: effects of operational parameters on droplet distribution. *Comput. Electron. Agric.* 170, 105282. doi: 10.1016/j.compag.2020.105282

Miranda-Fuentes, A., Llorens, J., Rodríguez-Lizana, A., Cuenca, A., Gil, E., Blanco-Roldána, G., et al. (2016). Assessing the optimal liquid volume to be sprayed on isolated olive trees according to their canopy volumes. *Sci. Total. Environ.* 568, 296–305. doi: 10.1016/j.scitotenv.2016.06.013

Miranda-Fuentes, A., Rodríguez-Lizana, A., Cuenca, A., González-Sánchez, E. J., Blanco-Roldán, G. L., Gil-Ribes, J., et al. (2017). Improving plant protection product applications in traditional and intensive olive orchards through the development of new prototype air-assisted sprayers. *Crop Prot.* 94, 44–58. doi: 10.1016/j.cropro.2016.12.012

Niu, M., Fang, H., Qiao, L., Jian, S., Zhu, Z., Peng, Q., et al. (2019). Design and experiment of high clearance type recycling tunnel sprayer. *J. Chin. Agric. Mechanization.* 40, 41–48. doi: 10.13733/j.jcam.issn.2095-5553.2019.11.07

Rehberg, R. A., Trivedi, P., Bahureksa, W., Sharp, J. L., Stokes, S. C., Menger, R., et al. (2020). Quantification of insecticide spatial distribution within individual citrus trees and efficacy through asian citrus psyllid reductions under different application methods. *Pest Manage. Sci.* 77, 1748–1756. doi: 10.1002/ps.6195

Rosell, J. R., and Sanz, R. (2012). A review of methods and applications of the geometric characterization of tree crops in agricultural activities. *Comput. Electron. Agric.* 81, 124–141. doi: 10.1016/j.compag.2011.09.007

Salcedo, R., Granell, R., Palau, G., Vallet, A., Garcerá, C., Chueca, P., et al. (2015). Design and validation of a 2D CFD model of the airflow produced by an air-blast sprayer during pesticide treatments of citrus. *Comput. Electron. Agric.* 116, 150–161. doi: 10.1016/j.compag.2015.06.005

Salcedo, R., Vallet, A., Granell, R., Garcerá, C., Moltó, E., Chueca, P., et al. (2017). Eulerian–Lagrangian model of the behaviour of droplets produced by an air-assisted sprayer in a citrus orchard. *Biosyst. Eng.* 154, 76–91. doi: 10.1016/j.biosystemseng.2016.09.001

Song, J., He, X., Zhang, J., Liu, Y., and Zeng, A. (2012). Design of Π-type recycling tunnel sprayer. *Trans. Chin. Soc. Agric. Machinery.* 43, 31–36. doi: 10.6041/j.issn.1000-1298.2012.04.007

Wang, D., Zhang, J., Li, W., Xiong, B., Zhang, S., Zhang, W., et al. (2017) Design and test of dynamic variable spraying system of plant protection UAV. *Trans. Chin. Soc. Agric. Machinery.* 48, 86–93. doi: 10.6041/j.issn.1000-1298.2017.05.010

Xiao, K., Ma, Y., and Gao, G. (2017). An intelligent precision orchard pesticide spray technique based on the depth-of-field extraction algorithm. *Comput. Electron. Agric.* 133, 30–36. doi: 10.1016/j.compag.2016.12.002

Xu, T., Yu, F., Cao, Y., Du, W., and Ma, M. (2017). Vertical distribution of spray droplet deposition of plant protection multi rotor uav for japonica rice. *Trans. Chin. Soc. Agric. Machinery.* 48, 101–107. doi: 10.6041/j.issn.1000-1298.2017.10.012

Yandún Narváez, F. J., Salvo Del Pedregal, J., Prieto, P. A., Torres-Torriti, M., and Auat Cheein, F. A. (2016). LiDAR and thermal images fusion for ground-based 3D characterisation of fruit trees. *Biosyst. Eng.* 151, 479–494. doi: 10.1016/j.biosystemseng.2016.10.012

Yang, S., Tang, Q., Zheng, Y., Liu, X., Chen, J., and Li, X. (2020). Model migration for CFD and verification of a six-rotor UAV downwash. *Int. J. Agric. Biol. Eng.* 13, 10–18. doi: 10.25165/j.ijabe.20201304.5569

Zhai, C., Zhao, C., Wang, N., Long, J., Wang, X., Weckler, P., et al. (2018). Research progress on precision control methods of air-assisted spraying in orchards. *Trans. Chin. Soc. Agric. Eng.* 34, 1–15. doi: 10.11975/j.issn.1002-6819.2018.10.001

Zhang, Y., Lan, Y., Bradley, K., and Xue, X. (2016). Development of aerial electrostatic spraying systems in the united states and applications in China. *Trans. Chin. Soc. Agric. Eng.* 32, 1–7. doi: 10.11975/j.issn.1002-6819.2016.10.001

Zhang, H., Qi, L., Wu, Y., Cheng, Z., Liu, W., Musiu, E., et al. (2019). Distribution characteristics of rotor downwash airflow field under spraying on orchard using unmanned aerial vehicle. *Trans. Chin. Soc. Agric. Eng.* 35, 44–54. doi: 10.11975/j.issn.1002-6819.2019.18.006

Zhao, Y., Xiao, H., Mei, S., Song, Z., Ding, W., Jin, Y., et al. (2017). Current status and development strategies of orchard mechanization production in China. *J. China Agric. Univ.* 22, 116–127. doi: 10.11841/j.issn.1007-4333.2017.06.14

Zheng, Y., Chen, B., Lv, H., Kang, F., and Jiang, S. (2020a). Research progress of orchard plant protection mechanization technology and equipment in China. *Trans. Chin. Soc. Agric. Eng.* 36, 110–124. doi: 10.11975/j.issn.1002-6819.2020.20.014

Zheng, Y., Jiang, S., Chen, B., Lv, H., Wan, C., and Kang, F. (2020b). Review on technology and equipment of mechanization in hilly orchard. *Trans. Chin. Soc. Agric. Machinery.* 51, 1–20. doi: 10.6041/j.issn.1000-1298.2020.11.001

frontiers | Frontiers in Plant Science

TYPE Original Research
PUBLISHED 07 November 2022
DOI 10.3389/fpls.2022.1030962

OPEN ACCESS

EDITED BY
Ruirui Zhang,
Beijing Academy of Agricultural and Forestry Sciences, China

REVIEWED BY
Lang Xia,
Institute of Agricultural Resources and Regional Planning (CAAS), China
Xinyu Xue,
Ministry of Agriculture and Rural Affairs, China
Caicong Wu,
China Agricultural University, China

*CORRESPONDENCE
Jiangtao Qi
qijiangtao@jlu.edu.cn

†These authors have contributed equally to this work and share first authorship

SPECIALTY SECTION
This article was submitted to Technical Advances in Plant Science, a section of the journal Frontiers in Plant Science

RECEIVED 29 August 2022
ACCEPTED 19 October 2022
PUBLISHED 07 November 2022

CITATION
Li Y, Bao Z and Qi J (2022) Seedling maize counting method in complex backgrounds based on YOLOV5 and Kalman filter tracking algorithm. *Front. Plant Sci.* 13:1030962. doi: 10.3389/fpls.2022.1030962

Seedling maize counting method in complex backgrounds based on YOLOV5 and Kalman filter tracking algorithm

Yang Li[1,2,3†], Zhiyuan Bao[1,2†] and Jiangtao Qi[1,2*]

[1]Key Laboratory of Bionic Engineering, Ministry of Education, Jilin University, Changchun, China, [2]College of Biological and Agricultural Engineering, Jilin University, Changchun, China, [3]Key Laboratory of Tea Quality and Safety Control, Ministry of Agriculture and Rural Affairs, Tea Research Institute, Chinese Academy of Agricultural Sciences, Hangzhou, China

Maize population density is one of the most essential factors in agricultural production systems and has a significant impact on maize yield and quality. Therefore, it is essential to estimate maize population density timely and accurately. In order to address the problems of the low efficiency of the manual counting method and the stability problem of traditional image processing methods in the field complex background environment, a deep-learning-based method for counting maize plants was proposed. Image datasets of the maize field were collected by a low-altitude UAV with a camera onboard firstly. Then a real-time detection model of maize plants was trained based on the object detection model YOLOV5. Finally, the tracking and counting method of maize plants was realized through Hungarian matching and Kalman filtering algorithms. The detection model developed in this study had an average precision mAP@0.5 of 90.66% on the test dataset, demonstrating the effectiveness of the SE-YOLOV5m model for maize plant detection. Application of the model to maize plant count trials showed that maize plant count results from test videos collected at multiple locations were highly correlated with manual count results (R^2 = 0.92), illustrating the accuracy and validity of the counting method. Therefore, the maize plant identification and counting method proposed in this study can better achieve the detection and counting of maize plants in complex backgrounds and provides a research basis and theoretical basis for the rapid acquisition of maize plant population density.

KEYWORDS

object detection, YOLOv5, video tracking, maize plants, counting prediction

Introduction

Crop planting density counts the number of plants per unit area, which has a great impact on the yield and quality of crops and is one of the important factors of agricultural production systems (Zhi et al., 2016; Zhai et al., 2018; Adams et al., 2019; Chapepa et al., 2020; Ndou et al., 2021). The research on maize planting density plays an important role in early breeding decisions to improve yield (Zhai et al., 2018). Therefore, it is essential to estimate the population density of maize accurately and timely.

To estimate plant population densities, the traditional field assessments method counts the number of plants in a randomly selected partition manually of a field and uses the average of multiple partitions to express plant population density. This method is time-consuming, labor-intensive, and inaccurate. To solve this problem, some studies have used color RGB images to count crops in the field (Lv et al., 2019; Zhao et al., 2021; Qi et al., 2022). These studies are based on traditional image processing algorithms that primarily use color information to segment crop areas for crop counting. These methods have high counting accuracy (approximately 90%) under certain conditions but have the following shortcomings. Firstly, the color information is easily affected by the surrounding light intensity and crop status. For example, plants looked darker on cloudy days than on sunny days and may have different colors at different stages of growth. Secondly, some counting methods are closely related to location and time. Typically, these methods require the necessary calibration by manually counting plants in a small portion of the field to build a regression model between pixel counts and actual plant counts. Then the regression model was applied to the rest of the images to achieve automatic processing. Therefore, a regression model established at one site (or growth stage) usually cannot be applied directly to another site (or growth stage), and the model needs to be re-validated or calibrated at a new site (or growth stage).

In recent years, many crop detection and counting methods based on traditional image processing (Zhao et al., 2021), machine learning (Lv et al., 2019), and deep learning technology (Qi et al., 2022) have been studied. For the three types of methods mentioned above, traditional image processing methods are easily disturbed by factors such as illumination, noise, and weed background. The shallow features such as color, shape, and texture extracted by machine learning methods have limited expression ability, and lack universality and adaptability. Deep convolutional neural networks (CNN) have shown powerful performance in object detection for agricultural images in recent years (Zhao et al., 2019). Many algorithms based on deep learning models have been successfully applied to the detection of a variety of crops. For example, researchers have explored the use of models such as YOLO and Faster-RCNN for the detection of fruits (Koirala et al., 2019; Häni et al., 2020), trees (Zhou et al., 2021), and crops (Hu et al., 2013; Jin et al., 2019). These studies reported promising detection accuracy and thus per-image counting accuracy.

For the counting methods based on image sequences, how to prevent the repeated counting of the same object in a continuous image sequence is a key problem. Methods to address this problem can be divided into three main categories. The first class of methods uses 3D reconstruction techniques to reconstruct space point cloud information from 2D images, then detection and counting were made in the 3D space (Häni et al., 2020; Gené-Mola et al., 2020). Since a plant is unique in the 3D space, a plant that is repeatedly counted in 2D images will be highly overlapped in the 3D space. Therefore, repeated counting of a plant can be avoided in the 3D space. The second class of methods uses the position and pose information of the imaging device to estimate the geometric correspondence between the same target in two consecutive images (Stein et al., 2016). Using this method, objects detected in two images captured at different locations can be associated, then the objects could be tracked and counted. The third type of method is the tracking method based on the object detection results. The key to this method is to establish the associations between detection results and the trackers (Gao et al., 2022; Lin et al., 2022). The mentioned three types of methods can achieve high counting accuracy under certain conditions, but they have certain shortcomings and problems. The method based on 3D reconstruction technology has a high computational cost and the 3D reconstruction results are easily affected by the external environment. The computational cost of the second method is lower than that of the method based on 3D reconstruction techniques, but the applied sensors (e.g., RTK GPS) made the cost of systems becomes very high. The detection-based tracking counting method has a low cost, but the robustness of this strategy is still insufficient to a certain extent. Since the IoU threshold is obtained from a small portion of the image sequence data, the threshold may fail when the test image sequence is obtained in a different environment (Jiang et al., 2019). Recently, other new tracking strategies can handle this problem. For example, the research of tracking algorithms based on correlation filtering has made promising progress recently, especially in the Kalman filtering method (Wang et al., 2019; Zhang et al., 2022).

The target detection model YOLOv5 has fast detection speed, and many target tracking algorithm has been applied to the tracking and quantity statistics of vehicles and pedestrians recently. Research shows that YOLOv5 and detection-based tracking algorithm could quickly and accurately count objects in videos. At the same time, UAVs have shown great potential as remote sensing platforms for crop growth monitoring in recent years (Wang et al., 2019). So it is necessary to explore the

research on the detection and counting of maize plants by combing of CNN and drones. In this study, the image datasets were collected by a low-altitude UAV first. Then the maize plants detection method based on the SE-YOLOV5m model was trained. And the trained SE-YOLOV5m model and Kalman filter algorithm were combined to track and count maize plants in individual videos. Finally, the counting method was tested and evaluated on test videos.

Materials and methods

Image acquisition and processing methods

The DJI Phantom 4 was used for taking pictures of corn canopy. The Phantom 4 featured a fully stabilized 3-Axis gimbal system with a 4k 12-megapixel camera and up to 27 minutes of flight time. The collection site was Nong'an County, Changchun (125.153436 N, 44.166099 E). According to the identification system, maize development can be divided into vegetative (V) and reproductive (R) stages. The V stages are designated numerically as V(n), where (n) represents the number of leaves with visible collars. We collected videos for plants from stages V4 to V6, which are the vegetative growth stages of maize plants (Zea mays L., Jingke 968) when the fourth, fifth, and sixth leaf collars are visible. The images and videos containing the maize plants were taken in different weather conditions (cloudy and sunny) with the UAV flying at a height of approximately 4 meters. The width and height of the images were 3840 and 2160 pixels, respectively. The collected videos are divided into a detection dataset and a counting dataset according to the ratio of 6:4. Images were extracted every 10 frames from every video in the detection set. They were used to train and validate the detection model together with the collected images. And videos in the counting dataset were used to validate the performance of the final counting algorithm. The training samples were manually labeled using Labelimg software (Tzutalin, 2015). Since the size of the original images was 3840 and 2160 pixels, which were too large for labeling and training. So the original images were first cropped to 960 and 540 pixels, respectively. The maize plants between the V4 and V6 stages look like small bell mouths when viewed from the top. It is obviously different from the rest of the leaves in color, brightness, and shape, so this feature is mainly used as the labeling standard. Some labeled images are shown in Figure 1. After labeling, a total of 2200 images were obtained, which contains 22235 maize plants. The images in the detection dataset were split into the a training set, a validation set, and a test set in the ratio of 8:1:1. In order to prevent overfitting and improve the generalization ability of the model, several date augmentations methods were applied. Such as image perturbation, changing brightness, changing contrast, changing saturation, changing hue, adding noise, random scaling, random crop, flipping, rotating, random erasing, and so on. In addition, Mosaic (Glenn, 2022) was also used. The data processing flow and data enhancement examples are shown in Figure 1.

Maize plants detection model

For the maize plant quantity statistics method proposed in this study, the first thing to study is the design of maize plant detection model. The model of YOLOv5 (Glenn, 2022) series is able to substantially improve the detection speed while maintaining the detection accuracy of existing models, and is one of the optimal choices for target detection. So the model of YOLOv5 series was used to build the maize plants detection

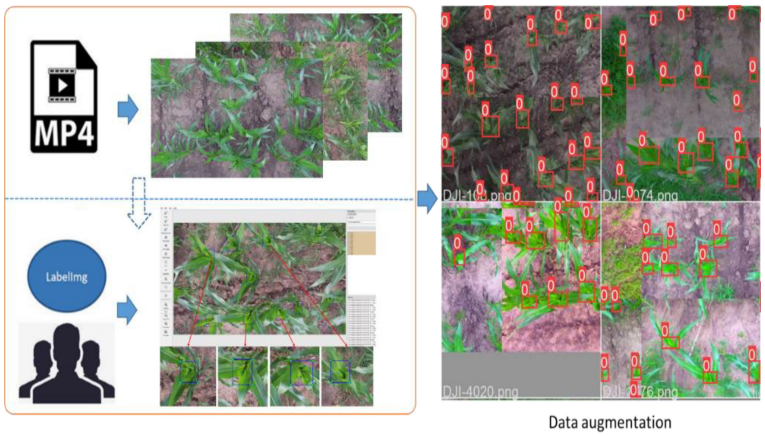

FIGURE 1
Data processing flow and data enhancement examples.

model. The YOLOv5 model is an upgraded version based on YOLOv3 (Redmon and Farhadi, 2018). Four object detection models of different depths and widths can be trained by using the official code. The YOLOv5s has the smallest depth and width in the YOLOv5 series. The other three networks are deepened and broadened on the basis of it. The YOLOv5 directly uses a single neural network to predict and classify input images to achieve end-to-end object detection. And it proposes cross-scale prediction, which enables the network to detect objects at three different scale features and adapt to multiple object detection tasks of different sizes. The backbone and the neck of the model use CSPDarknet53 (Wang et al., 2020) and the PAN (Liu et al., 2018) structure, respectively. Two different CSP modules are used in different parts of the model. Specifically, the C3_x module is applied to the backbone, the other C3_F_x module is used in the later structure. Comparing the speed and accuracy of the four different YOLOv5 models in Table 1, it can be seen that the mAP of YOLOv5m is 2.9% higher than that of YOLOv5s, and 0.8% and 1.6% lower than that of the YOLOv5l model and the YOLOv5x model, respectively. On the other hand, the model size of YOLOv5m is 26.7 MB larger than that of YOLOv5s, but it is 1/2 and 1/4 of that of YOLOv5l and YOLOv5x, respectively. Therefore, after balancing the detection accuracy and the model size of the network, the YOLOv5m model was used as the base for research.

Related research shows that visual attention mechanism can improve the accuracy of deep learning models (Yang et al., 2020). To improve the efficiency and accuracy of detecting maize plants, the Squeeze and Excitation Networks (SENet) (Hu et al., 2018) was introduced in the CNN. The SENet could obtain the weight of each channel of the features and then uses the weight to filter the key features, which could improve the representation capability of CNN. As shown in Figure 2, the SE module mainly contains squeeze and excitation operations (Hu et al., 2018). It performs a squeeze operation firstly, then performs an excitation on the global features to obtain the weights of different channels and the relationship between the channels. As shown in Figure 3, the structure of improved SE-YOLOv5m was proposed in this study. As shown in the figure, the SE module is embedded in the C3_x module and C3_F_x module individually. The purpose of the SE module is to enhance the feature extraction ability of the model by emphasizing the key feature of maize plants and suppressing background features to improve the detection accuracy in multiple scenarios.

TABLE 1 Comparison of model prediction results.

Models	mAP (%)	Average detection speed (ms)	Model size (MB)
YOLOV5s	87.65	18.2	14.1
YOLOV5m	90.24	20.3	40.8
YOLOV5l	91.02	22.4	89.2
YOLOV5x	92.15	25.6	166

Counting model based on YOLOV5

Firstly, the YOLOV5 model was used to detect maize plants in continuous static images. Then a tracker based on Kalman filter (Kalman, 1960) was used to track the maize plants to avoid repeated counting of them in continuous image sequences. Based on the trackers, each maize plant would be given a unique tracking number, so that every maize plant would only be counted only once. The tracking counting model contains three steps: maize plants state estimation, association and matching of maize plants between frames, and trackers update.

Maize plants state estimation

To track each maize plant detected by the detection model, the following state variable was used to represent the status of the maize plants:

$$\boldsymbol{t} = (\boldsymbol{u}, \boldsymbol{v}, \boldsymbol{s}, \boldsymbol{r}, \dot{\boldsymbol{u}}, \dot{\boldsymbol{v}}, \dot{\boldsymbol{s}}) \quad (1)$$

where u, v, s, r are the horizontal and vertical coordinates of the center point of the plant bounding box in image coordinates (in pixels), the area of the bounding box (in pixels), and the aspect ratio, respectively. $\dot{u}, \dot{v}, \dot{s}$ are their corresponding first derivatives with respect to time in image coordinates.

The plant tracking problem is a discrete-time series problem and consists of the following two main steps: the first is prediction process. Through the Kalman filter dynamic model, the state variables of the maize plant in the current frame would be used to predict the state variables in the next frame. The second step is the update process. The observed variables (detected bounding box) of the maize plant in the next frame would be used to update the state variables predicted in the prediction process (Jiang et al., 2019). Since the camera has a high frame rate, the position change of the target between video sequences is very small. So the motion of the camera can be regarded as a uniform motion. Therefore, it is assumed that the visual detection and tracking system is linearly correlated with the time change. A standard Kalman filter with constant velocity motion and linear observation model was used, which takes a 4-dimensional state (u, v, s, r) as the direct observation model of the maize plant.

The state parameters u, v, s, r of the tracker are initialized according to the detection results in the first frame, and $\dot{u}, \dot{v}, \dot{s}$ are set to 0. After the first frame ($i \geq 2$), the state variables (t) and the state covariance matrix ($\boldsymbol{P}$) of the trackers in the ith image are

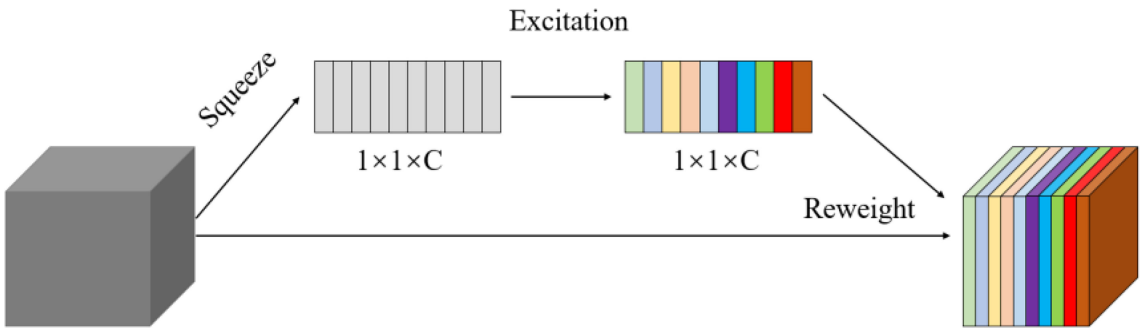

FIGURE 2
The structure of Squeeze and excitation (SE).

estimated using the data of the trackers in the (*i-1*)th image in the prediction process. The following formulas were used in the prediction process (Jiang et al., 2019):

$$\hat{t}_k^{i|i-1} = F\hat{t}_k^{i-1|i-1}, F = \begin{bmatrix} 1 & 0 & 0 & 0 & 1 & 0 & 0 \\ 0 & 1 & 0 & 0 & 0 & 1 & 0 \\ 0 & 0 & 1 & 0 & 0 & 0 & 1 \\ 0 & 0 & 0 & 1 & 0 & 0 & 0 \\ 0 & 0 & 0 & 0 & 1 & 0 & 0 \\ 0 & 0 & 0 & 0 & 0 & 1 & 0 \\ 0 & 0 & 0 & 0 & 0 & 0 & 1 \end{bmatrix} \quad (2)$$

$$P_{i|i-1} = FP_{i-1|i-1}F^T + Q, Q = \begin{bmatrix} 1 & 0 & 0 & 0 & 1 & 0 & 0 \\ 0 & 1 & 0 & 0 & 0 & 1 & 0 \\ 0 & 0 & 1 & 0 & 0 & 0 & 1 \\ 0 & 0 & 0 & 1 & 0 & 0 & 0 \\ 0 & 0 & 0 & 0 & 10^{-2} & 0 & 0 \\ 0 & 0 & 0 & 0 & 0 & 10^{-2} & 0 \\ 0 & 0 & 0 & 0 & 0 & 0 & 10^{-4} \end{bmatrix} \quad (3)$$

Where $\hat{t}_k^{i|i-1}$ is the *a priori* state estimate for the *k*th plant tracker in the *i*th frame, $\hat{t}_k^{i-1|i-1}$ is the a posteriori state estimate for the *k*th plant tracker in the (*i-1*)th frame, ***F*** is the state transfer matrix, $P_{i|i-1}$ is the *a priori* state covariance matrix for

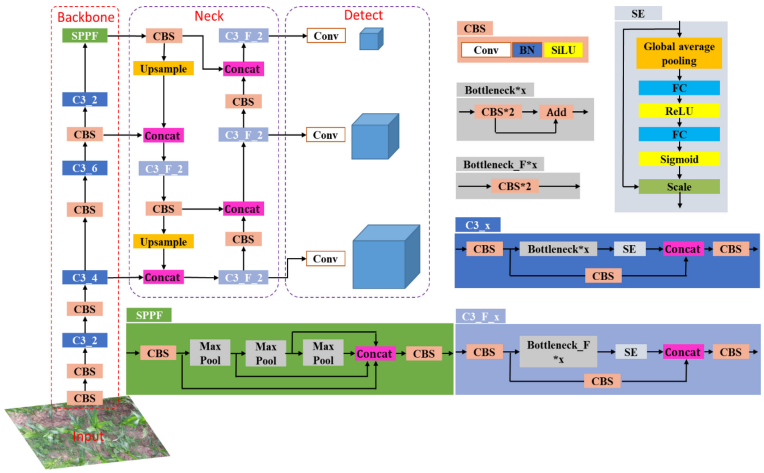

FIGURE 3
The structure of improved SE-YOLOV5m model. CBS contains a Conv, a BN and a SiLU (sigmoid liner relu) activation function, where Conv is 2D Convolutional layer, BN indicates batch normalization. C3_x indicates the use of a CBS structure with X residual modules (ResUnit), e.g. in the first C3_x, one residual components are used, hence C3_1. C3_F_X has the same meaning as C3_X.

the *i*th frame, $P_{i-1|i-1}$ is the a posteriori state covariance matrix for the (*i-1*)th frame, and *Q* is the random process noise matrix.

The following formula is used to calculate the posterior state covariance matrix of the *i*th frame image and the posterior state of the tracker.

$$S_i = HP_{i|i-1}H^T + R, H = \begin{bmatrix} 1 & 0 & 0 & 0 & 0 & 0 & 0 \\ 0 & 1 & 0 & 0 & 0 & 0 & 0 \\ 0 & 0 & 1 & 0 & 0 & 0 & 0 \\ 0 & 0 & 0 & 1 & 0 & 0 & 0 \end{bmatrix}, R$$

$$= \begin{bmatrix} 1 & 0 & 0 & 0 \\ 0 & 1 & 0 & 0 \\ 0 & 0 & 10 & 0 \\ 0 & 0 & 0 & 10 \end{bmatrix} \quad (4)$$

$$K_i = P_{i|i-1}H^T S_i^{-1} \quad (5)$$

$$P_{i|i} = (I - K_i H)P_{i|i-1}(I - K_i H)^T + K_i R K_i^T \quad (6)$$

$$y^i = d^t - H\hat{t}^{i|i-1}_{paired} \quad (7)$$

$$\hat{t}^{i|i}_{paired} = \hat{t}^{i|i-1}_{paired} + K_i y^i \quad (8)$$

where S_i is the covariance matrix of the measurement residuals for the *i*th frame and *H* is the measurement matrix that maps the tracker state variables to the measurement state variables (detection frame). *R* is the measurement error covariance matrix. K_i is the Kalman filter gain in the *i*th frame, and *I* is the identity matrix. y^i is the measured residual between the tracker's *a priori* estimated state of the *i*th image and the matched detection frame, and $\hat{t}^{i|i-1}_{paired}$is the amount of the tracker's a posteriori estimated state.

Association and matching between frames

In the update process, the trackers in the (*i-1*)th frame and the detection results ($\boldsymbol{D_i}$) of the *i*th frame were used. Since the detection results could be valued as the ground truth for the current frame, it is necessary to match the detection results with the trackers and thus update the Kalman filter. In this study, the IoU-based Hungarian algorithm (Kuhn, 2005) was used to establish the association between the detection results and the trackers. Figure 4 is a schematic diagram of a maize plant detection and a tracking bounding box. As shown in the figure, the white rectangle ABCD represents a maize plant bounding box predicted by the detector, and the yellow rectangle EFNM represents a maize plant bounding box predicted by the tracker. The overlap degree of the tracked bounding box and the detected bounding box is represented by formula (9). The closer the value of IoU is to 1, the higher the overlap and correlation between the detection bounding box and the tracking bounding box.

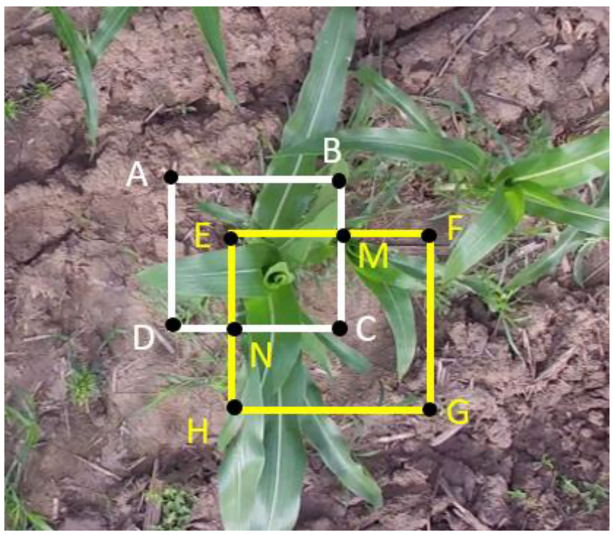

FIGURE 4
The schematic diagram of a maize plant detection and a tracking bounding box.

$$IoU = \frac{S_{EMCN}}{S_{ABCD} + S_{EFGH} - S_{EMCN}} \quad (9)$$

Then the IOU was used in the Hungarian algorithm to calculate the cost matrix to establish the corresponding matching relationship between the maize plant tracked bounding box predicted by Kalman filter and the detection bounding box predicted by detectors. Assuming that maize plants have been tracked in the *i*th frame image denoted as $T_i=\{T_1,T_2,\ldots,T_m\}$, and maize plants detected in the $(i+1)$th frame image denoted as $D_i=\{D_1,D_2,\ldots,D_n\}$. The matching correlation matrix $\boldsymbol{C}$ is obtained by calculating the IoU of the tracking frame $\boldsymbol{T}$ and the detection frame $\boldsymbol{D}$. The calculation formula is shown in equation (10).

$$\boldsymbol{C} = (c_{i,j})_{mxn} = IoU(T, D) \quad (10)$$

The threshold T_{thresh} was set to process the matching incidence matrix $\boldsymbol{C}$ to obtain the result matrix $\boldsymbol{R}$. The processing formula is shown in equation (11).

$$R = (r_{i,j})_{mxn} = \begin{cases} 0, & c_{i,j} < T \\ 1, & c_{i,j} > T \end{cases} \quad (11)$$

In the formula, T_{thresh} is equal to 0.3. when $r_{i,j}$ is 1, it means that the *i*th tracked maize plant is successfully associated with the *j*th detected maize plant. At the same time, it should be ensured that each tracked maize plant can only be associated with one detected maize plant. That is, equation (12) needs to be met.

$$max\sum_{i=1}^{M}\sum_{j=1}^{N} c_{i,j}r_{i,j} \quad s.t.\ (\sum_{i=1}^{M} r_{i,j} = 1, \sum_{j=1}^{N} r_{i,j} = 1) \quad (12)$$

Trackers update

After the matching of detection bounding boxes and trackers, detection bounding boxes ($\boldsymbol{D_i}$) and trackers ($\boldsymbol{T_{i-1}}$) can be divided into three categories: trackers associated with detection boxes, unmatched trackers, and unmatched detection bounding boxes. The trackers associated with detection boxes will be used in the update process. As for unmatched detection boxes, a new tracker will be created for each of them separately and will be added to the existing collection of trackers. For every unmatched tracker, its $\boldsymbol{V_{lost}}$ will be increased by 1, which means it loses the target once. When the cumulative number of lost targets reaches the set threshold $\boldsymbol{T_{lost}}$, it will be removed from the tracker set.

Since one tracker theoretically corresponds to one maize plant, the number of trackers is the number of maize plants. However, because the detection model may miss or misdetect, this will cause errors in the number of trackers and eventually lead to errors in the count of maize plants. For the missed detection problem of the detector, this study solves this problem by adding a parameter threshold $\boldsymbol{T_{lost}}$ to the algorithm. When the missing detection of the detector causes the unmatched tracker appears, the $\boldsymbol{V_{lost}}$ of the tracker will be increased by 1, which means that the tracker loses the target once. When the $\boldsymbol{V_{lost}}$ reaches the set threshold $\boldsymbol{T_{lost}}$, it will be removed from the tracker set. For the problem of false detection problem, the algorithm judges by setting the threshold $\boldsymbol{T_{life}}$. Only when the cumulative number of tracker existences of a plant is greater than the threshold $\boldsymbol{T_{life}}$, it will be regarded as a valid count.

A quantitative statistical method based on cross-line counting

If the detection model misses a maize plant in several frames and then detects it again in another frame, the original tracking ID will be discarded and then a new ID will be created. When maize plants appear at the edge of the image, the view of the center of plants is prone to distortion. At this time, the performance of the tracker and detector would be affected by this. Therefore, a counting baseline was defined in the image to improve the counting accuracy. As shown in Figure 5, the counting baseline (the yellow line) is defined at the center (1/2 height) of the image. The counting baseline served as a reference line to count maize plants. The tracked bounding box would be regarded as a valid count when it crosses the counting baseline (in Figure 5B). At the same time, the color of the tracking box will change from red to yellow, indicating that the tracker has been counted.

Test results and discussion

Model training and testing

The python version and framework used were Python 3.8 and Pytorch 1.5.0, respectively. Ubuntu 16.04 was used with the Intel Core I7 6700K processor (64GB RAM) and the Nvidia GeForce RTX 3090. CUDA 10.1 parallel computing framework and CUDNN 7.6 deep neural network acceleration library were used. The batch size and epochs were set to 24 and 300, respectively. Other hyperparameters used the default values given by the official website. A pretrained weight trained on Microsoft Common Objects in Context (MS COCO) dataset (Lin et al., 2015) was used to initialize the weight of the model. In order to validate the performance of the algorithm, precision, recall rate, missed rate, and average precision (AP) are used to evaluate the trained model. The calculation formulas are as follows:

$$P = \frac{TP}{TP + FP} \quad (13)$$

$$R = \frac{TP}{TP + FN} \quad (14)$$

FIGURE 5
Demonstration of the counting baseline for counting. The yellow line is the counting baseline. The top shows the *n* th frame; the bottom shows the *n+i* th frame. **(A, B)** shows the n-th frame and n+1 th frame, respectively.

$$M = \frac{FN}{TP + FN} \tag{15}$$

$$AP = \int_0^1 P(R)dR \tag{16}$$

where P is the precision, R is the recall, M is the miss detection rate, TP is the number of maize correctly detected by the model, FP is the number of backgrounds misclassified as maize plants and FN is the number of maize misclassified as background. Since the category detected in this study is only the maize plant, the AP (average precision) is equivalent to the commonly used mAP (mean average precision).

Detection results of the model on maize plants

The trained Faster RCNN, SSD, YOLOV5, and SE-YOLOV5 models were tested on the test dataset respectively. The results are shown in Table 2. Comparing in terms of accuracy and speed in Table 2, it can be seen that the YOLOV5 series models are superior to the SSD model in both accuracy and speed. Although the YOLOV5 series models are comparable to Faster RCNN in terms of accuracy, their speed is more than 7 times that of Faster RCNN. The mAP of SE-YOLOv5m is 1.21 higher than that of YOLOv5m. Meanwhile, the model size and the average detection

TABLE 2 Comparison of different detection models on the test set.

Models	mAP (%)	Average detection speed (ms)	Model size (MB)
YOLOV5m	90.24	20.3	40.8
SE-YOLOV5m	91.45	20.4	42.7
SSD	78.32	44.2	82.78
Faster R-CNN	91.88	180.4	110.8

speed of the SE-YOLOv5m model are close to that of the YOLOv5m model. Thus, the SE-YOLOv5m network model was adopted in this experiment after considering the detection accuracy and the lightweight requirement of the network.

Accuracy evaluation of the model under different weed proportions

Because weeds are easy to grow in the seedling stage of maize, excessive weeds may even affect the growth of maize. Therefore, the complex environment in this study mainly refers to different weed proportion. The presence of weeds in some areas of the maize field may have an impact on the accuracy of the detection model. Therefore, the above test set was split into three parts according to different the proportion of weeds in the field: a dataset with a weed proportion less than 30% (denoted by A), a dataset with a weed proportion between 30% and 60% (denoted by B) and a dataset with the weed proportion greater than 60%. Among them, the number of pictures in test sets A, B, and C are 80, 90, and 50, respectively. The tested models are the above-mentioned SE-YOLOV5 model and other state-of-art models. The detection results are shown in Table 3. The test sample results under different weed proportions are shown in Figure 6. It can be seen from the table and the figure that different weed proportions in the field have no significant

TABLE 3 Comparison of detection results under different weed rates.

Models	Dataset A	Dataset B	Dataset C
YOLOV5m	91.24	91.26	90.46
SE-YOLOV5m	92.68	92.65	92.02
SSD	79.24	79.12	78.62
Faster R-CNN	92.88	92.88	92.88

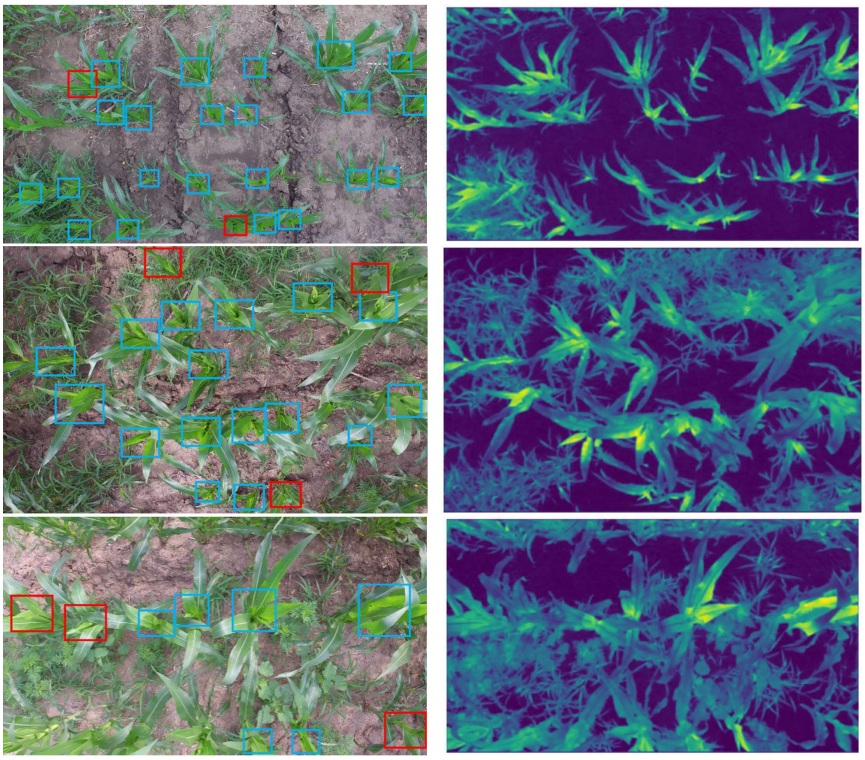

FIGURE 6
Detection results and feature maps of SE-YOLOV5m under different weed proportions. The left column shows detection results; the right column shows the corresponding feature maps of the last layer in the first C3_2 module of SE-YOLOV5m. From top to bottom are representative images with weed proportions less than 30%, between 30% and 60% and more than 60%, respectively. In the figure, the blue boxes and red boxes are the *TP* and *FN*.

influence on the detection accuracy of the maize plant detection models. The reason may be that weeds are different from maize plants in color, texture, and shape, so detection models are able to distinguish weeds from maize plants more directly. Then, the convolution feature maps of maize plants are visualized in Figure 6 to further analyze the reasons. It can be seen in Figure 6 that the features extracted by the model can well distinguish weeds from maize plants. In addition, it can also be seen from the FN samples in the figure (red boxes in the first column) that when the core leaves of the maize plant are partially obscured or the view of the central leaves is skewed, the model would have a certain degree of missed detection. It can also be seen from the corresponding feature map that the model can not extract effective feature information to distinguish maize plants at this time.

Counting accuracy regression analysis and evaluation

Videos in the counting dataset were segregated into 23 video clips for evaluating the developed counting algorithm, and they were individually counted by three researchers. Each video clip represented an approximately 3 m long segment in the videos. Frame rate and length of each video were about 30 frames per seconds (FPS) and 10 s, respectively. Then, the counting results were averaged to obtain the actual number of maize plants in the corresponding video. The counting algorithm based on SE-YOLOV5m was tested on the videos. Based on the proposed algorithm, the corn plant video tracking experiment was carried out. Figure 7 is an example of tracking a maize plant video sequence based on the proposed algorithm. As can be seen in the figure, the No. 24 corn plant has been detected and tracked for 55 consecutive frames in the video. Due to the disturbance of wind, the key features of the No. 50 maize plant are occluded in the 10^{th} and 44^{th} frames, which leads to intermittent missed detection. The algorithm can still track the target in subsequent images and keep the original ID unchanged, which is because T_{lost} is set in this study. When T_{lost} is not set, the algorithm cannot track the target in subsequent images. Therefore, it can be seen that although there is a short-term missed detection phenomenon in the video, the algorithm in this study could still effectively track maize plants.

In order to verify the performance of the proposed algorithm, 23 videos in the counting dataset are used as experimental data for comparative experiments. The comparison models were to replace the SE-YOLOv5m model in the proposed algorithm with the trained YOLOv5m, SSD, and Faster R-CNN models, respectively. The confusion matrix was used as the evaluation index to compare the performance of the

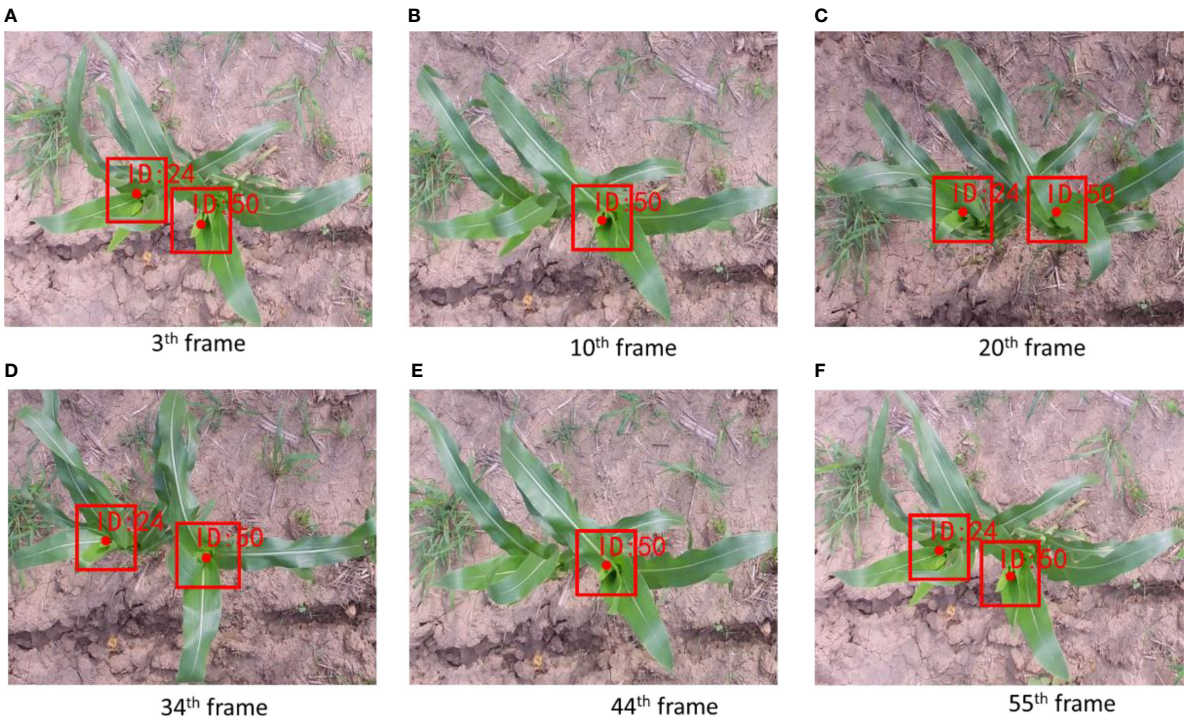

FIGURE 7
Tracking example of intermittently detected maize plant. **(A–F)** shows the result in the 3th frame, 10th frame, 20th frame, 34th frame, 44th frame and 55th frame, respectively.

four algorithms quantitatively. The experimental results are shown in Figure 8. At the same time, the frame rates of the proposed algorithm and the algorithm based on the above three models are 28.2, 28.4, 20.2, and 5.2, respectively. It can be seen from the results that the running speed of the proposed algorithm is similar to that of the counting algorithm based on YOLOv5m, but its accuracy is higher. The performance of the counting algorithm based on SSD is poor, mainly because the SSD model has low detection accuracy, which can also be confirmed in Table 2. Compared with the counting algorithm based on Faster R-CNN, the proposed method is faster on the basis of comparable accuracy. Although the counting algorithm based on Faster R-CNN performs well in terms of accuracy, there is still a lot of room for optimization in terms of running speed. Therefore, according to the comprehensive analysis of accuracy and speed, we can see that the performance of the proposed algorithm is the best among the four methods. Taking one of the videos as an example, there are a total of 311 frames of a video collected by UAV, and the statistical results are shown in Figure 9. Among them, the statistical result of the number of the 104th frame is 4, and the statistical result of the number of the first 241 frames is 14. During the process of tracking and matching, the number of some maize plants was lost at the edge (some plants don't have ID numbers), but the cross-line counting method effectively solved this problem. It shows that under the interference of ground weeds and wind, the algorithm in this study could accurately count the number of maize plants.

Conclusion

(1) The YOLOV5m model which incorporates a channel attention mechanism (SENet) was constructed to achieve effective detection of maize plants in a complex background. The mAP of the SE-YOLOV5m model on the test set was 90.66% (IoU 0.5), indicating the effectiveness of the SE-YOLOV5m model for detecting maize plants. The proposed SE-YOLOV5m model was able to infer at 20.4 ms on a GPU on an image with the size of 960 pixels × 540 pixels, which have the potential to be applied to embedded terminals. Evaluation under different weed proportions shows that different weed proportions in the field have no significant influence on the detection accuracy of the maize plant detection models.

(2) A deep-learning-based method for counting maize plants in a field was proposed, which used an improved YOLOV5 model with a Kalman filter. The mazie plant counting method proposed in this paper was compared with the counting algorithms based on YOLOv5, SSD and Faster R-CNN algorithms. The test results show that the proposed method is significantly better than the SSD-based algorithm in terms of

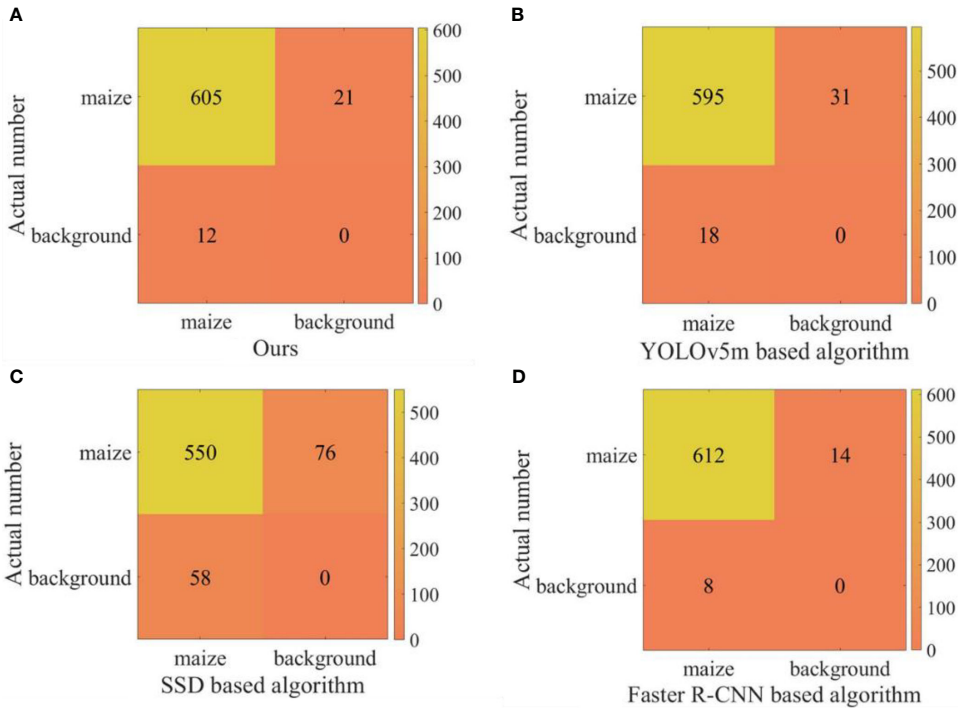

FIGURE 8
The confusion matrix of of the four algorithms. **(A–D)** shows the confusion matrix of Ours algorithm, YOLOv5m based algorithm, SSD based algorithm and Faster R-CNN based algorithm, respectively.

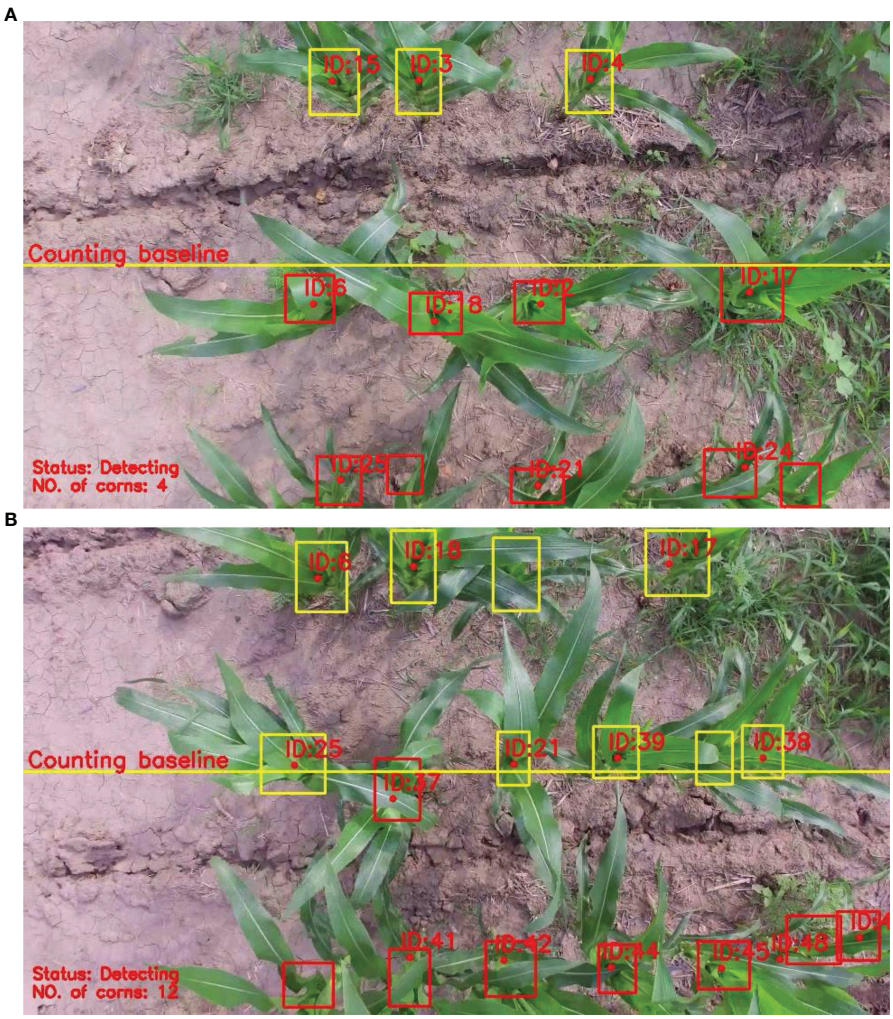

FIGURE 9
Visual video counting result of the algorithmic. The number on the bounding box is the ID of the mazie plant being tracked, and the solid point is the center of the mazie plant being tracked. The test video contains a total of 311 frames. In the figure, the 104 and 241 are typical frames. **(A, B)** shows the result in the 104th frame and 241th frame, respectively. Corrections has been post in the Production Forum.

accuracy and speed. Its speed is similar to that of the counting algorithm based on YOLOv5, but its accuracy is higher. Its accuracy is similar to that of the algorithm based on Faster R-CNN, but the frame rate is about 23 higher. Therefore, the proposed counting method is an effective method to achieve fast and accurate counting of the number of maize plants. In addition, the detection methods and annotated images used in this study could be used by the other researchers and engineers to further develop maize plants detection and counting methods.

Data availability statement

The raw data supporting the conclusions of this article will be made available by the authors, without undue reservation.

Author contributions

YL: conceptualization, methodology, writing—original draft. ZB: resources, software, data curation, and investigation. JQ: methodology, supervision, writing—review and editing, and funding acquisition. All authors contributed to manuscript revision, read, and approved the submitted version.

Funding

This study was supported by the National Natural Science Foundation of China (31971783) and the Central

Public-Interest Scientific Institution Basal Research Fund (1610212022004).

Conflict of interest

The authors declare that the research was conducted in the absence of any commercial or financial relationships that could be construed as a potential conflict of interest.

Publisher's note

All claims expressed in this article are solely those of the authors and do not necessarily represent those of their affiliated organizations, or those of the publisher, the editors and the reviewers. Any product that may be evaluated in this article, or claim that may be made by its manufacturer, is not guaranteed or endorsed by the publisher.

References

Adams, C., Thapa, S., and Kimura, E. (2019). Determination of a plant population density threshold for optimizing cotton lint yield: A synthesis. *Field Crops Res.* 230, 11–16. doi: 10.1016/j.fcr.2018.10.005

Chapepa, B., Mudada, N., and Mapuranga, R. (2020). The impact of plant density and spatial arrangement on light interception on cotton crop and seed cotton yield: an overview. *J. Cotton Res.*, 3 (3), 21–215. doi: 10.1186/s42397-020-00059-z

Gao, F., Fang, W., Sun, X., Wu, Z., Zhao, G., Li, G., et al. (2022). A novel apple fruit detection and counting methodology based on deep learning and trunk tracking in modern orchard. *Comput. Electron. Agric.* 197, 107000. doi: 10.1016/j.compag.2022.107000

Gené-Mola, J., Gregorio, E., Cheein, F. A., Guevara, J., Llorens, J., Sanz-Cortiella, R., et al. (2020). Fruit detection, yield prediction and canopy geometric characterization using LiDAR with forced air flow. *Comput. Electron. Agric.* 168, 105121. doi: 10.1016/j.compag.2019.105121

Glenn, J. (2022) *yolov5. git code*. Available at: https://github.com/ultralytics/yolov5 (Accessed 14 March 2022).

Häni, N., Roy, P., and Isler, V. (2020). A comparative study of fruit detection and counting methods for yield mapping in apple orchards. *J. Field Robot.* 37 (2), 263–282. doi: 10.1002/rob.21902

Hu, L., Luo, X., Zeng, S., Zhang, Z., Chen, X., and Lin, C. (2013). Plant recognition and localization for intra-row mechanical weeding device based on machine vision. *Transactions of the Chinese Society of Agricultural Engineering* 29, 10, 12–18. doi: 10.3969/j.issn.1002-6819.2013.10.002

Hu, J., Shen, L., and Sun, G. (2018). "Squeeze-and-excitation networks," in *IEEE/CVF Conference on Computer Vision and Pattern Recognition*. (New York, NY, USA: IEEE). pp. 7132–7141

Jiang, Y., Li, C., Paterson, A. H., and Robertson, J. S. (2019). DeepSeedling: deep convolutional network and kalman filter for plant seedling detection and counting in the field. *Plant Methods* 15 (1), 141. doi: 10.1186/s13007-019-0528-3

Jin, X., Madec, S., Dutartre, D., de Solan, B., Comar, A., and Baret, F. (2019). High-throughput measurements of stem characteristics to estimate ear density and above-ground biomass *Plant Phenom.* 2019, 10. doi: 10.34133/2019/4820305

Kalman, R. E. (1960). A new approach to linear filtering and prediction problems. *J. Fluids Eng. Trans. ASME* 82, 35–45. doi: 10.1115/1.3662552

Koirala, A., Walsh, K. B., Wang, Z., and McCarthy, C. (2019). Deep learning for real-time fruit detection and orchard fruit load estimation: Benchmarking of 'MangoYOLO'. *Precis. Agric.* 20 (6), 1107–1135. doi: 10.1007/s11119-019-09642-0

Kuhn, H. W. (2005). The Hungarian method for the assignment problem. *Naval Res. Logist.* 52 (1), 7–21. doi: 10.1002/nav.20053

Lin, Y., Chen, T., Liu, S., Cai, Y., Shi, H., Zheng, D., et al. (2022). Quick and accurate monitoring peanut seedlings emergence rate through UAV video and deep learning. *Comput. Electron. Agric.* 197, 106938. doi: 10.1016/j.compag.2022.106938

Lin, T., Maire, M., Belongie, S., Bourdev, L., Girshick, R., Hays, J., et al. (2015). *Microsoft COCO: Common objects in context* (Berlin, Germany: Springer Verlag).

Liu, S., Qi, L., Qin, H., Shi, J., and Jia, J. (2018). "Path aggregation network for instance segmentation," in *IEEE/CVF Conference on Computer Vision and Pattern Recognition*. (New York, NY, USA: IEEE). 8759–8768.

Lv, J., Ni, H., Wang, Q., Yang, B., and Xu, L. (2019). A segmentation method of red apple image. *Sci. Hortic.* 256, 108615. doi: 10.1016/j.scienta.2019.108615

Ndou, V., Gasura, E., Chivenge, P., and Derera, J. (2021). Grain yield gains and associated traits in tropical x temperate maize germplasm under high and low plant density. *Euphytica* 217 (10), 186. doi: 10.1007/s10681-021-02918-5

Qi, J., Liu, X., Liu, K., Xu, F., Guo, H., Tian, X., et al. (2022). An improved YOLOv5 model based on visual attention mechanism: Application to recognition of tomato virus disease. *Comput. Electron. Agric.* 194, 106780. doi: 10.1016/j.compag.2022.106780

Redmon, J., and Farhadi, A. (2018). "Yolov3: An incremental improvement," in *arXiv preprint*. Ithaca, NY, USA: Cornell University.

Stein, M., Bargoti, S., and Underwood, J. (2016). Image based mango fruit detection, localisation and yield estimation using multiple view geometry. *Sensors* 16 (11), 1915. doi: 10.3390/s16111915

Tzutalin, (2015) *LabelImg. git code*. Available at: https://github.com/tzutalin/labelImg (Accessed 1 Feb 2020).

Wang, C. Y., Liao, H. Y. M., Wu, Y. H., Chen, P. Y., Hsieh, J. W., and Yeh, I. H. (2020). "CSPNet: A new backbone that can enhance learning capability of CNN," in *IEEE/CVF Conference on Computer Vision and Pattern Recognition Workshops (CVPRW)*. (New York, NY, USA: IEEE). pp. 390–391)

Wang, Z., Walsh, K., and Koirala, A. (2019). Mango fruit load estimation using a video based MangoYOLO–kalman filter–hungarian algorithm method. *Sensors* 19, 2742. doi: 10.3390/s19122742

Yang, G., He, Y., Yang, Y., and Xu, ,. B. (2020). Fine-grained image classification for crop disease based on attention mechanism. *Front. Plant Sci.* 11. doi: 10.3389/fpls.2020.600854

Zhai, L., Xie, R., Ming, B., Li, S., and Ma, Da. (2018). Evaluation and analysis of intraspecific competition in maize: A case study on plant density experiment. *J. Integr. Agric.* 17 (10), 2235–2244. doi: 10.1016/S2095-3119(18)61917-3

Zhang, W., Wang, J., Liu, Y., Chen, K., Li, H., Duan, Y., et al. (2022). Deep-learning-based in-field citrus fruit detection and tracking. *Horticult. Res.* 9, uhac003. doi: 10.1093/hr/uhac003

Zhao, Y., Zheng, B., Chapman, S. C., Laws, K., George-Jaeggli, B., Hammer, G. L., et al (2021) Detecting sorghum plant and head features from multispectral UAV imagery. *Plant Phenom.* 2021, 14. doi: 10.34133/2021/9874650

Zhao, Z., Zheng, P., Xu, S., and Wu, X. (2019). Object detection with deep learning: A review. *IEEE Trans. Neural Networks Learn. Syst.* 30 (11), 3212–3232. doi: 10.1109/TNNLS.2018.2876865

Zhi, X., Han, Y., Li, Y., Wang, G., Du, W., Li, X., et al. (2016). Effects of plant density on cotton yield components and quality. *J. Integr. Agric.* 15 (7), 1469–1479. doi: 10.1016/S2095-3119(15)61174-1

Zhou, W., Zhu, X., and Chen, F. (2021). Spruce counting based on lightweight mask r-CNN with UAV images. *Int. J. Circuits Syst. Signal Process.* 15, 634–642. doi: 10.46300/9106.2021.15.70

frontiers | Frontiers in Plant Science

TYPE Original Research
PUBLISHED 09 November 2022
DOI 10.3389/fpls.2022.1037760

OPEN ACCESS

EDITED BY
Ruirui Zhang,
Beijing Academy of Agricultural and Forestry Sciences, China

REVIEWED BY
Songchao Zhang,
Nanjing Institute of Agricultural Mechanization (CAAS), China
Fiaz Ahmad,
Bahauddin Zakariya University, Pakistan
Haikuan Feng,
Beijing Research Center for Information Technology in Agriculture, China

*CORRESPONDENCE
Chunling Chen
chenchunling@syau.edu.cn

SPECIALTY SECTION
This article was submitted to Technical Advances in Plant Science, a section of the journal Frontiers in Plant Science

RECEIVED 06 September 2022
ACCEPTED 17 October 2022
PUBLISHED 09 November 2022

CITATION
Yu F, Jin Z, Guo S, Guo Z, Zhang H, Xu T and Chen C (2022) Research on weed identification method in rice fields based on UAV remote sensing. *Front. Plant Sci.* 13:1037760. doi: 10.3389/fpls.2022.1037760

Research on weed identification method in rice fields based on UAV remote sensing

Fenghua Yu[1,2], Zhongyu Jin[1], Sien Guo[1], Zhonghui Guo[1], Honggang Zhang[1], Tongyu Xu[1,2] and Chunling Chen[1,2]*

[1]College of Information and Electrical Engineering, Shenyang Agricultural University, Shenyang, China, [2]Department of Science and Technology, Liaoning Agricultural Information Engineering Technology Research Center, Shenyang, China

Rice is the world's most important food crop and is of great importance to ensure world food security. In the rice cultivation process, weeds are a key factor that affects rice production. Weeds in the field compete with rice for sunlight, water, nutrients, and other resources, thus affecting the quality and yield of rice. The chemical treatment of weeds in rice fields using herbicides suffers from the problem of sloppy herbicide application methods. In most cases, farmers do not consider the distribution of weeds in paddy fields, but use uniform doses for uniform spraying of the whole field. Excessive use of herbicides not only pollutes the environment and causes soil and water pollution, but also leaves residues of herbicides on the crop, affecting the quality of rice. In this study, we created a weed identification index based on UAV multispectral images and constructed the $WDVI_{NIR}$ vegetation index from the reflectance of three bands, RE, G, and NIR. $WDVI_{NIR}$ was compared with five traditional vegetation indices, NDVI, LCI, NDRE, and OSAVI, and the results showed that $WDVI_{NIR}$ was the most effective for weed identification and could clearly distinguish weeds from rice, water cotton, and soil. The weed identification method based on $WDVI_{NIR}$ was constructed, and the weed index identification results were subjected to small patch removal and clustering processing operations to produce weed identification vector results. The results of the weed identification vector were verified using the confusion matrix accuracy verification method and the results showed that the weed identification accuracy could reach 93.47%, and the Kappa coefficient was 0.859. This study provides a new method for weed identification in rice fields.

KEYWORDS

rice weeds, UAV, multispectral imaging, vegetation indices, remote sensing

1 Introduction

China is a large country of rice cultivation, and there are more varieties and classifications of rice in China. Field weeds plague the development of rice production and are a major factor in preventing high and stable rice yields (Feng et al., 2018). According to statistics, weed damage alone in 150 million acres of arable land worldwide causes more than $7 billion in losses each year, accounting for approximately one-third of the total damage caused by diseases, insects, and weeds, and directly causes 125 million tons of grain loss (Liu et al., 2014).Since weeds have a fast growth rate and well-developed root system, they are in an advantageous position to compete with rice for growth resources, thus inhibiting rice growth (Liu et al., 2020). Among them, weeds in paddy fields are diverse, with complex grass phase and a long occurrence period (Duarte et al., 2021; De Simone et al., 2022). By competing with rice for water, fertilizer, light, and space, they change the microecological environment of paddy fields, affect the photosynthesis, nutrition, and reproductive growth of rice, and are intermediate hosts of pests and diseases, aggravating the occurrence of pests and diseases, leading to yield reduction and decline of rice quality, and causing huge losses to rice production (Luo et al., 2020). In the current rice weed management process, chemical weed control is currently the most effective and widely used method of weed control in rice fields, commonly used to spray herbicides uniformly and covering the entire operating area in a disorderly "spot" or "sheet" form (Eppinga et al., 2020; Druskin et al., 2021; Wang et al., 2021). The presence of weeds can lead to excessive spraying of herbicides (Siva Kumar et al., 2020; Su et al., 2022). How to achieve accurate application of weed and reduce the use of agrochemicals is a key issue; the prerequisite to solving this problem is to achieve accurate and rapid detection and identification of weeds (Maes and Steppe, 2019). The rice weeds management process, chemical weed control, is currently the most effective and widely used method of weed control in rice fields, commonly used to spray herbicides uniformly and cover the entire operating area in a disorderly "spot" or "sheet" form. The presence of weeds can lead to overspray of herbicides. How to achieve accurate application of weed and reduce the use of agrochemicals is a key issue, and the prerequisite to solving this problem is to achieve accurate and rapid detection and identification of weeds (Carroll, 2020). Based on low-altitude UAV remote sensing technology, we can carry out accurate monitoring of weeds in rice fields and generate agricultural UAV weed application prescription maps, and carry out UAV precision weeding for rice, (Otsu et al., 2019), which is a new idea to solve the current herbicide overapplication problem. The prerequisite of herbicide precision application is to obtain remote sensing images of rice fields and analyze the weed distribution status in them, get a grid-shaped weed distribution map, and generate an herbicide operation prescription map (Matsunami et al., 2009). The use of UAVs to collect remote sensing images of rice fields and perform weed analysis has been similarly reported around the world.

The use of UAV remote sensing technology has enabled rapid image acquisition and weed mapping in crops such as sunflower, mango, and rice (Jin et al., 2022). While identifying weeds in rice, an important issue is the need to locate weeds against a green vegetation background (Stroppiana et al., 2018). When the technologies of remote sensing data acquisition, stitching and correction are more mature, backward research on the resolution of remote sensing data becomes the main bottleneck of remote sensing development (Tao and Wei, 2022). When parsing remote sensing data, machine learning is widely used for image classification, and weed image recognition models have been developed using deep learning neural networks in an increasing number of literatures (Kawamura et al., 2021). Andrea et al. used convolutional neural networks to distinguish maize plants from weeds in the early growth stage of the crop, and trained the convolutional neural networks using the data set generated in the segmentation stage, and the recognition accuracy reached 97.23% (Punithavathi et al., 2023). Flores et al. used support vector machine model (SVM), neural network (NN), random forest (RF), GoogLeNet and VGG-16 models for recognition detection after collecting image shape, color and texture feature values in a greenhouse environment to simulate field conditions, and finally the recognition accuracy of the VGG-16 model in distinguishing soybean seedlings from corn weeds reached. The accuracy of the VGG-16 model in distinguishing soybean seedlings from corn seedlings was 96.2%, which was the highest among the above five model methods (Hirohiko, 2002; Liu and Yu, 2013; Druskin et al., 2021). Sujaritha designed an automatic image classification system for extracting leaf texture using fuzzy real-time classification counting, which was able to correctly identify sugarcane crops among 9 different weeds, and the accuracy of the system in detecting weeds was 92.9% (Sujaritha et al., 2017). Spectral index can provide an important basis for the identification of rice weeds. Many studies have added spectral index to improve the identification accuracy of rice weeds. Barrero et al. used Neural Networks to detect gramineous weeds 50 days after the emergence of rice field using visible light band and NGRDI index image fusion. The M/MGT index values obtained from the detection results ranged from 80 to 108%. MP values range from 70 to 85% (Barrero and Perdomo, 2018). Stroppiana et al. used spectral information, SAVI and GSAVI spectral indices and unsupervised clustering algorithms to classify weeds in the early stages of the growing season, with an overall accuracy higher than 94% (Stroppiana et al., 2018). Kawamura et al. used a combination of hue-saturation-brightness, canopy height model, spatial texture, color index of vegetation extraction and excess green. A classifier combining simple linear iterative clustering algorithm and random forest algorithm was used to identify weeds in the early growth stage of small rice plants. out-of-bag accuracy is higher than 0.915 (Kawamura et al., 2021).

Currently, related research mainly focuses on the identification and detection of weeds in paddy fields, while relatively little research

has been conducted on how to generate accurate operation prescription maps for agricultural drones through weed distribution information in paddy fields (Mohidem et al., 2021). Northern coldland rice is usually weeded 15-20 days after transplanting, therefore, in this study, remote sensing images of rice tillering stage were selected to identify weeds. By observing the UAV remote sensing images, weeds in northern cold rice were found to have less differences in textural characteristics, similar shapes and the same color as rice at the tillering stage (Motavalli et al., 2012; Souri et al., 2022). Weeds have group aggregation, and it is difficult to distinguish them from rice using UAV visible remote sensing images, while spectra can reflect their physicochemical information and highlight their aggregation characteristics. Therefore, this paper uses spectra to identify weeds in rice fields. In this study, the DJI Phantom 4 UAV and its multispectral camera were used to collect multispectral remote sensing images of paddy fields (Zhu et al., 2020). With rice weeds as the identification target, the vegetation index was constructed to highlight the spectral characteristics of weeds (Lu and Zhang, 2020; Nawaz et al., 2021). The density partitioning algorithm is used to obtain the distribution information of the weeds in the rice field and generate the weed distribution map with the best classification effect (Wang et al., 2019). It provides a decision basis for the application of precision pesticides by agriculture UAV.

2 Materials and methods

2.1 Study area and experimental details

The trial site was located at the precision agriculture aerial research base of Shenyang Agricultural University, Gengzhuang Town, Haicheng City, Liaoning Province (40° 58' 45.39" N, 122° 43' 47.01" E), and the test variety was "Japonica 653", a variety widely grown in Liaoning. In this study, the UAV multispectral images and visible images were collected separately from the test field on June 23, 2021. The weeds in the study area were mainly barnyard grass and Monochoria korsakowii Regel & Maack, which were verified in the field.

2.2 Data acquisition

The multispectral remote sensing image data collection equipment was Phantom 4 RTK UAV combined with ground station software DJI GS PRO for route planning. Multispectral remote sensing UAV flight altitude of 25 meters, UAV longitudinal and lateral route overlap rate of 85%. six 1/2.9-inch CMOS, including five monochrome sensors for multispectral imaging single sensor, effective pixels 2.08 million. five characteristic wavelength specific information as shown in Table 1.

TABLE 1 Characteristic wavelengths of multispectral UAV remote sensing platform.

Name	Central wavelength	Wavelength range
Blue (B)	450 nm	± 16 nm
Green (G)	560 nm	± 16 nm
Red (R)	650 nm	± 16 nm
Red edge (RE)	730 nm	± 16 nm
Near Infrared (NIR)	840 nm	± 26 nm

The multispectral camera has an FOV of 62.7°, a focal length of 5.74 mm, and an aperture of f/2.2. Monochrome sensors gain in the range of 1-8 multiples.The flying speed of the UAV is set to 5m/s, the altitude is 30m, and the heading and side-direction repetition rate is 80%.

The Phantom 4 RTK quadrotor UAV was used as the flight platform to acquire visible light remote sensing images, with a built-in RTK differential positioning system and a positioning accuracy of 1 cm + 1 ppm, 1 ppm means that the error increases by 1 mm for every 1 km of flight (Lambert et al., 2019; Niu et al., 2021). DJI flight software was used to plan the route of the test area, and orthophoto raw data from the test field were obtained by taking photos at regular intervals.

In this study, multispectral and visible images were acquired for weed identification using a Phantom 4 RTK UAV on June 18, 2021 (Wei et al., 2021). The validation data in this study were visually interpreted using a manual visual interpretation method for the visible images, and a total of 141,483 pixel points were selected, including 48,255 pixel points for the weed category and 93,228 pixel points for the non-weed category.

2.3 UAV remote sensing image processing

Pix4D image processing software was used to orthorectify and crop the visible images of the test area collected by UAV, and finally high-resolution orthophotos of the rice fields were obtained.

When the Phantom 4 RTK multispectral UAV remote sensing platform observes the target radiant energy, the radiation distortion caused by the sensor response characteristics and external natural conditions (including solar radiation conditions and atmospheric transmission conditions, etc.) causes distortion of the remote sensing images and affects the interpretation and decoding of remote sensing images; therefore, the radiation calibration of multispectral images is needed. In this study, first, three reflectivity plates with 60% reflectivity were laid flat on the ground near the measurement area, and the Phantom 4 RTK multispectral took off to a height of 7 times the side length of the plates, adjusted the aircraft position so that the plates were in the center of the camera frame and ensured that there was no shadow

on the plates, then adjusted the gimbal to -90°, kept the EV value at 0 and took a set of photos manually (Naji, 2018). The multispectral image is used to correct the reflectivity of the acquired UAV remote sensing image.

2.4 Research methods

2.4.1 Construction of Vegetation Index

Most of the existing multispectral remote sensing UAV images are used as input of the weed identification model by the NDVI, EVI, DVI and other indices, but the above vegetation indices are more used to carry out inversion studies of physical and chemical parameters of rice, while the accuracy of rice weed identification still has some shortcomings (Clevers and Verhoef, 1993). In this study the characteristic vegetation indices of the weed(WDVI) were constructed by analyzing the spectral characteristics between the weeds and the rice, and the specific construction methods are as follows.

(1) UAV multispectral wavelengths of x_B、x_G、x_R、x_{RE}、x_{NIR} .

(2) Selection of the band x_t(t∈B、G……*NIR*) as the characteristic transfer band.

(3) Construct the characteristic spectral ratio of multiple groups using other characteristic bands x_f(f∈B、G……*NIR*, and f≠t) as a ratio to x_t , both $W_f = \frac{x_f}{x_t}$.

(4) After taking the logarithm of the ratio result, the correlation with nitrogen content remained good. Therefore, two sets of characteristic spectral ratios W_f (f∈B、G……*NIR*) , were selected and the characteristic transfer index of weeds(WDVI) was constructed using Equation 1:

$$WDVI = log_{W_f} B_f = log_{\frac{x_b}{x_t}} \frac{x_a}{x_t} \quad (1)$$

In this study, five vegetation indices were constructed using five bands, as shown in Table 2

TABLE 2 Five medium Combination Vegetation Index.

Name	Formula
WDVI1	$WDVI_{NIR} = \log_{\frac{G}{NIR}} \frac{RE}{NIR}$
WDVI2	$WDVI_{NIR} = \log_{\frac{R}{NIR}} \frac{RE}{NIR}$
WDVI3	$WDVI_{NIR} = \log_{\frac{RE}{NIR}} \frac{R}{NIR}$
WDVI4	$WDVI_{NIR} = \log_{\frac{R}{NIR}} \frac{G}{NIR}$
WDVI5	$WDVI_{NIR} = \log_{\frac{G}{NIR}} \frac{R}{NIR}$

2.4.2 Weed identification modeling methods

Threshold segmentation is the earliest method studied and used in image segmentation, which has the characteristics of clear physical meaning, easy implementation, and good real-time performance (Setojima et al., 1989; Qin et al., 2013). According to the regional weed distribution map after visual interpretation of visible light remote sensing images and experience knowledge, this study adjusts the gray segmentation threshold of the multispectral index to determine the distribution range of weeds in the index. The grid threshold partition mapping function is as follows:

$$f(x,y) = \begin{cases} 0 & 0 \le f(x,y) \le t \\ L-1 & t < (x,y) \le L-1 \end{cases} \quad (2)$$

Let the size of the raster image be M × N, and the gray level number be L, and f (x, y) denotes the gray level of the pixel with coordinates (, y), where x ∈ [1, M] and y ∈ [1, N].

According to the gray segmentation threshold, the grid image of weed distribution is extracted (Bouman et al., 1992). The algorithm to remove small patches is used to remove scattered grids in the grid images, and the spatial distribution map of weeds is obtained. The grid resampling algorithm was used to resample the grid to 1m × 1m, and the UAV application prescription diagram was generated. Weed analysis process as shown in Figure 2.

2.5 Evaluation indicators

Confusion matrix is a standard format for representing accuracy evaluation in the form of a matrix with n rows and n columns. In image accuracy evaluation, it is mainly used to compare the classification results with the actual measured values, and the accuracy of the classification results can be displayed inside a confusion matrix. The confusion matrix is calculated by comparing the position and classification of each actual measured image element with the corresponding position and classification in the classified image. In this study, the overall accuracy of the confusion matrix and the Kappa coefficient are used as classification effectiveness evaluation metrics.

3 Results and analysis

3.1 Results of vegetation index for weed identification in rice

The WDVI construction method was used and in this study five weed-sensitive indices were selected (Wan et al., 2020; Xia et al., 2021). Five traditional vegetation indices such as GNDVI (Green Normalized Difference Vegetation Index), NDVI (Normalized Difference Vegetation Index), LCI(Leaf Chlorophyll Index), NDRE(Normalized Differential Red Edge

vegetation inde), and OSAVI(Optimized Soil Adjusted Vegetation Index) were selected for comparison, and a total of ten vegetation indices were used to generate pseudo-color maps for the identification of the rice weed vegetation index, and the results are shown in Figure 3.

It can be seen from Figure 3 that different vegetation indices have different sensitivities to weeds in rice fields, and some fields have water cotton in them, but water cotton is different from weeds and requires different agents, so water cotton cannot be considered as a weed. From the effect of weed identification by different vegetation indices, the best result was obtained by using $WDVI_{NIR}$.

$$WDVI_{NIR} = \log_{\frac{G}{NIR}} \frac{RE}{NIR} \tag{3}$$

In $WDVI_{NIR}$, NIR is the near-infrared wavelength reflectance of the multispectral UAV, G is the green wavelength reflectance, and RE is the red edge. $WDVI_{NIR}$ can distinguish weeds from rice and spirogyra communis more clearly (Figure 4).

3.2 Results of rice weed classification based on density splitting

Since the test area was large, the manual visual interpretation workload would be very large if the entire area were analyzed, so field 9 at Figure 1, where the number of weeds was at a medium level, was selected for analysis, and the visible light from the UAV in field 9 is shown in Figure 5. Using the manual visual interpretation method, the density segmentation threshold was determined using the criterion of covering all weeds. The results show that the density segmentation results can cover all weeds when the threshold values are 0 and 5. The results of the density segmentation are shown in Figure 6.

After density segmentation, the results were analyzed by removing small patches operation, using majority analysis method to remove small patches, and setting the transform kernel size as 3, 5, 7, 9, 11, 13, 15, 17, 19, 21, 23, 25, 27, 29, 31, 33, respectively. The results of the analysis are verified using the confusion matrix for accuracy, and the overall accuracy verification curve is shown in Figure 7, and the manual visual interpretation vector diagram used to verify the accuracy is shown in Figure 8. The verification results show that the highest accuracy of the confusion matrix verification is achieved when the size of the transformation kernel is set to 27, i.e., the best effect of removing small patches. The results after removing the small patches are shown in Figure 9.

The images processed by density segmentation and removal of small patches lack spatial continuity, which is not conducive to raster resampling operations during the production of UAV prescription maps. Therefore, the Clump Clustering algorithm is used for smoothing. The expansion kernel size and erosion kernel size are set to 3, 4, 5, 6, 7, 8, 9, respectively, and the kernel values are all 1 for cluster processing. The processed results are verified with precision using a confusion matrix, and the overall accuracy verification curves are shown in Figure 10. The validation results show that the overall accuracy of the confusion matrix is the highest when the expansion kernel size and the erosion kernel size are set to 3. The results after the clustering process are shown in Figure 11.

3.3 Weed UAV precision operation prescription map generation

The UAV application operation must consider parameters such as flight speed and spray width of the plant protection UAV, and the prescription map must be raster data during the

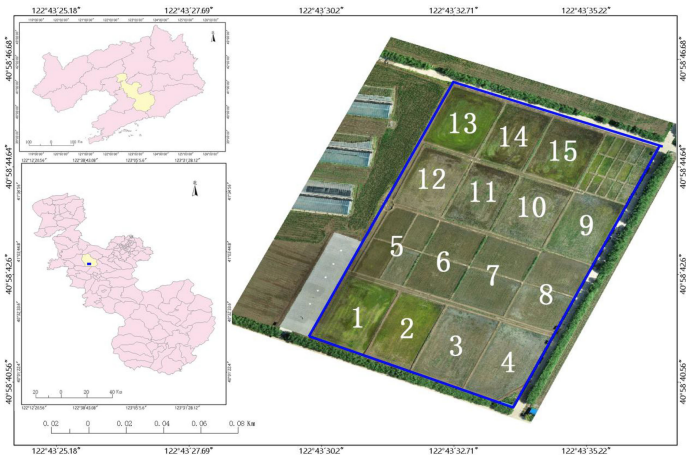

FIGURE 1
Location map of test site.

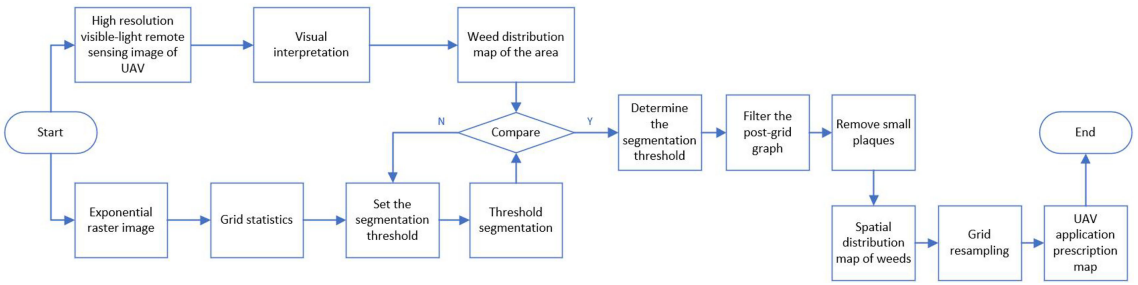

FIGURE 2
Rice weed identification process.

operation. Therefore, this study converts the vector data of weed identification results into raster data and resamples the raster data to the appropriate size. Take DJI plant protection drone T30 as an example, DJI T30 plant protection drone can operate 240 mu of fields per hour, the maximum operating flight speed is 7m/s, the volume of the operating tank is 30L, the number of nozzles is 16, the maximum effective spraying width is 4-9m, and the size of the prescription map grid required for operation is 1m*1m.Therefore, the raster data identified in this study are resampled to 1m*1m, and the raster data before resampling is shown in Figure 12, and the raster data after resampling are shown in Figure 13.

4 Discussion

Using UAV remote sensing technology to monitor weeds in rice fields and generate prescription maps to provide a decision basis for accurate herbicide application by plant protection machinery is one of the important methods to guide accurate rice weeding and is also a research focus of precision agriculture. We established a new weed-sensitive vegetation index using a low-cost UAV multispectral remote sensing platform, then used image recognition to accurately identify rice weeds and combined with GIS information to generate a prescription map for precise operation of agricultural drones for weeds in rice fields. The main idea of vegetation index construction in this study is to use mathematical transformation method to combine multispectral bands into a new vegetation index, and after RE and G are compared with NIR respectively, it is found that the ratio results have better sensitivity with weeds. The proposed WDVI vegetation index may also have decreased recognition accuracy and lack of generalizability when used in other field data sets. The reason for this may be that the vegetation index was constructed using data statistics and the mathematical mapping relationship between sensitive bands and weeds was not explored in the agronomic mechanism; the influence of different regions and varieties on the change in rice weeds was

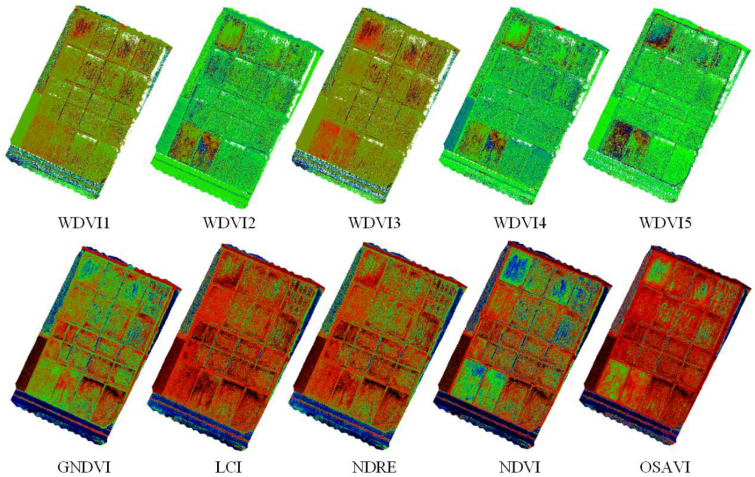

FIGURE 3
Results of weed identification with different vegetation indices.

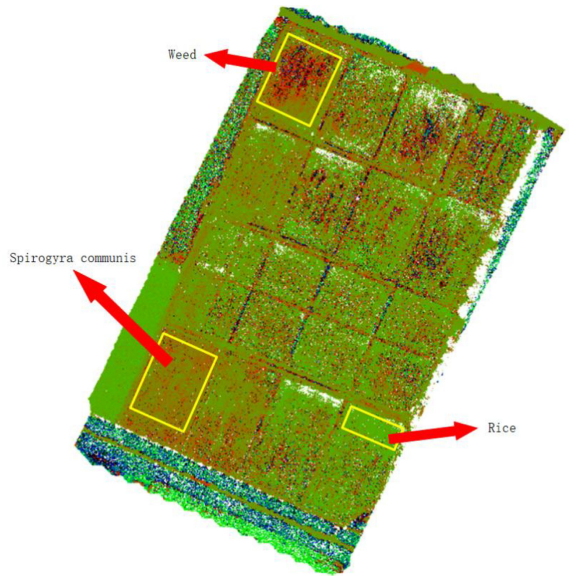

FIGURE 4
Results of $WDVI_{NIR}$ vegetation index.

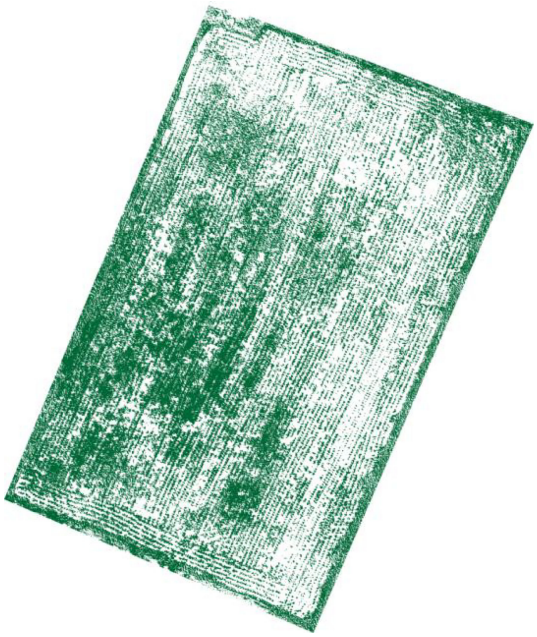

FIGURE 6
Density segmentation results.

not considered in the research process (Yu et al., 2021). However, because the calculation of the vegetation index is simple and easy to realize the development and integration of detection devices, the method of rice weed identification based on the vegetation index still has considerable research value (Xia et al., 2022). The above problems should be explored and studied more deeply in future research experiments.

FIGURE 5
Visible image of field No. 9.

In this study, the accuracy of weed recognition in rice field was 93.47%. Compared with other scholars (Lan et al., 2021), it was found that the accuracy of weed recognition was comparable. However, compared with deep learning, spectral recognition of weeds has higher efficiency, saves time and requires less computing power, so it has more advantages.

In this study, we used manual labeling to tag multispectral remote sensing images from UAVs at pixel level for weed model training and accuracy verification. However, the manual labeling process is inefficient and time consuming. Manual tagging will affect the process of model development if remote sensing data increases substantially (Tobajas et al., 2020; Amziane et al., 2021). Therefore, in future research, it is necessary to introduce semi-supervised or weakly supervised analysis methods to reduce the workload of manual labeling. At the same time, remote sensing images are collected by a UAV, and a server is used offline to identify weeds and generate application prescription maps. In this mode of operation, data collection and data analysis are separated, and the best time for weed control is easily missed for weeds in larger rice production fields. Due to the current rapid development of the computing performance of embedded chips (Yang et al., 2022), which makes the real-time acquisition and analysis of UAV multispectral images possible, if the embedded chips can be deployed on UAVs and the analysis models on

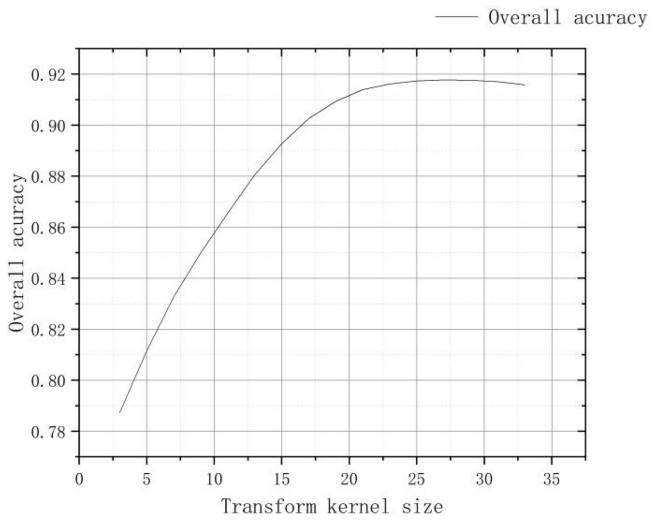

FIGURE 7
Confusion matrix verification accuracy curve after removing small patches.

servers can be migrated to UAVs to realize the real-time processing of weed identification, the interval between data acquisition and data analysis can be effectively broken, and the process integration of UAV identification of weeds in fields can be realized, which will greatly enhance the application scope of remote sensing identification of weeds by UAV.

4.1 Conclusion

In this study, we created a weed identification index based on multispectral UAV images and constructed the $WDVI_{NIR}$vegetation index from the reflectance of three bands, RE, G, and NIR. $WDVI_{NIR}$ was compared with five traditional vegetation indices,

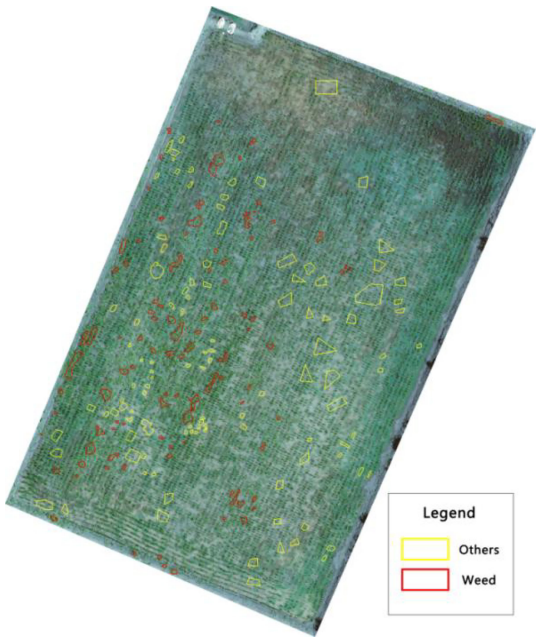

FIGURE 8
Manual visual interpretation vector map.

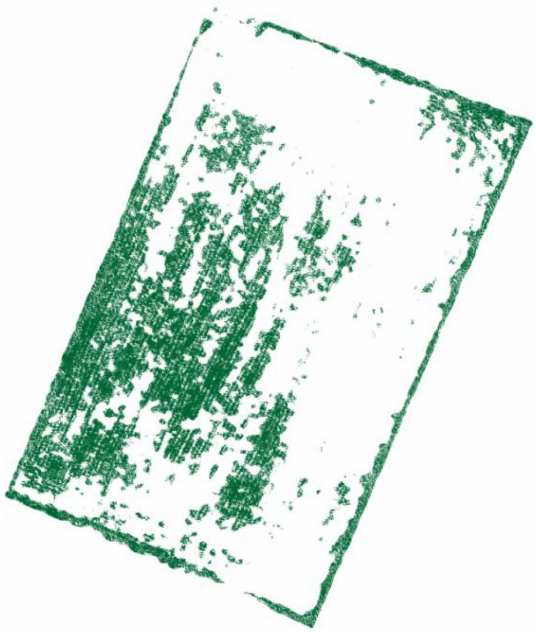

FIGURE 9
Results after removal of small plaques.

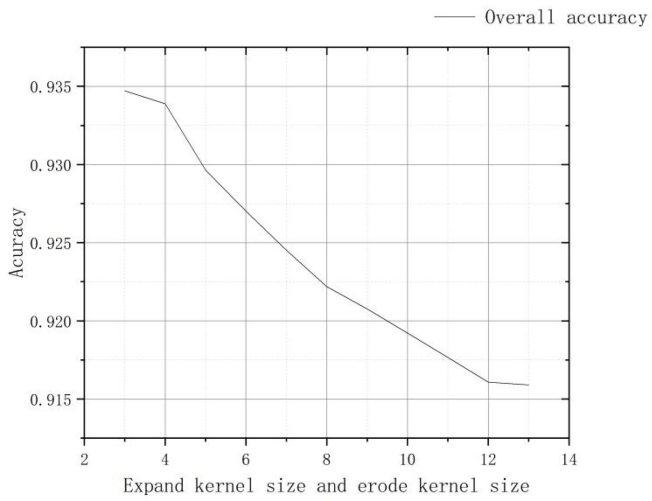

FIGURE 10
Confusion matrix verification accuracy curve after clustering process.

NDVI, LCI, NDRE, and OSAVI, and the results showed that $WDVI_{NIR}$ was the most effective for weed identification and could clearly distinguish weeds from rice, water cotton, and soil.

In this study, a weed identification method based on $WDVI_{NIR}$ was constructed, and the weed index identification results were subjected to small patch removal and clustering processing operations to output weed identification vector results. The weed identification vector results were verified by using the confusion matrix accuracy verification method, and the results showed that the weed identification accuracy could

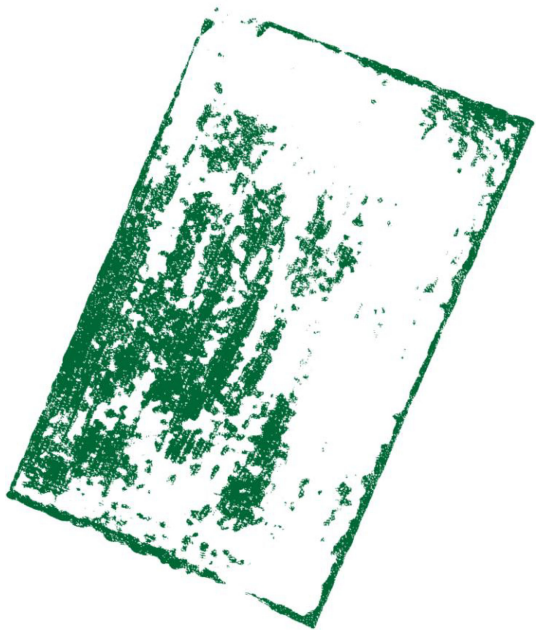

FIGURE 11
The result after clustering process.

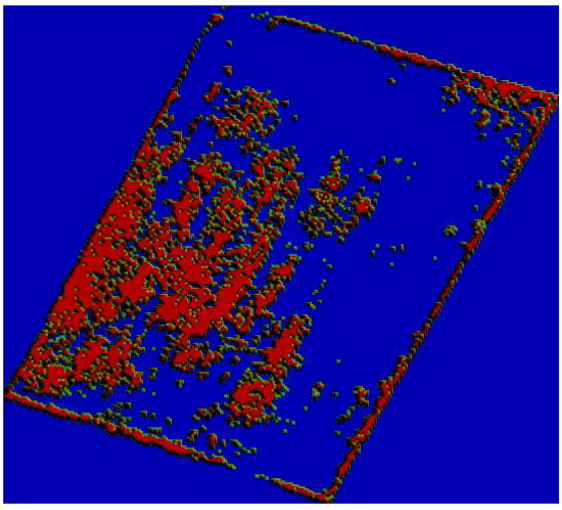

FIGURE 12
Before raster resampling.

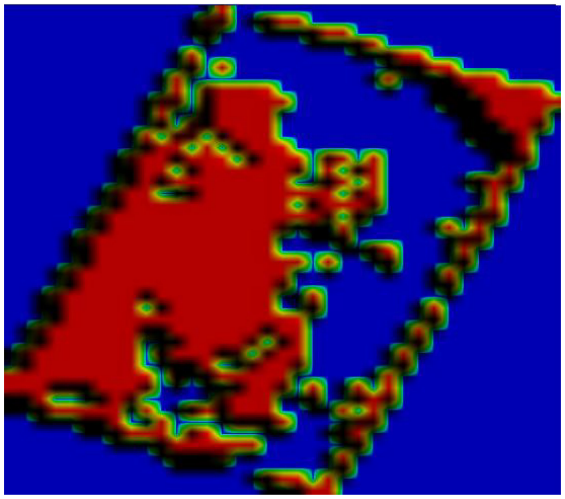

FIGURE 13
After raster resampling.

reach 93.47%, and the Kappa coefficient was 0.859. Moreover, this study integrates the parameters of plant protection UAV operation and takes DJI UAV as an example to convert the weed recognition vector results into raster data with raster size of 1m*1m to make a UAV application prescription map for field application, which provides a new method for weed recognition in rice fields.

Data availability statement

The raw data supporting the conclusions of this article will be made available by the authors, without undue reservation.

Author contributions

FY and ZJ conceived and designed the experiments. SG, ZG, and HZ performed the experiments. FY analyzed the data. ZJ and SG wrote the original manuscript. FY, ZJ, TX, and CC reviewed and edited the original manuscript. All authors contributed to the article and approved the submitted version.

Funding

This work was supported by the key research project of the Liaoning Provincial Department of Education (No. LSNZD202005).

Conflict of interest

The authors declare that the research was conducted in the absence of any commercial or financial relationships that could be construed as a potential conflict of interest.

Publisher's note

All claims expressed in this article are solely those of the authors and do not necessarily represent those of their affiliated organizations, or those of the publisher, the editors and the reviewers. Any product that may be evaluated in this article, or claim that may be made by its manufacturer, is not guaranteed or endorsed by the publisher.

References

Amziane, A., Losson, O., Mathon, B., Dumenil, A., and Macaire, L. (2021). Reflectance estimation from multispectral linescan acquisitions under varying illumination-application to outdoor weed identification. *Sensors (Basel Switzerland)* 21 (11), 3601. doi: 10.3390/S21113601

Barrero, O., and Perdomo, S. A. (2018). RGB And multispectral UAV image fusion for gramineae weed detection in rice fields. *Precis. Agric.* 19 (5), 809–822. doi: 10.1007/s11119-017-9558-x

Bouman, B. A. M., Uenk, D., and Haverkort, A. J. (1992). The estimation of ground cover of potato by reflectance measurements. *Potato Res.* 1 (4), 249–262. doi: 10.1007/BF02357604

Carroll, J. (2020). Aerial imaging aids precision agriculture. *Vision Syst. Design* 1.

Clevers, J. G. P. W., and Verhoef, W. (1993). LAI estimation by means of the WDVI: A sensitivity analysis with a combined PROSPECT-SAIL model. *Remote Sens. Rev.* 7 (1), 43–64. doi: 10.1080/02757259309532165

De Simone, L., Ouellette, W., and Gennari, P. (2022). Operational use of EO data for national land cover official statistics in Lesotho. *Remote Sens.* 14 (14), 3294. doi: 10.3390/RS14143294

Druskin, V., Mamonov, A. V., and Zaslavsky, M. (2021). Distance preserving model order reduction of graph-laplacians and cluster analysis. *J. Sci. Computing* 90 (1), 1–30. doi: 10.1007/S10915-021-01660-3

Duarte, L., Teodoro, A. C., Sousa,, Joaquim, J., and Pádua, L. (2021). QVigourMap: A GIS open source application for the creation of canopy vigour maps. *Agronomy* 11 (5), 952. doi: 10.3390/AGRONOMY11050952

Eppinga, M. B., Baudena, M., Haber, E. A., Rietjerk, M., Wassec, M. J., and Santos, M. J. (2020). Spatially explicit removal strategies increase the efficiency of invasive plant species control. *Ecol. Appl. Publ. Ecol. Soc. America.* 31 (3), e02257. doi: 10.1002/eap.2257

Feng, S., Xu, T. Y., Yu, F. H., and Wang, N. Y. (2018). Research of method for inverting nitrogen content in canopy leaves of japonica rice in northeastern China based on hyperspectral remote sensing of unmanned aerial vehicle. *Spectrosc. Spectral Anal.* 39 (10), 3281–3287. doi: 10.3964/j.issn.1000-0593(2019)10-3281-07

González, M.E.P., and Revilla, J.I.G. (2020). A new environmental and spatial approach to the tiwanaku world heritage site (Bolivia) using remote sensing (UAV and satellite images). *Geoarchaeology* 35 (3), 416–429. doi: 10.1002/gea.21778

Hirohiko, M. (2002). Development of identification methods and elucidation of emergence ecology on gramineous weeds of paddy fields in Japan. *J. Weed Sci. Technol.* 47, 175–184. doi: 10.3719/weed.47.175

Jin, X., Bagavathiannan, M., McCullough, P. E., Chen, Y., and Yu, J. (2022). A deep learning-based method for classification, detection, and localization of weeds in turfgrass. *Pest Manage. Sci.* 78 (11), 4809–4821. doi: 10.1002/PS.7102

Kawamura, K., Asai, H., Yasuda, T., Soisouvanh, P., and Phongchanmixay, S. (2021). Discriminating crops/weeds in an upland rice field from UAV images with the SLIC-RF algorithm. *Plant Production Sci.* 24 (2), 198–215. doi: 10.1080/1343943X.2020.1829490

Lambert, J. P. T., Childs, D., and Freckleton, R. P. (2019). Testing the ability of unmanned aerial systems and machine learning to map weeds at subfield scales: a test with the weed alopecurus myosuroides (Huds). *Pest Manage. Sci.* 75 (8), 2283–2294. doi: 10.1002/ps.5444

Lan, Y. B., Huang, K. H., Yang, C., Lei, L. C., Ye, J. H., Zhang, J. L., et al. (2021). Real-time identification of rice weeds by UAV low-altitude remote sensing based on improved semantic segmentation model. *Remote Sens*. 13 (21), 4370. doi: 10.3390/rs13214370

Liu, H. J., Lee, S. H., and Saunders, C. (2014). Development of a machine vision system for weed detection during both of off-season and in-season in broadacre no-tillage cropping lands. *Am. J. Agric. Biol. Sci*. doi: 10.3844/ajabssp.2014.174.193

Liu, H., and Yu, Y. H. (2013). Affine translation surfaces in euclidean 3-space. *Proc. Japan Academy Ser. A Math. Sci.* 89 (9), 111–113. doi: 10.3792/pjaa.89.111

Liu, H. Y., Zhu, H. C., Li, Z. H., and Yang, G. J. (2020). Quantitative analysis and hyperspectral remote sensing of the nitrogen nutrition index in winter wheat.Int. J. *Remote Sens.* 41, 858–881. doi: 10.1080/01431161.2019.1650984

Luo, H. W., He, L. X., Du, B., Pan, S. G., Mo, Z. W., Duan, M. Y., et al. (2020). Biofortification with chelating selenium in fragrant rice: effects on photosynthetic rates, aroma, grain quality and yield formation. *Field Crops Res.* 255, 107909. doi: 10.1016/j.fcr.2020.107909

Lu, J., and Zhang, L. (2020). Data mining technology of computer testing system for intelligent machining. *Neural Computing Appl*. 2020, 1–11. doi: 10.1007/s00521-020-05369-6

Maes, W. H., and Steppe, K. (2019). Perspectives for remote sensing with unmanned aerial vehicles in precision agriculture. *Trends Plant Sci.* 24, 152–164. doi: 10.1016/j.tplants.2018.11.007

Matsunami, M., Matsunami, T., and Kokubun, M. (2009). Growth and yield of new rice for Africa (NERICAs) under different ecosystems and nitrogen levels. *Plant Prod. Sci.* 12, 381–389. doi: 10.1626/pps.12.381

Mohidem, N. A., Che'Ya, N., Juraimi, A., Ilahi, F. W. F., Roslim, M. H. M., Sulaiman, N., et al. (2021). How can unmanned aerial vehicles be used for detecting weeds in agricultural fields? *Agriculture* 11 (10), 1004. doi: 10.3390/AGRICULTURE11101004

Motavalli, S., Hossienzadeh, M., Derafshi, K., and Alijani, M. A. (2012). Coastline change detection using remote sensing and GIS at TONEKABON coast area during 1984 and 2010, MAZANDARAN PROVINCE, IRAN. *Life Sci. J.* 9 (4), 4174–4181. doi: 10.7537/marslsj090412.622

Naji, T. A.H. (2018). Study of vegetation cover distribution using DVI, PVI, WDVI indices with 2D-space plot. *J. Physics: Conf. Ser.* 1003 (1), 012083. doi: 10.1088/1742-6596/1003/1/012083

Nawaz, M., Mehmood, Z., Bilal, M., Munshi, A. M., Rashid, M., Yousaf, R. M., et al. (2021). Single and multiple regions duplication detections in digital images with applications in image forensic. *J. Intelligent Fuzzy Syst.* 40 (6), 10351–10371. doi: 10.3233/JIFS-191700

Niu, K., Bai, S. H., Zhou, L. M., Zhao, B., Liu, L. J., Yuan, Y. W., et al. (2021). Design and experimental research of variable formula fertilization control system based on prescription diagram. *Appl. Sci.* 12 (1), 325. doi: 10.3390/APP12010325

Otsu, K., Pla, M., Duane., A., and Brotons, L. (2019). Estimating the threshold of detection on tree crown defoliation using vegetation indices from UAS multispectral imagery. *Drones* 3 (4), 80. doi: 10.3390/drones3040080

Punithavathi, R., Rani, A.D. C., Sughashini, K. R., Kurangi, C., Nirmala, M., and Ahmed, H. F. T. (2023). Computer vision and deep learning-enabled weed detection model for precision agriculture. *Comput. Syst. Sci. AND Eng.* 44 (3), 2759–2774. doi: 10.32604/CSSE.2023.027647

Qin, J. Q., Impa, S. M., Tang, Q. Y., Yang, S. H., Yang, J., Tao, Y. S., et al. (2013). Integrated nutrient, water and other agronomic options to enhance rice grain yield and n use efficiency in double-season rice crop. *Field Crops Res.* 148, 15–23. doi: 10.1016/j.fcr.2013.04.004

Setojima, M., Akamatsu, Y., and Hirose, Y. (1989). Updating of actual vegetation map by plural satellite data and output of the vector map. *J. Remote Sens. Soc. Japan* 9 (2), 189–203. doi: 10.11440/rssj1981.9.189

Siva Kumar, A. P., Vasumathi, D., and Naik, M. V. (2020). An improved intelligent approach to enhance the sentiment classifier for knowledge discovery using machine learning. *Int. J. Sensors Wireless Commun. Control* 10 (4), 582–593. doi: 10.2174/2210327910999200528114552

Souri, A. H., Chance, K., Sun, K., Liu, X., and Johnson, S. (2022). Dealing with spatial heterogeneity in pointwise-to-gridded- data comparisons. *Atmospheric Measurement Techniques* 15 (1), 41–59. doi: 10.5194/AMT-15-41-2022

Stroppiana, D., Villa, P., Sona, G., Ronchetti, G., Candiani, G., Pepe, M., et al. (2018). Early season weed mapping in rice crops using multi-spectral UAV data. *Int. J. Remote Sens.* 39 (15-16), 5432–5452. doi: 10.1080/01431161.2018.1441569

Sujaritha, M., Annadurai, S., Satheeshkumar., J., and Mahesh, L. (2017). Weed detecting robot in sugarcane fields using fuzzy real time classifier. *Comput. Electron. Agric*. 134, 160–171. doi: 10.1016/j.compag.2017.01.008

Su, J. Y., Yi, D. W., Coombes, M., Liu, C. J., Zhai, X. J., McDonald-Maier, K., et al. (2022). Spectral analysis and mapping of blackgrass weed by leveraging machine learning and UAV multispectral imagery. *Comput. Electron. Agric.* 192, 106621. doi: 10.1016/J.COMPAG.2021.106621

Tao, T., and Wei, X. H. (2022). A hybrid CNN–SVM classifier for weed recognition in winter rape field. *Plant Methods* 18 (1), 1–12. doi: 10.1186/S13007-022-00869-Z

Tobajas, J. C., Gallart, M., Casamada, J. L., and Gil, E. (2020). On-farm evaluation of prescription map-based variable rate application of pesticides in vineyards. *Agronomy* 10 (1), 102. doi: 10.3390/agronomy10010102

Wan, L., Cen, H. Y., Zhu, J. P., Zhang, J. F., Zhu, Y. M., Sun, D. W., et al. (2020). Grain yield prediction of rice using multi-temporal UAV-based RGB andmultispectral images and model transfer – a case study of small farmlands inthe south of China. *Agric. For. Meteorol.* 291, 108096. doi: 10.1016/j.agrformet.2020.108096

Wang, L. L., Lan, Y. B., Zhang, Y. L., and Chen, P. C. (2019). Applications and prospects of agricultural unmanned aerial vehicle obstacle avoidance technology in China. *Sensors (Basel Switzerland)* 19 (3), 642. doi: 10.3390/s19030642

Wang, Z. Y., Wang, Z. H., Li, H., Ni, P., and Liu, J. (2021). A modified approach of extracting landfast ice edge based on sentinel-1A InSAR coherence image in the gulf of bothnia. *J. Mar. Sci. Eng.* 9 (10), 1076. doi: 10.3390/JMSE9101076

Wei, L. L., Luo, Y. S., Xu, L., Zhang, Q., Cai, Q. B., and Shen, M. J. (2021). Deep convolutional neural network for rice density prescription map at ripening stage using unmanned aerial vehicle-based remotely sensed images. *Remote Sens.* 14 (1), 46. doi: 10.3390/RS14010046

Xia, Y., Fang., J., Chao., P., Pan., Z. H., and Shang, J. S. (2021). Cost-effective and adaptive clustering algorithm for stream processing on cloud system. *GeoInformatica*. doi: 10.1007/S10707-021-00442-1

Xia, F., Quan, L., Lou, Z., Sun, D., Li, H., and Lv, X. (2022). Identification and comprehensive evaluation of resistant weeds using unmanned aerial vehicle-based multispectral imagery. *Front. Plant Sci.* 13, 938604. doi: 10.3389/FPLS.2022.938604

Yang, M., Xu, X., Li, Z. Y., Song, X. Y., and Xue, H. Y. (2022). Remote sensing prescription for rice nitrogen fertilizer recommendation based on improved NFOA model. *Agronomy* 12 (8), 1804. doi: 10.3390/AGRONOMY12081804

Yu, S. Q., Liu, J. X., Han, Z., Li, Y., Tang, Y. D., and Wu, C. D. (2021). Representation learning based on autoencoder and deep adaptive clustering for image clustering. *Math. Problems Eng*. 2021, 3742536. doi: 10.1155/2021/3742536

Zhu, J., Wang, J., DiTommaso., A., and Zhou, W. J. (2020). Weed research status, challenges, and opportunities in China. *Crop Prot*. 134, 104449. doi: 10.1016/j.cropro.2018.02.001

frontiers | Frontiers in Plant Science

TYPE Original Research
PUBLISHED 01 December 2022
DOI 10.3389/fpls.2022.1041791

OPEN ACCESS

EDITED BY
Ruirui Zhang,
Beijing Academy of Agricultural and Forestry Sciences, China

REVIEWED BY
Lian Hu,
South China Agricultural University, China
Zhonghua Miao,
Shanghai University, China

*CORRESPONDENCE
Jiangtao Qi
qijiangtao@jlu.edu.cn

SPECIALTY SECTION
This article was submitted to Technical Advances in Plant Science, a section of the journal Frontiers in Plant Science

RECEIVED 11 September 2022
ACCEPTED 10 November 2022
PUBLISHED 01 December 2022

CITATION
Zhang W, Chen X, Qi J and Yang S (2022) Automatic instance segmentation of orchard canopy in unmanned aerial vehicle imagery using deep learning.
Front. Plant Sci. 13:1041791.
doi: 10.3389/fpls.2022.1041791

Automatic instance segmentation of orchard canopy in unmanned aerial vehicle imagery using deep learning

Weirong Zhang[1,2], Xuegeng Chen[3], Jiangtao Qi[1,2]* and Sisi Yang[4]

[1]Key Laboratory of Bionic Engineering, Ministry of Education, Jilin University, Changchun, China, [2]College of Biological and Agricultural Engineering, Jilin University, Changchun, China, [3]College of Mechanical and Electrical Engineering, Shihezi University, Shihezi, China, [4]Institue of Scientific and Technical Information of Jilin, Department of Science and Technology of Jilin, Changchun, China

The widespread use of unmanned aerial vehicles (UAV) is significant for the effective management of orchards in the context of precision agriculture. To reduce the traditional mode of continuous spraying, variable target spraying machines require detailed information about tree canopy. Although deep learning methods have been widely used in the fields of identifying individual trees, there are still phenomena of branches extending and shadows preventing segmenting edges of tree canopy precisely. Hence, a methodology (MPAPR R-CNN) for the high-precision segment method of apple trees in high-density cultivation orchards by low-altitude visible light images captured is proposed. Mask R-CNN with a path augmentation feature pyramid network (PAFPN) and PointRend algorithm was used as the base segmentation algorithm to output the precise boundaries of the apple tree canopy, which addresses the over- and under-sampling issues encountered in the pixel labeling tasks. The proposed method was tested on another miniature map of the orchard. The average precision (AP) was selected to evaluate the metric of the proposed model. The results showed that with the help of training with the PAFPN and PointRend backbone head that AP_seg and AP_box score improved by 8.96% and 8.37%, respectively. It can be concluded that our algorithm could better capture features of the canopy edges, it could improve the accuracy of the edges of canopy segmentation results.

KEYWORDS

deep learning, instance segmentation, orchard, canopy, convolutional neural network, unmanned aerial vehicles

1 Introduction

Technology and equipment for plant protection are crucial for agricultural output (Ouyang et al., 2020). In apple farming, spraying is one of the most important commonly applied canopy management practices, it should be conducted during the stage of apple growth aims to raise the quality of apples and obtain higher yield. However, the low utilization rate of pesticides has been an important factor in the development of China's application technology (Ru et al., 2015), the utilization rate of pesticides in conventional application methods is only 30%, which not only affects the effectiveness of pest control, but also causes environmental pollution.

The integration of agricultural machinery and information technology is a necessary tool for the development of modern agriculture, which can improve the efficiency of agricultural resources utilization and accelerate the process of agricultural modernization (Chen et al., 2020). With the continuous development of the precision agriculture, remote sensing applications have diversified to include satellite, manned airplanes or unmanned aerial vehicles (UAVs) (Mulla, 2013). UAV images are more easily obtained and it implies lower operational costs, less weather constraints (Rasmussen et al., 2016). UAVs are used for the most autonomous and accurate way to obtain tree's information.

A considerable amount of research on orchard canopy information focus on the identification and counting of individual trees (Morales et al., 2018; Cheng et al., 2020; Qi et al., 2021). In fact, due to geometric features of plant canopies can offer relevant indicators, individual canopy-related features interested farmers but the most accurate estimations for canopies all mostly based on destructive and costly labour-intensive manual measurements (Gower et al., 1999; Jonckheere et al., 2004; Ma et al., 2017). To overcome these disadvantages, UAV-based imagery in conjunction with computer vision methodologies have become widely used on the research of tree extraction (Nyamgeroh et al., 2018; Durfee et al., 2019).

Brede et al. (2017) concluded that UAV-borne laser scanning(ULS) has the potential to perform comparable to Terrestrial Laser Scanning for estimating forest canopy height. ULS combines the strengths of above and under canopy surveys, the results showed that in easy forest stand conditions, the performance of ULS point cloud is comparable with the terrestrial solutions (Liang et al., 2019). The UAV-based LiDAR data can be effectively used in canopy cover estimation, individual tree segmentation-based method had the highest accuracy in estimation of canopy cover (R2 = 0.92, rRMSE = 3.5%) can provide references for sustainable management (Wu et al., 2019). Laser scanning data of stem curve was obtained by using UAV. Novel data processing algorithms were applied for the point clouds to extract the stem curves and diameters at breast height (Hyyppa et al., 2020). However, these methods using LiDAR represents an important limitation for costly.

There exist other methods that use multispectral cameras to descriptor such as canopy shape, crown contour and canopy volume. In order to estimate tree height, Wu et al. (2020) compared several methods. Height estimations of mango and avocado trees were compared to canopy metrics obtained from Airborne Laser Scanning (ALS) and UAV-based RGB and multi-spectral photography. Chang et al. (2020) used UAV-based multispectral pictures to compare the canopy shape and vegetation indicators of range trees. The findings revealed a strong correlation between tree height and canopy volume measured from the ground and by UAV. Gallardo-Salazar et al. (2020) analyzed included different vegetation indices estimated with a high-resolution orthomosaic and obtained total height and the crown diameter of individual trees, the consistency of the the normalized-difference vegetation index (NDVI) as the most recommended to evaluate productivity results for its application in the field.

When focusing on RGB images, a large number of studies of tree phenotype in orchards can be found. Using image processing techniques, Yıldız et al. (2020) determined the canopy area of apple trees. Regression analysis employed both circular and elliptical calculating techniques. Using a local-maxima-based technique on UAV-derived Canopy Height Models (CHMs), Mohan et al. (2017) assessed the applicability of low-altitude visible light image and structurefrom-motion (SFM) algorithm). To distinguish between overlapping tree crown projections, Ponce et al. (2021) developed a novel method for crop tree identification using image analysis techniques, doing away with the usage of vegetation indices and machine learning-based approaches. The aforementioned methods, however, are likely to have a low fidelity for interlaced orchards. Cheng et al. (2020) provided a segmentation approach for mingled fruit tree canopies with irregular forms that makes use of a Gaussian Mixture Model and XGBoost to accurately recover the individual apple and cherry trees from mingled canopies.

In recent years, the performance of the CNN network in detecting complicated phenomena has been excellent due to the accessibility of massive datasets and the ongoing advancement of GPU processing power. A growing variety of artificial intelligence algorithms have been used in horticulture research and remote sensing for agriculture (Kamilaris and Prenafeta-Boldú, 2018; Zhou et al., 2020; Yang and Xu, 2021; Qi et al., 2022). Mo et al. (2021) proposed a deep learning-based instance segmentation method YOLACT of litchi trees. The boundary and location information of the canopy have been obtained by using the Digital Orthophoto Map (DOM). A Convolutional Neural Network (CNN) based on the Deeplab v3+ architecture was used to detect full-grown isolated Mauritia flexuosa palms, and has achieved better performance than those of other CNN

networks used for performance comparison (Morales et al., 2018). Lou et al., (2022) used thrss widely object detection methods such as the Faster region-based CNN (Faster R-CNN) (Ren et al., 2015), You Only Look Once version 3 (YOLOv3) (Redmon et al., 2018), and single shot detection (SSD) (Liu et al., 2016) to identify tree crowns and their widths in two loblolly pine plantations, respectively.

Due to unsystematic tree branches overlapping and shadows, the accuracy of the deep learning-based image segmentation algorithms needs to be improved. In horticultural computer vision, however, it has always been challenging to detect the boundary of tree canopies.

In this regard, we offer an innovative technique for precisely segmenting the borders of apple trees using aerial photos taken with RGB cameras placed on UAVs. This approach aims to address the issue of incorrect segmentation of tree canopies in dense orchards with complex backgrounds, including branches and shadows. Firstly, RGB images were processed in DJI Terra software to yield a Digital Orthophoto Map (DOM), then DOM was sliced into smaller images for training the deep learning model. Second, the feature of canopy instances was extracted using the PAFPN (Liu et al., 2018) as backbone neck and PointRend (Kirillov et al., 2020) as a new backbone head based on the instance segmentation of the Mask R-CNN (He et al., 2017) framework. Our method is called MPAPR R-CNN. This segmentation is eventually combined into a miniature orchard map, with each little picture containing the canopy's pixel count by segmentation network. The whole system was put to the test in an apple orchard, and the comparison experiment findings showed how well it works for identifying apple tree canopy.

2 Materials and methods

2.1 Study area

As shown in Figures 1A, B, the study was conducted during the summers of 2022 at the JingXiang Orchard in Weihai City, Shandong Province, China. The location is characterized by a temperate monsoon climate, with average annual precipitation of 400–600 mm and an average effective temperature during the study period (July–August) of 28°C. The local climate is perfect for the cultivation of apples.

The orchards under study are high-density planting patterns with a 3.5-meter route between rows and a tree spacing of 0.8 meters. It should be emphasized that the planting and management model adheres to the region's suggested

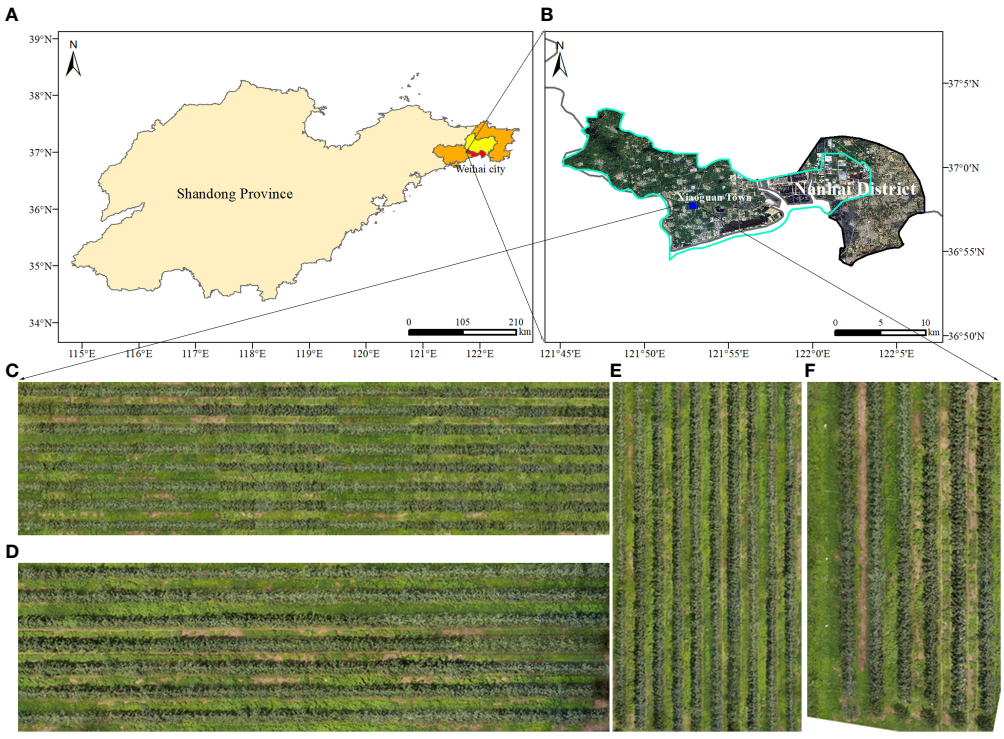

FIGURE 1
Test location of image capture. **(A, B)** The location of the experimental orchard. **(C-E)** Digital orthophoto maps for training and **(F)** for testing in canopy detection.

production techniques. 'Four location DOMs containing apple orchards of different ages were used for canopy identification in this paper, where C, D and E of Figure 1 were used as training for the model, while Map F was used as a test map for the model training results.

2.2 Unmanned aerial vehicle image collection

Apple trees were captured with the DJI Phantom 4 Multispectral (P4, SZ DJI Technology Co., Ltd., Shenzhen, Guangdong, China). The P4 is employed because it can be programmed to fly independently, and the collected visible images can be processed to generate orthophoto images, or other drones equipped with low-cost RGB visible light can be used. For multispectral imaging, this UAV was outfitted with one RGB sensor and five monochrome sensors, which have six 1/2.9-inch CMOS, including one color sensor for visible imaging and five monochrome sensors for multispectral imaging. Individual sensors have 2.08 million effective pixels (2.12 million total pixels). Figure 2 depicts the takeoff of a drone for data collection.

The purpose of this paper is to solve the problem of UAV canopy image segmentation in complex backgrounds, and we selected the area where weeds are most abundant for UAV flight. To minimize any shadow effects, the flight was conducted during sunny or cloudy weather conditions at high noon, with very light winds, between approximately 11:30 am and 12:30 pm. The DJI GO Pro software was used to set up the flight for autonomous management. The pictures have an 80% mean forward overlap and a 70% mean side overlap. The aircraft was maintained at a cruise speed of 2 m/s an altitude of 15 m above ground and during the flight. The aircraft maintained a cruise speed of 2 m/s during flight at 15m and 20m altitude, while the ground sample distance (GSD) was 0.79cm/pixel and 1.06cm/pixel, respectively.

2.3 Canopy segmentation framework

We first summarize the whole process of the proposed framework for detecting orchard canopy and then discuss in detail each phase of the model. As shown in Figure 3, the framework consists of three major parts: (1) image dataset construction and preprocessing; (2) training and inference and (3) image stitching.

2.3.1 Image preprocessing and dataset construction

In this part, DJI Terra software was used to convert the UAV canopy images into DOM. Since the resolution of DOM is too large, the images need to be cropped to meet the appropriate size required for computer operation, then we use Labelme software for annotation, and then perform image enhancement to generate the image dataset of orchard canopy for defect and segmentation model training and testing.

2.3.2 Training and testing of datasets

In this section, we proposed to design our framework based on Mask R-CNN. In order to fit the tree canopy detection and segmentation task, as in Figure 4, we introduced the PAFPN and PointRend into the original architecture. The proposed model

FIGURE 2
The DJI P4 Multispectral.

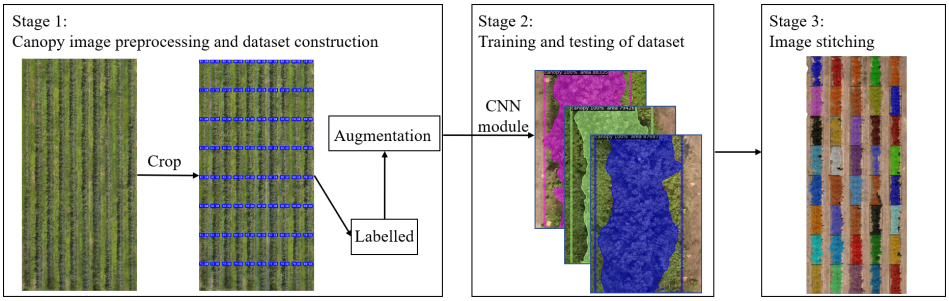

FIGURE 3
Canopy segmentation framework.

can obtain enhanced features with both rich context information and edge information, leading to better performance of canopy detection and segmentation results. In addition, considering the shape characteristics of canopy in cropped image, we modifed the aspect ratios of anchor boxes in the RPN network. Specific network design will be described in the later section.

2.3.3 Image stitching

After the deep learning model had been trained and the test photos had been post-identified, this segmentation is eventually combined into a miniature orchard map using Adobe Photoshop CC 2019 software. With each little picture containing the canopy's pixel count by segmentation network, the orthophotography can be used to provide application recommendations to variable application machinery.

2.4 Canopy segmentation method

2.4.1 Image preprocessing and dataset construction

Using DJI Terra software, over 500 photos taken by the P4 UAV of the experimental regions every flight were photogrammetrically processed to create the RGB DOM. Through the training of a large amount of data, the model based on deep learning can achieve great prediction results for complex classification and detection tasks.

DOM resolution is too huge for processing, especially for deep-learning-based methods, thus the high-resolution picture was chopped using the Adobe Photoshop CC 2019 software slicing tool, and the DOM was ultimately divided into 500 little pixel images of 450*600. To boost the variety of the canopy

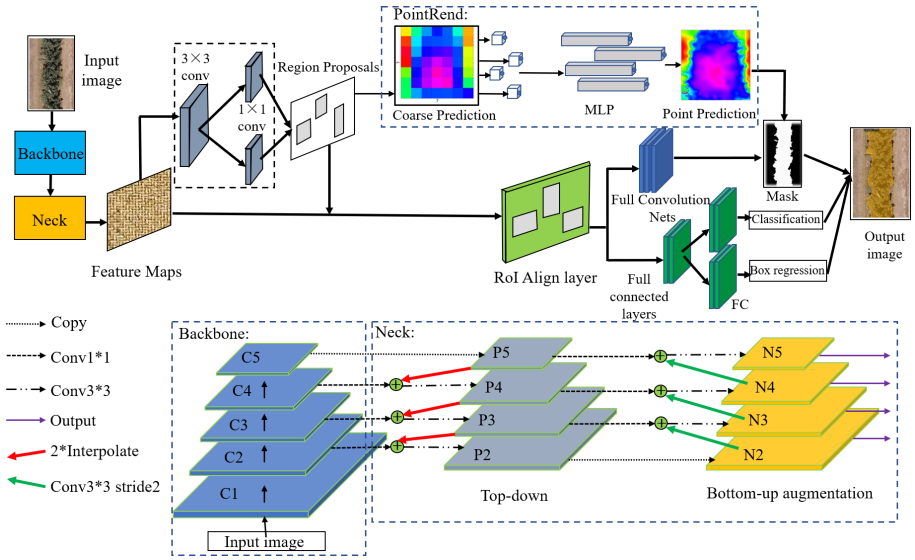

FIGURE 4
Canopy segmentation model base on Mask R-CNN. * indicates that the height and width of the convolution kernel matrix are multiplied.

photos for the deep learning network, techniques including noise addition, random blurring, panning, vertical mirroring, and diagonal flipping were applied. A final dataset of 2000 enhanced canopy images were produced as a consequence of the data augmentation strategies, which also expedited the dataset's creation, improved the resilience and generalization of the model training, and decreased the likelihood of overfitting. Finally, we divided the training and validation sets for 2000 images in the ratio of 8:2.

2.4.2 Architecture of mask R-CNN

Mask R-CNN is a classical image segmentation algorithm that detects target objects in an image and marks the outline of the object region, extracting the relevant pixels for area calculation. Faster R-CNN for target recognition and a Fully Convolutional Network (FCN) for semantic segmentation are combined to create Mask R-CNN. The Faster Convolutional Network (FCN) is utilized for mask prediction, boundary regression, and classification based on the target discovered by the Faster R-CNN. These include a feature extraction layer using ResNet/ResNeXt as the convolutional backbone, a region suggestion network (RPN), bilinear interpolation (ROIAlign), and fully connected FC and FCN.

The selected region of interest (RoI), after mapping to the feature map, is further pixel-corrected by the ROIAlign layer. The resultant feature map is delivered to a region proposal network (RPN) to create positive and negative samples. Because the picture enhancement in this investigation did not involve a 90-degree rotation to increase the dataset, the orientation of the canopy photographs in this study all stretched along the vertical direction. The initial model was enhanced by balancing the distribution of various picture forms and constructing anchor points with three distinct scales of 0.3, 0.5, and 1 in aspect ratio to increase the identification and segmentation accuracy of the canopy.

2.4.3 Feature extraction network

To achieve more effective detection, ResNeXt is regarded as the backbone network for feature extraction of the input image. ResNeXt is built on ResNet modular structure and incorporates the high recognition performance of split-transform-merge in Inception. The right side of Figure 5 shows the structure of each basic unit.

In Figure 5, ResNeXt uses multiple convolution modules to perform feature extraction from bottom-up, and group convolution uses the same topology on different input channel paths. By using cardinality as a super parameter, it's able to achieve a more efficient network. For a 256-dimensional input with cardinality of 32, the network encodes 256 channels into 4 channels, and the features are extracted in 32 different embedding spaces by 32 different groups consisting of continuous 1×1 conv, 3×3 conv, and 1×1 conv.

2.4.4 Feature fusion network

In multilayer convolutional neural networks, features at shallow layers are usually more representative of edge morphology, which is crucial for accurate pixel classification and instance segmentation (Kong et al., 2016), and it is precisely the determination of instance edges that is most important for segmentation of crown images. Specially, we adopt a path augmentation feature pyramid network (PAFPN) to enhance the feature hierarchy with rich low-level features by adding a bottom-up path augmentation module and a feature fusion operation module.

The part of Neck in Figure 6 shows the PAFPN module in details. Each cube represents a corresponding feature tensor. In the original ResNeXt-FPN backbone network, features are extracted from the final convolutional layer of conv1–conv5 parts of ResNeXt101, which are called C_1, C_2, C_3, C_4 and C_5 in this paper. Based on the bottom-up network architecture, the feature extraction layers compute hierarchical feature maps. Feature maps generated by FPN are represented by P_2, P_3, P_4, P_5.

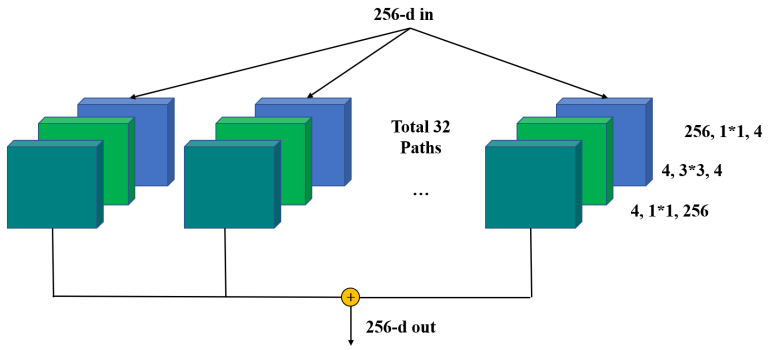

FIGURE 5
Backbone Network-ResNeXt. * indicates that the height and width of the convolution kernel matrix are multiplied.

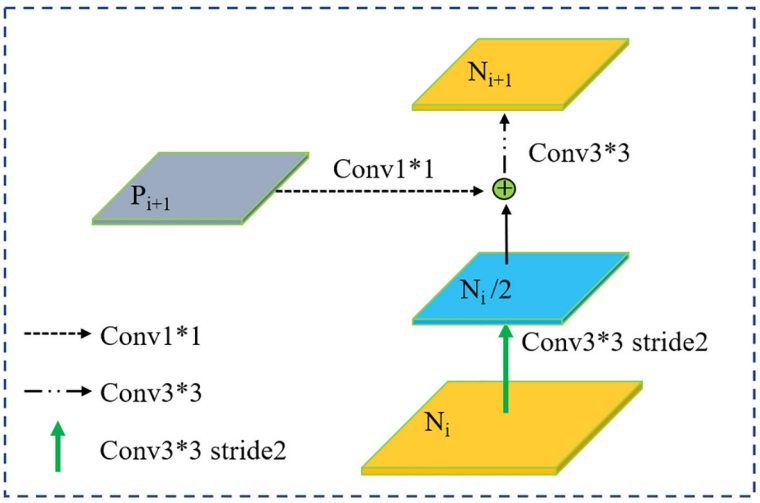

FIGURE 6
Bottom-up path augmentation. * indicates that the height and width of the convolution kernel matrix are multiplied.

The feature maps of the added bottom-up path augmentation module are represented as N_2, N_3, N_4 and N_5 corresponding to P_2 to P_5. The concrete operations for bottom-up path augmentation module are illustrated in Figure 6. Firstly, $N_i/2$ is obtained by a 3 × 3 convolutional layers with stride 2 to down-sampled, where the size of $N_i/2$ is reduced by a factor of two. Then the down-sampled feature map is concatenated with P_{i+1}. At last, the fused feature map goes through another 3 × 3 convolutional layer to generate new feature map N_{i+1}. Then, feature fusion operations are carried out to incorporate higher level feature maps to the lower-level ones for contextual feature fusion.

2.4.5 Optimized boundary feature based on PointRend technique

As objects have irregular boundaries, most segment methods can classify pixels inside the object accurately but pay less attention to the accuracy drop caused by upsampling on the edge of the object increases the loss of prediction. Image segmentation tasks of original Mask R-CNN focus on regular grids to classify each pixel in the image has an obvious drawback of shivering or over-smoothed edges of segmentation, which makes the boundary of the mask unsatisfactorily and greatly undermines the accuracy of canopies edge segment.

As a result, to address this issue, we employed a high-quality PointRend module to recover clear and sharp mask edges. This module can adaptively choose a non-uniform set of points by a subdivision strategy to densely sample and label the boundary pixels while minimizing the indistinct segmentation results. Point selection, point-wise feature extraction, and point head make up the three primary components of PointRend.

The point selection module chooses suitable sampling points flexibly and adaptively to predict to avoid excessively computed pixels, and focuses on the points located near object boundaries.

After the target segmentation model output feature map as the initialization output map of the PointRend model, the strategy of point selection is to render the output image in a coarse-to-fine manner. The first prediction is the coarsest and is performed on the point of a regular grid. As shown in Figure 7, in each iteration, the points on a regular grid from the low spatial resolution feature map will be predicted coarsest first. The output result is sampled up by bilinear interpolation to achieve the denser feature prediction map. Then on the high-resolution segmentation map, where the N most uncertain points are concentrated in the edges, the confidence interval is [0,1] close to 0.5. Points are selected by Equation (1). Once N points are selected, point-wise feature extraction is performed. These N points are the points that are finally filtered out for re-confirmation. And so on, iterating step by step to obtain the final segmentation map with the target resolution.

$$n_i^* = \underset{n_i}{\operatorname{argmin}} |p(n_i) - 0.5| \quad (1)$$

where $p(n_i)$ is the probability for point n_i belonging to the binary mask; n_i^* is the selected point.

For training, the point selection strategy is a random sampling-based selection strategy. First, kN candidate points (k>1) are randomly sampled from the feature map to address the uncertain regions while keeping a uniform distribution. Then kN points are sorted while estimating the uncertainty. The most uncertain βN points are selected, where $\beta \in [0,1]$. These points are concentrated in the most uncertain area, such as road

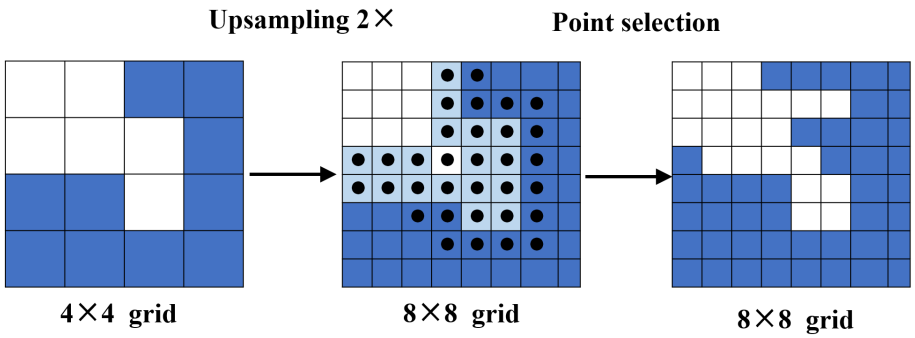

FIGURE 7
The strategy of the point selected.

boundaries. Last, the surplus (1−β) N points are distributed from a uniform distribution.

The coarse prediction and fine-grained features are combined to create the point-wise feature of the selected points extraction module. Regarding fine-grained features, bilinear interpolation is used to extract the finely detailed segmentations from each point chosen from the sort in the feature map to display the fine segmentation details. These segmentations are then stored in feature vectors, which contain fine-grained features.

Fine-grained features may contain only relatively low-level information and do not obtain specific region information, but the coarse predicted feature can provide a more general and globalized context, with a 2-dimensional vector for class-2 prediction at each point in the region.

The pointed head is a simple Multi-layer Perceptron (MLP) used to represent prediction labels based on point-wise features, which can share weights across all points. Moreover, because the MLP predicts a segmentation label for each point, it can be trained by the segmentation loss of a specific task. Note that when the backbone head is replaced with PointRend, the loss of the segment network is increased by loss point, but this does not affect the final segmentation accuracy.

2.4.6 Loss function

The loss function of the Mask R-CNN with PointRend has four components, the classification loss of the bounding box, the position regression loss of the bounding box, and the loss of the mask. The loss function L for each sample ROI in the network is

$$L = L_{\text{box}} + L_{\text{cls}} + L_{\text{mask}} + L_{\text{point}} \tag{2}$$

There are three components: L_{box} is the classification calculation loss, L_{cls} is the position regression loss of the bounding box and L_{mask} is the mask calculation loss. The bounding box loss function, the classification calculation loss, and the mask calculation loss are shown as follows:

$$L_{box}\left(t_i^*, t_i\right) = \text{smooth}_{\text{L1}}\left(\text{t}_i^* - \text{t}_\text{i}\right) \tag{3}$$

$$\text{smooth}_{\text{L1}}(\text{x}) = \begin{cases} 0.5\text{x}^2 & (|\text{x}| < 1) \\ |\text{x}| - 0.5 & (|\text{x}| \geqslant 1) \end{cases} \tag{4}$$

where $\text{t}_\text{i}=(\text{t}_\text{x},\text{t}_\text{y},\text{t}_\text{w},\text{t}_\text{h})$, $\text{t}_i^* = (\text{t}_x^*, \text{t}_y^*, \text{t}_y, \text{t}_w^*)$ 。

$$\text{L}_{\text{cls}}\left(\text{p}_i^*, \text{p}_\text{i}\right) = -\log\left[\text{p}_i^*\,\text{p}_\text{i} + \left(1 - \text{p}_i^*\right)(1 - \text{p}_\text{i})\right] \tag{5}$$

where p_i represents the probability anchor is predicted to be positive samples, p_i^* represents the foreground true probability of the anchor point, i.e. a value of 1 when in the foreground and 0 when in the background anchor samples.

$$L_{mask}\left(s_i^*, s_i\right) = -\left(\text{s}_i^*\log(\text{s}_\text{i}) + \left(1 - \text{s}_i^*\right)\log(1 - \text{s}_\text{i})\right) \tag{6}$$

where, s_i represents the probability mask is predicted to be the irightvalue the s_i^* is the label value of the mask.

$$L_{point}\left(s_i^*, s_i\right) = \text{seg\_loss} + \text{points\_loss} \tag{7}$$

where seg_loss represents the cross-entropy loss of the overall pixel point, points_loss represents the cross-entropy loss of the uncertain point.

2.5 Algorithm platform

The model training platform is a laptop with Ubuntu 18.04 operating system. The deep learning model in this paper is the Detectron2 framework based on PyTorch, while CUDA 11.1 is used to accelerate the training process. Table 1 describes the specific environment configuration.

Mask R-CNN employs the alternating optimization training technique. Stochastic Gradient Descent (SGD), a quick and efficient gradient descent technique for convolutional neural networks, is used as the training optimization approach. The

TABLE 1 Image processing unit host hardware and software environment.

Name	Version
CPU	Intel(R) Core(TM)i7-11800H
GPU	NVIDIA Geforce RTX 3050(4GB)
Operating System	Ubuntu 18.04
Computing Architecture	CUDA 11.1
Deep learning Framework	PyTorch1.5.0
Anaconda	Anaconda3(Python3.7.2)

maximum number of training iterations is 25000, the number of samples (batch size) used in each trainer is 1, the number of samples in a batch of training samples (one epoch) is 128, and the learning rate decay multiplier (gamma) is 0.2, the learning rate decay is performed after 10000 and 20000 iterations, the number of warm-up iterations is 1000, momentum is 0.9, and weight decay coefficient is 0.001.

2.6 Evaluation indicators

To validate the performance of the model, Mean Average Precision (m_{AP}) is used as a metric to evaluate the accuracy of the training model. m_{AP} is an algorithm performance metric used to predict target locations and categories, and refers to the average of the Average Precision (A_P) of multiple categories, and a higher m_{AP} value indicates a better model is better. In image segmentation, a curve can be plotted for each category based on the accuracy P (Precision) and recall R (Recall), and the Average Precision A_P is the area under that curve. Multiple metrics are calculated as follows:

$$P = \frac{T_P}{T_P + F_P} \tag{8}$$

$$R = \frac{T_P}{T_P + F_N} \tag{9}$$

$$A_P = \int_0^1 P(R)\mathrm{d}R \tag{10}$$

where T_P denotes the number of samples correctly predicted as positive, F_P denotes the number of samples in which negative samples are predicted as positive, F_N denotes the number of samples in which positive samples are predicted as negative, and k denotes the number of categories; P refers to the accuracy rate, which is the proportion of correctly detected samples to all samples actually detected; and R refers to the recall rate, which is the proportion of the number of correctly detected samples to the number of samples that should be detected.

3 Results

To better validate the performance of the optimized segmentation model, comparative experiments were conducted to demonstrate the detection and segmentation capabilities of the model under different configurations.

3.1 Different anchor and backbone

Since the target of detection in this paper is the tree canopy, combined with the canopy growth and the slender characteristics of the collected image data set along the top and bottom directions, the aspect ratio of anchor was adjusted to {1:1, 1:2, 1:3} to suit the canopy detection.

The ResNeXt network is implemented by simply cascading layers of the same structure and implementing a split-transform-merge strategy at each level of the network. Based on the ResNet network structure, a new dimension called “cardinality” is proposed. For canopy detection, we need to verify whether the improvements in the ResNeXt network improve the detection and segmentation accuracy. To test the impact of the improved anchor frame ratio and feature extraction network, we designed a set of comparison experiments. We use the standard metrics average precision (AP, AP50, AP75) to evaluate our results. The results are shown in Table 2.

Table 2 shows that the improved anchor ratio and ResNeXt both affect the accuracy of the segmentation. Since the canopy distributed along the up-down direction is not rotated by 90 degrees in the data enhancement operation, the detection task of the canopy dataset is better facilitated when the RPN network uses a more elongated anchor frame for the generation of the region suggestion frame. In addition, performing a set of transformations using low-dimensional embeddings by constructing bases in the base block, split-transform-merge strategy can make the deep learning model learn more features. Therefore, improved anchors and ResNeXt were used as part of the Mask R-CNN model for feature extraction and as the base network for subsection 3.2.

3.2 Best model configuration

The key differences between our suggested canopy detection and segmentation method and the original Mask R-CNN architecture are two. In order to get feature maps with rich low-level information, we first applied a PAFPN module to the original Mask R-CNN. The second is that we utilized Pointrend to enhance the accuracy of edge segmentation results. Based on Mask R-CNN with better anchor and ResNeXt, we create four distinct network frameworks to extract features in order to test

TABLE 2 The detect results of different Anchor and Backbone.

Backbone Network	ImprovedAnchor ratio	ResNeXt	AP_seg			AP_box		
			AP	AP50	AP75	AP	AP50	AP75
Mask R-CNN-FPN			57.24	79.51	79.87	65.14	78.93	77.42
	✓		58.34	79.89	81.32	65.93	80.29	79.18
		✓	58.96	81.26	81.41	66.71	82.56	80.39

✓ indicates that on the basis of the backbone network, add the corresponding module at ✓. The first line is Mask R-CNN-FPN, the second line is Mask R-CNN-FPN+Improved Anchor ratio, and the third line is Mask R-CNN-FPN+ Improved Anchor ratio+ResNeXt.

the impact of the new PAFPN and PointRend module, which are represented by RX-FPN (Mask R-CNN+ResNeXt+FPN), RX-PAFPN (Mask R-CNN+ResNeXt+PAFPN), PR-RX-FPN (Mask R-CNN+PointRend+ResNeXt+FPN) and our method(Mask R-CNN+PointRend+ResNeXt+PAFPN), respectively. Our method is called MPAPR R-CNN. Four group experiments are used to detect and segment orchard canopy images in this part.

Figure 8 compares the loss functions of the four instance segmentation models used in the experimental training phase. In Figure 8A, in comparison to RX-FPN and PR-PAFPN, PR-RX-FPN and MPAPR R-CNN have higher total loss due to the training loss function of PointRend contains point loss. However, it is still obvious in Figure 8A that the RX-PAFPN with enhanced feature pyramid network has lower loss in RX-FPN and RX-PAFPN without combining PointRend, and similarly, in PR-RX-FPN and MPAPR R-CNN with combining PointRend, the PAFPN module with MPAPR R-CNN model also has lower loss, which indicates that both PAFPNs effectively improve the original FPN network. This can also be seen in Figures 8C, D, where PAFPN has a significant effect on the model improvement, firstly, the loss_mask_point is reduced, and secondly, the point accuracy is higher. This further shows the improvement effect of PAFPN on the PointRend model.

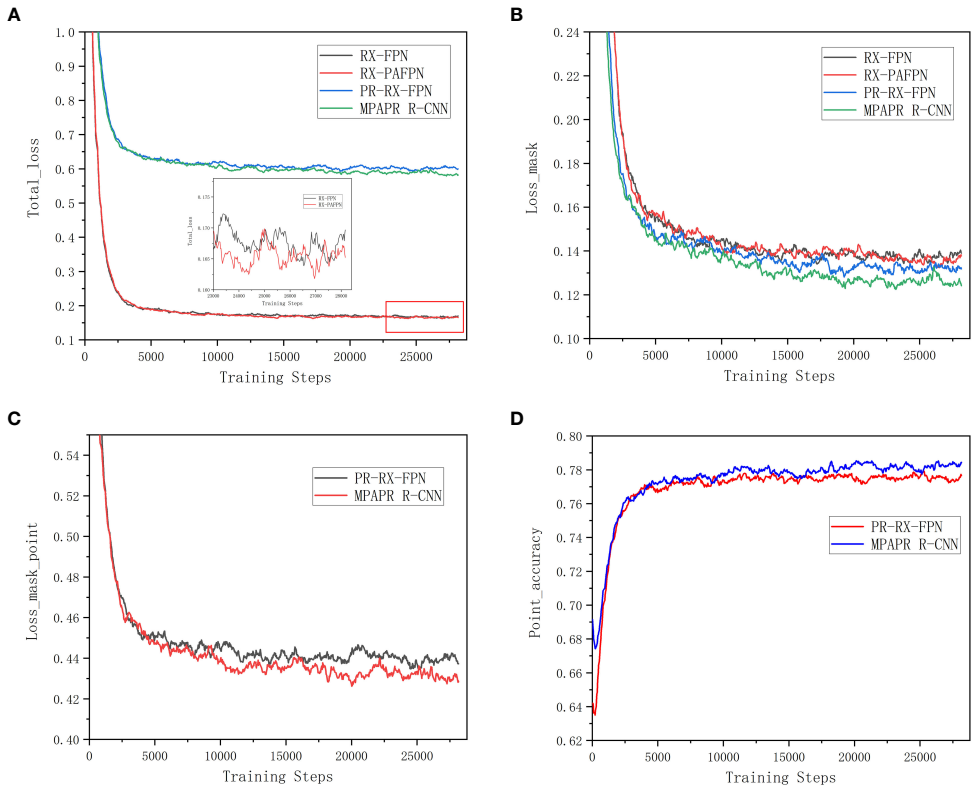

FIGURE 8
Loss and accuracy curves of several different instance segmentation algorithms in training stages. **(A)** Total loss curves. **(B)** Mask loss curves. **(C)** Mask point loss curves. **(D)** Point accuracy curves.

For the most important loss_mask of crown segmentation, Figure 8B shows that both PR-RX-FPN and MPAPR R-CNN with PointRend module have lower mask loss values than RX-FPN and RX-PAFPN without PointRend module. It indicates that the addition of the PointRend module has a more significant optimization effect on reducing the mask loss of the FPN and PAFPN networks. However, the lowest Loss_mask is the MPAPR R-CNN model with both PAFPN and PointRend.

The AP findings for each of the four networks are displayed in Table 3. MPAPR R-CNN outperforms competing methods in terms of AP-seg and AP-box score, which supports its efficacy in identifying canopy images. We can see from Table 3 that the suggested PAFPN and PointRend algorithm considerably alters the AP score of test outcomes. The AP seg and AP box scores of the RX-PAFPN are increased by 3.18% (from 59.64% to 62.82%) and 1.85% (from 67.61% to 69.46%), respectively, while the value of the AP 50 grows more considerably, improved by 6.28% (from 81.8% to 88.08%) and 6.16% (from 84.4% to 90.56%). The outcomes demonstrate that the PAFPN algorithm may successfully prevent information loss of low-level features and improve the original's capacity to extract features.

Meanwhile, as for the PointRend, the AP_seg and AP_box score of PR-RX-FPN is significantly improved by 7.71% (from 59.64% to 67.35%) and 7.52% (from 67.61% to 75.13%). The result demonstrates that the PointRend has more influence than PAFPN. This is because a uses both coarse and fine prediction of points and fuses the two features, which is more effective for canopy edges detection. Combined with PAFPN and PoitRend, MPAPR R-CNN obtained the most excellent canopy detection and segmentation results with AP_seg and AP_box score improved by 8.96% (from 59.64% to 68.6%) and 8.37% (from 67.61% to 75.98%), respectively. Therefore, MPAPR R-CNN is more effective for canopy detection task.

Examples of the results of several methods for canopy detection are shown in Figure 9. The good boundary segmentation performance of MPAPR R-CNN is shown in the figure by the yellow marker box. As can be shown, for the input image (Figure 9A), our approach (Figure 9C) outperforms Mask R-CNN paired with ResNeXt and FPN (Figure 9B) in terms of both canopy identification and segmentation. For instance, Mask R-CNN missed some edge information and incorrectly identifies the shadow of the tree as the canopy areas, but MPAPR R-CNN's findings for detecting the canopy are more accurate. Unlike Mask R-CNN, which has a rather rough segmentation contour, MPAPR R-CNN's segmentation contour is more defined.

3.3 Image stitching

After the deep learning model had been trained and the test photos had been post-identified and segmented, a high-resolution DOM map was created using Adobe Photoshop CC 2019 software. Figures 10 shows the visual outcomes of the models. Small slices of pictures on the stitched DOM may all be inferred with accurate geo-coordinate positions, since the RGB visible camera communicates position coordinates with the UAV during image acquisition. This has ramifications for the creation of changeable application prescription maps later on.

By increasing mAP by 2.19%, our innovative segmentation method significantly improved segmentation accuracy. In the canopy detection of a mass of branches and notably for tree margins, the pixel-level target was accurately recognized. Therefore, our suggested network's efficiency has been shown.

4 Discussion

4.1 Effect of shadows and surface vegetation on canopy edge detection is effectively solved

Most orchard canopy studies at this stage have focused on identifying the canopy of a single tree, but some researchers have also looked at methods to recognize and precisely count tree crowns with significant overlap rates. While there are many research references for techniques of geometric computation and image processing, the aforementioned two approaches are restricted to the relatively constant biological form of tree crowns and the straightforward backdrop of UAV image

TABLE 3 Comparison of AP results for four different methods.

Network	PAFPN	PointRend	AP_seg			AP_box		
			AP	AP50	AP75	AP	AP50	AP75
RX-FPN			59.64	81.8	79.16	67.61	84.4	81.14
RX-PAFPN	✓		62.82	88.08	82.71	69.46	90.56	82.78
PR-RX-FPN		✓	67.35	88.6	84.88	75.13	90.87	87.95
MPAPR R-CNN	✓	✓	68.6	90.78	85.31	75.98	91.19	89.15

✓ indicates that on the basis of the base network, add the corresponding module at ✓. The first line is the base network (RX-FPN). The second line is the base network+PAFPN, abbreviated as RX-PAFPN. The third line is the base network+PointRend, abbreviated as PR-RX-FPN. The fourth line is the base network+PAFPN+PointRend, abbreviated as MPAPR R-CNN.

10.3389/fpls.2022.1041791

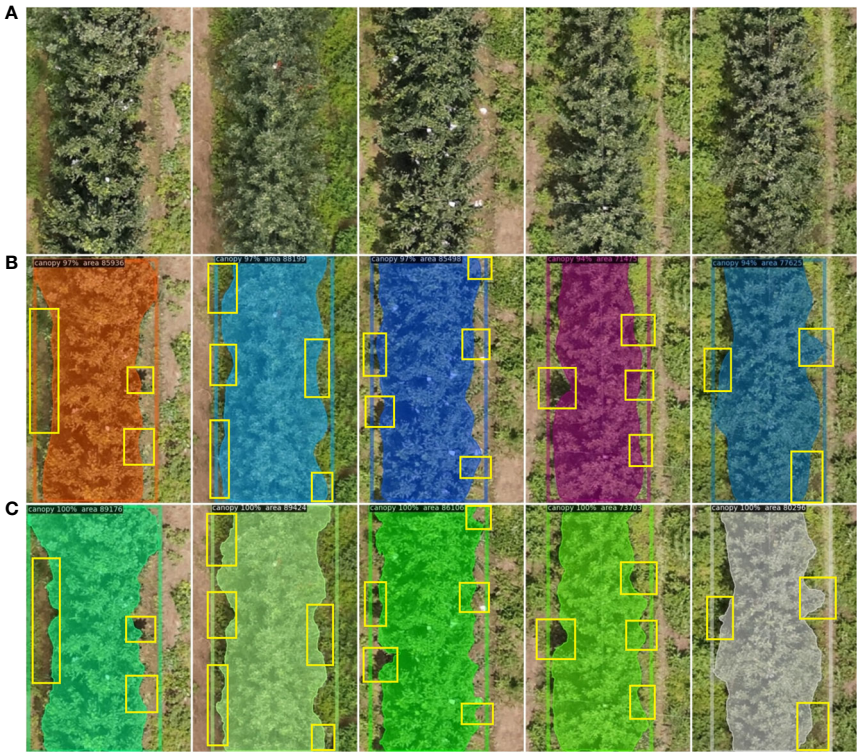

FIGURE 9
Some examples of canopy images of interferences. **(A)** Input of the detected raw image. **(B)** Mask loss curves. **(C)** Mask point loss curves.Yellow rectangular boxes indicate details with significantly different test results.

gathering. The geometric measuring method based on the form of the tree canopy is not reliable because the canopy shape may fluctuate significantly with the continual expansion of the tree canopy. In contrast, the instance segmentation approach might produce high performance by identifying the tree canopy's pixels and segmenting each canopy separately with more flexibility and resilience, or inference in a unified manner. The accuracy of threshold segmentation techniques used in traditional image processing can be significantly impacted by weeds on the ground.

MPAPR R-CNN can address this issue. Firstly, we changed the original ratio of anchor frames in the RPN network. The canopy in dataset distributed along the up-down direction due to images were not rotated by 90 degrees in the data enhancement operation, the detection task of the canopy dataset better facilitated when the RPN network uses a more elongated anchor frame, such as {1:1, 1:2, 1:3}, for the generation of the region suggestion frame. In addition, performing a set of transformations using low-dimensional embeddings by constructing bases in the base block, split-transform-merge strategy can make the deep learning model learn more features, which has been effective for the problem of color interference between the surface vegetation and the canopy.

The most important thing is there are two main distinctions between the original Mask R-CNN architecture and our proposed canopy detection and segmentation approach. This is so that the RPN can generate more precise candidate boxes, which is made possible by the PAFPN module's ability to help the backbone network gather features with rich low-level information. Furthermore, the PointRend module's combination of coarse- and fine-grained features enhanced the segmentation accuracy of ground and canopy edges that have a comparable color palette.

As shown in Figure 11, we visualized the process of PointRend module in canopy image inference. During the Inference process, each region is rendered by iterative coarse-to-fine. In each iteration, PointRend upsamples the previous segmentation result using bilinear differences, and then selects N uncertain points from this result. This was equivalent to purposefully selecting the N points that are difficult to segment, then extracting the feature vectors, and classifying them by MLP to get the new segmentation result, then up-sampling by a factor of 2, extracting the uncertain points, and then point prediction by MLP, and repeating this step until the prediction is completed. PointRend optimized the task of accurately recovering object edges during upsampling.

10.3389/fpls.2022.1041791

FIGURE 10
The visual results of stitching image.

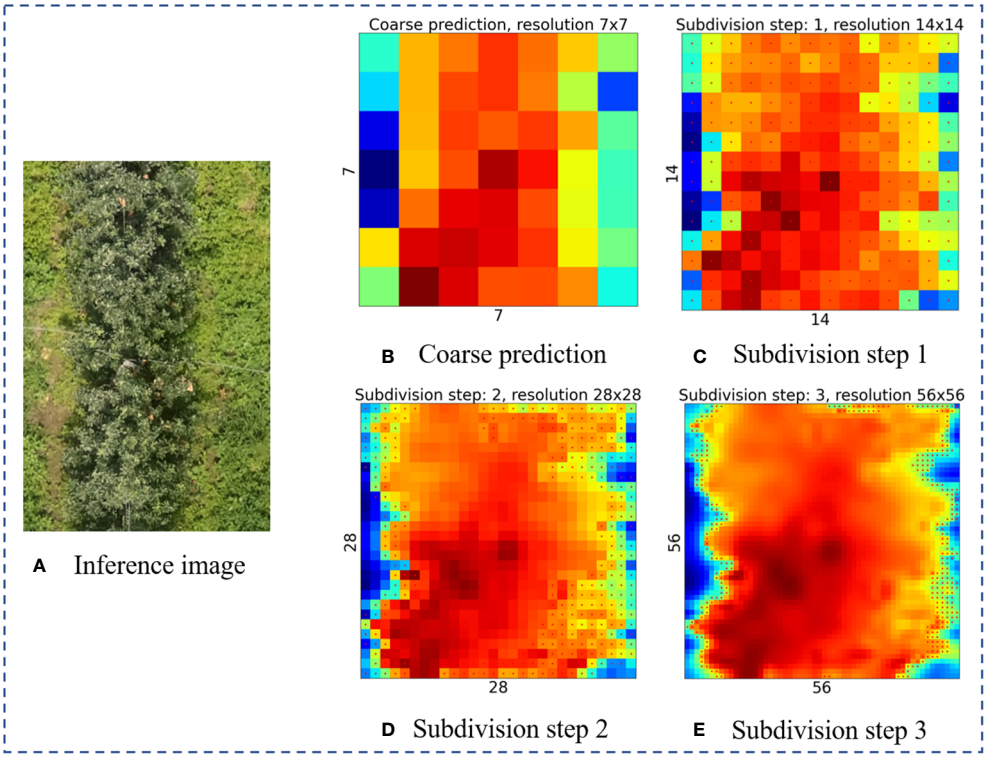

FIGURE 11
Example of inference image subdivision step. **(A)** The raw image used to visualize the inference process. **(B)** Course prediction. **(C–E)** Subdivision step 1-3, the bilinear differential upsampling is performed successively at a rate of 2x.

Therefore, MPAPR R-CNN effectively segmented under the influence of shadows and surface vegetation and improved the recognition accuracy of canopy edges.

4.2 Effectiveness, limitations of UAV in orchard detectron and future work directions

The instance segmentation method enhanced by Pointrend in apple tree orchard situations was initially put out in this work. Two researchers painstakingly annotated RGB photos of the tree canopy for at least three days to create the data sets required to train deep learning models. The labeling of individual branches requires careful identification because of the severe branch crosses that result from dense planting patterns. Additionally, the canopy shadow cast by the sun on aerial photographs when it is not directly overhead presents a difficult labeling challenge. Inadequate illumination or a little swing of the drone during the photo-taking process can further degrade the picture quality of the final orthophoto image, in addition to the effects of cloudiness or wind on the UAV. More crucially, the new research on precision management in orchards has shown considerable promise for UAV gathering of photos with excellent flying efficiency. Compared with UAVs equipped with expensive multispectral or hyperspectral cameras for canopy identification methods, carrying visible light cameras is cost-effective and promising for large area applications.

We propose to focus on two topics of improvement in the upcoming work plan. First, a study may be done using the multi-spectral photos that the DJI P4 UAV captured. Multi-spectral research on canopy segmentation and individual differences in the tree canopy may be analyzed based on the chlorophyll difference between the tree canopy and ground weeds. The second is the study and development of quick and effective orchard spraying tools based on low-altitude data from UAVs on orchard distribution and canopy differences, combined with ground spraying and UAV plant protection technologies.

5 Conclusions

In this paper, a novel orchard canopy detection and segmentation method based on the Mask R-CNN was

presented. By applying the PAFPN module and the PointRend into the original Mask R-CNN framework, combined with the improved anchor and ResNeXt, our well-trained model can automatically detect and segment canopy in orchard with high accuracy. It can be concluded that our algorithm could better capture features of the canopy edges, it could improve the accuracy of the edges of canopy segmentation results, which addressed the over- and under-sampling issues encountered in the pixel labeling tasks. It can be concluded that our algorithm could better capture features of the canopy edges, it could improve the accuracy of the edges of canopy segmentation results. Our future work will be to extend MPAPR R-CNN to many other UAV image applications.

Data availability statement

The raw data supporting the conclusions of this article will be made available by the authors, without undue reservation.

Author contributions

WZ collected and analyzed the data, and wrote the manuscript. XC supervised the project. JQ conceptualized the experiment, selected the algorithms, provided funding support and equipment. SY assisted in analyzing the data. All authors contributed to the article and approved the submitted version.

Funding

This study was supported by the National Natural Science Foundation of China (31971783). Financial support from the above fund and organizations is gratefully acknowledged.

Acknowledgments

The authors wish to thank the Jingxiang Orchard of Weihai City for the help in the collection of the ground data and field data.

Conflict of interest

The authors declare that the research was conducted in the absence of any commercial or financial relationships that could be construed as a potential conflict of interest.

Publisher's note

References

Brede, B., Lau, A., Bartholomeus, H. M., and Kooistra, L. (2017). Comparing RIEGL RiCOPTER UAV LiDAR derived canopy height and DBH with terrestrial LiDAR. *Sensors* 17 (10), 2371.

Chang, A., Jung, J., Maeda, M. M., and Landivar, J. (2017). Crop height monitoring with digital imagery from unmanned aerial system (UAS). *Comput. Electron. Agric.* 141, 232–237. doi: 10.1016/j.compag.2017.07.008

Chang, A., Jung, J., Maeda, M. M., and Landivar, J. (2020). Comparison of canopy shape and vegetation indices of citrus trees derived from UAV multispectral images for characterization of citrus greening disease. *Remote Sensing* 12 (24), 4122.

Cheng, Z., Qi, L., Cheng, Y., Wu, Y., and Zhang, H. (2020). Interlacing orchard canopy separation and assessment using UAV images. *Remote Sens.* 12, 767. doi: 10.3390/rs12050767

Chen, X., Wen, H., Zhang, W., Pan, F., and Zhao, Y. (2020). Development status and direction of agricultural machinery and information technology fusion. *Smart Agric.* 2 (4), 1–16. doi: 10.12133/j.smartag.2020.2.4.202002-SA003

Durfee, N., Ochoa, C. G., and Mata-Gonzalez, R (2019). The use of low-altitude UAV imagery to assess Western juniper density and canopy cover in treated and untreated stands the use of low-altitude UAV imagery to assess Western juniper density and canopy cover in treated and untreated stands. *Forests* 10 (4), 296. doi: 10.3390/f10040296

Gallardo-Salazar, J. L., and Pompa-García, M. (2020). Detecting individual tree attributes and multispectral indices using unmanned aerial vehicles: Applications in a pine clonal orchard. *Remote Sens.* 12 (24), 4144. doi: 10.3390/rs12244144

Gower, S. T., Kucharik, C. J., and Norman, J. M. (1999). Direct and indirect estimation of leaf area index, fAPAR, and net primary production of terrestrial ecosystems. *Remote Sens. Environ.* 70 (1), 29–51. doi: 10.1016/S0034-4257(99)00056-5

He, K., Gkioxari, G., Dollar, P., and Girschik, R. (2017). "Mask r-CNN," in *Proceedings of the IEEE international conference on computer vision*, Vol. 99. 2961–22969.

Hyyppa, E., Hyyppa, J., Hakala, T., Kukko, A., Wulder, M. A., White, J. C., et al. (2020). Under-canopy UAV laser scanning for accurate forest field measurements ISPRS. *J. Photogramm. Remote Sens.* 164, 41–60. doi: 10.1016/j.isprsjprs.2020.03.021

Jonckheere, I., Fleck, S., Nackaerts, K., Muys, B., Coppin, P., Weiss, M., et al. (2004). Review of methods for *in situ* leaf area index determination: Part i. theories, sensors and hemispherical photography. *Agricultural and forest meteorology* 121 (1-2), 19–35.

Kamilaris, A., and Prenafeta-Boldú, F. X. (2018). Deep learning in agriculture: A survey. *Computers and electronics in agriculture* 147, 70–90.

Kirillov, A., Wu, Y., He, K., and Girshick, R. (2020). "Pointrend: Image segmentation as rendering," in *Proceedings of the IEEE/CVF Conference on Computer Vision and Pattern Recognition*. 9799–9808.

Kong, T., Yao, A. B., Chen, Y. R., and Sun, F. C. (2016). "HyperNet: towards accurate region proposal generation and joint object detection," in *Proceedings of the IEEE conference on computer vision and pattern recognition*, Las Vegas. 845–853, IEEE.

Liang, X., Wang, Y., Pyörälä, J., Lehtomäki, M., Yu, X., Kaartinen, H., et al. (2019). Forest *in situ* observations using unmanned aerial vehicle as an alternative of terrestrial measurements. *Forest Ecosystem* 6 (1), 1–16. doi: 10.1186/s40663-019-0173-3

Liu, W., Anguelov, D., Erhan, D., Szegedy, C., and Reed, S. (2016). "SSD: single shot multibox detector," in *Proceedings of the European Conference on Computer Vision (ECCV)*. (Cham: Springer), 21–37.

Liu, S., Qi, L., Qin, H., Shi, J., and Jia, J. (2018). "Path aggregation network for instance segmentation," in *IEEE conference on computer vision and pattern recognition*, Salt Lake City, UT, USA. 8759–8768.

Lou, X., Huang, Y., Fang, L., Huang, S., Gao, H., Yang, L., et al. (2022). Measuring loblolly pine crowns with drone imagery through deep learning. *J. For. Res.* 33 (1), 227–38. doi: 10.1007/s11676-021-01328-6

Ma, Q., Su, Y., and Guo, Q. (2017). Comparison of canopy cover estimations from airborne LiDAR, aerial imagery, and satellite imagery. *IEEE J. Sel. Top. Appl. Earth Obs. Remote Sens.* 10, 4225–4236. doi: 10.1109/JSTARS.2017.2711482

Mohan, M., Silva, C. A., Klauberg, C., Jat, P., Catts, G., Cardil, A., et al. (2017). Individual tree detection from unmanned aerial vehicle (UAV) derived canopy height model in an open canopy mixed conifer forest. *Forests* 8 (9), 340. doi: 10.3390/f8090340

Mo, J., Lan, Y., Yang, D., Wen, F., Qiu, H., Chen, X., et al. (2021). Deep learning-based instance segmentation method of litchi canopy from UAV-acquired images. *Remote Sens.* 13 (19), 3919. doi: 10.3390/rs13193919

Morales, G., Kemper, G., Sevillano, G., Arteaga, D., Ortega, I., and Telles, J. (2018). Automatic segmentation of mauritia flexuosa in unmanned aerial vehicle (UAV) imagery using deep learning. *Forests* 9 (12), 736. doi: 10.3390/f9120736

Mulla, D. J. (2013). Twenty five years of remote sensing in precision agriculture: Key advances and remaining knowledge gaps. *Biosyst. Eng.* 114, 358–371. doi: 10.1016/j.biosystemseng.2012.08.009

Nyamgeroh, B. B., Groen, T. A., Weir, M. J. C., Dimov, P., and Zlatanov, T. (2018). Detection of forest canopy gaps from very high-resolution aerial images. *Ecol. Indic.* 95, 629–636. doi: 10.1016/j.ecolind.2018.08.011

Ouyang, J., De Bei, R., Fuentes, S., and Collins, C. (2020). UAV and ground-based imagery analysis detects canopy structure changes after canopy management applications. *OENO One* 54, 1093–1103. doi: 10.20870/oeno-one.2020.54.4.3647

Ponce, J. M., Aquino, A., Tejada, D., Al-Hadithi, B. M., and Andújar, J. M. (2021). A methodology for the automated delineation of crop tree crowns from UAV-based aerial imagery by means of morphological image analysis. *Agronomy* 12 (1), 43. doi: 10.3390/agronomy12010043

Qi, Y., Dong, X., Chen, P., Lee, K.-H., Lan, Y., Lu, X., et al. (2021). Canopy volume extraction of citrus reticulate blanco cv. shatangju trees using UAV image-based point cloud deep learning. *Remote Sens.* 13, 3437. doi: 10.3390/rs13173437

Qi, J., Liu, X., Liu, K., Xu, F., Guo, H., Tian, X., et al. (2022). An improved YOLOv5 model based on visual attention mechanism: Application to recognition of tomato virus disease. *Computers and electronics in agriculture* 194, 106780.

Rasmussen, J., Ntakos, G., Nielsen, J., Svensgaard, J., Poulsen, R. N., and Christensen, S. (2016). Are vegetation indices derived from consumer-grade cameras mounted on UAVs suficiently reliable for assessing experimental plots? *Eur. J. Agron.* 74, 75–92. doi: 10.1016/j.eja.2015.11.026

Redmon, J., and Farhadi, A. (2018). Yolov3: An incremental improvement. arXiv preprint arXiv:1804.02767

Ren, S., He, K., Girshick, R., and Sun, J. (2015). Faster r-CNN: Towards real-time object detection with region proposal networks. Advances in neural information processing systems 2015, 28.

Ru, Y., Jin, L., Jia, Z. C., Bao, R., and Qian, X. D. (2015). Design and experiment on electrostatic spraying system for unmanned aerial vehicle. *Trans. CSAE* 31 (8), 42–47. doi: 10.3969/j.issn.1002-6819.2015.08.007

Wu, D., Johansen, K., Phinn, S., Robson, A., and Tu, Y.-H. (2020). Inter-comparison of remote sensing platforms for height estimation of mango and avocado tree crowns. *Int. J. Appl. Earth Obs. Geoinf.* 89, 102091. doi: 10.1016/j.jag.2020.102091

Wu, X., Shen, X., Cao, L., Wang, G., and Cao, F. (2019). Assessment of individual tree detection and canopy cover estimation using unmanned aerial vehicle based light detection and ranging (UAV-LiDAR) data in planted forests. *Remote Sens.* 11, 908. doi: 10.3390/rs11080908

Yang, B., and Xu, Y. (2021). Applications of deep-learning approaches in horticultural research: A review. *Hortic. Res.* 8, 123. doi: 10.1038/s41438-021-00560-9

Yıldız, A. K., Keles, H., and Aras, S. (2020). Estimation of canopy area of fruit trees using light unmanned aerial vehicle (UAV) and image processing methods. *Turkish J. Agriculture-Food Sci. Technol.* 8 (5), 1039–1042. doi: 10.24925/turjaf.v8i5.1039-1042.3164

Zhou, D., Li, M., Li, Y., Qi, J., Liu, K., Cong, X., et al. (2020). Detection of ground straw coverage under conservation tillage based on deep learning. *Computers and electronics in agriculture* 172, 105369. doi: 10.1016/j.compag.2020.105369

frontiers | Frontiers in Plant Science

TYPE Original Research
PUBLISHED 26 January 2023
DOI 10.3389/fpls.2022.1087636

OPEN ACCESS

EDITED BY
Ruirui Zhang,
Beijing Academy of Agricultural and Forestry Sciences, China

REVIEWED BY
Qing Tang,
Beijing Research Center for Intelligent Equipment for Agriculture, China
Jiangtao Qi,
Jilin University, China

*CORRESPONDENCE
Shengde Chen
shengde-chen@scau.edu.cn
Yubin Lan
ylan@scau.edu.cn

SPECIALTY SECTION
This article was submitted to Technical Advances in Plant Science, a section of the journal Frontiers in Plant Science

RECEIVED 02 November 2022
ACCEPTED 23 December 2022
PUBLISHED 26 January 2023

CITATION
Chang K, Chen S, Wang M, Xue X and Lan Y (2023) Numerical simulation and verification of rotor downwash flow field of plant protection UAV at different rotor speeds.
Front. Plant Sci. 13:1087636.
doi: 10.3389/fpls.2022.1087636

Numerical simulation and verification of rotor downwash flow field of plant protection UAV at different rotor speeds

Kun Chang[1,2], Shengde Chen[1,2,3]*, Meimei Wang[4], Xinyu Xue[5] and Yubin Lan[1,2,3,6]*

[1]College of Electronic Engineering, College of Artificial Intelligence, South China Agricultural University, Guangzhou, China, [2]National Center for International Collaboration Research on Precision Agricultural Aviation Pesticides Spraying Technology, South China Agricultural University, Guangzhou, China, [3]Guangdong Laboratory for Lingnan Modern Agriculture, South China Agricultural University, Guangzhou, China, [4]Department of Mechanical Engineering, Anyang Institute of Technology, Nanjing Institute of Agricultural Mechanization, Ministry of Agriculture and Rural Affairs, Nanjing, China, [5]Nanjing Institute of Agricultural Mechanization, Ministry of Agriculture and Rural Affairs, Nanjing, China, [6]Department of Biological and Agricultural Engineering, Texas A&M University, College Station, TX, United States

In aerial spraying of plant protection UAVs, the continuous reduction of pesticides is an objective process. Under the condition of constant flight state (speed and altitude), the change of pesticide loading will inevitably lead to the shift of lift force and rotor speed generated by UAV rotor rotation, which will change the distribution of the rotor flow field and affect the effect of aerial spraying operation of plant protection UAV. Therefore, the rotor speed of UAV is taken as the research object in this paper, and the adaptive refinement physical model based on the Lattice Boltzmann Method (LBM) is used to numerically simulate the rotor flow field of the quadrotor plant-protection UAV at different speeds. A high-speed particle image velocimeter (PIV) was used to obtain and verify the motion state of the droplets emitted from the fan nozzle in the rotor flow field at different speeds. The results show that, with the increase of rotor speed, the maximum velocity and vorticity of the wind field under the rotor increase gradually, the top wind speed can reach 13m/s, and the maximum vorticity can reach 589.64s^{-1}. Moreover, the maximum velocity flow value is mainly concentrated within 1m below the rotor, and the maximum vorticity value is primarily concentrated within 0.5m. However, with the increase of time, the ultimate value of velocity and vorticity decreases due to the appearance of turbulence, and the distribution of velocity and vorticity are symmetrically distributed along the centre line of the fuselage, within the range of (-1m, 1m) in the X direction. It is consistent with the motion state of droplets under the action of the rotor downwash flow field obtained by PIV. The study

results are expected to reveal and understand the change law of the rotor flow field of plant protection UAVs with the dynamic change of pesticide loading to provide a theoretical basis for the development of precise spraying operation mode of plant protection UAVs and improve the operation effect.

KEYWORDS

plant protection UAV, dynamic load effect, lattice Boltzmann method (LBM), particle image of velocity (PIV), the numerical simulation

Introduction

The application technology of plant protection unmanned aerial vehicle (UAV) has the advantages of high operation efficiency, low operation cost, and no limitation of operation geographical area and crop growth, which is one of the key technologies to realize the modernization of field management (Dongyan et al., 2014; Yong et al., 2017). Early domestic researchers initially focused on application operation parameters and droplets deposition (Yuan-yuan, 2013; Shuai, 2014). Since 2016, the research scope of plant protection UAV applications began to multiply and extend to other application objects. For example, the distribution of spraying effect in the citrus orchard was studied under different operating parameters (Pan and Qiang, 2016); Study on spraying corn with droplets using JF01-10 plant protection UAV in different growing stages (Zheng et al., 2017); Study on wheat scab control by using DJI T30 plant protection UAV (Tang et al., 2018). That can be seen that plant protection UAVs have been widely used in modern precision agriculture (Huang et al., 2013; Shahbazi et al., 2014; Xiongkui et al., 2017; Chen et al., 2022). In particular, the quadrotor plant protection UAV, the most important type of plant protection UAV, has been effectively applied to prevent and control diseases, insects and weeds in various countries (Jiyu et al., 2018; Wang et al., 2019; Zhan et al., 2022).

Generally, in terms of studying the effect of droplets deposition and distribution, field experiments mainly use materials such as water-sensitive papers, Mylar sheets, Petri dishes and polyethene wires to study the related parameters of wind field distribution characteristics (Shengde et al., 2016; Xiaonan et al., 2017; Wang et al., 2018; Wu et al., 2019). Through these materials, the droplets in the vertical and horizontal planes can be collected in space movement. Still, only the deposition effect of the pesticide droplets can be observed, and the deposition motion state and mechanism of the droplets can not be directly revealed. The rotor wind field generated by the plant protection UAV is the most critical factor affecting aerial spray droplets deposition and distribution characteristics in the gradual settlement of pesticide droplets under the rotor wind field (Songchao et al., 2015; Songchao et al., 2017). In recent years, some researchers have also used wireless wind sensor networks, ultrasonic anemometer arrays and tensiometers to measure the change of instantaneous wind field under the rotor to reveal the influence mechanism of the rotor downwash wind field on droplets deposition (Jiyu et al., 2014a; Zhang et al., 2016; Songchao et al., 2017; Wang et al., 2018; Tang et al., 2019; Wu et al., 2019). In the whole process of aerial spraying of plant protection UAV, with the continuous reduction of the pesticide in the pesticide box, its mission load parameters are always in a constant dynamic change process. Therefore, the effect of the rotor wind field of plant protection UAV under dynamic load is bound to differ (Jiyu et al., 2014a; Jiyu et al., 2014b; Shengde et al., 2016; Chen et al., 2017). Nevertheless, the above research is only focused on the hover state or a particular condition to test and analyze, and the change of pesticide load in the actual operation condition determines that the rotor wind field distribution is a process of continuous change. Therefore, there are many limitations; the above research results cannot directly reflect plant protection UAV's rotor wind field distribution transformation in the whole operation process.

With the improvement of the computing power of computers and the gradual improvement of the theory of fluid mechanics, the cross combination of the two makes computational fluid dynamics (CFD) widely in-depth into various fields. Especially in the field of agriculture, computational fluid dynamics is often used to analyze the wind field changes of UAVs in flight. Through the numerical simulation method, the three-dimensional CFD model and two-phase flow model were established to study the influence of the downwash wind field of the plant protection UAV on the movement trajectory and distribution of droplets (Junfeng et al., 2017; Fengbo et al., 2018; Hao et al., 2019; Juan et al., 2019; Guo et al., 2020). However, in these previous numerical simulation studies, the complex structure of nozzle model is not accurate enough due to the physical model of nozzle in the numerical simulation. The physical model in numerical simulation can not completely represent the real nozzle structure. Nonetheless, all these studies provide specific references and guidance for the study of wind field simulation of plant protection UAVs.

For wind field distribution models under complex conditions, due to the inaccuracy of the physical model and the weak computational force, many simulations will simplify

the physical model and reduce the mesh density, resulting in some deviations. For example, in the simulation of the rotor wind field, the structure will be simplified, and the mesh density will be reduced so that the motion state in the rotor wind field can be obtained conveniently and quickly. The computational fluid dynamics method based on the Lattice Boltzmann method (LBM) has advantages in dealing with the complex model boundary of UAV rotors (Fakhari and Lee, 2015; Sheng et al., 2018). It can accurately deal with problems at both micro and macro scales (Tang et al., 2020a; Zhang et al., 2020; Tang et al., 2021; Wang et al., 2021). In addition, with the development of image processing technology, particle image velocimetry (PIV) has been applied to the analysis of spray under the rotor wind field (Jin et al., 2014; Tang et al., 2020b). However, there are few papers on the combination of numerical simulation and PIV image analysis technology to study the downwash flow state of the rotor wind field of plant protection UAVs under dynamic load.

Therefore, this study is devoted to studying the changes in the rotor wind field distribution of plant protection UAVs under dynamic loads (at different rotor speeds) and focuses on revealing the influence mechanism of rotor wind field on droplet distribution characteristics of plant protection UAVs at different rotor speeds. Because the Lattice Boltzmann method has obvious advantages in dealing with complex boundary conditions and non-stationary moving objects, XFlow software is used to simulate the distribution of the downwash wind field of the quadrotor plant protection UAV at different rotor speeds. At the same time, because PIV has the characteristics of non-contact, high measurement accuracy and fast processing speed, PIV is used in this study to measure the spray changes of the wind field under the rotor at different speeds. Through the combination of the two, the conditions of the downwash wind field and the velocity and vorticity of droplets under different rotor speeds are compared. It is hoped that this study can help researchers better understand the distribution characteristics of rotor wind field at different rotor speeds and further reveal the distribution characteristics and rules of droplet deposition under the influence of rotor wind field in the dynamic load state of the quadrotor plant protection UAV.

Materials and methods

Numerical simulation

Physical model

This paper takes the 410S quadrotor plant protection UAV (Xiamen Land and Air Technology Co., LTD.) as the research object. As one of the most representative models in the market at present, the UAV has the functions of manual or semi-automatic route flight, continuous spraying at break point, low voltage protection and so on. The expansion size is 1075×1075×490mm.

FIGURE 1
Quadrotor plant protection UAV.

The folding size is 635×666×490mm, the UAV empty weight is about 5kg (excluding the spraying system), the maximum takeoff weight is 25kg, the rotor size is 30 inches, and the spraying is 1.3-2 acres per sortie. The UAV is shown in Figure 1, and its main parameters are shown in Table 1.

The detailed parameters of the Xiamen Land and Air Technology Co., LTD. 410S quadrotor plant protection UAV are listed in Table 1.

The UAV rotor is the essential component to generate the rotor wind field, so it is essential to establish accurate 3D modelling for it. Therefore, in order to accurately simulate the wind field characteristics of the quadrotor UAV at different rotor speeds, it is necessary to conduct a three-dimensional reverse reconstruction of the rotor to establish the physical model of the rotor. In this paper, a handheld 3D scanner N700 (CREAFORM INC.) is used to scan the rotors in three dimensions to obtain the point cloud data of each scanning surface of the rotors, as shown in Figure 2A. Then Geomagic Studio software (Geomagic INC.) is used to post-process each scanned surface point and reconstruct the three-dimensional surface model of the rotor, as shown in Figure 2B. The body, landing gear and other components of the quadrotor UAV are based on surveying and mapping technology dimensions. Autodesk Inventor

TABLE 1 Parameters of the quadrotor plant protection UAV.

Parameters	Technical index
Rotor diameter/m	1.4
Typical application speed/m·s^{-1}	3-8
Rotor speed/rpm	0-3000
Load capacity/kg	10
Flight duration/min	8-10
Operate temperature/°C	-25-50

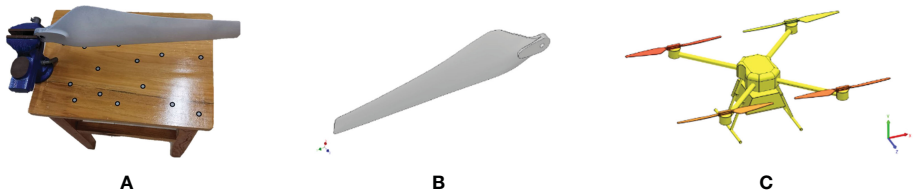

FIGURE 2
Three-dimensional model of quadrotor plant protection UAV.

Profession (Autodesk INC.) is used to establish a three-dimensional model. The complete three-dimensional model of the constructed electric quadrotor plant protection UAV is shown in Figure 2C.

Simulation calculation

Commonly used commercial Computational Fluid Dynamic (CFD) software, such as Fluent (ANSYS Inc.) and CFX (ANSYS Inc.), the dynamic mesh technique is usually used in dynamic simulation to analyse the hydrodynamic characteristics of rotors in a high-speed rotating motion. However, for complex quadrotor model boundary cases, the mesh reconstruction in the numerical simulation process usually consumes a large amount of computational time, and it is easy to produce negative volume in the calculation process, leading to calculation errors. XFlow (Next Limit Dynamics S.L.) is a fluid Dynamics simulation and analysis software based on the Lattice Boltzmann method (LBM), which does not need to mesh the model. It has advantages in solving complex boundary conditions and three-dimensional flow field problems of non-stationary moving objects. It can conveniently deal with fluid problems at micro and macro scales. Because this particle-based calculation method does not require traditional grid division and has high efficiency in the discretisation stage and accurate calculation results, this paper adopts the LBM-based XFlow software to simulate the downwash wind field of the quadrotor plant protection UAV.

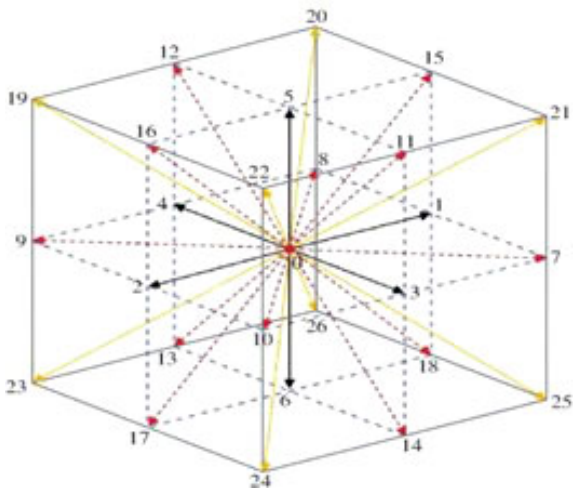

FIGURE 3
D3Q27 lattice model.

Simulation method

Xflow uses the LBM method, where the computation domain is a uniform cube cell. The LBM is a mesoscopic method, and the macroscopic Navier-Stokers equations can be derived from the lattice Boltzmann equation according to the Chapman-Enskog expansion. In many of the LBM models, XFlow adopts a three-dimensional lattice structure as shown in Figure 3, which includes 27 velocity vector directions (D3Q27), 1 discrete velocity vector lattice body to zero point in the centre, 6 discrete velocity vectors from the body of the heart to the centre of the lattice decent, 12 discrete velocity vector from body centre to lattice body midpoint, 8 discrete velocity vectors from the centre of the body to the top Angle of the lattice. Therefore, compared with the traditional LBM, there are higher-order spatial discretisation modes.

In this method, the lattice-Boltzmann equation is selected as the solution equation, and the lattice-Boltzmann transport equation is discretized on the lattice as

$$f_i(x + e_i, t + dt) = f_i(x, t) + W_i(x, t) \quad (1)$$

$$W_i = \frac{1}{\tau}(f_i - f_i^e) \quad (2)$$

Where f_i ——Particle velocity vector distribution function; e_i ——The velocity of the particle in the i direction; d_t——Time step; $f_i(x,t)$ ——The velocity distribution function of the particle in i the direction at x point at t time; w_i—— Collision operator; f_i^e—— One particle equilibrium distribution function; τ —— Dimensionless relaxation parameter.

After the approximate simplification of the collision operator, the equation is reduced to the Navier-Stokers equation, which is the governing equation to describe the fluid flow, and the fluid state with a low Mach number can be displayed.

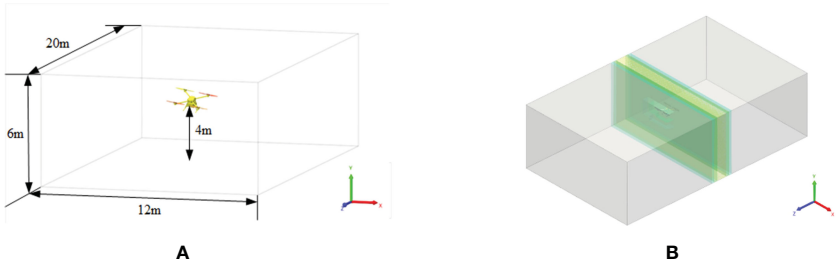

FIGURE 4
Fluid calculation domain and Discrete division of the computational domain.

Boundary conditions

The fluid calculation domain set by simulation is a cuboid with a space size of 12m×6m×20m. In the calculation domain, the height of the quadrotor plant protection UAV from the ground is 4m, as shown in Figure 4A.

By improving the spatial and temporal resolution of the calculation domain, the flow field data parameters of the rotor can be obtained more accurately to obtain the omnidirectional irregular flow turbulence scale. Since the simulation of rotor plant protection UAV focuses on the rotor surface, fuselage surface and the wake of the downwash wind field of the UAV, the global spatial refinement resolution size of the virtual wind tunnel is set to 0.2m to save computing resources and shorten computing time. The surface refinement method of the fuselage, main rotor and tail is set as an adaptive method, and the resolution of the fuselage and rotor is set as 0.05m. In order to further demonstrate the characteristics of the wake of the downwash wind field, the refinement space domain is set as 12m×6m×1m at the centre of the rotor, and the refinement resolution of the wake of the downwash wind field is set as 0.025m. After the parameters are set, the automatic discretisation effect diagram of numerical simulation is shown in Figure 4B. The motion characteristics of the four rotors are set to be rigid and rotate around the Y-axis of their respective coordinate systems.

In order to obtain the movement law of the quadrotor UAVs in the downwash field, numerical simulation analysis is carried out for the quadrotor UAVs in hovering state at different speeds of 1000rpm, 1500rpm, 2000rpm and 2500rpm. Because the rotor of the quadrotor plant protection UAV will produce velocity flow and vortex in the process of rotation, in order to analyse this phenomenon, the simulated phase diagram of two rotors of the quadrotor UAV in a hovering state is selected for analysis.

PIV experimental

UAV system platform

The UAV rotor used in the test is fixed on the plant protection UAV rotor platform, designed and manufactured by the Nanjing Institute of Agricultural Mechanization. The test platform mainly includes the rotor system, spray system, control system and lifting device. The main body of the test platform is composed of aluminium alloy profiles, which are suspended under the gantry frame. There are three adjustable attitudes ranging from -30°~30°, which can support using multiple UAVs, such as quadrotor, six-rotor and eight-rotor. The rotor system is specially customized for the test platform. The motor speed of the moving platform is controlled by the ground station software in real-time to achieve the corresponding wind field test

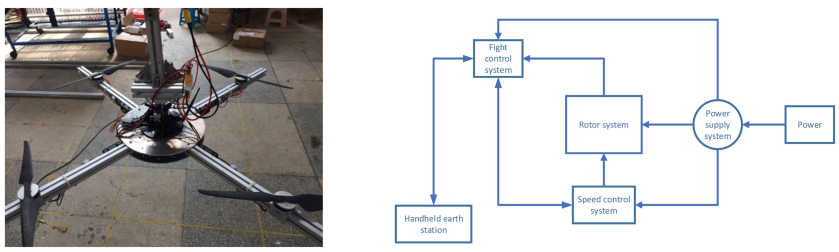

FIGURE 5
Plant protection UAV test platform.

TABLE 2 Power system parameters of plant protection UAV.

Parameters	Technical index
Rotor diameter/m	1.4
Rotor speed/rpm	0-3000
Operation duration time/min	10-15
Operate height/m	1-3

effect. At the same time, the parameter information of the platform can be monitored in real time, and the test data can be saved. The quadrotor structure is used in the test, and the height of the rotor is about 2m above the ground. The UAV system platform is shown in Figure 5.

Details of power system of plant protection UAV are shown in Table 2 below:

The spray system of the platform is installed next to the gantry frame and consists of a water pump and a control system. The spray system supports the hydraulic nozzle and centrifugal spray nozzle. The pressure range is 0~1.2*MPa*, the flow range is 0~2*L/min*, and the spray time is automatically controlled. In this experiment, a fan-shaped 110-02 nozzle designed and manufactured by Lechler is used to produce droplets with an average volume diameter of 120μm. Because the relative density and size of droplets meet the particle requirements required by the PIV test, the droplets produced by the sprinkler head can be directly used as tracer particles for the PIV test. Meanwhile, the nozzle is installed 35cm below the rotor.

PIV system

Because the rotor vortex caused by the downwash wind field of the quadrotor plant protection UAV is aperiodic, the PIV device is selected as the measurement tool to measure the fluid domain. PIV technology is a transient, multi-point, non-contact fluid dynamics measurement method, which can record the velocity distribution information of particles at a space point at the same time, provide abundant spatial structure and flow characteristics of the flow field, and has very high measurement accuracy. The PIV system consists of high-speed cameras (2048*2048, 32 FPS; TSI Incorporated, USA), a pulsed laser (380 mJ/pulse, wavelength = 532 nm; TSI Incorporated, USA), etc. The laser generated by the pulsed laser is combined through an optical system composed of a cylindrical mirror and a spherical mirror to generate a slice light source with a waist thickness of about 1 mm. The frame rate is resized according to the actual situation. In this experiment, the schematic setting of the whole PIV system experiment is shown in Figure 6.

A 50mm lens is used to generate a large enough field of view to capture the motion state of the flow field particles, which is the evolution of particles scattering from the nozzle into the air. The movement of droplet particles in the wind field under different rotor speeds is captured by setting Mask, as shown in Figure 7. In this experiment, the pulse width of the YAG laser pulse is 3-5ns, the time interval of two laser beams is 50μs, the time series between two pictures is 0.025s, and the maximum distance of particle movement is less than 1mm. Therefore, the query window is set to 36*36 pixels (a 4.6×4.6mm square) to ensure that the particle moves less than a quarter of the query window length, and the overlap rate is set to 50×50mm.

The results of PIV are obtained by obtaining the average value of flow field data from multiple consecutive double-frame images when the rotor speed is 0, 1000rpm, 1500rpm, 2000rpm and 2500rpm, respectively. Based on its high sampling

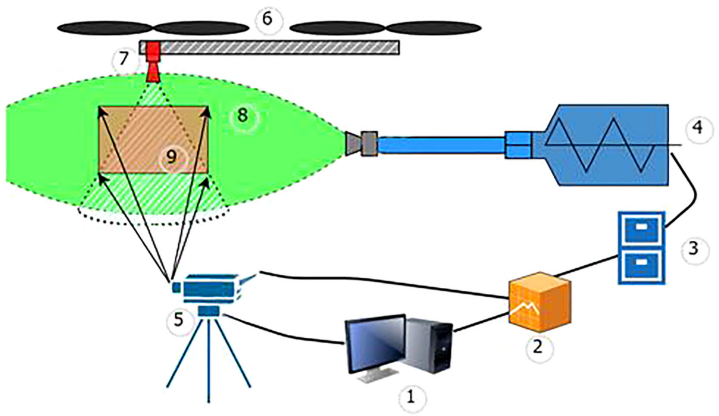

FIGURE 6
Schematic diagram of the experiment.

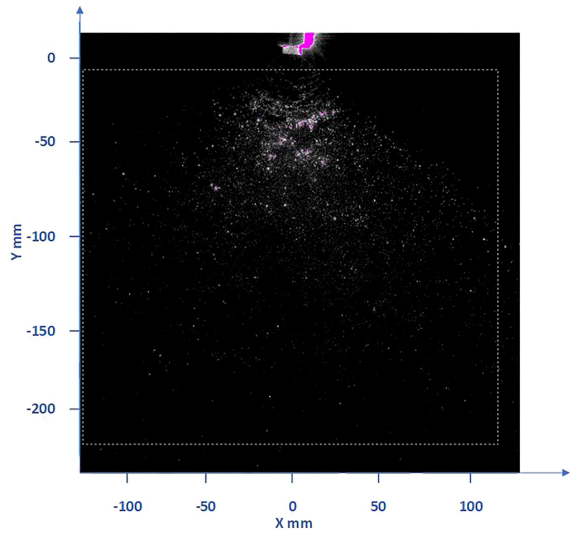

FIGURE 7
Image of droplets distribution in the downwash flow field of the nozzle under the rotor. (The red particles are the droplets irradiated by the laser, and the dashed box is the set Mask flow field analysis area).

frequency, the turbulent kinematic energy is calculated from the two position components of the velocity fluctuation as follows:

$$k = \frac{1}{2}\left(u'^2 + v'^2\right)$$

Where u' is the horizontal component, v' is the vertical component.

Insight 4G software is used to obtain two consecutive instantaneous AB frames spray images, analyze the flow field in the images, and generate the original data. Tecplot software is used to obtain the image data to generate the velocity vector map. The resolution of these images is 2048*2048 pixels. The nozzle is located at (0,0) in the coordinate system, and the rotor is located directly above the nozzle. Because the laser beam irradiates the droplet field from the right and the droplets have a refraction effect, the light on the left side is weaker than that on the right side, so the effect on the right side of the whole droplet field is obviously stronger than that on the left side, but the actual effect should be consistent. According to the rotor speed used in the numerical simulation analysis, the corresponding rotor speed of 1000rpm, 1500rpm, 2000rpm and 2500rpm is also selected for the PIV test to observe the influence of the wind field below the rotor on the droplet velocity flow and vortex in the test. The velocity and vorticity motion of droplets under the action of the wind field is analyzed.

Results and analysis

Numerical simulation of rotor flow field

Distribution of rotor velocity under numerical simulation

The rotor speeds studied in the test are respectively 1000rpm, 1500rpm, 2000rpm and 2500rpm. Therefore, 3s and 5s at different times are selected to study the distribution of flow fields at different rotor speeds to compare the differences of flow fields. Figure 8 is the velocity state phase diagram of the downwash wind field at 3s and 5s when the rotor speed of the quadrotor plant protection UAV is 1000rpm, 1500rpm, 2000rpm and 2500rpm, respectively. As can be seen from Figures 8A1-D1, with the increase of rotor speed, the speed value under the rotor of the quadrotor UAV gradually increases, with the maximum value increasing from 7.6m/s at 1000rpm to 15.7m/s at 2500rpm. Due to the presence of turbulence, the velocity core area under each rotor (velocity greater than 10m/s) also gradually breaks apart, forming four distinct velocity core areas. At the same time, a very low value of local velocity occurs just below the centre of each rotor in the process of rotor rotation. Furthermore, with the increase of rotor speed, the situation of extremely low local velocity becomes more apparent. By observing Figure 8A1 and Figure 8A2, it is found that when the rotation speed is 1000rpm, the situation of the very low local speed is not apparent, indicating that the quadrotor plant protection UAV is still in the relatively initial state when it is actually 1000rpm and has not reached the stable flight state.

As shown in Figures 8A2-D2, with the increase of rotor speed, the maximum speed under the rotor of the quadrotor UAV varies from 7.9m/s at 1000rpm to 14.6m/s at 2500rpm. This shows that the quadrotor plant protection UAV does not reach a stable flight state at 1000rpm while the maximum speed under the rotor decreases at 2500rpm. The reason for the decrease is that the velocity flow field under the rotor gradually diffuses around and becomes more widely distributed after a period of development. In addition, part of the wind bouncing on the ground also rises, which offsets the downwash wind, so the downwash force is weakened, and the maximum speed is reduced(as shown by the red arrow in the figure). By observing Figure 8, it can be seen that the contraction distortion of the velocity core area caused by the rotor is not apparent when the rotational speed is 1000rpm and 1500rpm in the figure. However, the contraction distortion of the velocity core area under the rotor is noticeable when the rotor speed is 2000rpm and 2500rpm. It indicates that the quadrotor plant protection UAV basically reaches a stable flight state when the rotor speed is above 2000rpm.

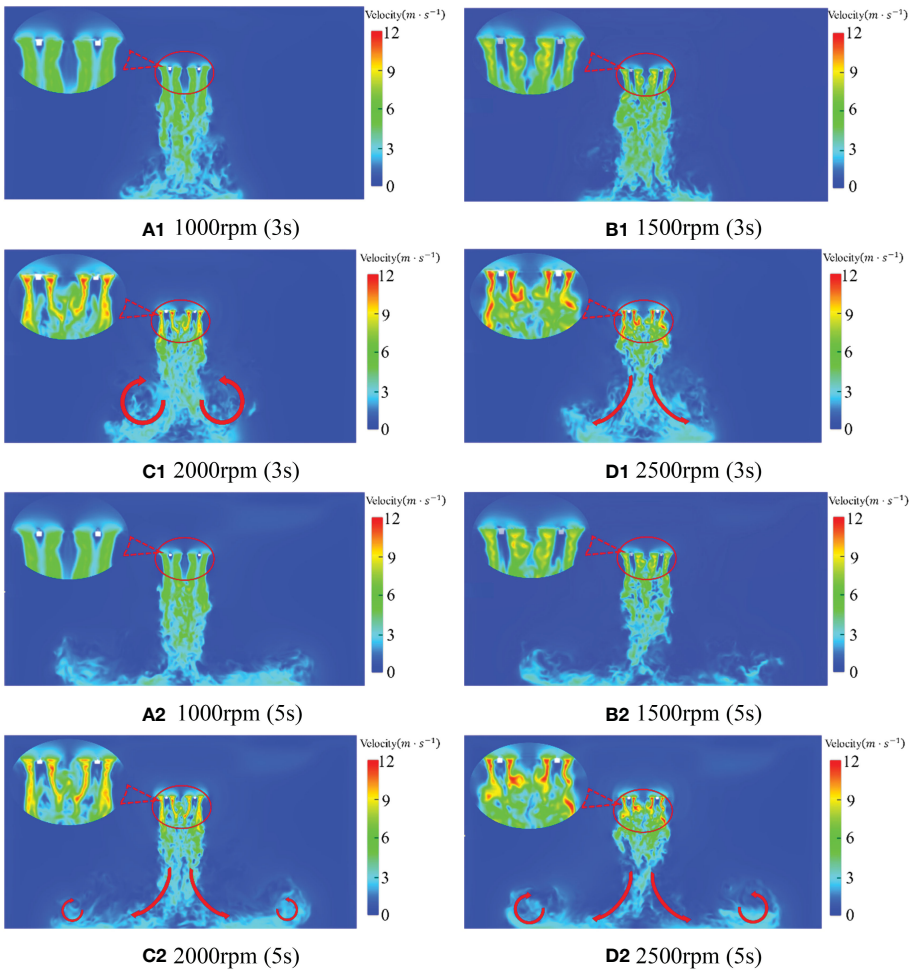

FIGURE 8
Rotor velocity distribution at different speed and time.

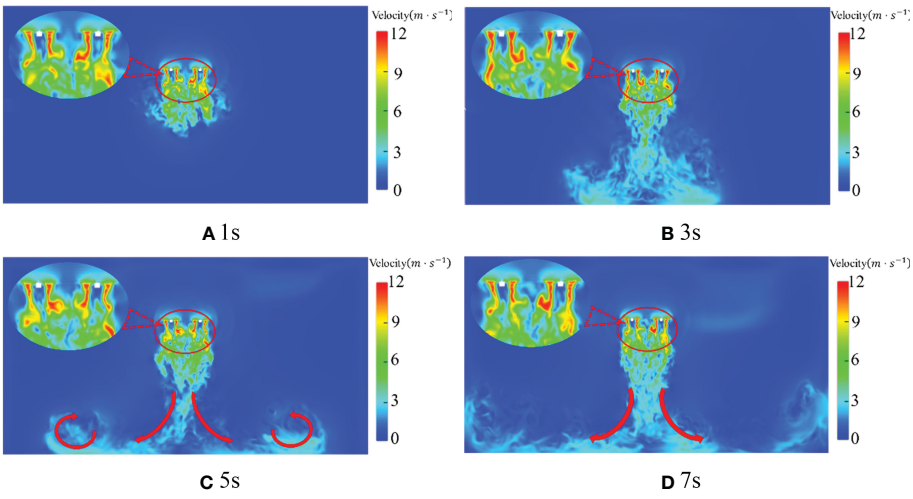

FIGURE 9
Rotor velocity distribution at a different time and 2500rpm.

Because the flow field has just reached the ground and generated turbulence at 3s and the flow field is formed at 5s when the rotor speed is 2500rpm, the rotor speed is 2500rpm for analysis. Figure 9 is the speed state phase diagram of the quadrotor plant protection UAV at 1s, 3s, 5s and 7s when the rotor speed is 2500rpm. It can be seen from Figures 9A-D that a jellyfish-like wind field with the speed decreasing from the fuselage has been generated around the quadrotor plant protection UAV at 1s. The maximum wind field at each time is 14.8m/s, 15.7m/s, 14.6m/s and 14.9m/s respectively. Thus, it can be seen that the wind field initially acts together in the high-speed area formed above the rotor, integrates with each other, diffuses to the top of the whole fuselage, and rapidly decreases from the fuselage to the surrounding areas. The velocity core area has been formed just below the rotor at 1s. With the gradual downward development of the wind field, the tail is broken more violently in the development process, strong turbulence appears below, and the influence range gradually increases downward. The flow field has reached the ground, and the maximum speed of the wind field also reaches the highest at this moment, which is 15.7m/s at 3s. Then the wind field, due to contact with the ground, collision with the ground, rebound and spread around, a violent turbulent phenomenon occurred(as shown by the red arrow in the figure). The maximum speed gradually reduced, kept below 15 m/s. It can be seen that with the increase of time, the velocity flow field under the quadrotor UAV gradually diffuses downward, and the range of the flow field gradually increases. After bouncing with the ground, the airflow is absorbed by the low pressure generated by the high-speed airflow, and the spiral airflow is gradually formed in the vertical space. Taking the centre line of the fuselage as the axis of symmetry, the flow field is about in the x-direction (-1m, 1m). At the same time, from the perspective of flow field development, the velocity flow field is basically developed and formed around 5s.

According to Figures 8, 9, when the rotor of the quadrotor UAV rotates, the velocity core area generated by the two rotors with opposite rotation directions is basically symmetric, and the overall posture of aggregation, contraction and downward pressure is presented after the development and formation. The local extremely low velocity under the rotor becomes more obvious with the increase of rotor speed. As the distance from the rotor increases, the velocity core area generated by the downwash wind field under the rotor gradually decreases, and the distance of about 1m below the rotor basically disappears.

Distribution of rotor vorticity under numerical simulation

Figure 10 is the cross-sectional phase diagram of the vortex state of the quadrotor plant protection UAV at the hover time of 1s, 3s, 5s and 7s when the rotor speed is 2500rpm. First of all, it can be seen from Figure 10 that the maximum vorticity at each moment reaches 337s^{-1}, 376s^{-1}, 304s^{-1} and 343s^{-1} respectively, showing that the maximum vorticity rises first and then decreases. The maximum vorticity around the rotor has reached 337s^{-1} at 1s, and the vortex on the rotor surface is concentrated and distributed around the rotor. Second, the vortex moves down in a vertical direction under each rotor. Due to the contraction distortion characteristic of the wingtip vortex, the contraction effect is induced by the following wake vortex. After leaving the rotor surface, the vortex gradually shrinks. Under the coupling effect of the vortex, the rotor vortex is damaged and eventually forms turbulence. As shown in Figure 10, with the fuselage centre line as the axis of

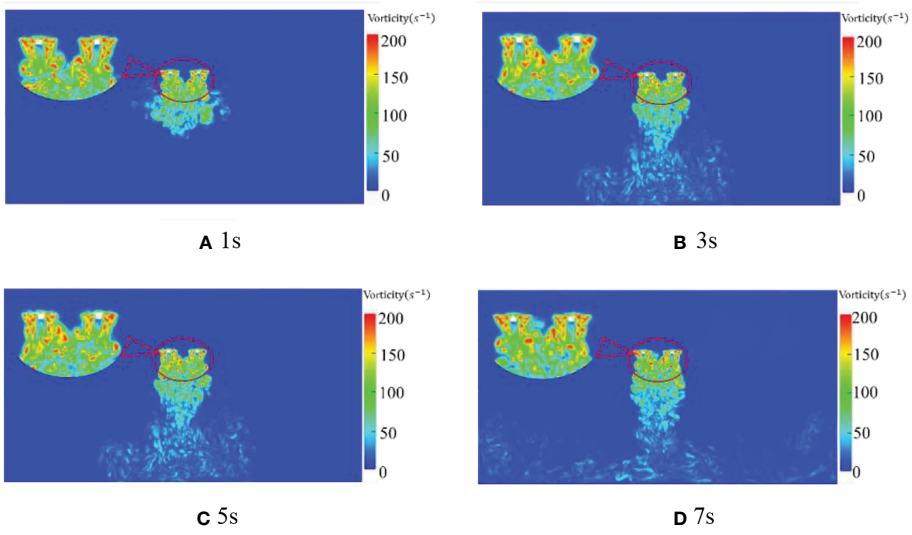

FIGURE 10
Distribution of rotor vorticity at different times and 2500 rpm.

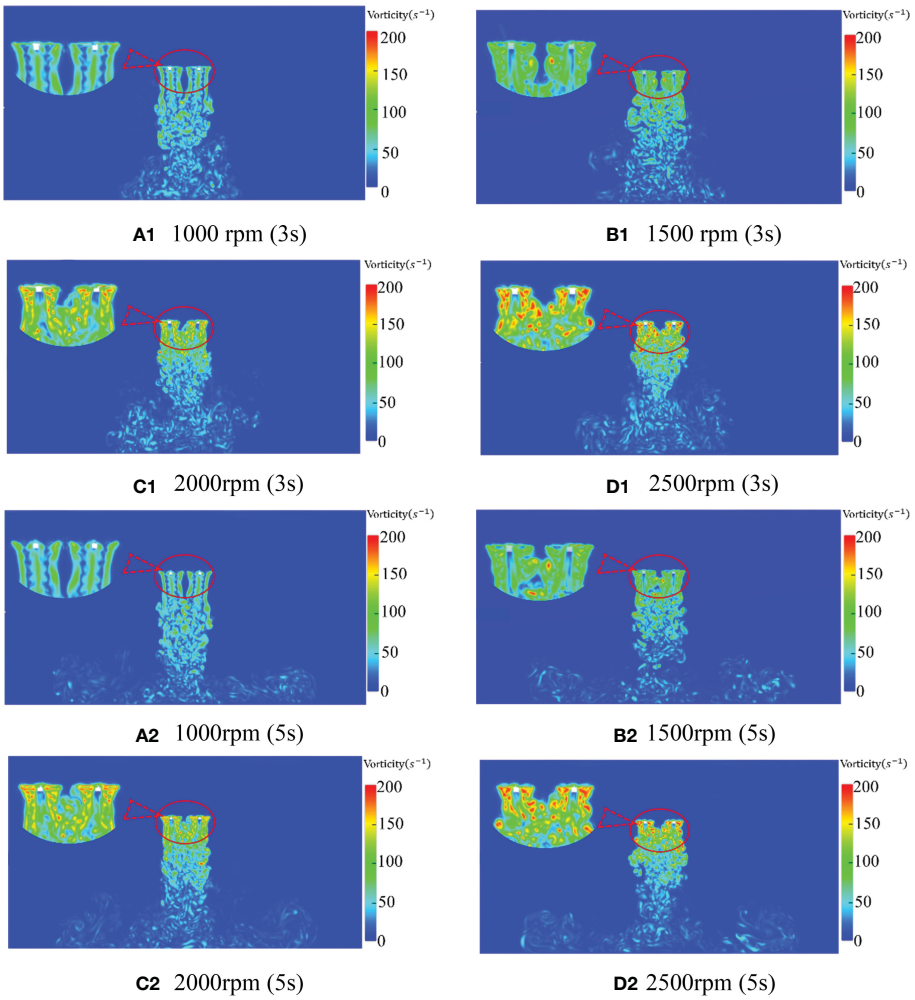

FIGURE 11
Distribution of rotor vorticity at different speeds and different times.

symmetry, the main vortex field is about in the x-direction (-1m, 1m).

With the passage of time, the maximum vorticity reaches $376s^{-1}$ at 3s. Then the larger value of vorticity begins to decline and mainly concentrates within 0.5m below the rotor. At the same time, the rest parts gradually move further below the rotor and contain larger vorticity. Larger vorticity may even appear within 2m below the rotor and then be destroyed by coupling, resulting in turbulence. However, the vorticity beyond 2m below the rotor is small and basically exists in the form of turbulence. This indicates that the quadrotor plant protection UAV produce a strong enrolling effect within 1m below the rotor and the enrolling effect is weaker, followed by 1m-2m. At the same time, in the vertical direction, the spiral vortex decreases with the increase of the distance from the rotor.

Since the velocity field at 3s and 5s time is mainly observed and analyzed in the wind field analysis, and a similar flow field also appears in the vortex field, this paper also analyze the vortex at various speeds at 3s and 5s time. Figure 11 is the vortex state phase diagram of the downwash wind field at 3s and 5s when the rotor speed of the quadrotor plant protection UAV is 1000rpm, 1500rpm, 2000rpm and 2500rpm, respectively. As shown in Figures 11A1-D1, the vorticity also increases, and the vortex changes more violently with the increase of rotor speed. In Figure 11A, the vortex within 1m below the rotor shows apparent symmetry, showing a relatively stable state as a whole. In the range of 1m-2m below the rotor, relatively chaotic turbulence is generated due to the coupling effect of the rotor vortex. In the range of 2m to 4m below the rotor, the turbulent effect is more apparent, and the vortex has a strong irregular movement. At the same time, the symmetrical vortex generated by the rotor decreases obviously with the increase of rotor speed. When the time is 3s, the symmetric vortices with the rotation speed of 1000rpm, 1500rpm, 2000rpm, and 2500rpm mainly appear within 1m, 0.8m, 0.6m, and 0.5m below the rotor, respectively. The maximum vorticity under the rotor also

changes from 216s^{-1} at 1000rpm to 376s^{-1} at 2500rpm with the increase of rotor speed.

Although part of the vortex symmetry is still maintained in Figure 11A2 compared with Figure 11A2, the maximum vorticity under the rotor is 213s^{-1} in Figure 11B2, and the vortex is greatly disorganized. In Figure 11B2, the vortex under the rotor even appears to have temporary disconnection. As seen from Figure 11B1, the maximum vorticity becomes 170s^{-1} with the increase of time at 1000rpm. This indicates that the vortex of the quadrotor plant protection UAV developed with time at this speed appeared disorder after reaching the ground at 3s. By observing the vortex state of 1500rpm, 2000rpm and 2500rpm at 5s, the maximum vorticity of 1500rpm and 2000rpm at 5s is 246s^{-1} and 283s^{-1}, respectively, which also shows a certain degree of disorder, but the degree of influence gradually decreases. The vortex state at 2500rpm appears more stable and develops more stably than 3s. By comparison, it can be seen that the greater the rotor speed, the longer the vortex needs to reach relative stability.

According to Figures 10, 11, when the rotor of the quadrotor UAV rotates, the vortices generated by the two rotors with opposite rotation directions are basically symmetric, and the overall posture of aggregation, contraction and downward is presented after the development and formation. Moreover, the greater the rotational speed, the longer it takes for the vortex to

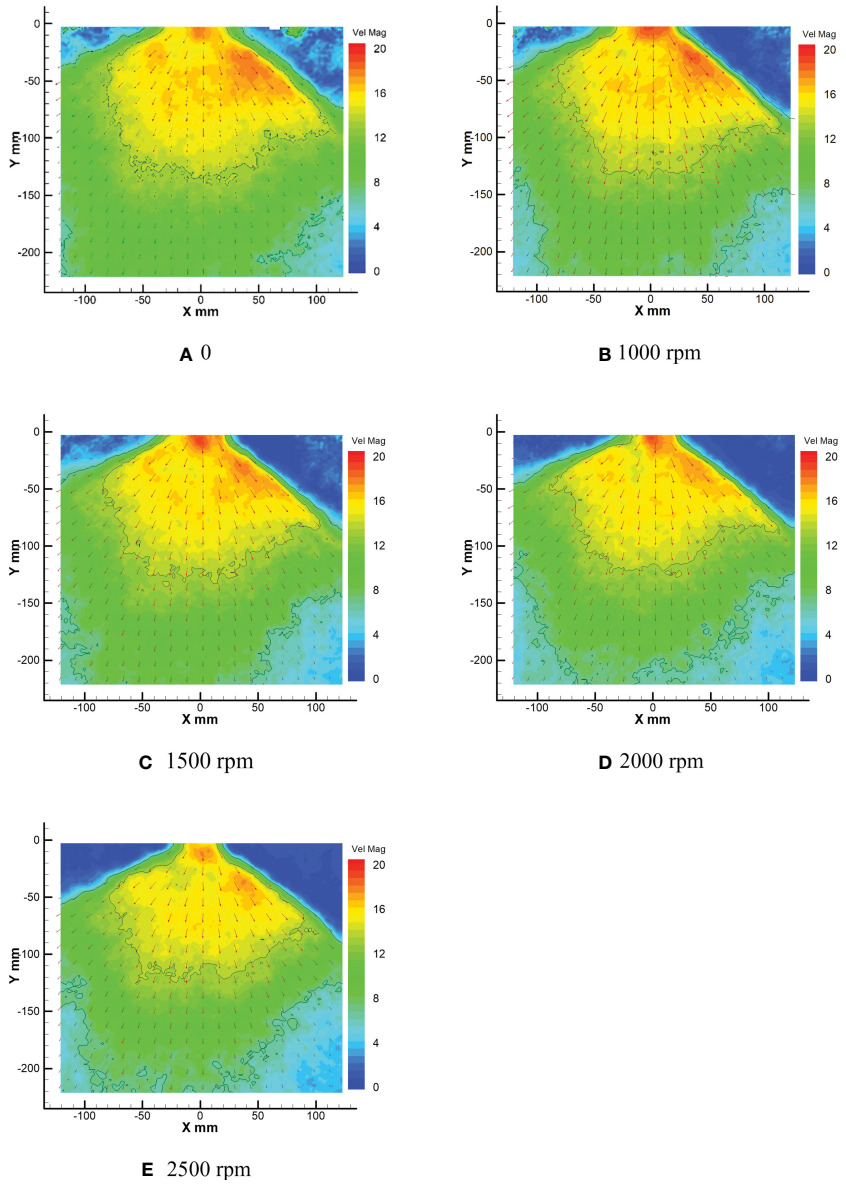

FIGURE 12
Average droplet velocity field at different rotor speeds.

reach a relatively stable state. At the same time, with the increase of the distance from the rotor, the vorticity gradually decreases, and the enrolling effect of the larger vortex group is mainly concentrated within 1m below the rotor.

PIV experiment of the rotor flow field

Distribution of rotor velocity under the PIV experiment

As shown in Figure 12, they are the droplet velocity fields at rotor speeds of 0, 1000rpm, 1500rpm, 2000rpm and 2500rpm, respectively. Figure 12A shows that the expanding state of droplets is mainly distributed in the sector. The effective range of droplets greater than 16 m/s (defined as high-speed) in the sector area is mainly distributed in the sector area of X (-70, 100) Y (0, -150), while the regional velocity in other areas is mainly in the range of 6-16 m/s (defined as medium-speed). The droplet velocity in the lower right corner is mainly below 6 m/s (defined as low-speed), which has been shown by curves in the figure of each area. There are medium-speed droplets in the air in the upper left and upper right corners and much turbulence. As the speed increases to 1000rpm (Figure 12B), compared with the wind field without downward pressure in Figure 12A, under the influence of the downwash wind field generated by the rotor, the speed and range of action of the droplets in the sector area have changed significantly. The turbulence pattern in the upper left and upper right corners shows a particularly significant change. The number of droplets decreases, and the velocity decreases significantly to almost zero. Under the nozzle, not only the velocity value but also the high-speed range of the droplets increases significantly. The high-speed area near the nozzle is shaped as a half ellipse with a long axis perpendicular to the Y-axis. The fan distribution of droplets generated by the nozzle is more obvious. The effective range of the high-speed area of droplets is mainly distributed in the fan area of X (-70, 90) Y (0, -140), the effective range of the medium-speed area decreases, and the low-speed area in the lower left and right corners increases. On the edge of both sides of the sector area, there are apparent channels of medium-speed droplets layer between the high-speed area and the air.

It can be seen from Figures 12C-E that with the increase of rotor speed, the downward pressure wind field is gradually enhanced, and the droplet high-speed area under the rotor contracts, obviously. Not only does the high-speed zone contract, but the droplet velocity decreases gradually. The effective range distribution of the high-speed zone gradually contracts from X (-65, 90) Y (0, -130) to the sector of X (-55, 85) Y (0, -110). In addition, the core area of the high-speed zone below the nozzle is the most obvious situation: the droplet area and velocity decrease. Even the core area is mostly disconnected from the surrounding area of the high-speed area (Figure 12E). At the same time, the low-speed area in the lower left corner and lower right corner of the area in the figure gradually increases with the increase of rotor speed, especially the expansion in the lower right corner is the most obvious.

By comparing the conditions in the high-speed area of each droplet velocity field in Figure 12, it can be found that the droplet velocity in the central area of the sector in the high-speed area tends to decrease successively. This trend not only indicates that the number of droplets is more concentrated in the unit volume, which causes the laser coming from the right side to be refracted more and weakens the intensity of the laser on the left side but also indicates that under the action of the wind field under the rotor, the speed of the droplets emitted from the fan nozzle weaken with the increase of the rotor speed. The expansion of the low-speed zone between the lower left corner and the lower right corner also proves that the droplet velocity from the fan nozzle weakens with the increase of rotor speed.

Similarly, Figure 13 shows the number distribution of droplets in different rotor speed intervals. Figure 13A shows that the maximum droplet velocity is about 18 m/s, and there are mainly two peaks in the quantity distribution of droplet velocity. The peak with the most significant number occurs in the interval of 8.5-9.5 m/s, followed by the interval of 15.5-16.5 m/s. The speed of droplets is primarily concentrated in the medium speed interval of 6-16 m/s, followed by high speed and low speed. Figure 13B shows the distribution of droplet velocity when the rotor speed is 1000rpm, and the maximum droplet velocity is about 19 m/s. With the appearance of the downwash wind field under the rotor, the maximum droplet velocity does not increase significantly, but the peak value of the number distribution of droplet velocity changes. However, the peak value of the medium-speed area becomes more. At the same time, a large number of low-speed droplets also appears in the low-speed area where there are only a few droplets, and the peak value is generated. The peak value of the medium-speed area is mainly distributed in the interval of 7-9 m/s, 11-12 m/s, 13.5-14.5 m/s, and 15-16 m/s, while the peak value of the low-speed area is mainly in the interval of 0.5-1.5 m/s.

Figures 13C-E show the quantity distribution of droplet velocity at 1500rpm, 2000rpm and 2500rpm of rotor speed, respectively. It can be seen from the figures of 13c and 13d that when the rotor speed is 1500rpm and 2000rpm, the maximum speed of the droplet field is basically 19m/s. However, in Figure 13E, when the rotor speed is 2500rpm, the maximum speed of the droplet field is only 18m/s, indicating that the droplet field is affected by the increase of the rotor speed. The maximum velocity of the droplet field is also weakened. At the same time, compared with Figure 13B, the total droplet velocity in the high-speed area decreases, and two apparent peaks appear in the medium-speed area. In addition, by comparing the medium-speed intervals of Figures 13C-E, it can be found that the peak value of the medium-speed zone extends from the intervals of 8-9 m/s and 15-16 m/s in Figure 13C to 6.5-8 m/s and 13.5-16 m/s, respectively, indicating that the number of droplets in the medium-speed zone gradually increases and the effect of wind

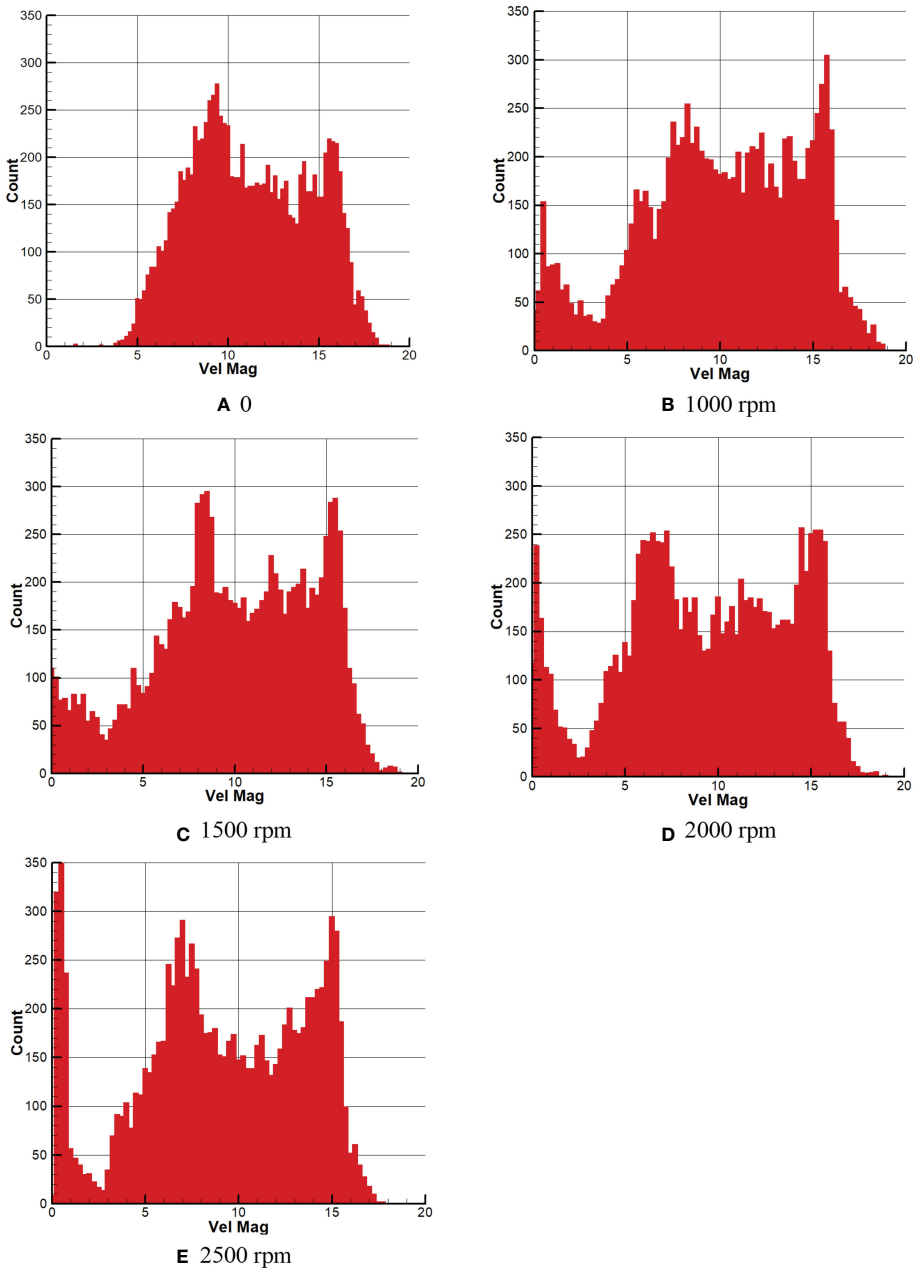

FIGURE 13
Quantitative distribution of average droplet velocity at different rotor speeds.

field downward pressure is obvious. At the same time, it can also be seen from the figures of the three, the number of droplets in the low-speed area also increases significantly. The number of droplets in the low-speed area with the speed toward zero concentration is the most obvious, especially in Figure 13E.

As seen in Figure 13, the speed in the overall droplet field is weakened due to the generation of the rotor wind field. Furthermore, with the increase of rotor speed, it can be seen that the droplet velocity in the low-speed area gradually concentrated at 0, and the turbulence in the whole study area basically disappear. Due to laser refraction caused by the concentration of the number of droplets on the right side, the droplets in the left area are not sufficiently obtained, and the velocity data are not apparent. Because of this, the peak value of the total number of droplets in the medium-speed area gradually tends to both sides of the medium-speed area, which makes two prominent peaks appear in the medium-speed area, which should be relatively gentle.

In conclusion, it can be seen from Figure 12 that the high-speed area generated at the nozzle location is obviously different due to the downwash wind field caused by the increase of rotor

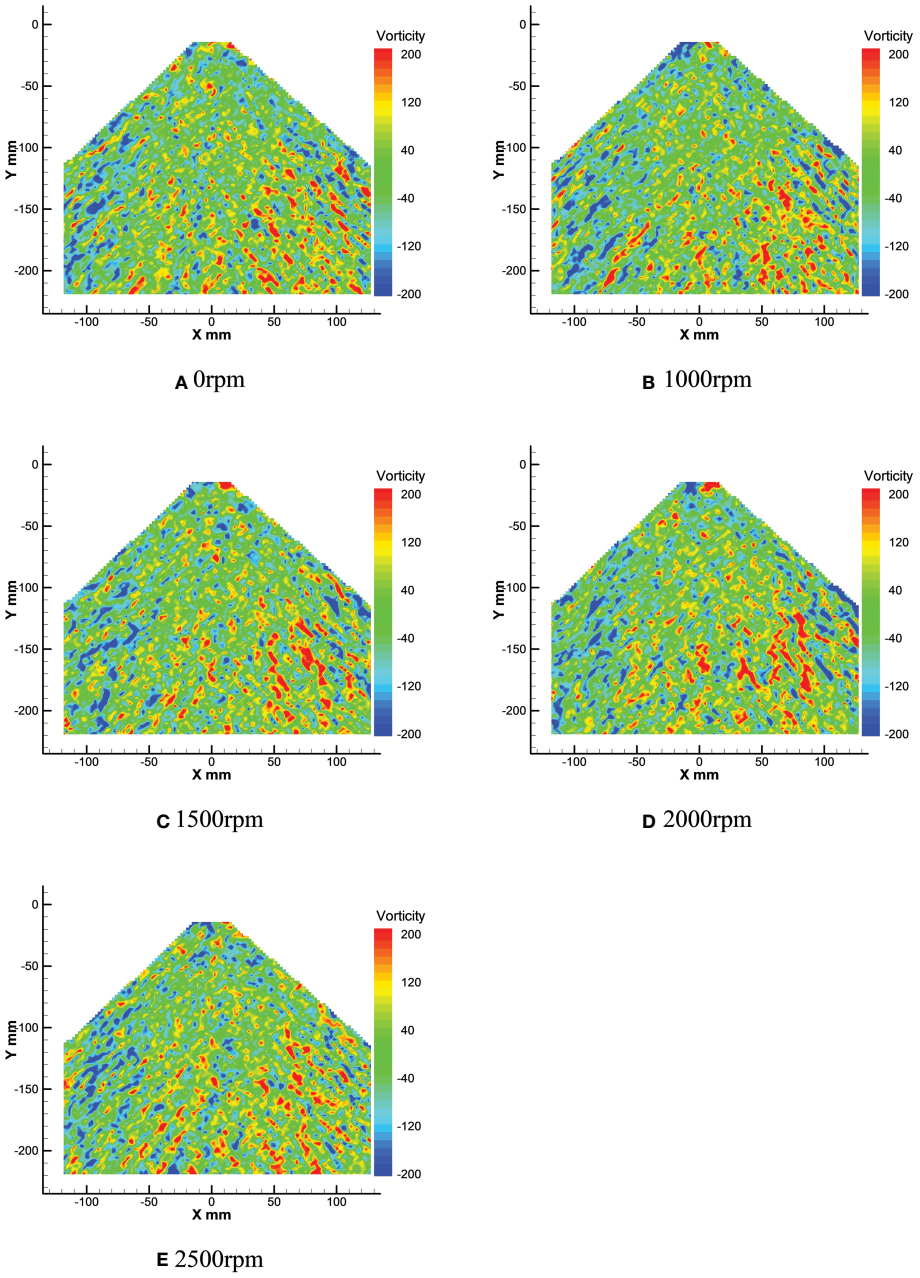

FIGURE 14
Average droplets vorticity field at different rotor speeds.

speed. With the increase of rotor speed, the downwash wind field is gradually strengthened, and the high-speed area at the nozzle is gradually contracted and decreased. At the same time, the total spray angle of the nozzle is gradually reduced, and the number of droplets in the sector area is gradually concentrated. The high-speed area gradually decreases, and the low-speed area gradually expands in the whole spray sector area. As can be seen from Figure 13, the maximum velocity of droplets in the sector area is 19 m/s, which is basically unchanged. When the total number of droplets in the high-speed area is 1000rpm, the number of droplets in the high-speed area is the largest, and the number of droplets in the high-speed area gradually decreases with the increase of the rotor speed. The number of droplets in the medium-speed zone and low-speed zone increases obviously. The turbulent conditions in the upper left and upper right corners disappear.

Distribution of rotor vorticity under the PIV experiment

Figure 14 shows the vortex field of the nozzle droplet at different rotor speeds. Figure 15 shows droplet vortex size and quantity distribution at different rotor speeds.

Through the vortex analysis of Figure 14, it can be seen that positive vortex and negative vortex cross in the droplets field, and it can be clearly seen that the left side of the droplets field is dominated by negative vortex, and the right side is dominated by positive vortex. Through numerical analysis of the vortex field, it can be seen that in Figure 14A, the extreme values of the vortex in the droplets field are -449.14s^{-1} and 819.02s^{-1} respectively. However, under the effect of the rotor wind field, the extreme value here changes. In Figure 14B, the extreme value of the vortex in the droplets field changes to -502.91s^{-1} and 463.75s^{-1}. Compared with Figure 14B, the positive vortex in the droplets field has significantly changed and decreased by 355.27s^{-1}, while the negative vortex in the droplets field has slightly changed and only increased by 53.77s^{-1}. In Figures 14C, 14D, the extreme value of the negative vortex in the droplets field decreases, both of which are around -485s^{-1}. The extreme value of the positive

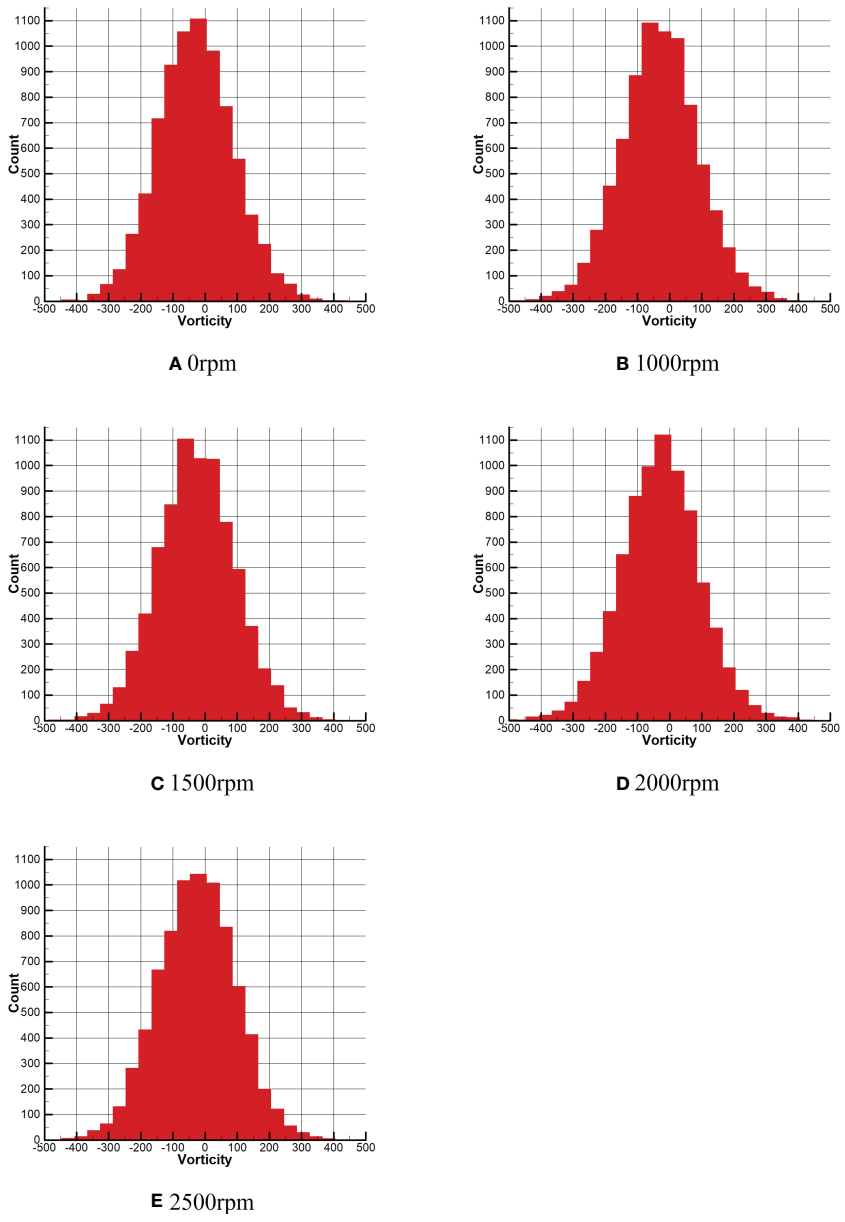

FIGURE 15
Quantity distribution of the average droplet vorticity at different rotor speeds.

vortex in Figure 14C reaches 589.64s^{-1}, while the extreme value of the positive vortex in Figure 14D reaches 478.32s^{-1}, decreasing by 111.44s^{-1}. In Figure 14E, the extreme values of the droplet field are -597.93s^{-1} and 463.27s^{-1} respectively. Compared with Figure 14D, the positive vortex in the droplets field decreased by 15.05s^{-1}, while the negative vortex in the droplet field changed greatly and increased by 113.51s^{-1}.

The vortex between (-500, 500) are selected as the X-axis, and the number of vortex under different vorticity is selected as the Y-axis for analysis in the Figure 15. As can be seen from Figure 15A, the total number of vortex in the range of (-100, 0) exceeds 1000. After the rotor wind field is generated, as shown in Figure 15B, the range of the total number of vortex exceeding 1000 changes to (-100, 50), and the range is expanded. In Figure 15C, the range where the total number of vortex exceeds 1000 remains basically unchanged. However, it can be seen from Figure 15D that the range of the total vortex exceeding 1000 becomes smaller, and only the range (-50, 0) exceeding 1000. However, from the whole of Figure 15D, the droplets are more concentrated on both sides of the 0 vortex. In Figure 15E, the range of vortex exceeding 1000 is mainly concentrated in the range (-100, 50), but the total number of vortex in this range is somewhat reduced compared with that in Figure 15B.

According to the combination of Figure 14 and Figure 15, the left side of the droplets field is dominated by negative vortex, while the right side is dominated by positive vortex. With the increase of rotor speed, the extreme value and number of vortex in the droplets field change in different degrees. The negative vortex in the droplets field increases first, then decreases and then increases, while the positive vortex decreases first, then increases and then decreases. Compared with the vortex under the effect of no wind field, the maximum value of negative vortex under the effect of rotor wind field is reduced by 148.79s^{-1}, while the maximum value of positive vortex is reduced by 355.27s^{-1}. Meanwhile, it can be seen from Figure 15 that under the effect of no wind field, the majority of vortex near 0 in the vortex field are negative vortex. However, with the increase of rotor speed, the number of positive vortex near 0 and negative vortex is gradually equal.

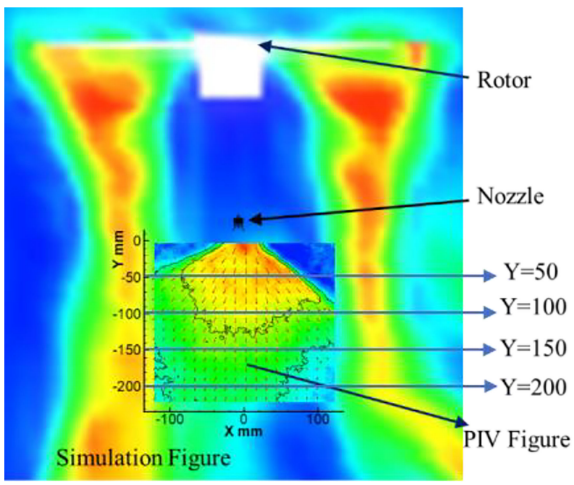

FIGURE 16
The schematic diagram.

Discussion

In this paper, the droplet velocity distribution at four different horizontal levels (Y=50mm, 100mm, 150mm, 200mm) of the coordinate system in PIV image is selected for comparative analysis and research with wind field velocity at four different horizontal levels corresponding to the coordinate system in numerical simulation. The schematic diagram of horizontal level selection is shown in Figure 16. In this study, the data under each level are averaged to obtain the average value. In the numerical simulation test, the data at the time of 3s is selected for analysis. In the data of PIV experiment, the vertical velocity data is selected as the analysis sample. Thus, the mean value and variance results of PIV test and numerical simulation are shown in Table 3, and the change trend of the mean value of PIV and numerical simulation is shown in Figure 17.

As can be seen from the Figure 17, with the increase of rotor speed, the average velocity of the wind field in the numerical simulation test shows an overall trend of increase, while the average velocity of droplets in the PIV test shows an overall trend of decrease, indicating that the wind field significantly reduces the average velocity of droplets. As can be seen from the Figure 17, in the numerical simulation test, the wind speed of four levels at each rotor speed has little difference.

However, in the PIV test, there is a large difference in droplet velocity under different levels. The average velocity of droplets at the level of Y=200 mm is the minimum, while the average velocity of droplets at the level of Y=100 mm is the maximum, even exceeding the average velocity of droplets at the level of Y=50 mm. This is because at the level of Y=50mm, the velocity of some droplets is close to 0 and the velocity variance is about 5.3, while at other levels, the velocity variance of droplets is about 2.6, thus dragging down the overall average velocity.

Meanwhile, it can also be seen from Figure 17 and Table 3 that the wind speed generated by the wind field increases gradually on the whole with the gradual increase of rotor speed. However, when the rotor speed is 1000rpm, the speed in the wind field is higher than that when the rotor speed is 1500rpm. According to the analysis results of the speed value, the variance of the speed value is smaller than that of other speeds when the rotor speed is 1000rpm. This indicates that when the rotator speed is 1000rpm, the vortex in this range is small and the velocity value is relatively uniform. Combined with the PIV test results, it can be seen that the variances of PIV

TABLE 3 The mean value and variance results of PIV test and numerical simulation.

	Rotor Speed/rpm	Y=50mm		Y=100mm		Y=150mm		Y=200mm	
		Mean	SD	Mean	SD	Mean	SD	Mean	SD
PIV	1000	9.9	5.32	11.35	2.65	9.17	2.56	6.96	1.74
	1500	9.75	5.31	11.38	2.61	9.03	2.61	7.06	1.68
	2000	9.53	5.22	11.8	2.93	8.37	2.51	6.03	1.43
	2500	8.91	5.50	10.99	2.84	8.19	2.61	6.1	1.53
Sim	1000	4.54	1.91	4.56	1.79	4.61	1.82	4.20	1.86
	1500	4.45	2.24	4.26	1.99	4.20	1.86	3.92	1.72
	2000	5.25	2.70	5.52	2.95	5.38	3.30	4.63	3.35
	2500	6.27	2.35	6.68	2.75	6.63	1.86	5.81	2.30

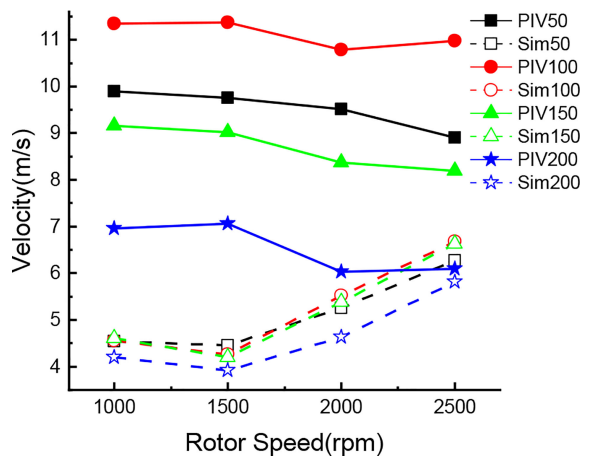

FIGURE 17
The change trend of the mean value of PIV and numerical simulation.

droplet speeds at these two speeds are also very close, indicating that the PIV test data can effectively reflect the accuracy of the numerical simulation. When the rotor speed in the numerical simulation exceeds 2000rpm, the droplet velocity in the PIV test decreases significantly, and the rotor downwash wind field has a significant influence on the movement velocity of droplets at all levels. Although the speed at the level of Y=200mm in numerical simulation is the smallest compared with other levels, combined with the change of droplets in PIV test, it has a certain influence on the droplets at the level of Y=200mm. Combined with the above analysis, it can be seen that this is because the numerical simulation of the wind field at Y=200mm began to appear a certain degree of vortex, which reduced the movement speed of droplets.

Through the above analysis, it can be seen that in the numerical simulation, the speed is relatively stable at 1000rpm and 1500rpm. Under these two rotor speeds, the droplet velocities at all levels in PIV are also basically stable, which proves that the droplet velocity under PIV test can effectively verify the reliability of the numerical simulation. At the same time, when the rotor speed exceeds 2000rpm, the speed in the numerical simulation increases significantly. Correspondingly, the droplet velocity in PIV test all decreased to varying degrees, among which the droplet velocity change was most obvious at the level of Y=200mm. Therefore, combined with the above analysis, PIV test can effectively verify the validity of the numerical simulation results.

At present, the mechanical analysis of droplet velocity and vorticity variation has not been effectively and comprehensively verified. In this paper, PIV test is used to effectively analyze the motion state of droplets field under the action of wind field. By analyzing the distribution of velocity flow and vortex in droplet field, it is concluded that under the action of wind field of rotor, the velocity of droplet is reduced, while the vortex shrinks and the vorticity increases. PIV test can reflect the reliability of numerical simulation results from the side. The downwash wind field of plant protection UAV is very complicated, and it has a very important influence on the deposition and drift of droplet. Therefore, based on the actual operation of plant protection UAVs, this paper expounds the influence mechanism of rotor wind field of plant protection UAVs on droplets distribution characteristics under different rotor speeds based on the distribution characteristics of rotor wind field under dynamic load (at different speeds), providing references for researchers in this field.

Conclusion

The XFlow software was used to simulate the downwash wind field of the quadrotor plant protection UAV at different rotor speeds, and the particle image velocimetry (PIV) was used to measure the motion state of droplets at different rotor speeds. The main findings of this experiment are summarized as follows:

The experimental results of numerical simulation show that the maximum velocity and vorticity of the downwash field under the rotor increase with the increase of rotor speed. However, with the increase of time, turbulence is generated, and the maximum values of the downwash wind velocity and vorticity decrease. The velocity flow field under the rotor becomes more widely distributed. In addition, the velocity flow and vortex under the rotor are symmetrically distributed in the centre line of the fuselage, mainly distributed in the range of (-1m, 1m) in the X direction. The larger value of velocity flow is mainly concentrated in the area within 1m below the rotor, and the vortex is mainly concentrated in the area within 0.5m.

The results of the PIV test show that with the increase of rotor speed, the total spray angle and the high-speed area of the spray area gradually shrink and decrease under the action of the downwash wind field, while the low-speed area in the spray area gradually expands. In addition, the maximum velocity of droplet particles under the rotor wind field is 19m/s. The number of droplet particles decreases gradually in the high-speed area, while the number of droplet particles increases gradually in the medium-speed area and low-speed area. When there is no downwash wind field, there is a lot of turbulence in the fan droplet area, and the maximum vorticity is the 819.02. But under the effect of the downwash wind field produced by the rotor, the vortex is contracted. Under the effect of no wind field, most of the eddies near 0 are negative vortex in the vortex field, but with the increase of rotor speed, the number of positive vortex near 0 and negative vortex is gradually equal.

Through comparative analysis of the PIV test and numerical simulation results, it can be seen that the maximum speed of the numerical simulation wind field in the area within 0.5m below the rotor reaches 15.7m/s. In the PIV test, the speed of the droplet in the droplet field in this range is about 18 m/s under the action of the nozzle pressure, and the speed of the turbulent droplet in the upper left and upper right corner outside the sector area is about 8m/s. Due to the increase of rotor speed and the enhancement of the downwash wind field, the turbulence disappears in the upper left and upper right corners of the sector area, and the number of low-speed droplets increases in the lower left and right corners of the sector area in the PIV test, which indicates that the PIV test results effectively verify the reliability of the numerical simulation results.

Data availability statement

The original contributions presented in the study are included in the article/supplementary material. Further inquiries can be directed to the corresponding authors.

Author contributions

KC, SC, and YL: conceptualization. KC: formal analysis and writing-original draft. SC, MW and YL: resources and supervision. SC, XX and YL writing-review and editing and funding acquisition. YL: project administration. All authors contributed to the article and approved the submitted version.

Funding

The study was funded by Laboratory of Lingnan Modern Agriculture Project(NT2021009), the National Natural Science Foundation of China (Grant No.31901411), the Basic and Applied Basic Research Foundation of Guangdong Province (2022A1515011535), The 111 Project (D18019), the science and technology planning project of Guangzhou (202201010642), the leading talents program of Guangdong Province (2016LJ06G689), Key-Area Research and Development Program of Guangdong Province(2019B020214003).

Acknowledgments

We acknowledged the contributions of specific colleagues, institutions, or agencies that aided the efforts of the authors.

Conflict of interest

The authors declare that the research was conducted in the absence of any commercial or financial relationships that could be construed as a potential conflict of interest.

Publisher's note

References

Chen, P., Douzals, J. P., Lan, Y., Cotteux, E., Delpuech, X., Pouxviel, G., et al. (2022). Characteristics of unmanned aerial spraying systems and related spray drift: A review. *Front. Plant Sci.* 13. doi: 10.3389/fpls.2022.870956

Chen, S., Yubin, L., Li, J., Zhou, Z., Liu, A., and Mao, Y. (2017). Effect of wind field below unmanned helicopter on droplet deposition distribution of aerial spraying. *Int. J. Agric. Biol. Eng.* 48 (08), 105–113. doi: 10.3965/j.ijabe.20171003.3078

Dongyan, Z., Yubin, L., and Liping, C. (2014). Current status and future trends of agricultural aerial spraying technology in China. *Trans. Chin. Soc. Agric. Machinery* 45 (10), 53–59. doi: 10.1064/j.issn.1000-1298.2014.10.009

Fakhari, A., and Lee, T. (2015). Numerics of the lattice boltzmann method on nonuniform grids: Standard LBM and finite-difference LBM. *Comput. Fluids* 107, 205–213. doi: 10.1016/j.compfluid.2014.11.013

Fengbo, Y., Xinyu, X., Chen, C., and Qingqing, Z. (2018). Effect of down wash airflow in hover on droplet motion law for multi-rotor unmanned plant protection machine. *Trans. Chin. Soc. Agric. Eng.* 34 (02), 64–73. doi: 10.11975/j.issn.1002-6819.2018.02.009

Guo, Q., Zhu, Y., Tang, Y., Hou, C., He, Y., Zhuang, J., et al. (2020). CFD simulation and experimental verification of the spatial and temporal distributions of the downwash airflow of a quad-rotor agricultural UAV in hover. *Comput. Electron. Agric.* 172, 1–11. doi: 10.1016/j.compag.2020.105343

Hao, Z., Lijun, Q., Yalei, W., Zhenzhen, C., Wanwan, L., Musiu, E., et al. (2019). Distribution characteristics of rotor downwash airflow field under spraying on orchard using unmanned aerial vehicle. *Trans. Chin. Soc. Agric. Eng.* 35 (18), 44–54. doi: 10.11975/j.issn.1002-6819.2019.18.006

Huang, Y., Thomson, S. J., Hoffmann, W. C., Lan, Y., and Fritz, B. K. (2013). Development and prospect of unmanned aerial vehicle technologies for agricultural production management. *Int. J. Agric. Biol. Eng.* 6 (3), 1–10. doi: 10.3965/j.ijabe.20130603.001

Jin, Z., Dong, Q., and Yang, Z. (2014). A stereoscopic PIV study of the effect of rime ice on the vortex structures in the wake of a wind turbine. *J. Wind Eng. Ind. Aerodynamics* 134, 139–148. doi: 10.1016/j.jweia.2014.09.001

Jiyu, L., Yubin, L., and Yeyin, S. (2018). Research progress on airflow characteristics and field pesticide application system of rotary-wing UAV. *Trans. Chin. Soc. Agric. Eng.* 34 (12), 104–118. doi: 10.11975/j.issn.1002-6819.2018.12.013

Jiyu, L., Zhiyan, Z., and Lian, H. (2014a). Optimization of operation parameters for supplementary pollination in hybrid rice breeding using round multi-axis multi-rotor electric unmanned helicopter. *Trans. Chin. Soc. Agric. Eng.* 30 (11), 1–9. doi: 10.3969/j.issn.1002-6819.2014.11.001

Jiyu, L., Zhiyan, Z., and Lian, H. (2014b). Optimization of operation parameters for supplementary pollination in hybrid rice breeding using uniaxial single-rotor electric unmanned helicopter. *Trans. Chin. Soc. Agric. Eng.* 30 (10), 10–17. doi: 10.3969/j.issn.1002-6819.2014.10.002

Juan, W., Yubin, L., Weixiang, Y., Pengchao, C., Jinli, L., and Yingbin, Y. (2019). Effects of working height of single-rotor unmanned aerial vehicle on drift and droplets deposition distribution of areca tree. *Trans. Chin. Soc. Agric. Machinery* 50 (07), 109–119. doi: 10.6041/j.issn.1000-1298.2019.07.011

Junfeng, W., Wenbin, X., Jianlong, W., Xiaoying, W., and Botao, L. (2017). Numerical simulation on gas-liquid phase flow of Large-scale plant protection unmanned aerial vehicle spraying. *Trans. Chin. Soc. Agric. Machinery* 48 (09), 62–69. doi: 10.6041/j.issn.1000-1298.2017.09.008

Pan, Z., and Qiang, L. (2016). Evaluation of spraying effect using small unmanned aerial vehicle(UAV)in citrus orchard. *J. Fruit Sci.* 33 (01), 34–42. doi: 10.13925/j.cnki.gsxb.20150182

Shahbazi, M., Théau, J., and Ménard, P. (2014). Recent applications of unmanned aerial imagery in natural resource management. *GISci. Remote Sens.* 51 (4), 339–365. doi: 10.1080/15481603.2014.926650

Shengde, C., Yubin, L., Jiyu, L., Zhiyan, Z., Ji, J., and Aimin, L. (2016). Effect of spray parameters of small unmanned helicopter on distribution regularity of droplet deposition in hybrid rice canopy. *Trans. Chin. Soc. Agric. Eng.* 32 (17), 40–46. doi: 10.11975/j.issn.1002-6819.2016.17.006

Sheng, W., Jie, H., Yubin, L., Xuanchun, Y., and Yuhua, L. (2018). Influence of wing tip vortex on drift of single R otor plant protection unmanned aerial vehicle. *Trans. Chin. Soc. Agric. Machinery* 49 (08), 127–137+160. doi: 10.6041/j.issn.1000-1298.2018.08.015

Shuai, Y. (2014). *Spray droplet deposition and distribution inside crop canopy and control efficiency applied by unmanned aerial vehicle* (Beijing, China: Chinese Academy of Agricultural Sciences). Master.

Songchao, Z., Xinyu, X., and Weicai, Q. (2015). Simulation and experimental verification of aerial spraying drift on n-3 unmanned spraying helicopter. *Trans. Chin. Soc. Agric. Eng.* 31 (03), 87–93. doi: 10.3969/j.issn.1002-6819.2015.03.012

Songchao, Z., Xinyu, X., Zhu, S., Lixin, Z., and Yongkui, J. (2017). Downwash distribution of single-rotor unmanned agricultural helicopter on hovering state. *Int. J. Agric. Biol. Eng.* 10 (5), 14–24. doi: 10.25165/j.ijabe.20171005.3079

Tang, Q., Chen, L., Zhang, R., Deng, W., Xu, M., Xu, G., et al. (2021). Effects of application height and crosswind on the crop spraying performance of unmanned helicopters. *Comput. Electron. Agric.* 181, 1–18. doi: 10.1016/j.compag.2020.105961

Tang, Y., Hou, C. J., Luo, S. M., Lin, J. T., Yang, Z., and Huang, W. F. (2018). Effects of operation height and tree shape on droplet deposition in citrus trees using an unmanned aerial vehicle. *Comput. Electron. Agric.* 148, 1–7. doi: 10.1016/j.compag.2018.02.026

Tang, Q., Zhang, R., Chen, L., Deng, W., Xu, M., Xu, G., et al. (2020a). Numerical simulation of the downwash flow field and droplet movement from an unmanned helicopter for crop spraying. *Comput. Electron. Agric.* 174, 1–14. doi: 10.1016/j.compag.2020.105468

Tang, Q., Zhang, R., Chen, L., Xu, G., Deng, W., Ding, C., et al. (2020b). High-accuracy, high-resolution downwash flow field measurements of an unmanned helicopter for precision agriculture. *Comput. Electron. Agric.* 173, 1–12. doi: 10.1016/j.compag.2020.105390

Tang, Q., Zhang, R., Ding, C., Chen, L., Xu, M., Xu, G., et al. (2019). Application of ultrasonic anemometer array to field measurements of the downwash flow of an agricultural unmanned helicopter. *Trans. ASABE* 62 (5), 1219–1230. doi: 10.13031/trans.13336

Wang, C., He, X., Wang, X., Wang, Z., Wang, S., Li, L., et al. (2018). Testing method and distribution characteristics of spatial pesticide spraying deposition quality balance for unmanned aerial vehicle. *Int. J. Agric. Biol. Eng.* 11 (2), 18–26. doi: 10.25165/j.ijabe.20181102.3187

Wang, G., Lan, Y., Qi, H., Chen, P., Hewitt, A., and Han, Y. (2019). Field evaluation of an unmanned aerial vehicle (UAV) sprayer: effect of spray volume on deposition and the control of pests and disease in wheat. *Pest Manag Sci.* 75 (6), 1546–1555. doi: 10.1002/ps.5321

Wang, L., Xu, M., Hou, Q., Wang, Z., Lan, Y., and Wang, S. (2021). Numerical verification on influence of multi-feature parameters to the downwash airflow field and operation effect of a six-rotor agricultural UAV in flight. *Comput. Electron. Agric.* 190, 1–10. doi: 10.1016/j.compag.2021.106425

Wu, Y., Qi, L., Zhang, H., Musiu, E. M., Yang, Z., and Wang, P. (2019). Design of UAV downwash airflow field detection system based on strain effect principle. *Sensors (Basel)* 19 (11), 1–18. doi: 10.3390/s19112630

Xiaonan, W., Xiongku, H., Changlin, W., Zhichong, W., Longlong, L., Shilin, W., et al. (2017). Spray drift characteristics of fuel powered single-rotor UAV for plant protection. *Trans. Chin. Soc. Agric. Eng. (Transactions CSAE)* 33 (01), 117–123. doi: 10.11975/j.issn.1002-6819.2017.01.016

Xiongkui, H., Bonds, J., Herbst, A., and Langenakens, J. (2017). Recent development of unmanned aerial vehicle for plant protection in East Asia. *Int. J. Agric. Biol. Eng.* 29 (06), 5–12. doi: 10.19518/j.cnki.cn11-2531/s.2017.0130

Yong, G., Nan, W., and Baoxing, J. (2017). Development status of unmanned aircraft for agricultural plant protection. *Agric. Eng.* 7 (02), 24–25+28.

Yuan-yuan, G. (2013). *Study on distribution of pesticide droplets in gramineous crop canopy and control effect sprayed by unmanned aerial vehicle (UAV) study on distribution of pesticide droplets in gramineous crop canopy and control effect sprayed by unmanned aerial vehicle (UAV)* (Harbin, China: Northeast Agricultural University). Master.

Zhan, Y., Chen, P., Xu, W., Chen, S., Han, Y., Lan, Y., et al. (2022). Influence of the downwash airflow distribution characteristics of a plant protection UAV on spray deposit distribution. *Biosyst. Eng.* 216, 32–45. doi: 10.1016/j.biosystemseng.2022.01.016

Zhang, H., Qi, L., Wu, Y., Musiu, E. M., Cheng, Z., and Wang, P. (2020). Numerical simulation of airflow field from a six–rotor plant protection drone using lattice Boltzmann method. *Biosyst. Eng.* 197, 336–351. doi: 10.1016/j.biosystemseng.2020.07.018

Zhang, B., Tang, Q., Chen, L.-p., and Xu, M. (2016). Numerical simulation of wake vortices of crop spraying aircraft close to the ground. *Biosyst. Eng.* 145, 52–64. doi: 10.1016/j.biosystemseng.2016.02.014

Zheng, Y., Yang, S., Zhao, C., Chen, L., Yubin, L., and Tan, Y. (2017). Modelling operation parameters of UAV on spray effects at different growth stages of corns. *Int. J. Agric. Biol. Eng.* 10 (3), 57–66. doi: 10.3965/j.ijabe.20171003.2578

Frontiers in
Plant Science

Cultivates the science of plant biology and its applications

The most cited plant science journal, which advances our understanding of plant biology for sustainable food security, functional ecosystems and human health.

Discover the latest Research Topics

See more →

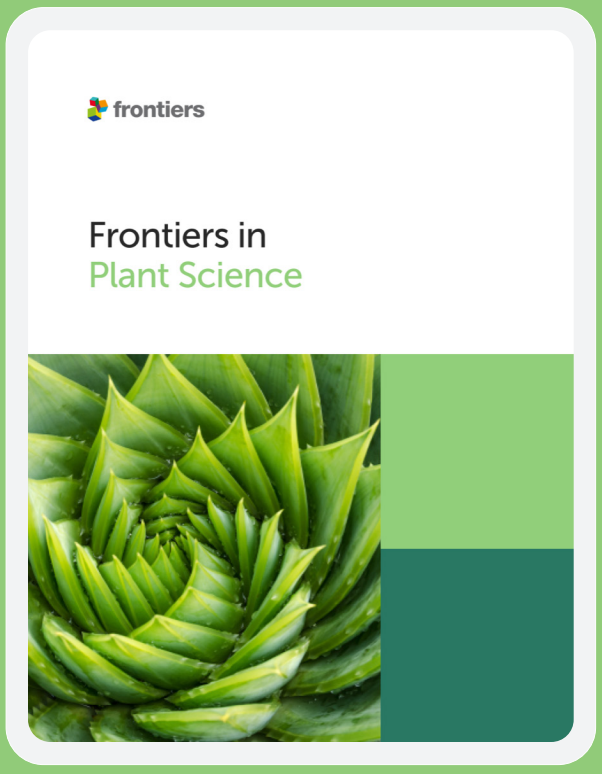

Frontiers

Avenue du Tribunal-Fédéral 34
1005 Lausanne, Switzerland
frontiersin.org

Contact us

+41 (0)21 510 17 00
frontiersin.org/about/contact